

# Ferromagnetic thin films of Fe and Fe<sub>3</sub>Si on low-symmetric GaAs(113)A substrates

## DISSERTATION

zur Erlangung des akademischen Grades  
doctor rerum naturalium  
(Dr. rer. nat.)  
im Fach Physik

eingereicht an der  
Mathematisch-Naturwissenschaftlichen Fakultät I  
Humboldt-Universität zu Berlin

von

Herr M.Tech. M.Sc. Pranaba Kishor Muduli  
geboren am 01.11.1978 in Jagatsigpur, Indien

Präsident der Humboldt-Universität zu Berlin:  
Prof. Dr. Hans Jürgen Prömel (in Vertretung)

Dekan der Mathematisch-Naturwissenschaftlichen Fakultät I:  
Prof. Thomas Buckhout, PhD

Gutachter:

1. Prof. Dr. Klaus H. Ploog
2. Prof. Dr. K. R. A. Ziebeck
3. Prof. Dr. W. Ted Masselink

eingereicht am: 29. September 2005  
Tag der mündlichen Prüfung: 15. Dezember 2005

## Zusammenfassung

In dieser Arbeit werden das Wachstum und die Eigenschaften von dünnen ferromagnetischen Filmen auf niedrig-symmetrischen GaAs(113)A- Substraten studiert. Die zwei in dieser Arbeit untersuchten ferromagnetischen Metalle, Fe und Fe<sub>3</sub>Si, besitzen eine kubische Kristallstruktur und haben eine enge Gitteranpassung an das GaAs-Substrat. Dadurch ist es möglich, die [113]- Orientierung mittels Molekularstrahlepitaxie (MBE) auf GaAs(113)A- Substraten zu stabilisieren. Diese Dissertation behandelt drei wichtige Aspekte: (i) Wachstum und strukturelle Charakterisierung, (ii) magnetische Eigenschaften und (iii) Magnetotransporteigenschaften der Fe und Fe<sub>3</sub>Si Filme auf GaAs(113)A-Substraten.

Das Wachstum der Fe- und Fe<sub>3</sub>Si-Filme wurde bei einer Wachstumstemperatur von 0 bzw. 250 °C optimiert. Bei diesen Wachstumstemperaturen zeigen die Schichten eine hohe Kristall- und Grenzflächenperfektion. Die strukturellen Eigenschaften der Fe(113)- und Fe<sub>3</sub>Si(113)-Filme sind vergleichbar mit denen, die bei [001]-orientierten Filmen erreicht werden. Weiterhin wird die Stabilität der Fe<sub>3+x</sub>Si<sub>1-x</sub>-Phase über einen weiten Kompositionsbereich innerhalb der Fe<sub>3</sub>Si-Stöchiometrie demonstriert.

Die Beschreibung der magnetischen Eigenschaften der Fe- und Fe<sub>3</sub>Si-Filme konzentriert sich auf die magnetische Anisotropie als Funktion von drei verschiedenen Parametern: der Schichtdicke (für Fe-Filme), der Wachstumsbedingungen und der Komposition (für Fe<sub>3</sub>Si-Filme). Die Abhängigkeit der magnetischen Anisotropie innerhalb der Schichtebene von der Schichtdicke weist zwei Bereiche auf: einen Bereich mit dominanter uniaxialer magnetischer Anisotropie (UMA) für Fe-Filme  $\leq 50$  MLs und einen Bereich mit vierfacher magnetischer Anisotropie für Fe-Filme  $\geq 70$  MLs. Weiterhin wird eine magnetische Anisotropie senkrecht zur Schichtebene in sehr dünnen Filmen gefunden. Der Grenzflächenbeitrag sowohl der uniaxialen als auch der senkrechten Anisotropiekonstanten, die aus der Dickenabhängigkeit bestimmt wurden, sind unabhängig von der [113]-Orientierung und somit eine inherente Eigenschaft der Fe/GaAs-Grenzfläche. Die anisotrope Bindungskonfiguration zwischen den Fe und den As oder Ga Atomen an der Grenzfläche wird als Ursache für die UMA betrachtet. Die magnetische Anisotropie der Fe<sub>3</sub>Si-Filme auf GaAs(113)A-Substraten zeigt eine komplexe Abhängigkeit von den Wachstumsbedingungen und der Komposition der Filme. Dabei tritt eine zusätzliche UMA unter bestimmten Bedingungen auf. Die Anisotropiekonstante der vierfachen magnetischen Anisotropie verringert sich mit steigenden Si-Gehalt, was aufgrund der reduzierten Symmetrie in der Umgebung der Fe-Atome beim Einbau von Si erwartet wird.

In den Magnetotransportuntersuchungen tritt sowohl in Fe(113)- als auch in Fe<sub>3</sub>Si(113)-Filmen eine antisymmetrischen Komponente (ASC) im planaren Hall-Effekt auf, die innerhalb eines phänomenologischen Modells, das auf der Symmetrie des Kristalls basiert, verstanden werden kann. Das Modell zeigt, dass dieser Effekt als Hall-Effekt zweiter Ordnung beschrieben werden kann. Reine Fe-Schichten und stöchiometrische Fe<sub>3</sub>Si-Filme zeigen dasselbe Vorzeichen der ASC. Die Erhöhung der atomaren Ordnung in stöchiometrischen Fe<sub>3</sub>Si-Filmen, die die D0<sub>3</sub> Kristallstruktur widerspiegelt, wird als mögliche Ursache für dieselben Vorzeichen in der ASC vorgeschlagen. Die Temperatur-abhängigkeit der ASC zeigt weiterhin einen Vorzeichenwechsel für leicht nichtstöchiometrische ( $0.05 \leq x \leq 0.15$ ) Fe<sub>3+x</sub>Si<sub>1-x</sub> Filme unterhalb einer bestimmten kritischen Temperatur, die mit Erhöhung des Si-Gehalts ansteigt.

### Schlagwörter:

Ferromagnetische Halbleiter-Mischlingstrukturen, Hochindexlagebestimmung, Planarer Hall effekt, Antisymmetric magnetoresistivity spanner

## Abstract

In this work, the growth and properties of ferromagnetic thin films are studied on low-symmetric GaAs(113)A substrates. The two ferromagnetic metals studied in this work, namely Fe and Fe<sub>3</sub>Si have cubic crystal structure and exhibit a close lattice match with GaAs. This allows to stabilize the [113]-orientation of the films on GaAs(113)A by using molecular-beam epitaxy (MBE). This dissertation deals with three important aspects: (i) growth and structural characterization, (ii) magnetic properties, and (iii) magnetotransport properties of Fe and Fe<sub>3</sub>Si films on GaAs(113)A substrates.

Using MBE, the growth of Fe and Fe<sub>3</sub>Si films is optimized at growth temperatures of 0 and 250 °C, respectively, where the layers exhibit high crystal quality and a smooth interface/surface. The structural properties of the Fe(113) and Fe<sub>3</sub>Si(113) films are shown to be comparable to the [001]-oriented films. The stability of Fe<sub>3+x</sub>Si<sub>1-x</sub> phase over a range of composition around the Fe<sub>3</sub>Si stoichiometry is also demonstrated.

The magnetic properties of Fe and Fe<sub>3</sub>Si films are mainly focused on the magnetic anisotropy as a function of three different parameters: thickness (for Fe films), growth conditions, and composition (for Fe<sub>3</sub>Si films). The evolution of the in-plane magnetic anisotropy with film thickness exhibits two regions: a uniaxial magnetic anisotropy (UMA) for Fe film thicknesses  $\leq 50$  MLs, and a four-fold magnetic anisotropy for Fe film thicknesses  $\geq 70$  MLs. The existence of an out-of-plane perpendicular magnetic anisotropy is also detected in ultrathin Fe films. The interfacial contribution of both the uniaxial and the perpendicular anisotropy constants derived from the thickness-dependent study are found to be independent of the [113] orientation and are hence an inherent property of the Fe/GaAs interface. The origin of the UMA is attributed to anisotropic bonding between Fe and As or Ga at the interface, similarly to Fe/GaAs(001). The magnetic anisotropy in Fe<sub>3</sub>Si on GaAs(113)A exhibits a complex dependence on the growth conditions and composition, with an additional UMA appearing under certain conditions. The four-fold magnetic anisotropy constant is found to decrease with Si content as expected due to the reduced symmetry environment of Fe atoms upon adding Si.

Magnetotransport measurements of both Fe(113) and Fe<sub>3</sub>Si(113) films shows the striking appearance of an antisymmetric component (ASC) in the planar Hall effect, which can be understood from a phenomenological model based on the symmetry of the crystal. The model shows that the effect can be ascribed to a second-order Hall effect. Pure Fe films and nearly stoichiometric Fe<sub>3</sub>Si films exhibit an identical sign of the ASC. The improvement of the atomic ordering in stoichiometric Fe<sub>3</sub>Si samples, which establishes the D0<sub>3</sub> crystal structure, is proposed as a possible origin of the same sign of the ASC. The temperature dependence of the ASC also shows a sign reversal for slightly off-stoichiometric ( $0.05 \leq x \leq 0.15$ ) Fe<sub>3+x</sub>Si<sub>1-x</sub> films below a certain critical temperature that increases with increasing Si content.

## Keywords:

Ferromagnet-semiconductor hybrid structures, High-index orientation, Planar Hall effect, Antisymmetric magnetoresistivity tensors

## Parts of this work have already been published:

J. Herfort, H.-P. Schönherr, P. K. Muduli, and K. H. Ploog, *Magnetic anisotropy of ultrathin epitaxial Fe films grown on As terminated GaAs(001)- $2 \times 1$  substrates*, in International Symposium on Compound Semiconductors: Post-Conference Proceedings, edited by M. R. Melloch and C. Tu., pages 96, **101**, IEEE, Piscataway, 2004.

P. K. Muduli, J. Herfort, H.-P. Schönherr, and K. H. Ploog, *Evolution of magnetic - anisotropy and spin-reorientation transition in Fe films grown on GaAs(113)A substrates by molecular-beam epitaxy*, J. Appl. Phys. **97**, 123904 (2005) (7 pages).

P. K. Muduli, J. Herfort, L. Däweritz, H.-P. Schönherr, and K. H. Ploog, *Magnetic anisotropy of Fe films on GaAs(113)A substrates*, Appl. Phys. A **81**, 901 (2005) (Rapid Communications) (6 pages).

P. K. Muduli, K.-J. Friedland, J. Herfort, H.-P. Schönherr, and K. H. Ploog, *Antisymmetric contribution to the planar Hall effect of Fe<sub>3</sub>Si films grown on GaAs(113)A substrates*, Phys. Rev. B **72**, 104430 (2005) (9 pages).

K.-J. Friedland, J. Herfort, P. K. Muduli, H.-P. Schönherr, and K. H. Ploog, *Planar Hall effect in epitaxial Fe layers on GaAs(001) and GaAs(113)A substrates*, J. Supercond. **18**, 309 (2005).

P. K. Muduli, J. Herfort, H.-P. Schönherr, and K. H. Ploog, *Epitaxial Fe<sub>3</sub>Si films stabilized on GaAs(113)A substrates*, J. Cryst. Growth, **285**, 508 (2005) (7 pages).

## Conference contributions:

K.-J. Friedland, P. K. Muduli, J. Herfort, H.-P. Schönherr, and K. H. Ploog, *Planar Hall effect in epitaxial Fe layers on GaAs(001) and GaAs(113)A substrates*, 3rd International Conference on Physics and Applications of Spin-Related Phenomena in Semiconductors (PASPS III), Santa Barbara (USA), July 21-23 (2004).

K.-J. Friedland, M. Bowen, J. Herfort, P. K. Muduli, H. -P. Schönherr, and K. H. Ploog, *Intrinsic contributions to the planar Hall effect in epitaxial Fe and Fe<sub>3</sub>Si films on GaAs substrates*, 11th Advanced Heterostructure Workshop, Kohala Coast (USA), December 5-10 (2004).

P. K. Muduli, J. Herfort, H.-P. Schönherr, and K. H. Ploog, *Magnetic properties of Fe and Fe<sub>3</sub>Si films on GaAs(113)A substrates*, 338. WE-Heraeus-Seminar: Nanomagnetism: New Insights with Synchrotron Radiation, Bad Honnef, January 05 - 07 (2005).



# Contents

<b>1</b>	<b>Introduction</b>	<b>1</b>
1.1	GaAs(113)A—a historic review . . . . .	3
1.2	FM/SC with GaAs(113)A: Motivation . . . . .	5
<b>2</b>	<b>Experimental Techniques</b>	<b>6</b>
2.1	The growth process . . . . .	6
2.1.1	The MBE chamber . . . . .	6
2.1.2	Reflection high-energy electron diffraction . . . . .	8
2.2	High resolution X-ray diffraction . . . . .	9
2.3	X-ray Reflectivity . . . . .	11
2.4	Magnetic characterization . . . . .	12
2.4.1	In situ Magneto-optic Kerr effect . . . . .	13
2.4.2	Ex situ SQUID magnetometry . . . . .	14
2.5	Magnetotransport measurements . . . . .	17
<b>3</b>	<b>Fe films on GaAs(113)A substrates</b>	<b>19</b>
3.1	Introduction . . . . .	19
3.2	Fe on GaAs(113)A: Motivation . . . . .	20
3.3	Growth and structural properties . . . . .	23
3.3.1	Mechanism and evolution of growth: RHEED . . . . .	25
3.3.2	Strain and structural properties by HRXRD . . . . .	27
3.3.3	Summary of structural properties . . . . .	29
3.4	Magnetic properties . . . . .	30
3.4.1	Onset of ferromagnetism . . . . .	30
3.4.2	Thermal spin excitations: the size effect . . . . .	31
3.4.3	Evolution of in-plane magnetic anisotropy . . . . .	33
3.4.4	Spin-reorientation transition . . . . .	36
3.4.5	Magnetic free energy of the (113)-plane of Fe . . . . .	37
3.4.6	Thickness dependence of anisotropy constants . . . . .	39
3.4.7	Mechanism of magnetization reversal . . . . .	44
3.4.8	Evolution of out-of-plane magnetic anisotropy . . . . .	47
3.4.9	Summary: Magnetic properties of Fe/GaAs(113)A . . . . .	49
3.5	Magnetotransport properties . . . . .	50
3.5.1	Anisotropic magnetoresistance . . . . .	51
3.5.2	Planar Hall effect . . . . .	53
3.5.3	Phenomenological model . . . . .	56
3.5.4	Summary: Magnetotransport properties of Fe . . . . .	61

<b>4</b>	<b>Fe<sub>3</sub>Si films on GaAs(113)A substrates</b>	<b>62</b>
4.1	Growth and structural properties . . . . .	65
4.1.1	Optimization of the growth process . . . . .	65
4.1.2	Growth of films with different composition . . . . .	68
4.1.3	Study of long-range atomic ordering in Fe <sub>3+x</sub> Si <sub>1-x</sub> films . . . . .	72
4.1.4	Electrical Resistivity . . . . .	74
4.1.5	Summary of structural properties . . . . .	75
4.2	Magnetic properties . . . . .	75
4.2.1	Effect of growth conditions on magnetic anisotropy . . . . .	75
4.2.2	Composition dependence of magnetic properties . . . . .	80
4.2.3	Summary of magnetic properties of Fe <sub>3+x</sub> Si <sub>1-x</sub> films . . . . .	84
4.3	Magnetotransport properties . . . . .	85
4.3.1	Anisotropic magnetoresistance . . . . .	85
4.3.2	Planar Hall effect: Composition dependence . . . . .	86
4.3.3	Summary: Magnetotransport properties of Fe <sub>3+x</sub> Si <sub>1-x</sub> films . . . . .	92
<b>5</b>	<b>Summary</b>	<b>93</b>
<b>A</b>	<b>Complete magnetoresistivity tensor elements for the crystal class m3m</b>	<b>95</b>
<b>B</b>	<b>Transformation into the (113) system</b>	<b>97</b>
	<b>Acknowledgement</b>	<b>110</b>
	<b>Curriculum Vitae</b>	<b>113</b>
	<b>Selbständigkeitserklärung</b>	<b>114</b>

# List of Figures

1.1	Ball-and-stick model of the bulk-truncated GaAs{113} surface. (a) Top view for the (113)A surface; (b) side view, cut along the $[\bar{3}\bar{3}2]$ direction exposing a cut through the (113)A (top) and the $(\bar{1}\bar{1}\bar{3})$ B (bottom) surfaces. The size of the atoms indicates the atoms in one atomic plane. The two different kinds of unit cells are indicated in gray. Figure inspired from Ref. [1].	4
2.1	Top-view of the MBE set-up showing different chambers. III-VGC: III-V compound semiconductor growth chamber, MGC: metal growth chamber, SEC: sample exchange chamber, SLC: sample loading chamber, STR: sample transfer rod, and SRA: sample rotation assembly, and RG: RHEED gun.	7
2.2	Definitions of diffraction geometry for an asymmetric Bragg diffraction.(a) grazing-incidence geometry (b) grazing-exit geometry and (c) skew-geometry for the plane (hkl) making an angle $\varphi$ to the sample surface. $\theta_B$ is the Bragg angle.	9
2.3	(a) Scans in reciprocal space for two different reciprocal lattice points (hkl) (symmetric) and $(h_1k_1l_1)$ (asymmetric). (b) Reciprocal space construction for the asymmetric reflection $(h_1k_1l_1)$ . $\mathbf{k}_s$ and $\mathbf{k}_0$ are the wave vectors for the diffracted and the incident X-rays, respectively. $\mathbf{S} = \mathbf{k}_0 + \mathbf{k}_s$ is the scattering vector.	11
2.4	The Kerr effect geometries: longitudinal (magnetization along the plane incidence of the light), transverse (magnetization perpendicular to the plane incidence of the light) and polar (magnetization in the plane incidence of the light).	13
2.5	The DC SQUID construction and principle: (a) Shows the two Josephson junctions forming a superconducting ring, which forms the DC SQUID.(b) Shows the output voltage as a function of applied flux. A tiny flux signal produces a corresponding voltage swing across the SQUID, which conventional electronics can measure. Figure inspired by Ref. [2].	15
2.6	The geometry of magnetotransport measurements. (a) Magnetic field is applied in-plane. The longitudinal magnetoresistance is referred to as anisotropic magnetoresistance ( $R_{xx}$ ) and the transverse magnetoresistance ( $R_{xy}$ ) as planar Hall effect. (b) Magnetic field is applied perpendicular to the film plane and the transverse resistance is measured. This is the usual Hall effect geometry. For ferromagnets this is sum of ordinary and extraordinary Hall effect.	17

3.1	(a) Ball and stick model for the bulk-truncated GaAs(001) and Fe(001) surfaces with the unit cells indicated in gray. (b) The corresponding bulk-truncated surfaces of Fe(113) and GaAs(113)A with the unit cells indicated in gray. (c) The side view of (b) along the in-plane $[\bar{1}10]$ axis. Size of the atoms indicate one layer of atoms. The figure demonstrate the close lattice match between the (113) planes of GaAs and Fe. The lower surface symmetry of (113)-plane is also apparent (see text). . . . .	21
3.2	RHEED pattern from GaAs(113)A substrates before the growth of Fe taken at 0 °C along (a) $[33\bar{2}]$ and (b) $[\bar{1}10]$ azimuths. The streaky RHEED pattern indicates an ordered and smooth surface morphology. . . . .	22
3.3	AFM images of two 26-nm-thick Fe samples grown at (a) 15 °C and (b) 0 °C. The root mean square (RMS) roughness changes from 10 Å to 3–5 Å when the growth temperature changes slightly from 15 to 0 °C. . . . .	23
3.4	Comparison of measured X-Ray Reflectivity profile (solid dots) with a simulated profile (continuous line) of 13-nm-thick Fe and 2.8-nm-thick iron oxide layers on GaAs(113)A substrates. . . . .	24
3.5	Evolution of RHEED patterns during the continuous growth of Fe (without substrate rotation) on GaAs(113)A and 0 °C along $[33\bar{2}]$ and $[\bar{1}10]$ . The first RHEED pattern from Fe begin to appear at about 3 MLs and become prominent at about 5 MLs. . . . .	26
3.6	Evolution of RHEED (b) line profiles, (c) Integrated Intensity, and (d) FWHM along $[\bar{1}10]$ for the (0 $\bar{1}$ ) reflection of Fe with monolayer coverage as shown in (a) during the continuous growth of Fe (without substrate rotation). Islanding persist up to 20 MLs. . . . .	27
3.7	X-ray reciprocal space maps of a 20-nm-Fe film grown on GaAs(113)A substrates for the asymmetric (004) (first column) and (224) (second column) reflection of GaAs in grazing incidence geometry (GI; first row) and grazing exit (GE; second row). The reciprocal lattice units (rlu) are $\lambda/2d$ , where $\lambda$ is the wavelength of $\text{CuK}_{\alpha 1}$ radiation and $d$ is the lattice plane spacing of the corresponding reflection. . . . .	28
3.8	X-ray reciprocal space map for the asymmetric (004) reflection of GaAs, in grazing incidence geometry, of two samples with Fe thickness (a) 7 nm (50 MLs) and (b)10 nm (70 MLs). The corresponding (002) peak of Fe is also shown. The Sample of 50 MLs is strained whereas the sample of 70 MLs is relaxed. . . . .	29
3.9	(a) Temperature dependence of remanent magnetization $M_r$ of Fe/GaAs(113)A films with different thickness. All curves are normalized with respect to the remanent magnetization at 10 K. The onset of RT ferromagnetic order is between 4.5 and 5.0 MLs. (b) Temperature dependence of susceptibility $\chi$ with an ac frequency of 9 and 140 Hz and ac field of 3.5 Oe for the 4-ML-thick sample. Note that the susceptibility is a dimensionless quantity. However, to specify the volume susceptibility, it is expressed in $\text{emu}/\text{cm}^3\text{Oe}$	31

3.10	(a) Temperature dependence of the spontaneous magnetization $M_s(T)$ normalized to $M_0$ for Fe films on GaAs(113)A substrates with different thicknesses. The solid lines are fits of Bloch $T^{3/2}$ law. (b) Size effect of spin wave excitations in epitaxial thin bcc-Fe Films on different substrates: spin wave parameter $B$ normalized to the bulk value of Fe as a function of the inverse thickness. . . . .	32
3.11	Magnetization loops of a 7 ML-Fe film with magnetic field applied in-plane along (a) $[33\bar{2}]$ and (b) $[\bar{1}10]$ . The open circles are for $T = 300$ K (RT) and the solid circles are for $T = 10$ K, respectively. The magnetization $M$ is normalized to the saturation magnetization at $T = 10$ K, $M_s^0$ after correction for the diamagnetic contribution of the GaAs substrate. . . . .	33
3.12	(a) Normalized magnetization curves along the major in-plane crystallographic directions $[33\bar{2}]$ and $[\bar{1}10]$ for a GaAs(113)A sample with 4 MLs of Fe coverage. (b) Magnetization curves along $[33\bar{2}]$ for at different temperatures. . . . .	34
3.13	(a) Room temperature magnetization curves of Fe films on GaAs(113)A for $d_{Fe} = 714$ MLs (100 nm) measured along the different in-plane crystallographic directions shown schematically in (b). The insets for the $[33\bar{2}]$ and $[\bar{1}10]$ directions show magnified portions of the magnetization curves in the low field region. . . . .	35
3.14	Magnetization curves of a set of three samples of thicknesses 50 MLs, 70 MLs and 140 MLs along the four major in-plane directions. The curves are normalized to their saturation magnetization after correction for the diamagnetic contribution of the GaAs substrate. . . . .	36
3.15	Three-dimensional plot of in-plane anisotropy energy density $E_{IPMA}$ (for $H = 0$ ) for the $[11\bar{3}]$ -oriented Fe film according to Eq. (3.4) with $r$ and $\theta_M$ as variable. Here $r$ is the anisotropy ratio given by $r = K_u^{eff}/K_1^{eff}$ and $\theta_M$ is the angle of magnetization with respect to the $[33\bar{2}]$ direction. . . . .	38
3.16	Illustration of the analytical fitting used to evaluate anisotropy constants in ultrathin Fe films with $d_{Fe} \leq 50$ MLs. Fitting of the magnetization curve of (a) 10 ML and (b) 4-ML-thick sample at 10 K for magnetic field applied along $[\bar{1}10]$ . For the 10-ML-thick sample the fitting was performed using Eq. (3.7) in the range, $-1 < m < 1$ . For the 4-ML-thick sample the fitting was performed in the region 1 using Eq. (3.8). The open circles represent experimental data whereas the solid lines represent the fits. . . . .	39
3.17	Illustration of the simulation using the Stoner-Wohlfarth model (SWM) to evaluate anisotropy constants in thick Fe films with $d_{Fe} \geq 70$ MLs. 140-ML-thick sample: hysteresis loop at 300 K along (a) $[33\bar{2}]$ and (b) $[\bar{1}10]$ , and the corresponding simulation (dotted lines) with $K_u^{eff}/M_s = 110$ Oe and $K_1^{eff}/M_s = 275$ Oe. Idem in (c) and (d) are for a 10-ML-thick sample with $K_u^{eff}/M_s = 316$ Oe and $K_1^{eff}/M_s = 135$ Oe, obtained from the fitting of the hard axis magnetization loop using Eq. (3.7) as described in the text. The coercive fields do not match with the experiment since the SWM does not take into account the micro-magnetic structure of the sample [3]. . . . .	40

3.18	Variation of effective uniaxial, $K_u^{\text{eff}}$ (first row) and four-fold, $K_1^{\text{eff}}$ (second row) anisotropy constants with inverse Fe film thickness $1/d_{\text{Fe}}$ at 10 K (first column) and 300 K (second column). Individual film thicknesses are also indicated at the top. A linear fit to the variation $K_u^{\text{eff}}$ vs $1/d_{\text{Fe}}$ for Fe film thickness above 20 MLs yields the surface/interface anisotropy constant $K_u^{\text{int}} = (2.1 \pm 0.5) \times 10^{-1} \text{ erg/cm}^2$ at 10 K and $(1.4 \pm 0.5) \times 10^{-1} \text{ erg/cm}^2$ at 300 K. $K_1^{\text{eff}}$ in the second row remains almost constant above 20 MLs as shown by the dotted lines. . . . .	41
3.19	(a) <i>in situ</i> MOKE loops for Fe (26 nm)/GaAs(113)A for different in-plane directions. Here, $0^\circ$ and $90^\circ$ indicate the $[33\bar{2}]$ and $[\bar{1}10]$ direction, respectively. The easy axis of magnetization is near to the $[03\bar{1}]$ direction or $45^\circ$ . Note that the magnetization is not completely saturated in all directions. (b) Simulated hysteresis loops for the Fe(113) film with a uniaxial ratio $r = 0.6$ and $2K_1/M_s = 440 \text{ Oe}$ . . . . .	44
3.20	(a) Plot of the coercive field, $H_c$ as a function of the in-plane direction, $\theta_H$ of the applied field for the sample presented in Fig. 3.19(a) with uniaxial ratio $r = 0.6$ . (b) The simulated coercive fields as a function of $\theta_H$ for a uniaxial ratio $r = 0.6$ and $2K_1/M_s = 440 \text{ Oe}$ (see text). . . . .	45
3.21	The evolution of local minima in the anisotropic energy of the Fe(113)-plane with the applied magnetic field for a uniaxial ratio of $r = 0.6$ . The one-jump and two-jump switching process are demonstrated for (a) $\theta_H = 0^\circ$ and (b) $\theta_H = 45^\circ$ . Here, $0^\circ$ indicates the $[33\bar{2}]$ direction. . . . .	46
3.22	(a) Out-of-plane magnetization curves for 5 ML and 140-ML-thick Fe films on GaAs(113)A at 2 K. The inset shows the thickness variation of saturation magnetization at 300 K (open circles) and 2 K (solid circles) (b) Variation of the effective perpendicular magnetic anisotropy constant with the inverse Fe film thickness $1/d_{\text{Fe}}$ . A linear fit (shown as a solid line) yields the interfacial contribution of PMA, $K_p^{\text{int}} = -(0.11 \pm 0.02) \times 10^1 \text{ erg/cm}^2$ . . . . .	48
3.23	Anisotropic magnetoresistance (AMR) from a set of three Fe/GaAs(113)A samples at 300 K. Here, $\theta_H = 0^\circ$ represents the $[33\bar{2}]$ direction, which is also the direction of current. . . . .	51
3.24	Experimental (symbols) and calculated (thick gray line) angular dependencies of the AMR (first coulumn) and the PHE (second column) for a 26-nm-thick Fe sample. Here, $\theta_H = 0^\circ$ indicates the $[33\bar{2}]$ direction, which is also the direction of current. Note that the PHE is described by the modified equation Eq. (3.20) (see text). The low-field curves were calculated using the Stoner-Wohlfarth model with the parameters, $K_1/M_s = 200 \text{ Oe}$ and $r = K_u/K_1 = 0.6$ . . . . .	52
3.25	(a) Field dependence and (b) angular dependence (at high field of $H = +2 \text{ kOe}$ ) of AMR for a 10-ML-Fe film measured at 300 K. Here, $0^\circ$ indicates the $[33\bar{2}]$ direction, which is also the direction for current. Note that the sample is not completely saturated at $H = +2 \text{ kOe}$ . . . . .	53
3.26	Planar Hall effect (PHE) from a set of three Fe/GaAs(113)A samples at 300 K. Here, $\theta_H = 0^\circ$ indicates the $[33\bar{2}]$ direction, which is also the direction for current. In all the samples, the presence of an antisymmetric component can be clearly seen for a magnetic field applied along any direction other than the $\langle 110 \rangle$ axes. . . . .	53

3.27	(a) Schematic presentation of the contact orientation labelled anticlockwise. The major crystallographic directions of the (113)-plane are also shown. (b) The PHE response from Fe films on GaAs(113)A at 300 K for two configurations as explained in the text. (c) Separation of the symmetric and antisymmetric contributions to the PHE. . . . .	54
3.28	The transverse resistivity ( $\rho_{xy}$ ) from Fe films on GaAs(113)A at 300 K for different orientation of the applied field. $0^\circ$ represents an in-plane applied field (i.e., PHE) and $90^\circ$ represents a field applied normal to the film plane (i.e., AHE). . . . .	55
3.29	(a) Angular dependence of $\rho_{xy}$ at 300 K of a 26-nm-thick Fe film on GaAs(113)A with a saturating in-plane magnetic field so that $\theta_H = \theta_M$ . Open circles represent experimental data and solid line is a fit using Eq. (3.20) (see text). (b) Separation of the symmetric and antisymmetric part of the PHE. Open circles represent experimental data and solid lines are fitted curves using a $\sin 2\theta_M$ behavior for symmetric part and $\rho_{\text{SATM}}^0 \cos \theta_M + \rho_{\text{SATM}}^1 \cos^3 \theta_M$ type behavior for antisymmetric part. . . . .	59
3.30	Planar Hall effect for an 10 ML-Fe(113) film at 300 K. (a) Field dependencies at different $\theta_H$ and angular dependence with an in-plane magnetic field of (b) $H = +2$ kOe and (c) $H = +0.5$ kOe. Open circles represent experimental data and solid lines are calculated curves using the SWM and Eq. (3.20) (see text). The major in-plane crystallographic directions for the (113)-plane are also shown with $0^\circ$ along $[33\bar{2}]$ . . . . .	60
4.1	Summary of the bulk properties of $\text{Fe}_3\text{Si}$ . (a) Ball and stick model for the bulk $\text{Fe}_3\text{Si}$ unit cell with different sublattices. (b) The calculated density of states (DOS) of Fe and $\text{Fe}_3\text{Si}$ for majority (closed lines) and minority (dotted lines) bands from Ref. [4]. These DOS predict no half metallic character for $\text{Fe}_3\text{Si}$ as can be seen from the close resembles of the DOSs of the two materials. (c) The phase diagram of Fe-Si alloys from Ref [5, 6], which shows that the phase boundary of the stable $\text{Fe}_3\text{Si}$ phase covers a range from 9 to 26.6 at.%Si (indicated in gray). . . . .	63
4.2	(a) Normalized <i>skew-symmetric</i> $\omega - 2\theta$ scans for $\text{Fe}_3\text{Si}/\text{GaAs}(113)\text{A}$ films grown at different growth temperatures $T_G$ from 100 to 500 $^\circ\text{C}$ . The curves are normalized to the GaAs(004) reflection and are shifted with respect to one another for clarity. The measurements were performed with an analyzer crystal in the the diffracted beam optics. The growth rate was 0.26 nm/min. The inset shows a plot of the RMS roughness $\sigma$ vs $T_G$ . The arrow indicates the optimized growth temperature of 250 $^\circ\text{C}$ . (b) Wide-range <i>skew-symmetric</i> $\omega - 2\theta$ scans for the same samples. The measurements were performed with an open detector. . . . .	65
4.3	AFM images of $\text{Fe}_3\text{Si}$ films as a function of the growth temperature. Note that the scan area of the sample grown at $T_G = 400$ $^\circ\text{C}$ is magnified to show the nanoscale “ripples-like” structures. . . . .	66
4.4	AFM images of $\text{Fe}_3\text{Si}$ films grown at 250 $^\circ\text{C}$ with growth rates of (a) 0.26 nm/min and (b) 0.13 nm/min, yielding RMS roughness of 5 and 1.6 $\text{\AA}$ , respectively. . . . .	67

4.5	Normalized <i>skew-symmetric</i> $\omega - 2\theta$ scans for $\text{Fe}_{3+x}\text{Si}_{1-x}/\text{GaAs}(113)\text{A}$ films grown at 250 °C with different Si cell temperatures. The curves are normalized to the $\text{GaAs}(004)$ reflection and are shifted with respect to each other for clarity. The dotted line shows a simulation for a sample with $(\Delta a/a)_\perp = 1.2\%$ . See text and Ref [7] for simulation details. . . . .	68
4.6	Relaxed lattice constant $a_{\text{Fe}_3\text{Si}}$ as a function of the Si content of the $\text{Fe}_{3+x}\text{Si}_{1-x}$ phase. Solid lines are guides for the eye. The mean value from the literature shown as the thick gray line is used to find the composition of the layers. The experimental values of $a_{\text{Fe}_3\text{Si}}$ on $\text{GaAs}(113)\text{A}$ substrates are shown as open circles. For comparison, the corresponding values of $a_{\text{Fe}_3\text{Si}}$ on $\text{GaAs}(001)$ substrates are also shown. (b) A plot of $(\Delta a/a)_\perp$ with deviation $x$ of $\text{Fe}_{3+x}\text{Si}_{1-x}$ layers. . . . .	69
4.7	Results of RHEED and AFM experiments on $\text{Fe}_{3+x}\text{Si}_{1-x}$ samples with composition $x = 0.39$ (first row) and $x = 0.05$ (second row). The first and second column represent the RHEED pattern of the $\text{Fe}_{3+x}\text{Si}_{1-x}$ films taken immediately after growth along $[3\bar{3}2]$ and $[\bar{1}10]$ , respectively, alongside <i>ex situ</i> AFM images (third column). . . . .	70
4.8	(a) AFM RMS roughness $\sigma$ (measured over a $5 \times 5 \mu\text{m}^2$ area) as a function of the composition $x$ of the films. All samples were grown at 250 °C except those shown as $\star$ . (b) The AFM images of the most stoichiometric samples with $x = 0.03$ and $x = -0.04$ exhibit an RMS roughness of about 6.5 Å. The sample with $x = -0.04$ was found to be rather inhomogeneous. . . . .	71
4.9	(a) Normalized <i>skew-symmetric</i> $\omega - 2\theta$ scans of $\text{Fe}_3\text{Si}/\text{GaAs}(113)\text{A}$ for the superlattice (002) reflection. The curves are normalized to the $\text{GaAs}(002)$ reflection and are shifted with respect to each other for clarity. (b) Intensity of (002) reflection $I_{(002)}$ , as a function of the composition $x$ for $\text{Fe}_{3+x}\text{Si}_{1-x}$ films on $\text{GaAs}(113)\text{A}$ and (001) substrates. . . . .	72
4.10	X-ray reciprocal space maps of stoichiometric $\text{Fe}_3\text{Si}$ films grown on $\text{GaAs}(113)\text{A}$ substrates for the symmetric and superlattice (113) reflection of $\text{GaAs}$ . The reciprocal lattice units (rlu) are $\lambda/2d$ , where $\lambda$ is the wavelength of $\text{CuK}_{\alpha 1}$ radiation and $d$ is the lattice plane spacing of the corresponding reflection. The presence of interference fringes for the most stoichiometric samples indicate the presence of the (113) reflection. . . . .	73
4.11	(a) Resistivity $\rho$ as a function of composition $x$ for the $\text{Fe}_{3+x}\text{Si}_{1-x}$ alloys at 300 K, 77 K and 4 K. (b) $(d\rho/dT) _{300\text{ K}}$ as a function of composition $x$ for the $\text{Fe}_{3+x}\text{Si}_{1-x}$ alloys. . . . .	74
4.12	Magnetic properties of $\text{Fe}_{3+x}\text{Si}_{1-x}$ films grown on $\text{GaAs}(113)\text{A}$ at different of growth temperature $T_G$ for a composition near $x = 0.3$ . The thickness of the films is in the range 40–45 nm. The magnetization curves were measured at 300 K along $[3\bar{3}2]$ (thin black), $[03\bar{1}]$ (thicker black) and $[\bar{1}10]$ (thick gray). . . . .	76



4.13	Saturation magnetization $M_s$ and coercive field $H_c$ of the $\text{Fe}_{3+x}\text{Si}_{1-x}$ films as a function of $T_G$ for a composition near $x = 0.3$ . A minimum coercive field and an optimum value of the saturation magnetization are achieved near the optimized growth temperature $T_G = 250$ °C. The arrow indicates samples with UMA whereas the dotted lines are guides to eye. The growth rate was maintained at 0.26 nm/min except the symbol ( $\star$ ) which indicates data for a sample grown at 250 °C with a growth rate of 0.13 nm/min. . . .	77
4.14	Comparison of the AFM surface morphology as a function of annealing temperature, $T_a$ . The <i>as-grown</i> sample represents a 41.5-nm-thick $\text{Fe}_{3+x}\text{Si}_{1-x}$ film with $x = 0.3$ grown at $T_G = 200$ °C with a growth rate of 0.26 nm/min. . . .	78
4.15	SQUID magnetization curves along different crystallographic directions for positive fields of samples with growth rate of (a) 0.26 nm/min (b) 0.13 nm/min, respectively. The insets show the magnified low-field region. . . .	79
4.16	Normalized SQUID magnetization curves at 300 K along different crystallographic directions for three different compositions $x$ . The thicknesses of these films are in the range of 35–50 nm. . . . .	80
4.17	Summary of the composition dependence of magnetic properties of $\text{Fe}_{3+x}\text{Si}_{1-x}$ films grown on GaAs(113)A substrates. The composition dependence of (a) the four-fold magnetic anisotropy constant $K_1$ normalized w.r.t. the saturation magnetization, $M_s$ , (b) the UMA ratio $r = K_u/K_1$ and (c) the saturation magnetization, $M_s$ . The open circle indicates a sample with $x = 0.03$ . . . . .	81
4.18	(a) Temperature dependence of the spontaneous magnetization $M_s(T)$ normalized to $M_0$ for $\text{Fe}_{3+x}\text{Si}_{1-x}$ films on GaAs(113)A substrates with different composition $x$ . The solid lines are fits of Bloch $T^{3/2}$ law. (b) Bloch constant or spin-wave parameter $B$ in $\text{Fe}_{3+x}\text{Si}_{1-x}$ films on GaAs(113)A substrates normalized to the bulk value of Fe as a function of the composition $x$ . . . .	83
4.19	Summary of AMR studies. (a) An example of the field dependence of AMR ( $\rho_{xx}$ ) for an $\text{Fe}_{3+x}\text{Si}_{1-x}$ (113) film with $x = 0.07$ at $T = 300$ K for different in-plane directions. (b) The angular dependence of $\rho_{xx}$ at a fixed saturating field of $H = 1$ kOe obtained at 300 K. (c) The AMR amplitude, $(\rho_{\parallel} - \rho_{\perp})$ as a function of composition $x$ of the $\text{Fe}_{3+x}\text{Si}_{1-x}$ (113) films measured at 300 K (solid circles) and 77 K (open circles). . . . .	85
4.20	(a) Optical microscopy image of the Hall bar structure employed for the magnetotransport studies. The contacts are labelled and the crystallographic directions of the (113)-plane are shown. (b) Planar Hall effect response for an $\text{Fe}_{3+x}\text{Si}_{1-x}$ film with $x = 0.07$ grown on GaAs(113)A at 300 K with magnetic field applied along $[3\bar{3}2]$ . (c) Separation of the symmetric and antisymmetric contribution to the PHE. . . . .	86
4.21	(a) Planar Hall effect response from an $\text{Fe}_{3+x}\text{Si}_{1-x}$ ( $x = 0.07$ ) film grown on GaAs(113)A with magnetic field applied in-plane along $[\bar{1}10]$ at 300 K, showing the vanishing ASC. (b) Angular dependence of $\rho_{xy}$ at 300 K with a saturating in-plane magnetic field so that $\theta_H = \theta_M$ . (c) Separation of the symmetric and antisymmetric part of the PHE. Open circles represent experimental data while the solid lines are fitted curves as discussed in Fig. 3.29. . . . .	87

4.22	(a) PHE for an $\text{Fe}_{3+x}\text{Si}_{1-x}(113)$ ( $x = 0.07$ ) film at 77 K with the magnetic field applied in-plane along $[33\bar{2}]$ . (b) Corresponding angular dependence of $\rho_{xy}$ at 77 K with a saturating in-plane magnetic field so that $\theta_H = \theta_M$ . (c) Separation of the symmetric and antisymmetric part of the PHE. Open circles represent experimental data while solid lines are fitted curves as explained in Fig. 3.29. . . . .	88
4.23	(a) Temperature and composition dependence of the $\rho_{\text{SATM}} = \rho_{xy}(H > +H_{\text{sat}}) - \rho_{xy}(H < -H_{\text{sat}})$ measured with a saturating field applied near to the $[33\bar{2}]$ direction. (b) Temperature dependence of $\rho_{\text{AHE}}$ for two typical samples with $x = 0.07$ and 0.15. . . . .	89
4.24	Temperature and composition dependence of the (a) symmetric PHE amplitude $\rho_s^{113}$ and (b) antisymmetric amplitude $\rho_{\text{SATM}} = 2(\rho_{\text{SATM}}^0 + \rho_{\text{SATM}}^1)$ measured in $[113]$ -oriented $\text{Fe}_3\text{Si}$ films obtained from the fitting of $\rho_{xy}$ at a saturating field. . . . .	90
4.25	Field dependencies along $[33\bar{2}]$ (first column) and the low-field angular dependencies (second column) for two samples with $x = 0.39$ (first row) and 0.07 (second row) measured at 77 K. Symbols indicate experimental data and the thick lines indicate simulation of the PHE as explained in the text. . . . .	91

# List of Tables

3.1	Summary of the XRR simulation results for Fe samples of different thicknesses and with Al capping layers. All dimensions are expressed starting from the top layer. Thicknesses and interface/surface roughness are expressed in nm, while the density is expressed in g/cm <sup>3</sup> . The density of layers are varied by about 25% to obtain the best fit. The top layer is assumed to be an oxide layer. . . . .	25
3.2	Table of the in-plane and out-of-plane anisotropy constants for different epitaxial Fe/GaAs systems at 300 K. The first column represents the results obtained in this work on Fe/GaAs(113)A substrates. The constants have not been adjusted to remove the effect of the capping layer. . . . .	42
3.3	Summary of magnetotransport measurements of Fe films on GaAs(113)A system at 300 K. . . . .	56

# Chapter 1

## Introduction

...Basic research in the physical sciences, especially in condensed matter physics, can result in important developments in applied physics and engineering.

—Gary A. Prinz

**The concept of spintronics** In recent times the density of information that can be processed, stored, and transferred per unit area of the device has been increased exponentially, thus demanding for faster processing speed. The miniaturization of these devices has proven to be among the most important developments toward processing more information more quickly. However, experts believe that the silicon-based microchips will reach the physical limits of miniaturization within the next 10 years [8]. In order to continue at the current rate of miniaturization, and to continue to increase the computing capability of electronic computers, fundamentally new technologies must be introduced in the design and manufacturing of computing elements. This has triggered a substantial amount of research based on new ideas, such as the exploitation of quantum mechanical spin of the electron. The discovery of the giant magnetoresistance effect (GMR) [9, 10] which is a quantum mechanical effect is just one of them. The storage capacity of magnetic materials has increased dramatically in recent years following this discovery. Another similar phenomenon called the tunnelling magnetoresistance effect [11] is already implemented in the latest magnetic random access memory devices. However, semiconductor manufacturers are still ignoring the electron spin, in spite of these advances in the magnetic recording industry. In semiconductors (SC), the spin degree of freedom can be exploited to develop new logic devices with enhanced functionality, higher speeds and reduced power consumption. This concept of spintronics [12, 13, 14, 15, 16, 17, 18, 19, 20] is based on the exploitation of the quantum mechanical spin of the electron, which is used to differentiate electrical carriers into two different types according to whether their spin projection onto a given quantization axis is  $\pm\frac{1}{2}$ . Spintronics offer opportunities for a new generation of devices combining standard microelectronics with the spin-dependent effects that arise from the interaction between the spin of the carrier and the magnetic properties of the material. However the realization of a working spintronics device such as prototype of the Datta-Das device [21] is not yet successful. The implementation of the spintronics devices faces several challenges which can be arranged into three distinct categories; (i) spin injection, (ii) spin transport/manipulation, and (iii) spin detection. There have been significant experimental and theoretical developments in each of these areas, yet there still exist a multitude of problems to overcome. In other words, before spin can become a

big business, researchers need to fulfill some fundamental requirements in SC; to create, transport, manipulate, store, and detect spin.

**Experimental approaches to spintronics** In order to utilize the spin degree of freedom in SC we need to fabricate appropriate materials, understand the spin-dependent phenomena, and control the spins. This thesis is related to the development and fabrication of materials that are useful for spintronics. The development of semiconductor-based materials with magnetic or spin-related properties can be broadly divided into two categories: (i) magnetic semiconductors or diluted magnetic semiconductors (DMS) and their heterostructures, and (ii) ferromagnetic-metal/semiconductor heterostructures (FM/SC). A basic obstacle for the use of DMS in room-temperature (RT) spintronic devices, however, is their relatively low Curie temperature. This thesis is linked with the second approach, the FM/SC, which include magnetic *3d*-transition-metals or their alloys with SC. These systems offer Curie temperatures well above RT. Successful spin injection has been reported for both the DMS [22, 23] and FM/SC [24, 25, 26, 27], though the efficiency remained low in the latter (at low temperatures). However, researchers have the opinion that a significant increase in spin injection efficiency can be achieved by optimizing the interface structure, because the spin injection process is strongly influenced by the details of the FM/SC interface. For example, it has been shown that in the case of Fe/(Al,Ga)As structures a decrease in interface roughness significantly increases the spin injection efficiency [28]. For this reason, FM/SC have experienced a tremendous boost of research activities. A detailed discussion of recent progresses in FM/SC, especially Fe/GaAs and related systems can be found in the review article by Wastlbauer and Bland [29].

**Nanoscale magnetic manipulation in FM/SC** The combination of ferromagnets with non-magnetic SC not only offer a new class of devices for spintronics but also provide a fertile ground for novel functionalities, such as control of magnetic anisotropy (due to different symmetry environment), spin-dependent transport, magnetoresistance, and magneto-optical effects. This refer to the field of nanoscale magnetism of thin-films, surfaces, interfaces and nanostructures which continue to attract researchers with the rapid development of thin film fabrication technology such as molecular-beam epitaxy (MBE) and the improvement of *in situ* surface characterization techniques. This development has opened the possibility of achieving very high-quality surfaces that are atomically flat over very wide dimensions. It became possible to study true two-dimensional (2D) magnetic systems and to address some fundamental issues of ferromagnetism. The crystal orientation and magnetic anisotropy of the ferromagnetic layers can be controlled by well-developed MBE growth techniques. In contrast to bulk magnetic materials, ultra-thin films enable the manipulation of magnetism via the thickness and, by use of artificial structure growth, to produce structures with properties that do not appear in nature.

The following phenomena can occur in thin film magnetic systems. (i) The most evident change that occurs, when going from the bulk material to lower dimensional structures is the reduction of coordination. In a bulk material, most of the electrons are involved in bonding with neighboring atoms and – since the Pauli principle requires that pairs of electrons of opposite spin form the bonds – most bulk materials are nonmagnetic. Normally, a lower coordination leads to more “unbound” electrons that can lead to magnetism. In a band picture one can say that at low dimensions we get a smaller band width, which favors (in the Stoner model) the formation of magnetic moments. Thus it is not

surprising to induce an enhancement of the magnetic moment (for a review see Ref. [30]) at low dimensions, though the effect may be counterbalanced by hybridization effects at the interfaces. (ii) At lower dimensions, the spin and orbital moment get increased which in turn, enhances the magnetic anisotropy [31]. The interest in the magnetic anisotropy of ultrathin films has originated from several theoretical predictions such as Néel's [32] prediction of a surface anisotropy due to the reduced symmetry in lower dimension. In fact, in thin films the magnetic behavior is mainly controlled by the magnetic anisotropy. As an example, Mermin and Wagner [33] have shown that, at finite temperatures, ferromagnetic order in 2D can be stabilized only via the anisotropies. (iii) As film thickness is decreased, the Curie temperature of the system decreases. This is due to the fact that the exchange interaction is reduced at the boundary atoms. The important consequence is that the saturation magnetization may change with film thickness due to changes in the Curie temperature. (iv) In many cases, a sensitive correlation between the magnetic properties and the film structure as well as surface or interface roughness is expected [34, 35].

Some of the above aspects will be considered in this work. A further interesting phenomena of fundamental interest is related to the ferromagnetic thin films with a high-index-orientation [36, 37] and is the subject of this work. In this thesis the [113] orientation of the FMs on GaAs(113)A is explored. For such an orientation of the films the reduced symmetry and coordination number is further enhanced and this offers a variety of opportunities to manipulate magnetic properties [37]. Besides the magnetotransport properties are also well-known to be affected by the symmetry of the crystals [38, 39, 40, 41]. The reduced symmetry problem of a high-index film orientation on the magnetotransport properties is another important subject of this thesis.

## 1.1 GaAs(113)A—a historic review

**The bulk-truncated GaAs(113)A** Depending on the surface termination, the unreconstructed GaAs(311) surface is categorized into GaAs(113)A and GaAs(113)B types. The type A surface contains twofold coordinated (001)-like As atoms (with two dangling bonds) and threefold coordinated (111)A-like Ga atoms (with one dangling bond) as shown in Fig. 1.1 [1, 42]. For the type B surface the position of As and Ga is reversed. The two different conventions of primitive rhombohedral and rectangular unit mesh of the bulk-truncated GaAs(113)A surface are also shown in the figure.

**Importance of the GaAs(113)A substrate** The GaAs(113) surface is considered to be a high-Miller-index semiconductor surface. The high-Miller-index surfaces, even though less extensively studied compared to the (001), (110) and (111) surfaces, have received increased attention in last ten years for several reasons. These surfaces exhibit a combination of bonding configurations that usually do not occur on any given low-Miller-index surface. The greater complexity of these surfaces is sometimes useful. For example, the "ideal" (113) surface, as already mentioned above, has equal densities of twofold-and threefold-coordinated surface atoms [43]. It can be viewed to be an average in some sense of the (001) and (111) surfaces. The different bonding configuration of the GaAs(113) surface has been argued to produce high-quality and defect-free epitaxial films [44]. The high-Miller-index surfaces are also interesting from a stability point of view to explore whether such surfaces can lead to lower surface energy compared to the low-Miller index

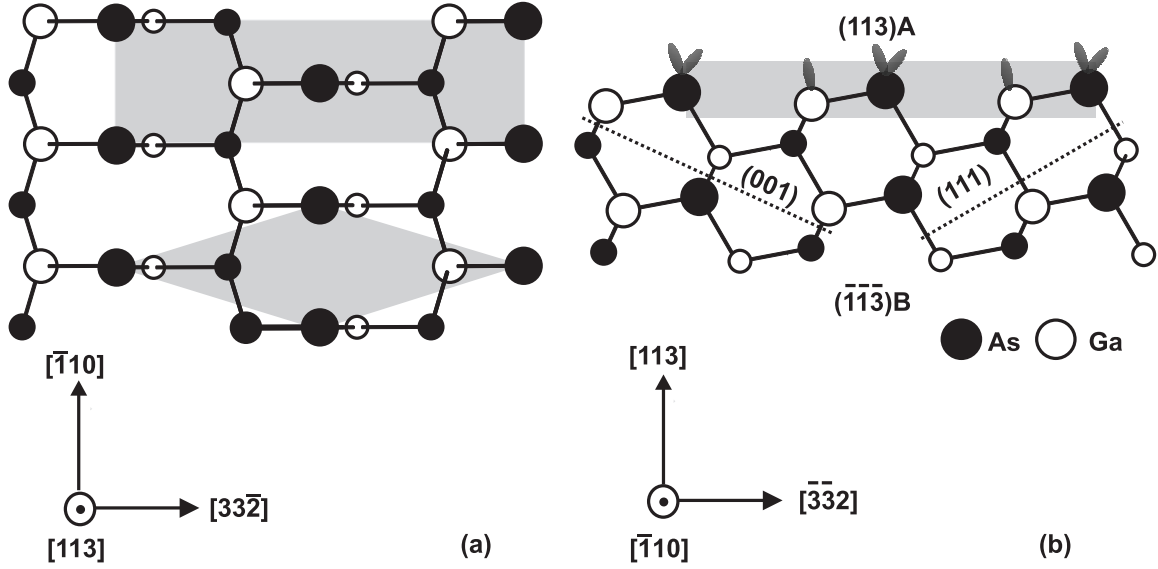


Figure 1.1: Ball-and-stick model of the bulk-truncated GaAs{113} surface. (a) Top view for the (113)A surface; (b) side view, cut along the  $[33\bar{2}]$  direction exposing a cut through the (113)A (top) and the  $(\bar{1}\bar{1}\bar{3})$ B (bottom) surfaces. The size of the atoms indicates the atoms in one atomic plane. The two different kinds of unit cells are indicated in gray. Figure inspired from Ref. [1].

surfaces. Another completely contrasting interest in GaAs(113)A substrates originates from the ability of the GaAs(113)A substrate to act as a template for fabrication of uniform semiconductor nanostructures [45, 46, 47, 48, 49, 50].

**The real GaAs(113)A surface** In spite of considerable studies performed on the growth of semiconductor nanostructures on GaAs(113)A substrates, the structure of the bare GaAs(113)A substrate employed in MBE is incompletely understood. In the first studies on GaAs(113)A, the surface was prepared by ion-beam annealing where a  $(1 \times 1)$ -low-energy electron diffraction pattern was reported [51, 52]. Nötzel *et al.* reported the formation of a regular array of  $\{331\}$ -facets in MBE-grown samples [45, 53]. The most important characteristics of this proposed surface was the high density of straight steps running along  $[33\bar{2}]$ , and the uniform height corrugation with a lateral periodicity of 3.2 nm and a corrugation depth of 1.02 nm. However, this finding could not be reproduced by other groups. Instead, based on scanning tunneling microscopy (STM) experiments Wassermeier *et al.* [54] proposed an  $(8 \times 1)$ -reconstruction and reproduce only the lateral periodicity of the surface corrugation model proposed by Nötzel *et al.* The depth of modulation, however, has been the subject of controversy and is argued to be 0.34 nm. The role of disorder also observed in the STM images has not been investigated yet. The finding of Wassermeier *et al.* [54] was later confirmed by kinematic reflection high-energy electron diffraction (RHEED) simulations [55], surface core-level spectroscopy [56, 57], and total energy calculations using density-functional theory [58]. Recently, a  $(4 \times 1)$ -reconstruction is also reported [42] on GaAs(113)A substrates for MBE samples obtained at higher substrate temperatures and lower  $\text{As}_4/\text{Ga}$  ratios compared to the growth conditions used to maintain the  $(8 \times 1)$ -reconstruction. There are also con-

flicting reports that the GaAs(113)A surface is as smooth as, if not smoother than, the GaAs(100) surface [59, 60, 61, 62].

## 1.2 FM/SC with GaAs(113)A: Motivation

In the present study, the major motivation to integrate ferromagnetic metals with GaAs(113)A substrates came from the unexplored properties of ferromagnets on this orientation. So far the growth of ferromagnets on GaAs substrates has been focused mainly on the low-index surfaces. Much less work is devoted to study ferromagnetic films on high-index semiconductor surfaces. To our knowledge, only very few studies on the growth and properties of magnetic metals on GaAs(113)A substrates have been reported [63, 64, 65]. To obtain a stable high-index surface of a ferromagnet is in general rather difficult. For instance, Fe films deposited on Cu(113) did not maintain the same orientation relationship with respect to the substrate, which led to a highly strained and distorted bcc Fe arrangement with (112) orientation [66]. As already mentioned, the thermal stability and the ordering of high-index surfaces with reduced symmetry and coordination number offer a variety of opportunities to induce new phenomena and are thus promising for new device applications of the FM/SC [37]. The GaAs(113)A surface in particular is characterized by a low surface symmetry and the two major in-plane axes, namely  $[33\bar{2}]$  and  $[\bar{1}10]$  are crystallographically inequivalent. This can be clearly seen from the rectangular unit cell of Fig. 1.1(a). There is a mirror symmetry along  $[33\bar{2}]$ , but none along  $[\bar{1}10]$ . This reduced symmetry in principle should have consequences on magnetic properties. It will be shown in subsequent chapters that this reduced symmetry has a very drastic influence on the magnetotransport properties. The ferromagnetic material specific motivation will be discussed in the respective chapters of Fe (chapter 3) and Fe<sub>3</sub>Si (chapter 4).

It is worthwhile to address another completely different motivation. As already mentioned, the GaAs(113)A substrate is well-known for its ability to act as a template for growing semiconductor nanostructures [45, 46, 47, 48, 49, 50]. Thus, it is natural to expect that this property of GaAs(113)A may be explored with ferromagnetic metals to form magnetic nanostructures by self-organization. In this work, a few preliminary attempts were made to explore this possibility. The growth of Fe was studied both on un-patterned and patterned GaAs(113)A substrates. Our preliminary studies on patterned GaAs(113)A substrates show almost uniform growth with magnetic properties more or less similar to that on un-patterned substrates. Furthermore, the limitation of the low growth temperature of Fe (see chapter 3), does not allow a wide variation of growth parameters. For these reasons, we mainly focus on growing ferromagnetic films whose structural properties are comparable to that of the films grown on GaAs(001) substrates. This allows us to study the effect of orientation and the reduced symmetry on the magnetic and magnetotransport properties.

The results presented in this thesis are divided into two chapters dealing with two material systems, namely, Fe/GaAs(113)A (chapter 3) and Fe<sub>3</sub>Si/GaAs(113)A (chapter 4). Each chapter is subdivided into three important sections dealing with (i) growth and structural properties (ii) magnetic properties, and (iii) magnetotransport properties. Chapter 2 introduces the experiential techniques used in this work.



# Chapter 2

## Experimental Techniques

In this chapter the growth process and some of the measurement techniques employed for the structural and magnetic characterization of the magnetic thin films will be presented. Since each technique probes a particular property of the sample, knowledge of the physical mechanisms behind that technique is essential to the understanding of its full capabilities and limitations.

### 2.1 The growth process

The hybrid structures of ferromagnetic thin films on GaAs(113)A to be presented in this work were grown by MBE which refers to a process of growing thin films using localized beams of atoms or molecules in an UHV environment to provide a source of the constituents to the growing surface of a substrate crystal. MBE, which was originally developed in the 1970s for growing high-purity epitaxial layers of compound semiconductors [67, 68], has now become a popular process for the growth of epitaxial films of metals, magnetic materials, oxides and even organic structures. MBE provides a more precise control of the crystal growth compared with other methods. This is because of the cleanliness of the surface obtained with this method due to the UHV environment. This allows the growth of multilayers or heterostructures with extremely sharp interfaces. MBE also provides the assessment of the crystal surface by a variety of *in situ* surface sensitive techniques that require high vacuum.

#### 2.1.1 The MBE chamber

The MBE system employed in this work consists of a sample introduction chamber, a sample exchange chamber, a III-V compound semiconductor growth chamber and a specially designed chamber for the growth of metals in an As-free environment. The metal growth chamber is connected to the III-V compound semiconductor growth chamber via the sample exchange chamber, maintained in ultrahigh vacuum (UHV). A schematic diagram of the MBE system is shown in Fig. 2.1. The III-V growth chamber is a conventional MBE chamber for growth of different types of compound semiconductor materials and accommodates both group III and group V sources such as Gallium, Indium, Aluminium, and Arsenic. These sources are standard effusion cells which produces a collimated molecular beam. Both the III-V and the metal chamber incorporate a reflection high-energy electron diffraction (RHEED) setup to investigate surface structures. The metal growth

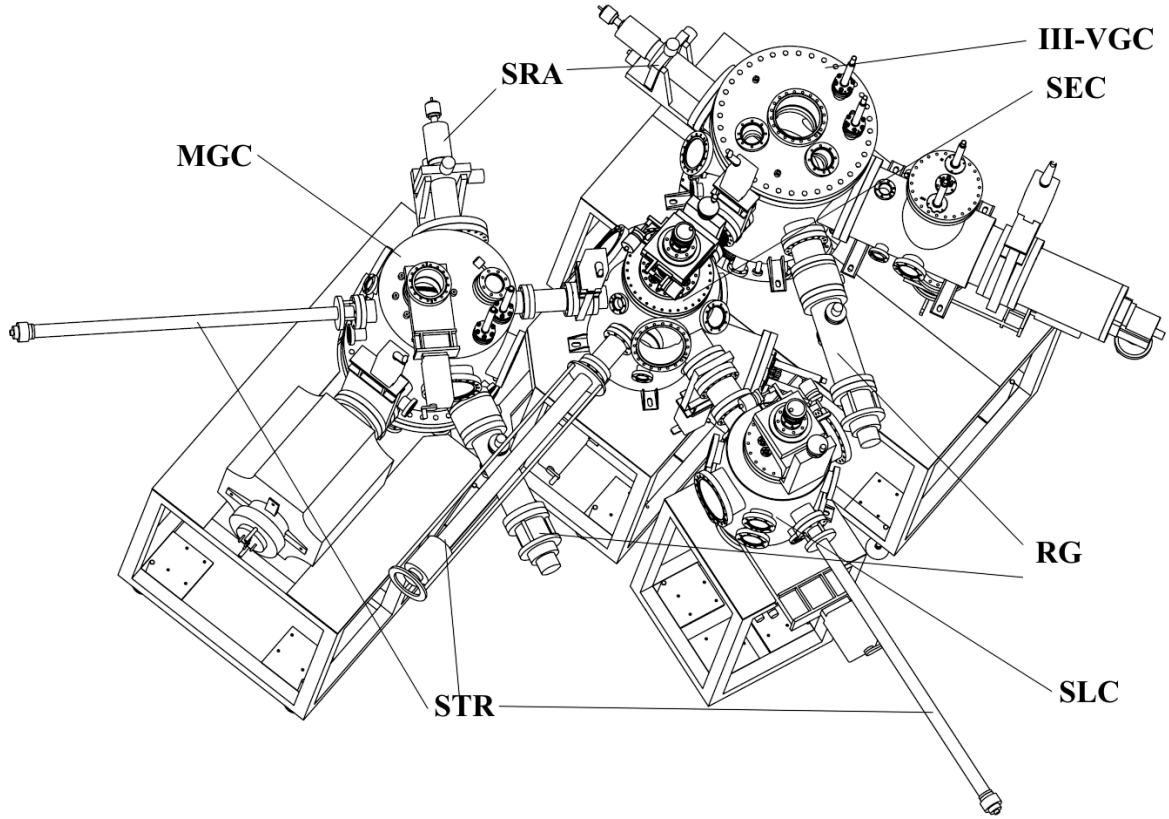


Figure 2.1: Top-view of the MBE set-up showing different chambers. III-VGC: III-V compound semiconductor growth chamber, MGC: metal growth chamber, SEC: sample exchange chamber, SLC: sample loading chamber, STR: sample transfer rod, and SRA: sample rotation assembly, and RG: RHEED gun.

chamber is equipped with several effusion cells such as Iron, Cobalt, Silicon, Aluminium, and Gallium and provides an Arsenic-free growth environment. A Bayard-Alpert ionization gauge is also included in the metal growth chamber to control the evaporation rates. The metal growth chamber has a magneto-optic Kerr effect (MOKE) magnetometer for *in situ* magnetic measurements. The sample can be transferred to the MOKE set-up after growth for magnetic characterization.

MBE growth requires UHV conditions ( $< 10 \times 10^{-9}$  Torr). This high vacuum is achieved by use of different high vacuum pumps such as cryo-pumps, Ti-sublimation pumps, and ion-pumps. In addition, a cryoshroud (liquid nitrogen shroud) encompasses the entire inner surface of the growth chamber in order to prevent the desorption of particles from the chamber walls. In this work, the buffer layers on the GaAs substrates were grown in the III-V growth chamber with a typical base pressure of about  $5 \times 10^{-8}$  Torr. The high pressure is essentially due to the partial pressure of the  $\text{As}_4$ . The typical base pressure for growth of Fe and  $\text{Fe}_3\text{Si}$  films in the metal growth chamber was about  $1 \times 10^{-10}$  Torr.

### 2.1.2 Reflection high-energy electron diffraction

Reflection high-energy electron diffraction (RHEED) is widely used as a sensitive technique for the *in situ* investigation of surface structures and growth processes in MBE. The geometry of RHEED is quite simple. A high-energy beam (typically 20 keV) is directed to the sample surface at a grazing angle ( $< 3^\circ$ ). The electrons are diffracted by the crystal structure of the sample and then impinge on a phosphor screen mounted opposite to the electron gun. The resulting diffraction pattern depends on the structure and the morphology of the probed surface. The grazing incidence angle ensures that only a few atomic layers are probed despite the high-energy of the incident electrons. Conceptually, perfectly flat surfaces should result in a diffraction pattern that consists of spots arranged on Laue rings. However, due to non-idealities in the electron beam and the sample's surface, streaks appear instead of spots [69, 70]. The distance between the streaks is inversely related to the surface lattice unit cell size. If a surface is atomically flat, then sharp RHEED patterns are seen. If the surface is rough, then the RHEED pattern is more diffuse. In many cases, because of surface roughness, the diffraction pattern is produced by transmission through the three-dimensional crystalline islands.

In kinematic scattering theory [70], the diffraction results when the Laue condition is satisfied:

$$\mathbf{k}_s - \mathbf{k}_0 = \mathbf{G}, \quad (2.1)$$

where  $\mathbf{k}_s$  and  $\mathbf{k}_0$  are the wave-vectors for the diffracted and the incident beams, respectively, and  $\mathbf{G}$  is the reciprocal lattice vector. For elastic scattering,  $|\mathbf{k}_s| = |\mathbf{k}_0|$  defines a sphere of radius  $|\mathbf{k}_0|$ , called the Ewald sphere. The intersections of the Ewald sphere and the reciprocal lattice points determine which diffraction conditions are allowed. For 20 keV electrons,  $|\mathbf{k}_0|$  is equal to  $785 \text{ nm}^{-1}$ , which is about 70 times larger than the reciprocal unit cell of GaAs [70]. Due to this large radius of the Ewald sphere, we observe streaks in RHEED.

Detailed discussions on RHEED theories can be found in the literature [70, 71] and will not be discussed here. A relevant topic in RHEED, useful for discussion in subsequent chapters, is the streak shape analysis. In general the diffracted beam (RHEED streak) profile is composed of two parts: a central spike due to the long-range order over the surface and a broad function due to the step disorder on the surface [72, 73]. Though in general the shape of the measured RHEED profile can be complicated, the width of the diffracted profile is usually inversely proportional to the average terrace separation. If the measured full-width-at-half-maximum (FWHM) is  $b$ , then the average terrace separation  $L_{av}$  is simply given by  $2\pi/b$ . This number is only approximate because the actual relation between the width of the diffracted profile and the mean terrace size depends specifically on the step distribution on the surface [72]. However, this basic idea will be used in the study of Fe growth to determine the island/terrace size or separation of growing Fe films. More details about the kinematic analysis of the RHEED diffraction profile can be found in Refs. [71, 72, 73].

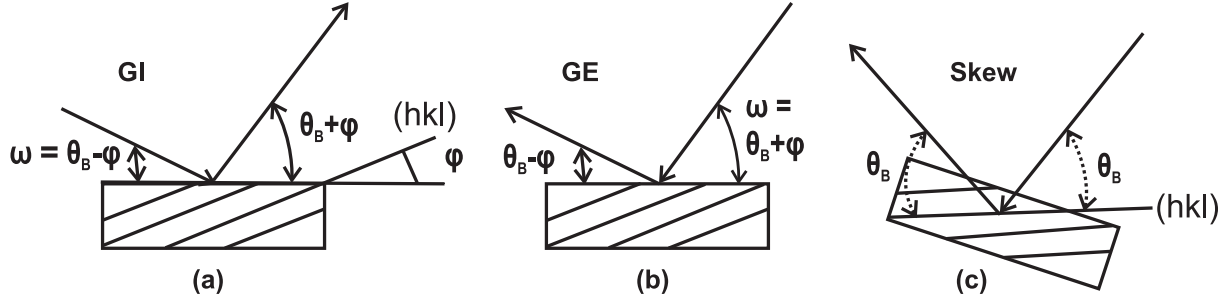


Figure 2.2: Definitions of diffraction geometry for an asymmetric Bragg diffraction. (a) grazing-incidence geometry (b) grazing-exit geometry and (c) skew-geometry for the plane (hkl) making an angle  $\varphi$  to the sample surface.  $\theta_B$  is the Bragg angle.

## 2.2 High resolution X-ray diffraction

High resolution X-ray diffraction (HRXRD) is employed in this work to characterize the basic structural properties of the ferromagnetic films. HRXRD is a powerful tool for non-destructive *ex situ* investigations of epitaxial layers. From HRXRD, information about the composition and uniformity of the epitaxial layers, layer thickness, strain and strain relaxation, as well as the presence of defects such as dislocations can be obtained. There are several text books and reviews [74, 75, 76, 77] on the analysis of epitaxial layers by HRXRD. Here only a brief description of some relevant topics will be presented.

**Geometries of asymmetric reflections** The two major kinds of scans in HRXRD, namely  $\omega - 2\theta$  scan and  $\omega$  scan, are sensitive to different properties of the layer. The  $\omega - 2\theta$  scan is sensitive to information such as strain, lattice constant and composition, whereas the  $\omega$  scan is sensitive to defects such as dislocations and mosaic spread. The  $\omega - 2\theta$  type scans can be used for both symmetric and asymmetric reflections resulting in quite different scattering geometries. The geometry of the  $\omega - 2\theta$  scan for an asymmetric reflection (hkl) making an angle  $\varphi$  with the sample surface is schematically defined in Fig. 2.2. There are three measurement geometries: grazing-incidence (GI), grazing-exit (GE) and skew. In the skew geometry (a quasisymmetric configuration), the sample is tilted with respect to its surface normal by the lattice plane inclination  $\varphi$ . Because of this tilting requirement, a four-circle diffractometer is required for the measurements in skew geometry.

**Determination of the strain and composition of the epitaxial layers** The lattice constant of a thin film that grows coherently on a single crystalline substrate is modified parallel to the growth direction. From X-ray diffraction, the information about lattice constant of the layer is obtained, which in principle is determined by Bragg's law:

$$2d_{hkl} \sin \theta_B = n\lambda, \quad (2.2)$$

where  $d_{hkl}$  is the spacing of the lattice planes with Miller indices (hkl) and  $\theta_B$  is the corresponding Bragg angle. From symmetric X-ray diffraction, information on the lattice constant of the layer perpendicular to the film plane  $a_{\perp}^L$  can be obtained. However, this is the strained lattice constant of the layer. For a tetragonal distortion of the layer, the

unstrained lattice constant of the layer  $a_0^L$  is related to the strained lattice constant by the following equation [77]:

$$a_0^L = \frac{C_{11}}{C_{11} + 2C_{12}}(a_0^L - a_0^s) + a_0^s, \quad (2.3)$$

where the constants  $C_{11}$  and  $C_{12}$  are the elastic stiffness of the layer and  $a_0^s$  is the relaxed lattice constant of the substrate. This unstrained lattice constant of the layer is used to determine the composition of the layer. For binary and ternary alloys, the composition is often determined from Vegard's law, which simply states that the lattice constant of a solid solution alloy varies linearly with composition, following a line drawn between the values for the pure constituents.

**Determination of thickness of the layers** A very accurate way to determine the layer thickness can be achieved from the so called thickness fringes, which are small periodic oscillations around the layer peak in an  $\omega - 2\theta$  scan. These fringes originate from the interference of the wave fields. The measurement of these interference peak separation,  $\Delta\theta_B$ , provides the thickness  $t$  [74]:

$$\Delta\theta_B = \frac{\lambda \sin(\theta_B \pm \varphi)}{t \sin 2\theta_B}, \quad (2.4)$$

where  $\lambda$  is the wavelength, and  $\varphi$  is the angle between the reflecting plane and the surface. Positive sign applies to the GI geometry and negative sign to the GE geometry. This is a very useful method, since the above equation does not contain anything about the material or diffraction conditions other than the Bragg angle and geometry. In practice, a more accurate computer simulation is usually employed to extract the layer thickness and other parameters. In this study, a computer program called **MadMax** was employed which uses a dynamical X-ray diffraction formalism using the Takagi-Taupin formalism [7].

**Reciprocal space map (RSM)** As the name suggest, the RSM refers to the intensity contour maps, keeping one of the Miller indices, e.g.,  $l$  in the reciprocal lattice, fixed, while the other two indices  $h$  and  $k$  are varied by  $\pm\Delta h$  and  $\pm\Delta k$ , respectively. This is achieved with a triple axis diffractometer, where an analyzer is placed behind the specimen and in front of the detector. The analyzer is mounted on an axis concentric with the specimen and is scanned independently of the sample. The experimenter can then map the intensity distribution with respect to the direction of the radiation scattered by the instrument. Usually, one measures several  $\omega - 2\theta$  scans for different  $\omega$  offsets with the analyzer crystal. The  $\omega - 2\theta$  scan in fact corresponds to a scan along the vector  $S_x[hkl]$  reflection in reciprocal space whereas the  $\omega$  scan is perpendicular to  $S_x[hkl]$  as shown in Fig. 2.3(a). The conversion of a peak position  $(\omega, 2\theta)$  to reciprocal space co-ordinates  $S_x$  and  $S_y$  can be obtained from Fig. 2.3(b) [75]:

$$S_x[h_1k_1l_1] = Q_x/2\pi = \frac{1}{\lambda}[\cos \omega - \cos(2\theta - \omega)] \quad (2.5)$$

$$S_y[h_1k_1l_1] = Q_y/2\pi = \frac{1}{\lambda}[\sin \omega + \sin(2\theta - \omega)]. \quad (2.6)$$

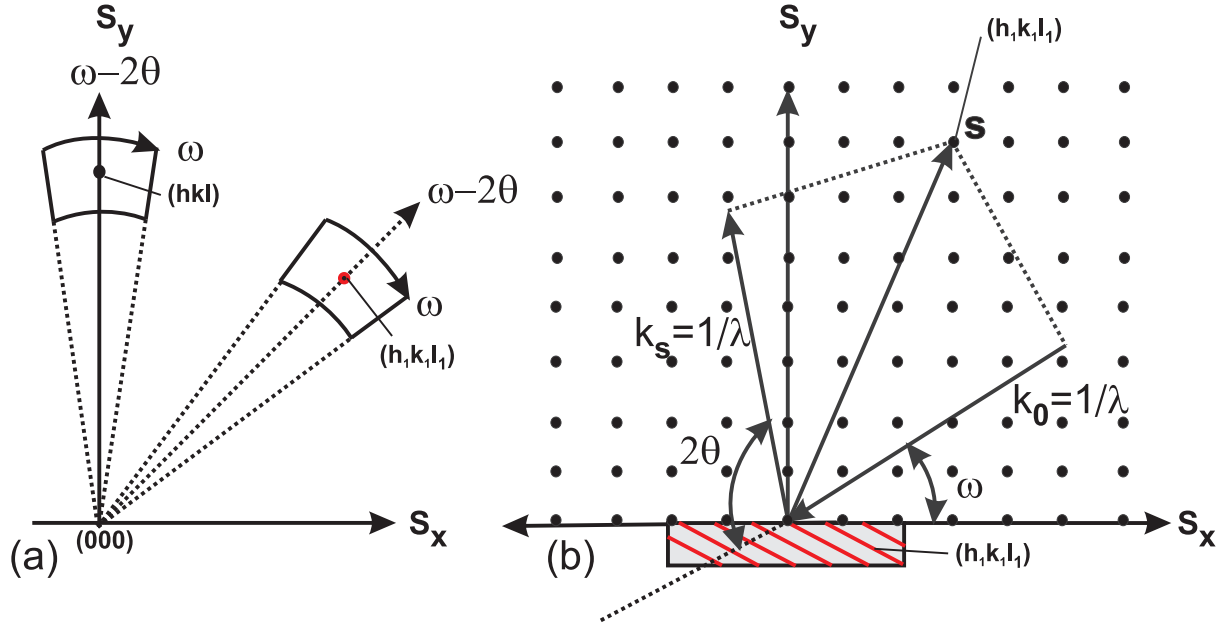


Figure 2.3: (a) Scans in reciprocal space for two different reciprocal lattice points (hkl) (symmetric) and ( $h_1k_1l_1$ ) (asymmetric). (b) Reciprocal space construction for the asymmetric reflection ( $h_1k_1l_1$ ).  $\mathbf{k}_s$  and  $\mathbf{k}_0$  are the wave vectors for the diffracted and the incident X-rays, respectively.  $\mathbf{S} = \mathbf{k}_0 + \mathbf{k}_s$  is the scattering vector.

Usually, the vector components  $S_x$  and  $S_y$  refer to directions perpendicular and parallel to the growth plane. The region that is accessible in reciprocal space depends on the geometry, the wavelength and the lattice constants of the epitaxial layers. In a RSM, the strain influences only the  $S_y$  direction whereas the mosaic spread or tilt is observed along the  $S_x$  direction in reciprocal space. Thus, using RSM, the strain and strain gradients can be separated from structural imperfections such as tilts and mosaicity.

## 2.3 X-ray Reflectivity

X-ray reflectivity (XRR) is a non-destructive, non-contacting method to measure film thickness, interface and surface roughness and density of films ranging from 20 Å to 1 μm total thickness. Films can be single or multilayer structures, and the thickness of the individual layers can be determined with no optical constant corrections required. The films can be epitaxial, polycrystalline or amorphous. The thickness of the film is measured from the periodicity of fringes, the density from the angle at which the intensity begins to drop and the roughness from the damping of the thickness fringes and rate of intensity decrease with angle. These are not affected by the crystallinity of the film. XRR is basically a grazing incidence scattering technique, with the incident and scattered beams at equal angles to the surface of the sample. In XRR, an X-ray beam strikes a solid-surface at a small angle ( $0 - 2^\circ$ ) and is totally reflected. Above the critical angle of total reflectance  $\theta_c$  the beam penetrates the sample. Measurement of the critical angle provides the determination of the density of the material. If the sample contains a single thin layer, X-rays are reflected from the air/layer as well as from the layer/substrate interfaces. This

leads to interference fringes. In this case the position of the  $m$ th order fringe maximum  $\theta_m$  can be shown to be related to the layer thickness  $t$  and the critical angle  $\theta_c$  by the following simple equation [77]:

$$\begin{aligned}\theta_m &= \sqrt{\{(m + 1/2)\lambda/2t\}^2 + \theta_c^2} & \text{for } n_s > n_l \\ &= \sqrt{(m\lambda/2t)^2 + \theta_c^2} & \text{for } n_s < n_l,\end{aligned}\tag{2.7}$$

where  $n_s$  and  $n_l$  are the refractive indices of the substrate and the layer for X-ray of wavelength  $\lambda$ . From this formula, the thickness of the layer can be derived.

For a layer structure consisting of several layers, the X-ray reflectivity is calculated by applying the recursive theory of Parratt [78], a generalization of the Fresnel reflectivity theory, to a system of flat, ideal layers, each with a constant electron density. The roughness of the real surfaces can be taken into account by considering the so called Born Approximation (BA) or Distorted Wave Born Approximation (DWBA) [79]. The BA is valid when the reflectivity is small, whereas DWBA is valid when the reflectivity approaches unity. In general, the reflection amplitude  $r$  which is valid for both the BA and DWBA, is written in the following form:

$$r = r_F \exp\{-1/2(\sigma_{j-1,j}^2 S_j S_{j-1})\},\tag{2.8}$$

where  $r_F$  is the reflection amplitude for a single ideal surface, also called as Fresnel amplitude.  $\sigma_{j-1,j}$  is the root-mean-square roughness between the  $j - 1$ th and  $j$ th layers.  $S_j$  and  $S_{j-1}$  are the scattering vectors for the  $j - 1$ th and  $j$ th layers, respectively. This can be substituted in the reflection amplitude from the interface between  $j - 1$ th and  $j$ th layers of the Parratt formalism to obtain:

$$r_{j-1,j} = \frac{f_{j-1} - f_j}{f_{j-1} + f_j} \exp(-1/2(\sigma_{j-1,j}^2 S_j S_{j-1})),\tag{2.9}$$

where  $f_j$  depends on the angle of incidence and complex refractive index of the  $j$ th layer as discussed in Ref [78]. This modified Parratt formalism will be used in this work for XRR simulations to evaluate the layer thickness and interface/surface roughness.

Both for HRXRD and XRR, a state-of-the-art Philips X'Pert Diffractometer was used which is a highly advanced, versatile materials characterization system. It consists of a multilayer X-ray mirror for parallelization of the divergent beam emitted by the X-ray source and a grooved Ge crystal acting as a monochromator in combination with that mirror. Interchangeable PreFIX incident and diffracted beam optics can be configured for an optimal measurement of high-resolution scans and reflectivity experiments. More information about this product can be found from the PaNalytical web site [80].

## 2.4 Magnetic characterization

The basic magnetic properties of the thin films were investigated by *in situ* Magneto-optic Kerr Effect (MOKE) and *ex situ* superconducting quantum interference device (SQUID) magnetometry. MOKE is a surface sensitive technique whereas SQUID is sensitive to the whole volume of the sample and is suitable for extraction of more accurate quantitative information.

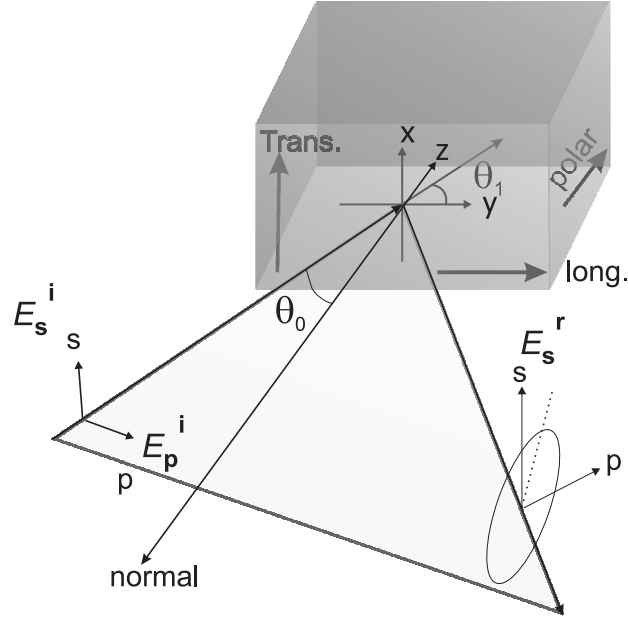


Figure 2.4: The Kerr effect geometries: longitudinal (magnetization along the plane incidence of the light), transverse (magnetization perpendicular to the plane incidence of the light) and polar (magnetization in the plane incidence of the light).

#### 2.4.1 In situ Magneto-optic Kerr effect

The magneto-optical Kerr effect (MOKE) is observed as a net rotation and elliptical polarization of incident linearly polarized light as it is reflected from a magnetized sample [81]. This change in the polarization state (or the intensity) of an incident electromagnetic wave arises due to the interaction of the electric and magnetic fields of the waves with the spin of the electrons in the material that occurs through the spin-orbit interaction. The magnitude of this change in polarization is proportional to the magnetization of the sample. The amount of rotation (in radians) and ellipticity (ratio between the minor and major axis of the ellipse) induced in the reflected beam is of the order of  $1/1000$ , i.e., relatively small. However, with standard noise elimination techniques this signal can be easily measured. The MOKE technique derives its surface sensitivity from the limited thickness of the deposited magnetic film, which can be as thin as one atomic layer [82, 83]. MOKE magnetometry has emerged as a very popular tool to characterize the magnetic properties of thin films due to its simplicity, low cost and high sensitivity.

In reflection mode, one distinguishes between three Kerr effects, depending on the relative orientation of the magnetization  $M$  with respect to the plane of incidence of the light: the polar, the longitudinal and the transverse Kerr effects as defined schematically in Fig. 2.4.

**Microscopic origin** According to Maxwell, the Faraday or Kerr effect is a consequence of the two circular modes (which composes the linear polarized light) having different velocities of propagation. This leads to a difference in the dielectric constants of left- and right-circularly polarized light and account for the Faraday or Kerr rotation. It is now established that the spin-dependent dielectric constant is a consequence of the spin-



orbit interaction which couples the electron spin to its motion [82, 83]. The change of the wave-functions due to the spin-orbit interaction is believed to give rise to a correct order-of-magnitude of the difference between the two refractive indices. A full derivation of the magneto-optic effect in a ferromagnet using perturbation theory can be found from Argyres [84].

**Macroscopic Formalism** Macroscopic descriptions of the magneto-optic effect are based on the analysis of the dielectric properties of a medium. Maxwell expressed linearly polarized light as being a superposition of two circularly polarized components, and realized that the Faraday or Kerr effect is a result of the different propagating velocities of the two circular modes. The dielectric property of a medium is characterized by a  $3 \times 3$  tensor  $\epsilon_{ij}$  with  $i, j = 1, 2, 3$ . In general, this dielectric tensor can be decomposed into symmetric and antisymmetric parts. The antisymmetric part of the dielectric tensor gives rise to the Faraday or Kerr effect. The Kerr rotation  $\phi'$  and ellipticity  $\phi''$  are usually calculated from the coefficients of the Fresnel reflection matrix by solving Maxwell's equations for the dielectric tensor of anisotropic media [82, 83, 85, 86]. The Kerr effects in the general case of arbitrary magnetization direction and oblique incidence can be obtained using the formalism of Yeol You *et al.* [86]:

$$\phi_{s,p} = \frac{\cos \theta_0 (\alpha_z \pm \alpha_y \tan \theta_1)}{\cos(\theta_0 \pm \theta_1)} \cdot \frac{in_0 n_1 Q}{n_1^2 - n_0^2}, \quad (2.10)$$

where the positive (negative) sign stands for  $p$ -polarized ( $s$ -polarized) light.  $\theta_0$ ,  $n_0$ , and  $\theta_1$ ,  $n_1$  are the angle of incidence and the refractive index of the nonmagnetic medium 0, and that of the magnetic medium 1, respectively (see Fig. 2.4). The parameter  $Q$  is defined as  $Q = i\epsilon_{xy}/\epsilon_{xx}$ .  $\alpha_x$ ,  $\alpha_y$  and  $\alpha_z$  are the direction cosines of the magnetization vector  $\mathbf{M}_s$ . In this equation, the Kerr effect is expressed as the product of two simple factors: the pre-factor is a simple function of the optical parameters of the media and the direction of the magnetization, and the second factor is the polar Kerr effect for normal incidence.

**Experimental setup** The experimental set-up for MOKE employed in this work is home made. The components of the MOKE system include a He-Ne intensity-stabilized laser ( $\lambda = 632.8$  nm), two Glan-Thompson polarizers, a photo-elastic modulator ( $f = 50$  kHz) and a photodiode detector. The plane of incidence, which includes the sample normal, and both the incident and reflected light rays, define the coordinate system for the MOKE apparatus. The other components such as the chopper and the lock-in amplifier are used to improve the signal-to-noise ratio.

## 2.4.2 Ex situ SQUID magnetometry

SQUID magnetometry is well-known as one of the most sensitive methods of magnetometry. This technique uses a combination of superconducting materials and Josephson junctions to measure magnetic fields with resolutions up to  $10^{-14}$  T or better.

**The DC SQUID** A DC SQUID is actually a rather simple device. It consists of two Josephson junctions connected in parallel on a closed superconducting loop as shown

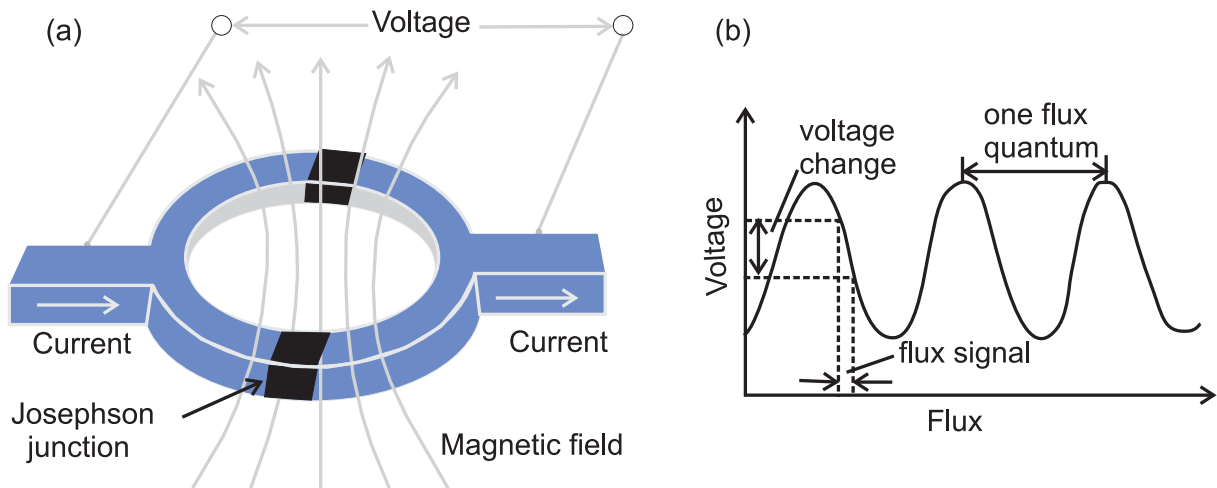


Figure 2.5: The DC SQUID construction and principle: (a) Shows the two Josephson junctions forming a superconducting ring, which forms the DC SQUID. (b) Shows the output voltage as a function of applied flux. A tiny flux signal produces a corresponding voltage swing across the SQUID, which conventional electronics can measure. Figure inspired by Ref. [2].

in Fig. 2.5(a) [2]. A fundamental property of superconducting rings is that they can enclose magnetic flux only in multiples of a universal constant called the flux quantum,  $h/2e = 2.07 \times 10^{-15}$  Wb. Because the flux quantum is very small, this physical effect can be exploited to produce an extraordinarily sensitive magnetic detector known as the SQUID. SQUIDS actually function as magnetic flux-to-voltage transducers where the sensitivity is set by the magnetic flux quantum. Applying current to the SQUID (biasing it) sends Cooper pairs of electrons tunnelling through the junctions. A magnetic field applied to the ring, however, alters the flow. Specifically, it changes the quantum-mechanical phase difference across each of the two junctions. These phase changes, in turn, affect the critical current of the SQUID. A progressive increase or decrease in the magnetic field causes the critical current to oscillate between a maximum value and a minimum one. The maximum occurs when the flux administered to the SQUID equals an integral number of flux quanta through the ring; the minimum value corresponds to a half-integral number of quanta. The flux applied to the SQUID can assume any value, unlike the flux contained within a closed superconducting ring, which must be an integral number. In practice, we do not measure the current but rather the voltage across the SQUID, which also swings back and forth under a steadily changing magnetic field as shown in Fig. 2.5(b). This quantum interference effect provides us with a digital magnetometer. Each “digit” represents one flux quantum. In fact, conventional electronics can detect voltages corresponding to changes in magnetic flux of much less than one flux quantum. Thus the SQUID in essence is a flux-to-voltage transducer, converting a tiny change of magnetic flux into a voltage.

**Practical SQUID Magnetometer** Although in some applications it is convenient to expose the SQUID directly to the magnetic field of interest, more often the magnetic signal is conveyed to the SQUID by a flux transformer. A flux transformer is a closed supercon-

ducting circuit consisting of two coils in series. One coil, the input coil, is magnetically coupled to the SQUID and is usually fabricated along with it; the second, or pick-up coil, is exposed to the field to be measured. This second coil acts as a magnetic antenna that couples external signals into the SQUID. It is a basic principle of superconductivity that the flux inside a closed superconducting circuit cannot change. Consequently, a change in field that causes the flux in the pick-up coil to change also causes a change in the flux in the input coil. The SQUID senses this latter flux change. The area of the pick-up coil is usually much greater than the area of the SQUID. The prime function of the transformer is to convert the high magnetic flux sensitivity of the SQUID itself into a high magnetic field sensitivity. Another advantage of using a flux transformer is that the input coil, which can be made as a wire or a thin film structure, can be configured to suit the measurement at hand. In particular, it can be wound so as to be sensitive not to the magnetic field itself, but to the gradient of the field in a chosen direction, or to a higher derivative of the field. In these cases, the flux transformer is referred to as a gradiometer. Since the gradient of the magnetic field falls off more rapidly with distance from the magnetic source than the field itself, a gradiometer tends to reject magnetic interference from distant sources, while remaining sensitive to closer objects. Again, a gradiometer is essentially sensitive to changes in the field gradient rather than its absolute value, and the technique of controlled resetting can be applied to yield a large dynamic range. The system used in this work implements a second-derivative gradiometer that minimizes background drifts in the SQUID detection system caused by relaxation in the magnetic field of the superconducting magnet. The second-derivative gradiometer is also more noise immune than a first-order gradiometer.

The MPMS SQUID system [87] used in this work is composed of several units: the dewar, the probe and SQUID assembly, and the electronic control system. The probe contains a high-precision temperature control system that allows measurements between 1.9 K to 400 K with an accuracy of 0.01 K (valid at low temperature). A superconducting electromagnet can deliver a field of up to  $5 \times 10^4$  G with a field accuracy of 0.1 G (for small magnetic fields). The dewar consists of an inner liquid helium reservoir, and an outer liquid nitrogen jacket to reduce excessive liquid helium boil-off. Liquid helium is used both to maintain the electromagnet in a superconducting state and to cool the sample space. The samples are mounted within a plastic straw and connected to one end of a sample rod which is inserted into the dewar. The other end is attached to a stepper motor which is used to position the sample within the center of the SQUID pickup coil. The generated magnetic field is well-shielded from the surroundings.

**Note: Errors in the measurement of saturation magnetization** It should be pointed out that the measurement of saturation magnetization  $M_s$  in the MPMS SQUID system were found to show a large error of about 200 emu/cm<sup>3</sup>. This error arises due to the error in  $M_s$  measured during different "SQUID runs". This means that, the value of  $M_s$  shows an error of about  $\leq 20\%$  when the same piece of the sample is remounted and centered again. The origin of this error is not precisely known yet. However, this error adds to the errors due to the determination of volume/thickness of the sample and the determination of saturation field. In the subsequent sections, all these errors are taken into account to find the net error in  $M_s$ .

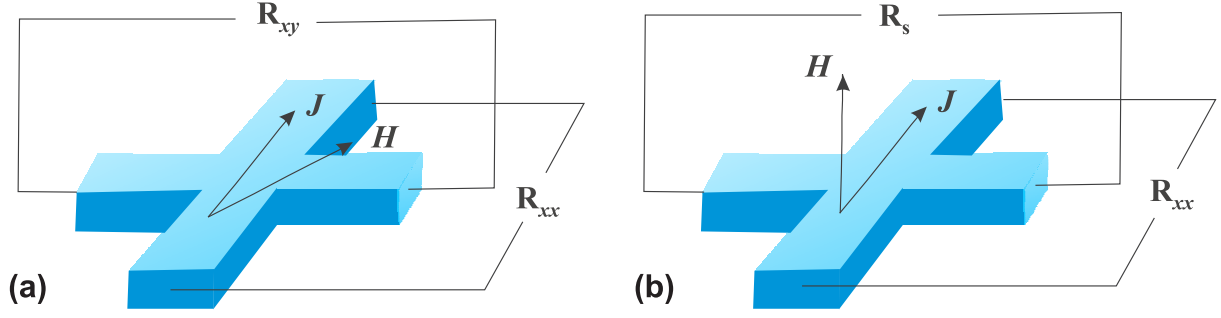


Figure 2.6: The geometry of magnetotransport measurements. (a) Magnetic field is applied in-plane. The longitudinal magnetoresistance is referred to as anisotropic magnetoresistance ( $R_{xx}$ ) and the transverse magnetoresistance ( $R_{xy}$ ) as planar Hall effect. (b) Magnetic field is applied perpendicular to the film plane and the transverse resistance is measured. This is the usual Hall effect geometry. For ferromagnets this is sum of ordinary and extraordinary Hall effect.

## 2.5 Magnetotransport measurements

Magnetotransport measurements provide a sensitive tool to study magnetic anisotropy and magnetization reversal in low-dimensional magnetic structures. They also provide information on transport-related phenomena such as the spin-dependent scattering mechanism of carriers. One important advantage of magnetotransport, particularly for the case of FM/SC hybrid structures, is its relative insensitivity to a semiconducting or insulating substrate. For thin films, it is difficult to subtract the magnetic contribution of the substrate in traditional magnetometry techniques like vibrating sample magnetometry or SQUID magnetometry. In magnetotransport, only the metallic portion of the sample (the thin film) is measured. Another advantage of magnetotransport is the simplicity of the experimental set-up and the relative low cost of the equipment.

The subject of galvanomagnetism is rather vast. One of the most important type of electrical resistance change in ferromagnetic metals, which is to be studied in this work, is the one associated with the direction of magnetization relative to the current. Magnetotransport measurements can be performed in several applied magnetic field geometries as defined schematically in Fig. 2.6. When the magnetic field is applied in-plane [Fig. 2.6 (a)], the longitudinal resistance  $R_{xx}$  is referred to as anisotropic magnetoresistance (AMR), and the transverse resistance  $R_{xy}$  as the planar Hall effect (PHE). For perpendicular magnetic field [Fig. 2.6 (b)], two contributions arise in the transverse resistance of ferromagnets. The ordinary Hall effect (OHE) arises from the Lorentz force while the Anomalous Hall effect (AHE) (also called extraordinary Hall effect) is related to the magnetization of the thin film. The electric field  $\mathbf{E}$  for arbitrary orientations of the external magnetic field  $\mathbf{H}$  and magnetization  $\mathbf{M}$  for a polycrystalline and single domain ferromagnetic sample is often written in the following way [39, 40]:

$$\mathbf{E} = \rho_{\perp} \mathbf{J} + (\rho_{\parallel} - \rho_{\perp}) \hat{\alpha} (\mathbf{J} \cdot \hat{\alpha}) + \rho_{\text{AHE}} \hat{\alpha} \times \mathbf{J}, \quad (2.11)$$

where  $\mathbf{J}$  is the current density and  $\hat{\alpha}$  is a unit vector in the direction of the magnetic moment of the single domain sample.  $\rho_{\perp}$  and  $\rho_{\parallel}$  are the longitudinal resistivities parallel and perpendicular to  $\hat{\alpha}$ , respectively.  $\rho_{\text{AHE}}$  is the transverse resistivity for the magnetization

perpendicular to the film plane. Thus the last term denotes the AHE. The first two terms represent both AMR and PHE. When the magnetic field is applied in the film plane with a current along the  $x$ -axis, we can find from Eq. (2.11) [39, 40]:

$$\rho_{xx} = \rho_{\perp} + (\rho_{\parallel} - \rho_{\perp}) \cos^2 \theta_M, \quad (2.12)$$

$$\rho_{xy} = \frac{1}{2}(\rho_{\parallel} - \rho_{\perp}) \sin 2\theta_M, \quad (2.13)$$

where  $\theta_M$  represents the angle between  $\mathbf{J}$  (or  $x$ -axis) and  $\hat{\alpha}$ . These Eqs. (2.12) and (2.13) are conventionally used to describe the AMR and PHE, respectively. It may be pointed out that the above three equations are simplified form for polycrystalline samples and do not necessarily describe the behavior of single crystalline samples. When a saturating field  $\mathbf{H}$  with components  $H_i = H\alpha_i$ , is applied to a crystal, the relationship between the electric field  $\mathbf{E}$  and current density  $\mathbf{J}$  is defined through the relation:

$$E_i = \rho_{ij}(\alpha) J_j, \quad (2.14)$$

where  $\rho_{ij}(\alpha)$  is a second-rank magnetoresistivity tensor and  $E_i$  ( $J_j$ ) are components of  $\mathbf{E}$  ( $\mathbf{J}$ ). Here, the Einstein summation convention is understood. The tensor  $\rho_{ij}(\alpha)$  depends on the direction cosines,  $\alpha_i$ . Since  $\rho_{ij}(\alpha)$  is a second-rank tensor it can be divided into its symmetrical and antisymmetrical parts:

$$\rho_{ij}^s(\alpha) = \frac{1}{2}[\rho_{ij}(\alpha) + \rho_{ji}(\alpha)], \quad (2.15)$$

and

$$\rho_{ij}^a(\alpha) = \frac{1}{2}[\rho_{ij}(\alpha) - \rho_{ji}(\alpha)]. \quad (2.16)$$

The Onsager's theorem [88] applied to a magnetically saturated crystal implies that:

$$\rho_{ij}(\alpha) = \rho_{ji}(-\alpha), \quad (2.17)$$

so that  $\rho_{ij}^s$  is an even function of the  $\alpha_i$  and  $\rho_{ij}^a$  is an odd function of the  $\alpha_i$ . In fact it can be easily shown that AMR originates from the symmetric part of the resistivity tensor whereas the AHE originates from the antisymmetric part of the resistivity tensor. Though there is very few literature examining the exact origin of PHE, usually the PHE is also attributed to the symmetric part of the resistivity tensor. However, as it will be shown in the subsequent chapters, this notion of the PHE is not strictly valid for the low-symmetric [113] orientation.

Magnetotransport experiments were performed in an usual set-up for Hall effect measurements. The methods of the sample preparation which was different for Fe and Fe<sub>3</sub>Si films will be discussed in the respective sections.

# Chapter 3

## Fe films on GaAs(113)A substrates

### 3.1 Introduction

Fe on GaAs is a model ferromagnet/semiconductor (FM/SC) hybrid structure. The first epitaxial growth of Fe films on GaAs was reported more than twenty years ago by J. R. Waldrop and R. W. Grant [89]. Later on, G. A. Prinz and others pioneer the work of single crystal Fe films on GaAs(001) and (110) substrates [90, 91, 92, 93, 94, 95, 96, 97, 98, 99, 100, 101, 102, 103]. There are several reasons that make Fe/GaAs system interesting for spintronics applications:

1. The close lattice match: the lattice constant of GaAs ( $a_0 = 5.654 \text{ \AA}$ ) is almost exactly twice that of bcc Fe ( $a_0 = 2.866 \text{ \AA}$ ). This leads to a lattice mismatch of only  $-1.4 \%$  if one considers half the lattice constant of GaAs.
2. Room temperature ferromagnetism: Bulk Fe has a high Curie temperature of 1040 K.

Because of the small lattice mismatch, the epitaxial growth of the stable bcc phase of Fe on GaAs(001), GaAs(110), GaAs(113)A, and GaAs(133)A substrates has been established and numerous studies optimizing growth conditions and analyzing the interface structure have been reported [3, 63, 89, 90, 91, 104, 105, 106, 107, 108]. The spin injection of Fe into GaAs has also been demonstrated [24, 25, 26], though the injection efficiency remains rather low. The exact origin of the low spin injection efficiency in this system is under considerable debate and proposals like conductance mismatch have been proposed [109]. However, Adelmann *et al.* have recently achieved high spin injection efficiency of about 50% by choosing suitable electrical bias conditions [27]. Therefore, there are good reasons to believe that high spin injection efficiency can be achieved in FM/SC. Nevertheless, optimization of the interface structure is an essential part to achieve high spin injection efficiency, because the spin injection process is strongly influenced by the details of the FM/SC interface. For example, it has been shown that for the case of Fe/(Al,Ga)As structures a decrease in interface roughness significantly increases the spin injection efficiency [28]. It is to be noted that Fe tends to react with Ga and/or As during epitaxial growth at a relatively low temperature, leading to a degradation of the interface quality as reported in the early studies [89, 100]. To avoid this problem, many subsequent studies of Fe growth were reported at low growth temperature, usually close to room temperature (RT) [63, 107, 108], which prevents the formation of  $\text{Fe}_2\text{As}$  [100] or  $\text{Fe}_3\text{Ga}_{2-x}\text{As}_x$  [106] compounds at the interface. There are also reports of Fe growth

on Ga terminated GaAs(001) templates [108, 110], which have been argued to avoid the formation of Arsenic related compounds at the interface. However, Schönherr *et al.* [63] have demonstrated that the growth of Fe on Ga terminated GaAs templates leads to the formation of macroscopic defects on the surface. For this reason, As-terminated GaAs surfaces were chosen and growth conditions were optimized to produce Fe films that exhibit a smooth surface morphology as well as a sharp interface.

Single crystal Fe films on GaAs also offer an opportunity to study magnetism at low-dimension with controllable magnetic properties. This is the subject of this chapter. Fe films on GaAs(001) substrates is well-known exhibit a dominant in-plane uniaxial magnetic anisotropy (UMA) below a certain thickness with the easy and hard axes along [110] and  $[\bar{1}10]$ , respectively [29, 100, 104, 107, 111, 112, 113]. This is unexpected given the crystal symmetry of Fe. The origin of this UMA can not be understood from the combination of common anisotropy energies like magnetocrystalline anisotropy energy, demagnetizing field energy and magnetoelastic coupling energy. Krebs *et al.* [100] added a UMA term to the total magnetic anisotropy energy to understand the observed magnetic properties in this system. They proposed that the Fe-GaAs bonding at the interface is responsible for the observed UMA. Hence, it is natural to believe that the surface reconstruction of the GaAs might play a role in the observed UMA. However, recent studies have shown that the surface reconstruction of GaAs is not responsible for the observed UMA [104, 114, 115]. Recently, Thomas *et al.* [116] showed that the in-plane anisotropic strain is absent for Fe films exhibiting UMA. Their results show no link between strain anisotropy and the UMA. However, they pointed out that for a quantitative modeling of the thickness dependence of the magnetic anisotropy, a strain anisotropy mediated by a magnetoelastic coupling term has to be included. Nevertheless, even with the substantial amount of research performed on this model system, the actual origin of the observed UMA remains an unanswered fundamental question in ferromagnetic thin-film studies.

## 3.2 Fe on GaAs(113)A: Motivation

In this work, a different orientation namely GaAs(113)A was chosen to study the effect of an orientation with reduced symmetry on the magnetic properties of the Fe/GaAs system, including the origin of UMA in these films. In Chapter 1.2 we have discussed some motivations regarding the study of FM/SC with GaAs(113)A. Fe being one of the most studied ferromagnet provides a good starting metal for integration with GaAs(113)A substrates.

**Lattice matching on the (113)-planes** As already mentioned Fe has only a lattice mismatch of  $-1.4\%$  with GaAs. The question then arises of whether this mismatch is satisfied in the (113) plane and how does the bulk truncated Fe(113) plane compare with that of GaAs(113). This question is answered in Fig. 3.1(b), where the bulk-truncated unit cells of the (113)-planes of Fe and GaAs are compared. For comparison, the corresponding unit cells of the (001)-plane of Fe and GaAs are also shown in Fig. 3.1(a). In the (001)-plane, the unit cell has the same dimensions as that of the lattice constants,  $a_{\text{GaAs}}$  and  $a_{\text{Fe}}$  and since,  $a_{\text{GaAs}} \simeq 2a_{\text{Fe}}$ , the lattice mismatch defined by  $(a_{\text{GaAs}} - 2a_{\text{Fe}})/a_{\text{GaAs}}$  is  $-1.4\%$ . Note that twice of the lattice constant is considered here. The rectangular unit cells of the (113)-planes of Fe and GaAs are shown in Fig. 3.1(b), by taking four (three) layers of

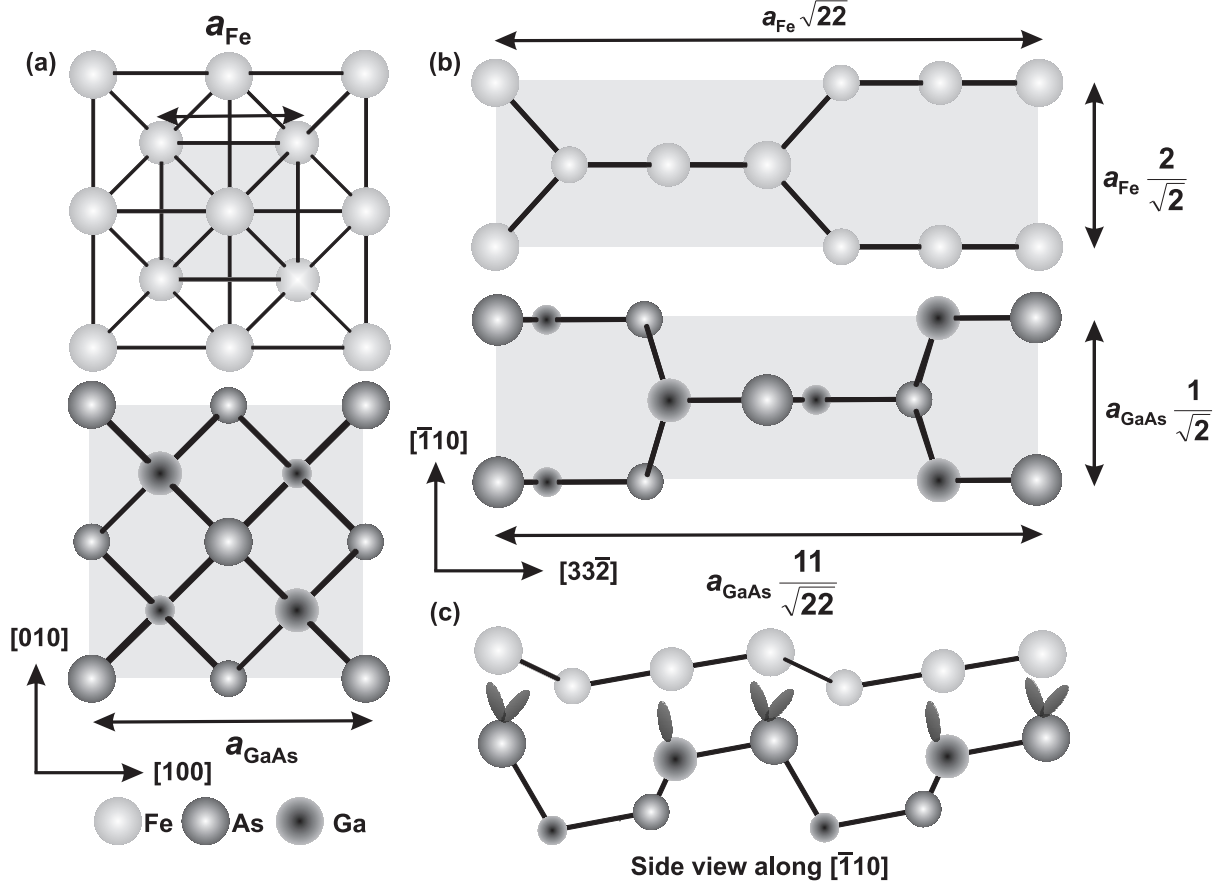


Figure 3.1: (a) Ball and stick model for the bulk-truncated GaAs(001) and Fe(001) surfaces with the unit cells indicated in gray. (b) The corresponding bulk-truncated surfaces of Fe(113) and GaAs(113)A with the unit cells indicated in gray. (c) The side view of (b) along the in-plane  $[\bar{1}10]$  axis. Size of the atoms indicate one layer of atoms. The figure demonstrate the close lattice match between the (113) planes of GaAs and Fe. The lower surface symmetry of (113)-plane is also apparent (see text).

surface atoms as shown in the side view in Fig. 3.1(c) for GaAs (Fe). Here, we define one layer as being formed by single atomic species exhibiting a  $(1 \times 1)$  unit mesh. The unit cell dimensions can be shown to be  $a_{\text{GaAs}}^{[33\bar{2}]} = 11a_{\text{GaAs}}/\sqrt{22}$  and  $a_{\text{GaAs}}^{[\bar{1}10]} = a_{\text{GaAs}}/\sqrt{2}$  for GaAs, which are nearly equal to that of Fe:  $a_{\text{Fe}}^{[33\bar{2}]} = 22a_{\text{Fe}}/\sqrt{22}$  and  $a_{\text{Fe}}^{[\bar{1}10]} = 2a_{\text{Fe}}/\sqrt{2}$ . Thus the lattice mismatch both along  $[33\bar{2}]$  and  $[\bar{1}10]$  results in the same value of  $-1.4\%$ . A careful examination of Fig. 3.1(b) also shows that the atomic arrangements on both GaAs and Fe (113)-planes are very similar, which in fact is expected, because of the identical cubic crystal structure.

**High-index surface and reduced symmetry** Another distinguishing feature of the (113)-plane (both for GaAs and Fe) is its low surface symmetry, with two major in-plane axes, namely  $[33\bar{2}]$  and  $[\bar{1}10]$ , that are crystallographically in-equivalent. This can be clearly seen from the atomic arrangements shown in the unit cells of Fig. 3.1(b). The  $[33\bar{2}]$  direction represents a mirror symmetry direction whereas the  $[\bar{1}10]$  direction does



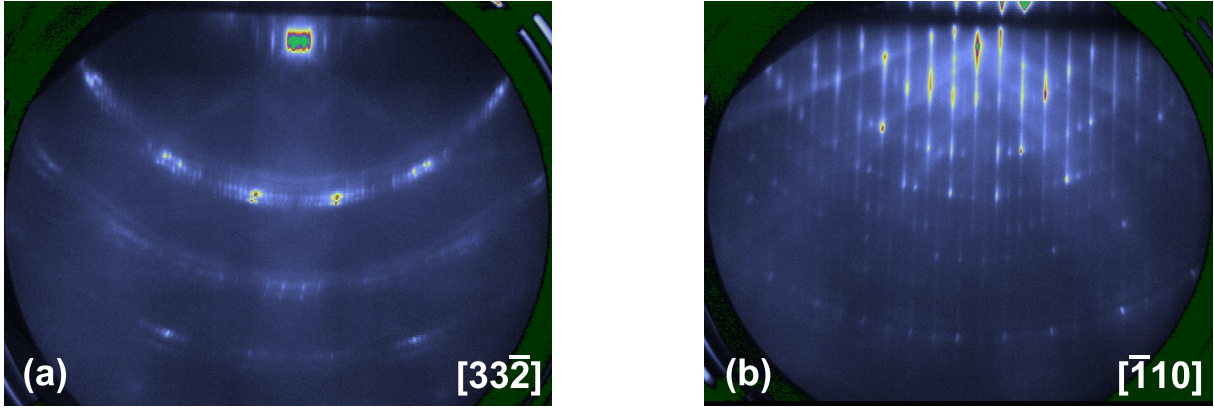


Figure 3.2: RHEED pattern from GaAs(113)A substrates before the growth of Fe taken at 0 °C along (a)  $[3\bar{3}2]$  and (b)  $[\bar{1}10]$  azimuths. The streaky RHEED pattern indicates an ordered and smooth surface morphology.

not have such a symmetry. The low symmetry of the GaAs(113) and the Fe(113) surface is basically a consequence of the high Miller-index plane, which in general offers a variety of opportunities for inducing new phenomena and are thus promising for new device applications of the FM/SC [37] as already mentioned in chapter 1.1.

**Understanding the UMA in the Fe/GaAs system** Both the (001) and (113)-planes of bcc Fe have the  $[\bar{1}10]$  in-plane axis in common. As already mentioned, the UMA in the Fe/GaAs(001) system distinguishes the crystallographically equivalent  $[\bar{1}10]$  and  $[110]$  axes of Fe. In case of Fe films on GaAs(113)A, the two major axes are already crystallographically in-equivalent. Thus a study of GaAs(113)A could provide further understanding of the origin of UMA in the Fe/GaAs system. The interfacial structure, and especially the bonding configuration between Fe and GaAs in the Fe/GaAs(113)A system, should be in principle very different, which can affect the UMA of ultrathin films. The effect of a low surface symmetry on UMA and other magnetic properties can also be explored.

**Six-fold versus four-fold magnetic anisotropy** The four-fold magnetic anisotropy usually observed in the case of thick Fe films on GaAs(001) is also expected to change, since none of the bulk easy axes, namely the  $\langle 100 \rangle$  axes, lies in-plane on the (113) surface. In fact, a projection of the  $\langle 100 \rangle$  easy axes onto the (113) surface exhibits a six-fold symmetry. Hence, a six-fold magnetic anisotropy could be expected similar to the case of Fe films on a Si(111) surface [117].

**Role of shape anisotropy** For the (113) surface of Fe, none of the bulk easy axes (the  $\langle 001 \rangle$  directions) lies in-plane. This makes it interesting to study the role of shape anisotropy (demagnetization energy) on the overall magnetic anisotropy of the system. The question of whether shape anisotropy can play a role in determining the UMA can be explored.

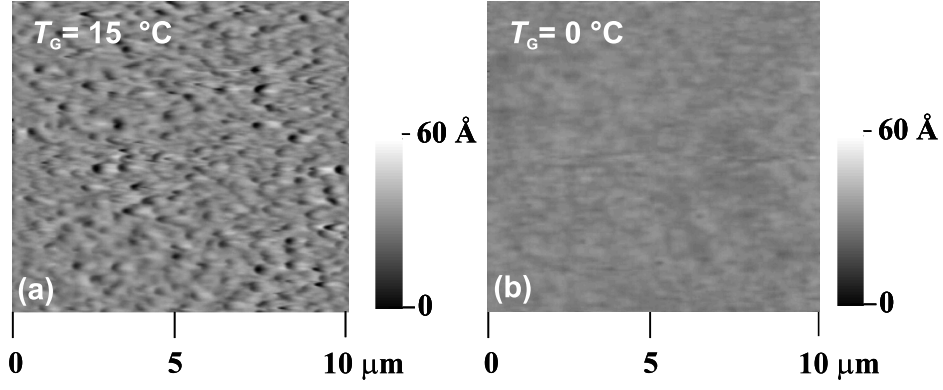


Figure 3.3: AFM images of two 26-nm-thick Fe samples grown at (a) 15 °C and (b) 0 °C. The root mean square (RMS) roughness changes from 10 Å to 3 – 5 Å when the growth temperature changes slightly from 15 to 0 °C.

### 3.3 Growth and structural properties

The growth of Fe films was performed in the multi chamber MBE system described in Sec. 2.1.1. GaAs(113)A templates were prepared in the separate III-V semiconductor growth chamber under As-rich conditions. Epi-ready single crystal commercial GaAs(113)A wafers cut to expose the (113)A surface were used. The sequential procedure to prepare GaAs(113)A templates is as follows. First a quarter wafer was loaded into the sample loading chamber, followed by heating the wafer for about 30 min to promote the water desorption. The wafer was then transferred to the III-V semiconductor growth chamber via the sample transfer chamber. The wafers were then heated to desorb the native oxide layer, which can be followed from the RHEED pattern. The oxide desorption temperature was 580 °C. The real thermocouple readings sometime vary by  $\pm 30$  °C. Hence the oxide desorption temperature of 580 °C of GaAs (from the supplier of the wafers) was used to calibrate the thermocouple reading. The growth temperature for the GaAs buffer layer was performed 30 °C above the oxide desorption temperature, i.e., at 610 °C following Ref [63]. The thickness of the buffer layer was between 70 and 100 nm. After the buffer layer growth, the samples were cooled with  $As_4$  flux kept open until 400 °C. The GaAs(113)A samples grown under these conditions exhibit the well-known  $(8 \times 1)$  reconstruction [42, 54, 55] similar to Ref [63]. In Fig. 3.2 we show the RHEED pattern of the starting GaAs(113)A surface along (a)  $[33\bar{2}]$  and (b)  $[\bar{1}10]$ . The RHEED pattern resembles that reported in literature [54, 55] for the  $(8 \times 1)$  reconstruction. The RHEED pattern is rather streaky and shows the Laue circles of several orders (specially along  $[33\bar{2}]$ ), indicating an ordered and smooth surface morphology.

**Optimization of the growth of Fe** The sample was then transferred to the metal chamber for growth of Fe. In this work, the optimized growth conditions from Schönherr *et al.* [63] are used. These authors demonstrated the requirement of relatively low growth temperature for the growth of Fe on GaAs(113)A substrates. The low growth temperature prevents the formation of As-related compounds and leads to a smooth surface morphology. To reproduce this finding, Fe films with slightly varying growth temperatures between 0 – 40 °C were grown. The requirement of low growth temperature is demon-

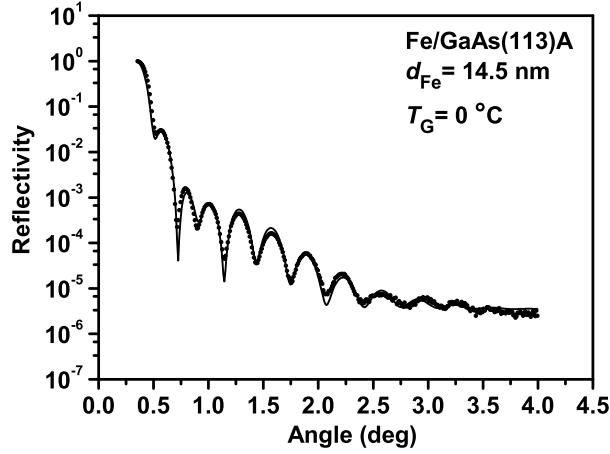


Figure 3.4: Comparison of measured X-Ray Reflectivity profile (solid dots) with a simulated profile (continuous line) of 13-nm-thick Fe and 2.8-nm-thick iron oxide layers on GaAs(113)A substrates.

strated in Fig. 3.3, which shows AFM images for two 26-nm-thick Fe samples grown at (a) 15 °C and (b) 0 °C. The root mean square (RMS) roughness changes drastically from 10 Å to 3 – 5 Å when the growth temperature changes slightly from 15 to 0 °C. Hence the growth of Fe was performed at a temperature of 0 °C. The low growth temperature of 0 °C, was achieved by directing the sample holder towards the cryopanel, which cools the substrate when kept overnight. However, during the growth, the substrate temperature increases slightly due to the radiation heating from the effusion cells and reaches about RT at the end of the growth. For SQUID measurements the samples were finally coated with a 20-nm-thick Al layer to prevent oxidation. The growth of the capping layer was also performed at 0 °C to avoid any diffusion of Al into Fe.

**Calibration of growth rate and XRR measurements** The growth of Fe was performed at a typical growth rate of 0.16 nm/min. The growth rate calibration was performed by the thickness determination from *ex situ* X-ray reflectivity (XRR), the basics of which have been discussed in Sec. 2.3. XRR was chosen to determine the film thickness since RHEED oscillations were not observed during growth of Fe. Also the HRXRD technique was found unsuitable because of the absence of the interference fringes for the Fe films of reasonable thickness (required for the sensitivity of HRXRD). Thickness and interface roughness were found by fitting the experimental XRR curves with the simulation using the Parratt [78] formalism and Distorted Wave Born Approximation (DWBA) [79], which are discussed in Sec. 2.3. The simulation is done with the program “X’Pert Reflectivity” supplied by PANalytical B. V., Almelo, Netherlands. Reasonable fits to the experimental XRR curves were obtained by assuming a thin top layer of iron oxide of thickness 2.5 – 3.0 nm, corresponding to approximately 1.5 nm of Fe in agreement with reported values in the literature [118]. In Fig. 3.4 we compare an experimental XRR curve with the simulation of 13-nm-thick Fe and 2.8-nm-thick iron oxide layers on GaAs. The matching of the experimental curve with simulation is excellent. Fringes of several orders are clearly seen, indicating a smooth interface/surface.

The results of XRR simulations for a variety of sample with different thicknesses and

Table 3.1: Summary of the XRR simulation results for Fe samples of different thicknesses and with Al capping layers. All dimensions are expressed starting from the top layer. Thicknesses and interface/surface roughness are expressed in nm, while the density is expressed in  $\text{g}/\text{cm}^3$ . The density of layers are varied by about 25% to obtain the best fit. The top layer is assumed to be an oxide layer.

Layer structure	Simulated Layer structure Model	Thicknesses (nm)	Interface/surface roughnesses	Density of simulated structures
Al/Fe/GaAs	$\text{Al}_x\text{O}_y/\text{Al}/\text{Fe}$	2.0/20.3/1.7	0.65/0.1/0.4/0.1	3.2/2.8/7.0
Al/Fe/GaAs	$\text{Al}_x\text{O}_y/\text{Al}/\text{Fe}$	1.8/12/21	1.6/1.8/0.2/0.1	2.7/1.8/7
Fe/GaAs	$\text{Fe}_x\text{O}_y/\text{Fe}$	3.0/24.0	0.6/0.2/0.6	5.1/9.0
Fe/GaAs	$\text{Fe}_x\text{O}_y/\text{Fe}$	2.7/2.6	0.5/0.5/0.1	4.3/6.0
Fe/GaAs	$\text{Fe}_x\text{O}_y/\text{Fe}$	2.8/13	0.8/0.3/0.4	5.2/8.6

with Al capping layers are summarized in Table 3.1. From the simulations of XRR profiles, we found the interface roughness of the Fe-GaAs interface to be less than 0.8 nm for all thicknesses studied, indicating a rather smooth interface between Fe and GaAs. The value of surface roughness also agrees well with the AFM measurements. For uncapped samples, the equivalent Fe film thickness was determined by adding 1.5 nm to the simulated Fe film thickness in Table 3.1 to take into account the iron oxide layer.

### 3.3.1 Mechanism and evolution of growth: RHEED

The growth of Fe was monitored by the evolution of RHEED patterns recorded along different azimuths. In Fig. 3.5, we show the development of the RHEED patterns taken along  $[33\bar{2}]$  and  $[\bar{1}10]$  during continuous growth of the Fe film and without substrate rotation. As can be seen, the intensity of the specular beam (indicated with an arrow) from GaAs was found to decrease drastically after growth of 1 ML ( $\sim 0.14$  nm) indicating the formation of disordered islands. The RHEED pattern was found to be still dominated by the GaAs substrate. After the second monolayer, the RHEED pattern almost disappears completely and only a diffuse background was seen. The first RHEED pattern from the Fe films was seen at 3 – 4 MLs, suggesting the coalescence of islands. For Fe films thicker than 10 MLs, we observe a streaky RHEED pattern along the  $[33\bar{2}]$  and  $[\bar{1}10]$  azimuths characteristic of the unreconstructed bcc Fe lattice. The second-order Laue circle was visible for a RHEED pattern along the  $[\bar{1}10]$  azimuth. Although the geometric structure of the RHEED pattern was already clear at about 3 – 4 MLs, an improvement in the width of the RHEED streaks can be clearly seen by comparing the RHEED pattern from 10 and 110 MLs of Fe coverage. To study the above facts more carefully, we measure the full-width-at-half-maximum (FWHM) and integrated intensity of a  $(0\bar{1})$  reflection of Fe as indicated by the white line in Fig. 3.6(a) showing the RHEED pattern from 140 MLs of Fe along  $[\bar{1}10]$ . In Fig. 3.6(b), the evolution of the line profile of the  $(0\bar{1})$  reflection of Fe with monolayer coverage is shown. Figure 3.6(c) shows the corresponding evolution of the integrated intensity of the line profile after background subtraction. A finite integrated intensity is observed at a nominal Fe coverage of 3 MLs. Then an increase of the RHEED intensity is observed until 20 MLs, indicating the presence of islands. After about 20 MLs of Fe coverage, the integrated intensity remains almost constant indicating the formation

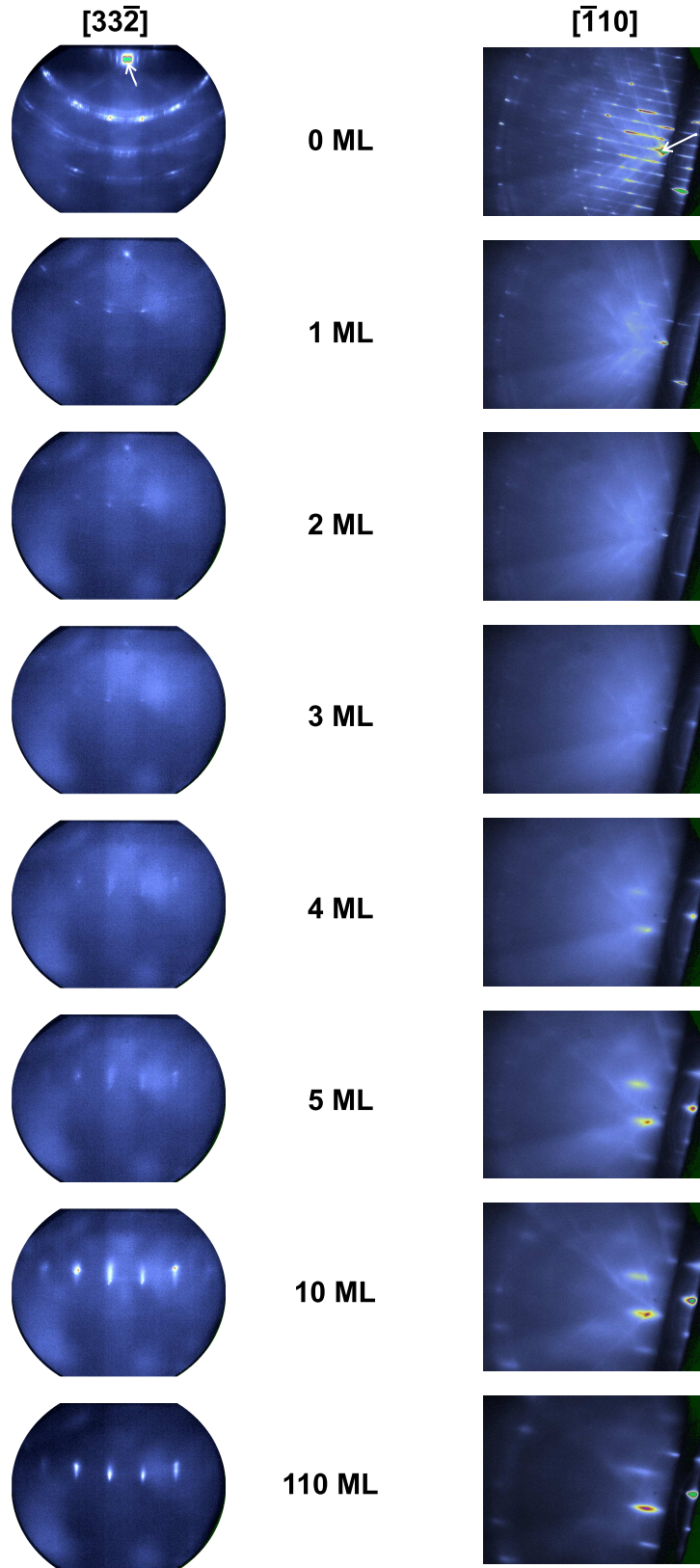


Figure 3.5: Evolution of RHEED patterns during the continuous growth of Fe (without substrate rotation) on GaAs(113)A and 0 °C along  $[3\bar{3}2]$  and  $[\bar{1}10]$ . The first RHEED pattern from Fe begin to appear at about 3 MLs and become prominent at about 5 MLs.

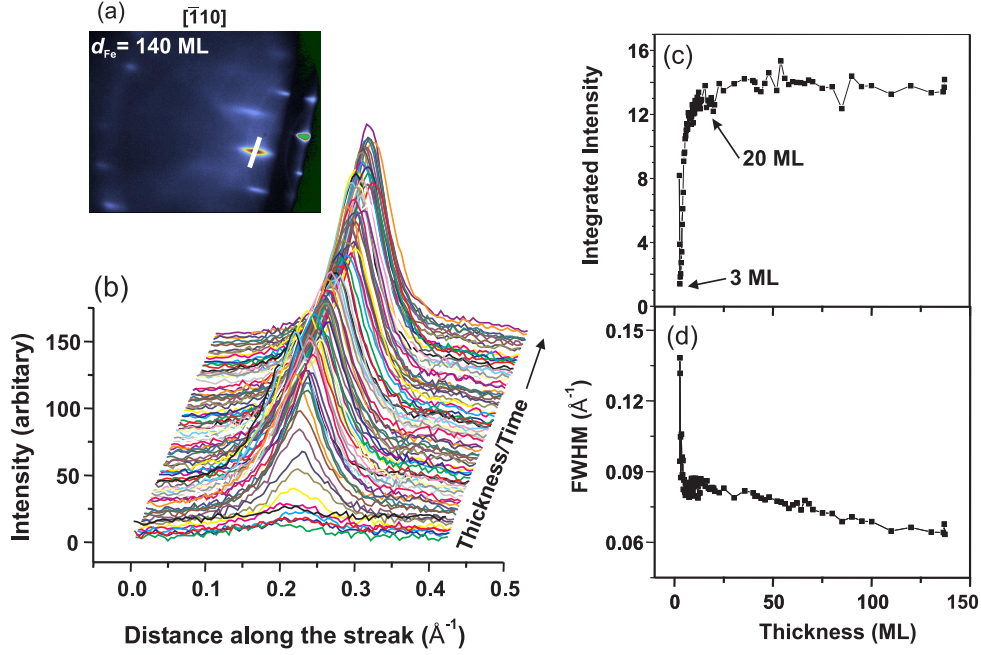


Figure 3.6: Evolution of RHEED (b) line profiles, (c) Integrated Intensity, and (d) FWHM along  $[\bar{1}10]$  for the  $(0\bar{1})$  reflection of Fe with monolayer coverage as shown in (a) during the continuous growth of Fe (without substrate rotation). Islanding persist up to 20 MLs.

of a 2D thin film.

The FWHM of the line profile first shows a rapid decrease followed by a slow decrease as shown in Fig. 3.6(d). The FWHM of a diffracted profile is usually inversely proportional to the average 3D island size or terrace size as discussed in Sec. 2.1.2. Thus we relate the first decrease of the FWHM to an increase of the 3D island size and the second slow decrease to an increase of the terrace size. The average terrace separation  $L_{av}$  is simply given by  $2\pi/\text{FWHM}$ . Thus the island size of the the starting Fe nuclei at 3 MLs is about 4.5 nm and the average terrace size is about 10 nm after 140 MLs of Fe growth. These numbers are only approximate because the actual relation between the width of the diffracted profile and the mean terrace size depends specifically on the step distribution on the surface [72].

### 3.3.2 Strain and structural properties by HRXRD

We use high-resolution X-ray diffractometry (HRXRD) to determine the crystalline quality and epitaxial relationship of the Fe films. From high-resolution X-ray diffraction (HRXRD) measurements, we do not find the symmetric Fe(113) reflection or any other reflections with all the indices odd, indicating the formation of a bcc phase of Fe. No other orientations, such as Fe(112), were detected parallel to the surface of the film, which are formed in the case of Fe films on Cu(113) substrates [66]. To examine the epitaxial relationship and crystal quality, we measure the asymmetric reflections of GaAs such as (004) and (224). For a perfect cube-on-cube epitaxy, the Fe(002) and Fe(112) reflections are expected in the neighborhood of the (004) and (224) reflections of GaAs. This is what is observed in the experiment, as shown in the reciprocal space maps in Fig. 3.7



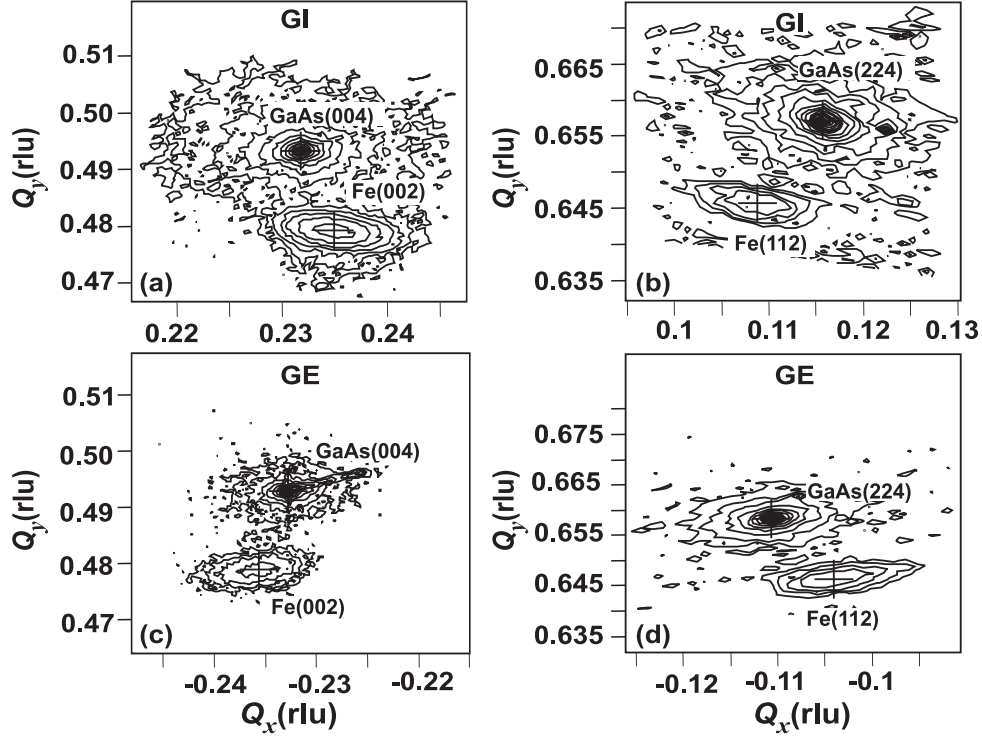


Figure 3.7: X-ray reciprocal space maps of a 20-nm-Fe film grown on GaAs(113)A substrates for the asymmetric (004) (first column) and (224) (second column) reflection of GaAs in grazing incidence geometry (GI; first row) and grazing exit (GE; second row). The reciprocal lattice units (rlu) are  $\lambda/2d$ , where  $\lambda$  is the wavelength of  $\text{CuK}\alpha_1$  radiation and  $d$  is the lattice plane spacing of the corresponding reflection.

measured in the GI and GE geometries for a 20-nm-thick Fe film. The reciprocal lattice units (rlu) are  $\lambda/2d$ , where  $\lambda$  is the wavelength of  $\text{CuK}\alpha_1$  radiation and  $d$  is the lattice plane spacing of the corresponding reflection. In the GI geometry the (004) reflection is detected only when the X-ray beam is made parallel to the  $[\bar{3}32]$  (not  $[3\bar{3}2]$ ) direction, indicating the low symmetry of the (113)-plane. The corresponding Fe peaks are indicated, which thus confirms the same orientation of the Fe film with respect to the GaAs(113)A crystal lattice, i.e.,  $\text{Fe}(113) \parallel \text{GaAs}(113)$  and  $\text{Fe}[\bar{3}32] \parallel \text{GaAs}[\bar{3}32]$ . This is consistent with our expectation on the basis of the close lattice match between Fe and GaAs and, hence demonstrates the stability of these films. From Fig. 3.7 and from the usual  $\omega - 2\theta$  scans, no indication of an interface compound formation was detected in the HRXRD spectra. Also, the good crystal quality of the layers is reflected in the FWHM of the layer which is about  $(0.005 \pm 0.002)$  rlu both along  $Q_x$  and  $Q_y$  which is comparable to that of Fe films on GaAs(001) substrates of the same thickness. As shown in Fig. 3.7, the Fe layer is partially relaxed (layer peak not lying vertically on the same line as the GaAs peak). From these maps we determine the perpendicular  $(\Delta a/a)_\perp$  and the parallel  $(\Delta a/a)_\parallel$  mismatch of the layer using the following equations:

$$\begin{aligned} (\Delta a/a)_\perp &= (Q_y^L - Q_y^S)/Q_y^L \\ (\Delta a/a)_\parallel &= (Q_x^L - Q_x^S)/Q_x^L, \end{aligned} \quad (3.1)$$

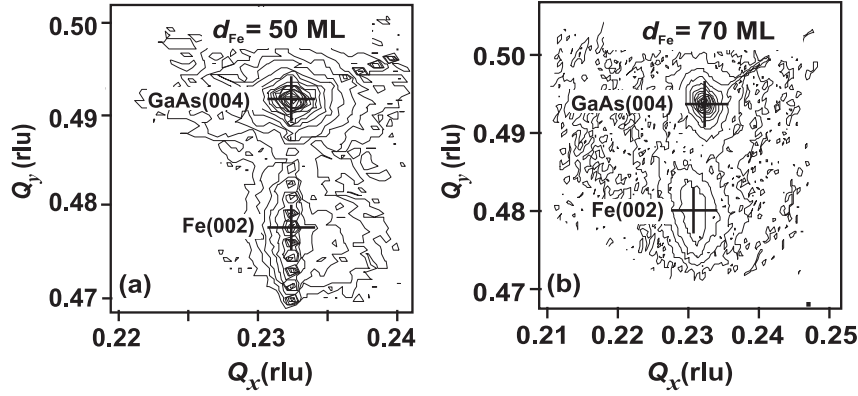


Figure 3.8: X-ray reciprocal space map for the asymmetric (004) reflection of GaAs, in grazing incidence geometry, of two samples with Fe thickness (a) 7 nm (50 MLs) and (b) 10 nm (70 MLs). The corresponding (002) peak of Fe is also shown. The Sample of 50 MLs is strained whereas the sample of 70 MLs is relaxed.

where  $Q_{x,y}^S$  and  $Q_{x,y}^L$  represent the position of substrate and layer peaks, respectively.

Detailed thickness dependence studies show that the relaxation of the layer takes place between 7 and 10 nm (or 50 and 70 MLs). The relaxation process can be seen more clearly in Fig. 3.8, in which the RSM of these two samples are shown near the asymmetric (004) reflection of GaAs (in grazing incidence geometry). The GaAs(004) reflection is located near  $Q_x^S = 0.233$  and  $Q_y^S = 0.492$ . For the 7-nm-thick sample, the layer peak is located at  $Q_x^L \approx 0.233$  and  $Q_y^L = 0.4774$ . The perpendicular mismatch of this film calculated using the above Eq. (3.1), is given by  $(2.9 \pm 0.5) \%$ , which is close to the theoretical value of 2.6 % calculated using an accurate elastic theory as described by Brandt *et al* [7]. The parallel mismatch is nearly zero and the layer is completely strained. In contrast, the layer peak for the 10-nm-thick sample is at  $Q_x^L = 0.2314$  and  $Q_y^L = 0.4791$ . The parallel mismatch in this case is about 0.68 %, indicating that the layer is partly relaxed. However, the value is less than the fully relaxed value of 1.4 %. Interference fringes are visible for the 7-nm-thick sample indicating the good crystal quality of the film. In fact, if one measures the (004) reflection in skew geometry, then these fringes are also observed in a normal  $\omega - 2\theta$  scan. Furthermore, the FWHM of the layer is reduced to  $(0.001 \pm 0.0005)$  rlu both along  $Q_x$  and  $Q_y$ .

### 3.3.3 Summary of structural properties

1. The growth of Fe films on GaAs(113)A substrates has been optimized at 0 °C to produce films with a smooth surface/interface and no detectable interfacial reactions. The structural properties are very well comparable to the case of the Fe films on GaAs(001) substrates.
2. The Fe films on GaAs(113)A substrates were found to grow through the formation of 3D islands, similar to the case of Fe films grown on GaAs(001) substrates. A coalescence of the islands occurs at a nominal coverage of 3 – 4 MLs, but unlike the case of (001) substrates, finite islanding does exist to a thickness of 20 MLs of Fe.



3. Most importantly, the Fe films were found to maintain the same orientation as that of the GaAs(113)A substrates, i.e.,  $\text{Fe}(113) \parallel \text{GaAs}(113)$  and  $\text{Fe}[33\bar{2}] \parallel \text{GaAs}[33\bar{2}]$ .
4. The layers are found to be strained for film thicknesses  $\leq 50$  MLs with relaxation of the layer starting for Fe film thicknesses  $\geq 70$  MLs.

## 3.4 Magnetic properties

In this section, the magnetic properties of the Fe films grown on GaAs(113)A substrates will be discussed. The magnetic measurements were performed using *in situ* MOKE and *ex situ* SQUID magnetometer. For SQUID measurements the Al capped layers were used. SQUID magnetometry measures the overall signal from the GaAs substrate and the film. The GaAs substrate adds a diamagnetic contribution to the overall signal and can be easily corrected by subtracting the diamagnetic slope. Hence all SQUID magnetization curves shown in this work are corrected for the diamagnetic contribution of GaAs.

### 3.4.1 Onset of ferromagnetism

The onset of ferromagnetism was studied by the temperature dependence of the remanent magnetization  $M_r$ . A plot of  $M_r$  versus temperature  $T$  for film thicknesses from 4.0 MLs to 30 MLs is shown in Fig. 3.9(a). The remanent magnetization  $M_r$  is normalized with respect to its value,  $M_r^0$  at 10 K. These measurements were performed while heating the sample from 10 K to 300 K. Before the measurements, the samples were magnetized along the  $[33\bar{2}]$  direction by applying a high field of 20 kOe. Since all these measurements were made with the magnetic field applied parallel to the easy axis (see Sec. 3.4.3), the remanent magnetization is essentially the same as the saturation magnetization  $M_s$ . For samples with thickness above 10 MLs, the RT remanence changes by less than 10 % of its value at 10 K, indicating a high Curie temperature of these samples. Samples below 10 MLs show a drastic change in remanence with temperature. The Curie temperature decreases strongly when decreasing the thickness and reaches 120 K for the 4-ML-thick sample. This reflects the reduced co-ordination in these ultrathin films. No sign of ferromagnetism was observed even at 2 K for the 3.5-ML-thick Fe sample. This implies that the first signature of ferromagnetic order in our films starts between 3.5 and 4.0 MLs. This is approximately the same thickness for which we observe the first RHEED pattern from the Fe layer (Sec. 3.3.1). Thus the onset of ferromagnetism in these layers can be ascribed to a percolation phenomenon during the coalescence of Fe islands, similar to that reported for Fe/GaAs(001) [115, 119].

The temperature dependence of  $M_r$  in Fig. 3.9(a) for the 4-ML-thick sample with a Curie temperature below RT does not exhibit a behavior typical for an ideal 2D-ferromagnet. The remanent magnetization  $M_r$  does not drop sharply as expected for an ideal 2D-ferromagnet and observed in the MOKE data of Bensch *et al.* [119] for Fe/GaAs(001). In fact, susceptibility versus temperature at an AC frequency of 140 Hz and AC magnetic field of 3.5 Oe reveal a peak at 107 K with a full width at half maximum (FWHM) of about 100 K as shown in Fig. 3.9(b). This large FWHM can be attributed to the averaging measurement method of SQUID magnetometry, which measures the magnetization averaged over the whole sample (several  $mm^2$ ) in contrast to the MOKE data of Bensch *et al.* [119], which probes only a small area of the sample. The islanding at the

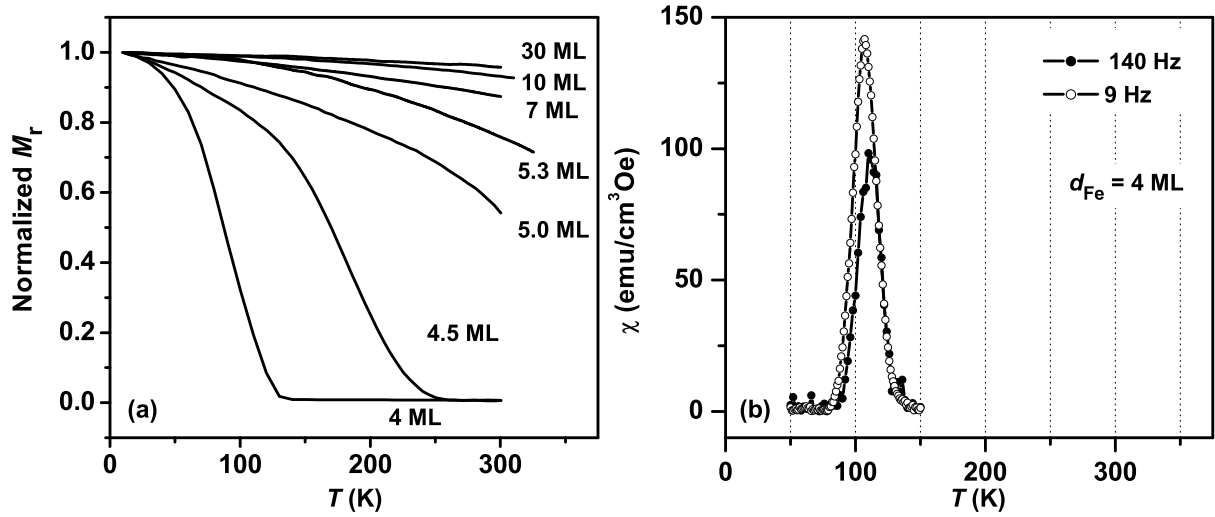


Figure 3.9: (a) Temperature dependence of remanent magnetization  $M_r$  of Fe/GaAs(113)A films with different thickness. All curves are normalized with respect to the remanent magnetization at 10 K. The onset of RT ferromagnetic order is between 4.5 and 5.0 MLs. (b) Temperature dependence of susceptibility  $\chi$  with an ac frequency of 9 and 140 Hz and ac field of 3.5 Oe for the 4-ML-thick sample. Note that the susceptibility is a dimensionless quantity. However, to specify the volume susceptibility, it is expressed in  $\text{emu}/\text{cm}^3\text{Oe}$

initial stages of growth, in agreement with RHEED observations of Sec. 3.3.1, leads to local variations in the Curie temperature due to the variation in thickness and hence to a broadening of the magnetic phase transition. A similar behavior was also observed in the SQUID measurements of Fe films on GaAs(001) substrates [115].

**Field cooled and zero field cooled curves** We have also investigated the possibility of a superparamagnetic phase for the 4-ML-thick sample in Fig. 3.9 which has been reported for the Fe/GaAs(001) system [108]. To check the presence of superparamagnetism, we measured the field-cooled and zero-field-cooled curves of magnetization versus temperature. No superparamagnetic transition was observed below the Curie temperature of 120 K for the 4-ML-thick sample. As will be discussed in the next section, the magnetization curves below 120 K show well-defined hysteresis and anisotropy. Hence the transition of  $M_s$  or  $M_r$  with  $T$  in Fig. 3.9 is truly a ferromagnetic phase transition.

### 3.4.2 Thermal spin excitations: the size effect

The studies of  $M_s(T)$  at different film thicknesses allow us to study the size effect of the thermal spin excitations on this orientation. In general, for temperatures well below the Curie temperature, the spontaneous magnetization  $M_s(T)$  is determined by the Bloch  $T^{3/2}$  law:

$$M_s(T) = M_0(1 - BT^{3/2}), \quad (3.2)$$

where  $B$  is the Bloch constant or spin-wave parameter with  $B_{\text{bulk-Fe}} = 5.2 \times 10^{-6} \text{ K}^{-3/2}$  for bulk  $\alpha$ -Fe [120]. The value of  $B$  determines how many spin waves are excited. A

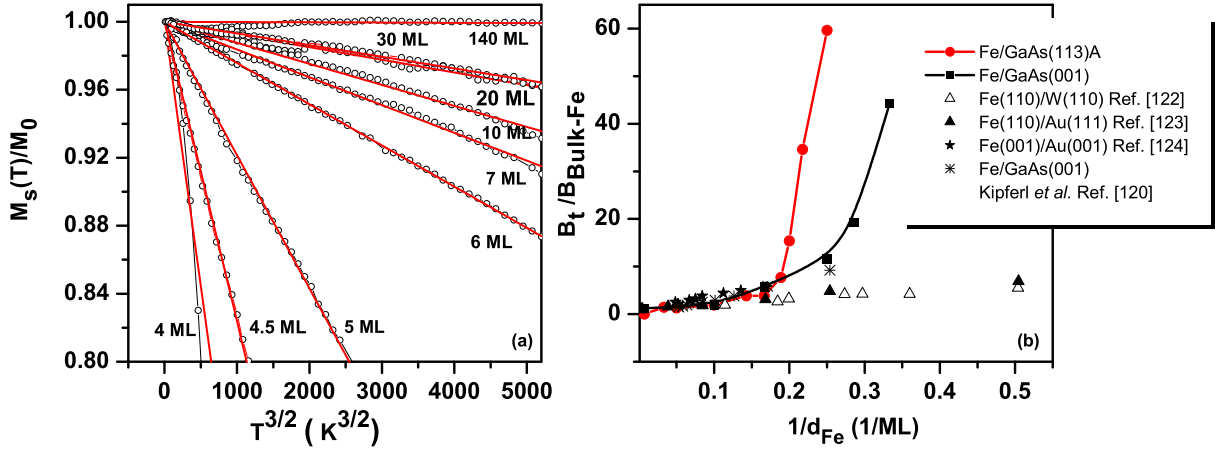


Figure 3.10: (a) Temperature dependence of the spontaneous magnetization  $M_s(T)$  normalized to  $M_0$  for Fe films on GaAs(113)A substrates with different thicknesses. The solid lines are fits of Bloch  $T^{3/2}$  law. (b) Size effect of spin wave excitations in epitaxial thin bcc-Fe Films on different substrates: spin wave parameter  $B$  normalized to the bulk value of Fe as a function of the inverse thickness.

significant increase of spin wave excitations or  $B$  has been measured in ultrathin Fe films. We examine the variation of  $B$  with film thickness from data presented in Fig. 3.9(a) of the last section. For all samples and the Bloch  $T^{3/2}$  law was found to be valid in the region where the magnetization changes by 20 %. Figure 3.10(a) shows the fitting of the spontaneous magnetization  $M_s(T)$  with the Bloch  $T^{3/2}$  law. Even if a  $T^{3/2}$  law is not developed theoretically for two-dimensional (2D) systems it has been shown by Mathon and Ahmad [121] that an “effective  $T^{3/2}$  law” is expected to be valid in a certain temperature range.

To obtain more quantitative information, the spin wave parameter  $B$  was normalized to the bulk value and is plotted as a function of inverse film thickness in Fig. 3.10(b). For comparison, we have also included the data for the Fe/GaAs(001) system derived from Ref [115]. Also the data from the literature for Fe(110)/W(110) [122], Fe(110)/Au(111) [123], Fe(001)/Au(001) [124], as well as previously reported data on Fe/GaAs(001) [120] are shown for comparison. The data clearly show an increase of  $B$  with decreasing film thickness, in agreement with literature for Fe/GaAs(001) [120] and other systems [122, 123, 124, 125]. Qualitatively, the increase of the spin wave parameter  $B$  in low-dimensional systems compared to the respective bulk material can be understood as a consequence of the reduced coordination of surface spins. Reduced exchange energy per spin will lower the energy of a spin wave with a given wave vector  $\mathbf{k}$ , leading to enhanced spin wave excitations at a specific temperature which are equivalent to an increase in the spin wave parameter  $B$ . The most distinguishing feature of Fe/GaAs(113)A in Fig. 3.10 is a considerable large value of the normalized spin wave parameter compared to all other systems. Recently Kipferl *et al.* [124] reported lower spin wave parameter of Fe films on GaAs(001) compared to that of Fe films on Au due to the presence of in-plane UMA in the former case. An increase in anisotropy leads to an additional energy gap in the dispersion relation. Therefore, fewer spin waves are excited which corresponds to a smaller spin wave parameter [124]. Hence we compare the anisotropy constants of Fe films

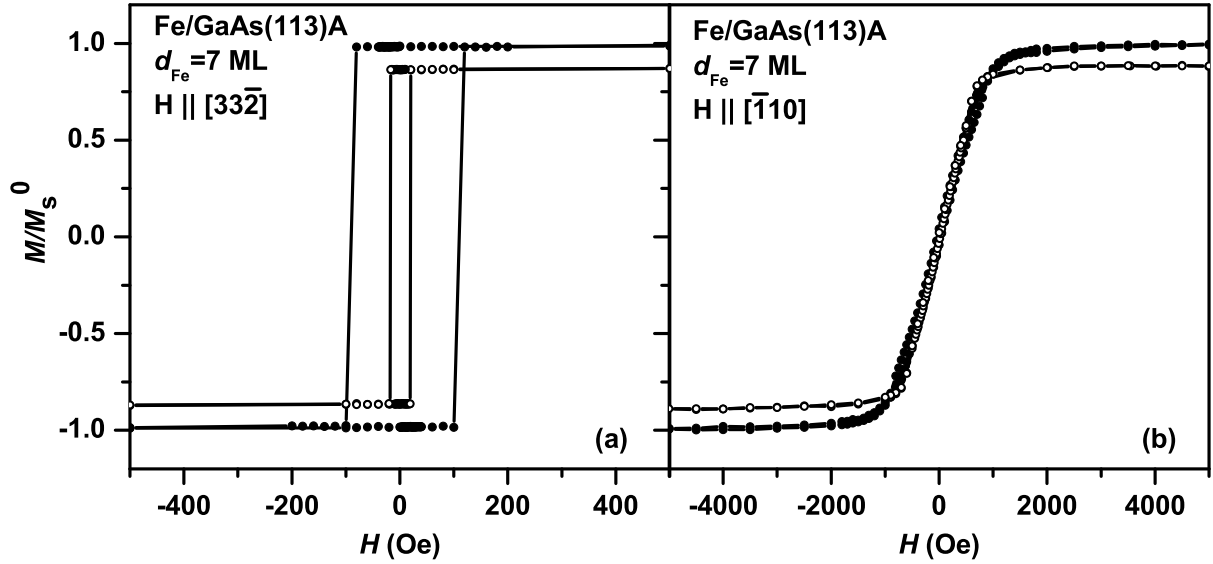


Figure 3.11: Magnetization loops of a 7 ML-Fe film with magnetic field applied in-plane along (a)  $[3\bar{3}2]$  and (b)  $[\bar{1}10]$ . The open circles are for  $T = 300$  K (RT) and the solid circles are for  $T = 10$  K, respectively. The magnetization  $M$  is normalized to the saturation magnetization at  $T = 10$  K,  $M_s^0$  after correction for the diamagnetic contribution of the GaAs substrate.

on GaAs(001) and GaAs(113)A, which also change with thickness (see Sec. 3.4.3). However, it is important to note that the UMA constants of Fe(113) films for  $d_{\text{Fe}} < 20$  MLs are lower compared to that of the Fe(001) films. This reduction of UMA can lead to enhanced spin wave excitations and an increased  $B$ .

Another observation from Fig. 3.10(b) is the non-linear behavior of  $B$  with inverse film thickness for Fe films on both GaAs(001) and (113)A substrates, which is usually not the case for other metallic systems shown in the figure. A possible origin of this behavior has been discussed by Kipferl *et al.* [120] and the presence of a strong *thickness-dependent* anisotropy has been proposed as a possible origin.

### 3.4.3 Evolution of in-plane magnetic anisotropy

#### In-plane uniaxial magnetic anisotropy in ultrathin films

Figure 3.11 shows magnetization curves for the 7-ML-thick Fe film (see Fig. 3.9,  $d_{\text{Fe}} = 7$  MLs) at two different temperatures with the magnetic field applied parallel to the two major in-plane perpendicular directions, namely the  $[3\bar{3}2]$  and  $[\bar{1}10]$  directions. The magnetization  $M$  is normalized to the saturation magnetization,  $M_s^0$  at  $T = 10$  K. As can be seen, the 7 ML-Fe film exhibit a strong UMA with the easy axis along  $[3\bar{3}2]$ . The hysteresis curve along this direction has a pure rectangular shape with a normalized remanence  $M_r/M_s \sim 1$ . This indicates that the Fe layer is essentially single domain in nature or with a preferred domain orientation pointing along the easy axis as suggested for Fe/GaAs(001) [126]. An increase in the coercive field at 10 K is observed compared to 300 K. The magnetization curve along the  $[\bar{1}10]$  direction does not show any hysteresis and the coercive field vanishes. The magnetization curve is completely reversible indicating a

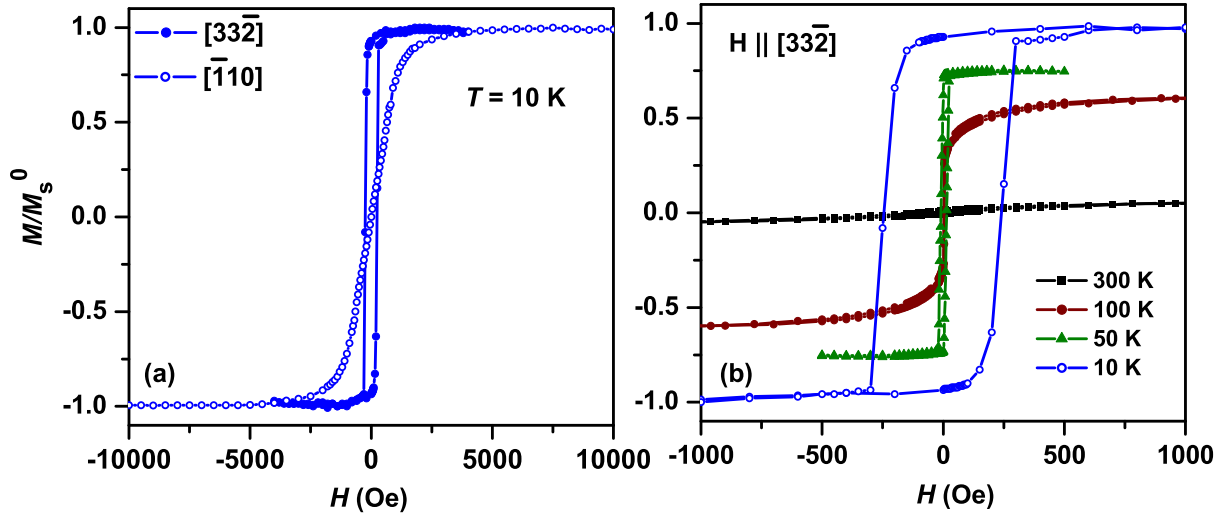


Figure 3.12: (a) Normalized magnetization curves along the major in-plane crystallographic directions  $[3\bar{3}2]$  and  $[\bar{1}10]$  for a GaAs(113)A sample with 4 MLs of Fe coverage. (b) Magnetization curves along  $[3\bar{3}2]$  at different temperatures.

hard axis of magnetization. The reversibility of the magnetization curve is suggestive of a rotation process [105]. The in-plane anisotropy field is about 2.5 kOe at 10 K and 1.5 kOe at 300 K. It should be noted that the saturation magnetization for this sample at 300 K decreases to about 10 % of its value at 10 K. However, the saturation magnetization for  $T \rightarrow 0$  is close to the value of bulk Fe ( $1740 \text{ emu/cm}^3$ ), indicating the absence of interfacial Fe-Ga-As compounds [115]. As an important observation, the UMA exhibits a hard axis along the  $[\bar{1}10]$  direction similar to the case of Fe/GaAs(001).

The first signature of a pronounced UMA was already observed at 4 MLs of Fe coverage. As shown in Fig. 3.12(a), the magnetization curves measured at 10 K along  $[3\bar{3}2]$  show an easy-axis behavior in contrast to the magnetization curves along  $[\bar{1}10]$ . In fact, the UMA persists up to the Curie temperature as shown in Fig. 3.12(b), which shows magnetization curves along  $[3\bar{3}2]$  at different temperatures. However, the shape of the magnetization curves of this 4-ML-thick sample differs from that of the 7-ML-thick sample in Fig. 3.11. First, the coercive field is larger at 10 K with a large switching width. Second, the magnetization curve along  $[3\bar{3}2]$  deviates from the perfect rectangular shape. We attribute these features to the presence of islanding at 4 MLs of Fe coverage as evidenced from RHEED studies of Sec. 3.3.1.

#### Four-fold magnetic anisotropy in thick films

In Fig. 3.13, we present the normalized magnetization curves of a 100-nm-thick Fe film measured at RT with the magnetic field applied parallel to the four major in-plane crystallographic axes of the (113) surface, namely  $[3\bar{3}2]$ ,  $[\bar{1}10]$ ,  $[03\bar{1}]$ , and  $[\bar{3}01]$ . The  $[03\bar{1}]$  and  $[\bar{3}01]$  directions lie at an angle of  $42.1^\circ$  and  $137.9^\circ$  relative to the  $[3\bar{3}2]$  direction, respectively [see Fig. 3.13(b)]. Hysteresis loops taken along the  $[03\bar{1}]$  and  $[\bar{3}01]$  directions show a normalized remanence of about 1, characteristic of magnetization reversal along an easy axis. It should be mentioned that the measurement along these two directions has an experimental error of  $1 - 5^\circ$ , which arises from a possible misalignment of the sample

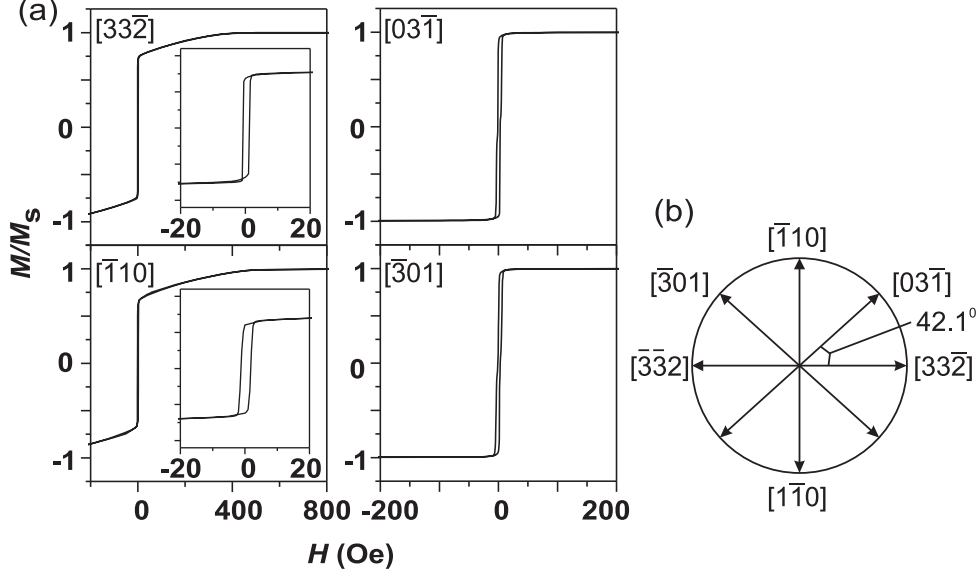


Figure 3.13: (a) Room temperature magnetization curves of Fe films on GaAs(113)A for  $d_{\text{Fe}} = 714$  MLs (100 nm) measured along the different in-plane crystallographic directions shown schematically in (b). The insets for the  $[33\bar{2}]$  and  $[\bar{1}10]$  directions show magnified portions of the magnetization curves in the low field region.

in the SQUID magnetometer. Thus, this sample exhibits a dominant in-plane four-fold anisotropy. Note that the in-plane  $\langle 03\bar{1} \rangle$  axes can be obtained from the intersection of the (113) plane with the  $\{010\}$  planes. Thus, the observation of easy axes along these in-plane  $\langle 03\bar{1} \rangle$  directions can be considered as analogous to the case of Fe on GaAs(001), where the in-plane  $\langle 001 \rangle$  axes are the easy axes of magnetization. When the magnetic field is applied along the  $[33\bar{2}]$  and  $[\bar{1}10]$  directions, the normalized remanence reduces to about 0.7. Along the  $[\bar{1}10]$  direction, a magnetically intermediate direction of bulk Fe, the magnetization curve shows an abrupt transition at a very low field of about 2 Oe followed by a gradual increase to saturation at approximately 500 Oe. This saturating field of 500 Oe is close to the coercive field calculated from the coherent rotation model for bulk Fe [105]. The magnetization curves along  $[33\bar{2}]$  and  $[\bar{1}10]$  are equivalent to one another. The saturation magnetization of this 100-nm-thick sample measured along the easy axes is close to the value of bulk Fe, i.e.,  $1740 \text{ emu/cm}^3$ . The RT coercive field along the easy axes is on the order of 7 – 10 Oe. This reflects the high crystal quality of the Fe films.

It is important to note that the easy axis of magnetization in thick films ( $d_{\text{Fe}} \geq 70$  MLs) is found to be along the in-plane  $\langle 03\bar{1} \rangle$  axes, which are not the easy axes of magnetization of bulk Fe. In fact, one of the easy axes of bulk Fe, namely the  $[001]$  direction lies out-of-plane at an angle of  $25.24^\circ$  to the surface normal and towards the  $[33\bar{2}]$  direction. However, we found no evidence of a perpendicular easy axis for the magnetic field applied along a set of out-of-plane directions having different inclination angles, measured from the surface normal and towards the in-plane  $[33\bar{2}]$  direction. These observations indicate that the demagnetizing energy in this system is very large as a result of which the easy axis of magnetization lies in-plane. This is also confirmed by other techniques, including polar Kerr effect and the extraordinary Hall effect. Furthermore, for these thicker films,

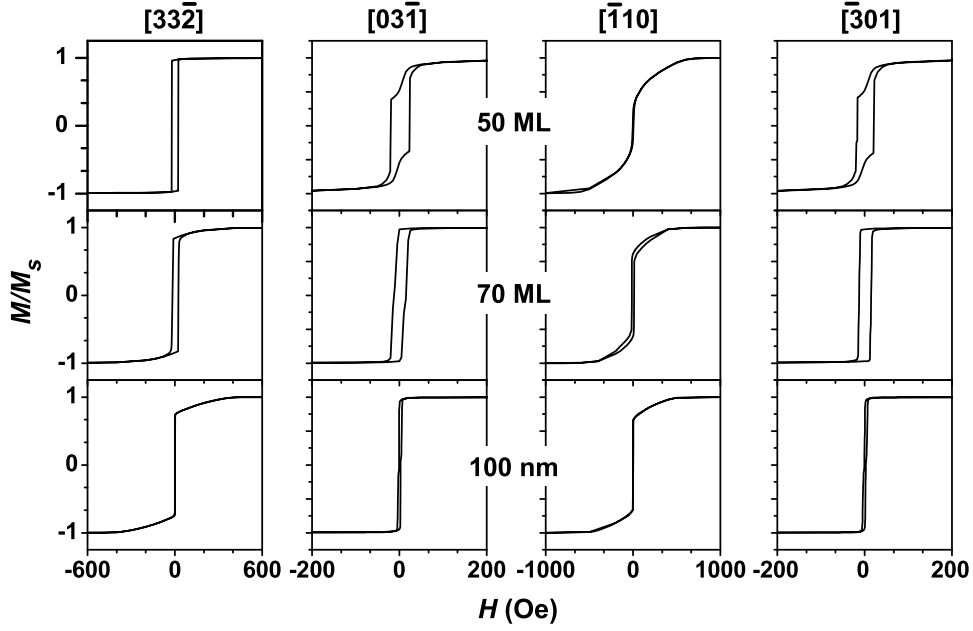


Figure 3.14: Magnetization curves of a set of three samples of thicknesses 50 MLs, 70 MLs and 140 MLs along the four major in-plane directions. The curves are normalized to their saturation magnetization after correction for the diamagnetic contribution of the GaAs substrate.

we do not observe the expected six-fold magnetic anisotropy as mentioned before. This can be understood by taking into account the large demagnetization energy of the Fe films, and will be discussed in more detail in later sections.

### 3.4.4 Spin-reorientation transition

To determine the thickness range in which the magnetic anisotropy changes from a dominating uniaxial type to a dominating four-fold type, we performed a series of magnetization measurements for different Fe film thicknesses between 7 and 714 MLs (100 nm). In Fig. 3.14, we show selected RT normalized magnetization curves for a set of three samples of thicknesses 50 MLs, 70 MLs and 140 MLs along the four major in-plane directions. As can be seen, the magnetization curves of the 50-ML-thick sample are significantly different from those of the 70 and 140-ML-thick samples and still exhibit a dominant UMA with the easy axis along  $[33\bar{2}]$ . The magnetization curve for this 50-ML-thick sample along the  $[\bar{1}10]$  direction and below saturation can be distinguished into two regions: a significant reversible part in the high-field region and a very small irreversible part in the low-field region. The reversible part is similar to the magnetization curve of the 7-ML-thick sample in Fig. 3.11(b), so that we infer this direction to be a hard axis of magnetization. The magnetization curves of the 70 and 140-ML-thick samples, on the other hand, exhibit a dominant four-fold anisotropy with the easy axes along the  $[03\bar{1}]$  and  $[\bar{3}01]$  directions. The magnetization curves of these two samples are more or less similar to that of the 100-nm-thick sample in Fig. 3.13. However, there are small differences too. The magnetization curve along the  $[33\bar{2}]$  direction exhibits a very small reversible part compared to the magnetization curve along the  $[\bar{1}10]$  direction, which is not the case for the 100-

nm-thick sample (in Fig. 3.13) where these two directions are almost equivalent. This reflects the non-vanishing contribution of the UMA in this thickness range. As a result, our experiments show that the Fe films of thickness  $\geq 70$  MLs exhibit a dominant four-fold magnetic anisotropy, whereas Fe films of thickness  $\leq 50$  MLs exhibit a dominant UMA. The reorientation of the easy axes occurs in the thickness range of 50 to 70 ML-Fe. In Fig. 3.8 it was shown that the relaxation of the layer also starts between 50 MLs and 70 MLs. This indicates that the relaxation of the layer and reorientation of the easy axes of magnetization are apparently correlated. Thomas *et al.* [116] have also reported a similar observation in Fe films on GaAs(001) substrates. They reported that the Fe films below 60 MLs (exhibiting a dominating UMA) are strained, and above 60 MLs (exhibiting a dominating four-fold anisotropy) are relaxed.

### 3.4.5 Magnetic free energy of the (113)-plane of Fe

The magnetization of Fe/GaAs is often understood by means of a simple rotational mechanism [103, 105, 111, 127]. In order to understand the magnetic properties of Fe films grown on the low-symmetric GaAs(113)A substrate, we consider the total magnetic anisotropy energy density for a film with cubic symmetry. The direction of the magnetization  $\mathbf{M}$  for a single domain sample is determined by the interplay between the anisotropy of the magnetic material and the external magnetic field. In this case, the magnetization curve of coherent rotation can be calculated by using a phenomenological expansion of the free-energy density. The free energy density of a single domain in a magnetic field  $\mathbf{H}$ , with a combination of cubic magnetocrystalline and UMA, can be written as:

$$E = K_1[\alpha_1^2\alpha_2^2 + \alpha_1^2\alpha_3^2 + \alpha_2^2\alpha_3^2] + K_2[\alpha_1^2\alpha_2^2\alpha_3^2] + K_u(\mathbf{M} \cdot \mathbf{u}/M)^2 + 2\pi(\mathbf{M} \cdot \mathbf{n})^2 - \mathbf{M} \cdot \mathbf{H}, \quad (3.3)$$

where  $K_1$  and  $K_2$  are the first two cubic anisotropy constants,  $K_u$  is the uniaxial anisotropy constant, and the last two terms refer to the demagnetization energy and Zeeman energy, respectively. Here,  $\alpha_1$ ,  $\alpha_2$  and  $\alpha_3$  are the direction cosines of  $\mathbf{M}$  relative to the cubic crystalline axes. The unit vector  $\mathbf{n}$  represent the direction the surface normal. The third term represents the UMA and the unit vector  $\mathbf{u}$  represents the hard axis of magnetization [117]. In the following it will be taken along the observed hard axis: the  $[\bar{1}10]$  axis.

The 4th term in Eq. (3.3), represents the demagnetization energy of these films and contains the factor  $(\mathbf{M} \cdot \mathbf{n})$ , which is the component of magnetization perpendicular to the film plane. For the Fe films studied here, this energy is very large, so that the magnetization is forced to lie in-plane as evidenced from experiments. Hence, this term can be neglected in the case of an in-plane magnetic field. If  $\theta_M$  is the angle between  $\mathbf{M}$  and the  $[33\bar{2}]$  direction, then the direction cosines of the magnetization  $\alpha_i$  defined with respect to the  $\langle 100 \rangle$  axes can be shown to be  $\alpha_1 = (3/\sqrt{22}) \cos \theta_M - (1/\sqrt{2}) \sin \theta_M$ ,  $\alpha_2 = (3/\sqrt{22}) \cos \theta_M + (1/\sqrt{2}) \sin \theta_M$ ,  $\alpha_3 = -(\sqrt{2/11}) \cos \theta_M$ . Thus the in-plane magnetic anisotropy energy density  $E_{\text{IPMA}}$  suitable for the (113)-plane can now be written as:

$$E_{\text{IPMA}} = (K_1/484)[89 + 16 \cos 2\theta_M + 48 \cos 4\theta_M] + K_u \sin^2 \theta_M - MH \cos \phi, \quad (3.4)$$

where  $\phi$  is the angle between  $\mathbf{M}$  and  $\mathbf{H}$ . Since  $K_2$  at RT is smaller than  $K_1$  by two orders of magnitudes for bulk Fe [128], the term involving  $K_2$  can be neglected. The reader may,



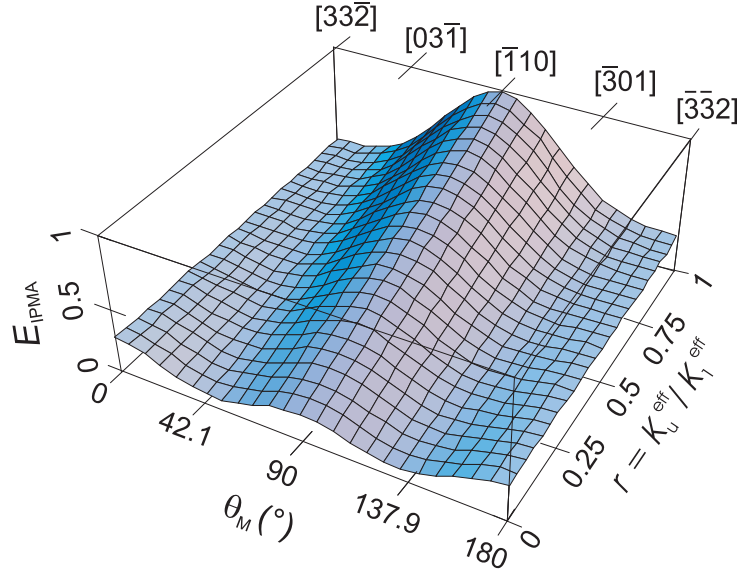


Figure 3.15: Three-dimensional plot of in-plane anisotropy energy density  $E_{\text{IPMA}}$  (for  $H = 0$ ) for the  $[113]$ -oriented Fe film according to Eq. (3.4) with  $r$  and  $\theta_M$  as variable. Here  $r$  is the anisotropy ratio given by  $r = K_u^{\text{eff}}/K_1^{\text{eff}}$  and  $\theta_M$  is the angle of magnetization with respect to the  $[33\bar{2}]$  direction.

however, note that unlike the case of the (001) surface, none of the  $\alpha_i$  is zero for the (113) surface. Thus the term involving  $K_2$  is nonzero, but very small. The in-plane magnetic anisotropy energy density at zero field can now be written as:

$$E_{\text{IPMA}} = (K_1^{\text{eff}}/484)[89 + 16 \cos 2\theta_M + 48 \cos 4\theta_M] + K_u^{\text{eff}} \sin^2 \theta_M, \quad (3.5)$$

where we have introduced  $K_1^{\text{eff}}$ ,  $K_u^{\text{eff}}$  to include the thickness dependence of these constants given by:

$$\begin{aligned} K_1^{\text{eff}} &= K_1^v + K_1^{\text{int}}/d_{\text{Fe}} \\ K_u^{\text{eff}} &= K_u^v + K_u^{\text{int}}/d_{\text{Fe}}, \end{aligned} \quad (3.6)$$

where  $K_1^v$ ,  $K_u^v$ ,  $K_1^{\text{int}}$ ,  $K_u^{\text{int}}$  describe the in-plane volume and interface four-fold and uniaxial magnetic anisotropy constants. Here,  $d_{\text{Fe}}$  is the thickness of the Fe film.  $K_{1,u}^{\text{int}}$  is assumed to comprise the contribution from the interface between the magnetic film and the substrate as well as that from the interface with the Al capping layer.

One can qualitatively understand the observed magnetic properties from Eq. (3.5). In Fig. 3.15 we show a three-dimensional plot of Eq. (3.5) as a function of the anisotropy ratio  $r = K_u^{\text{eff}}/K_1^{\text{eff}}$  and the in-plane angle  $\theta_M$ . The major in-plane directions are also shown, with  $\theta_M = 0^\circ$  corresponding to  $[33\bar{2}]$ . A change from a two-fold to four-fold symmetry with a decrease of  $r$  can be clearly seen. The minima in anisotropy energy density, which indicate the easy axis, moves from the two  $\langle 33\bar{2} \rangle$  directions to the neighborhood of the four  $\langle 03\bar{1} \rangle$  directions with decrease of  $r$ . This explains the gradual change from a UMA to a four-fold magnetic anisotropy, if we assume a decrease of  $r$  with increase in thickness. Hence, the four-fold magnetic anisotropy in thicker Fe films arises from the magnetocrystalline anisotropy and the large demagnetization energy of these Fe films.

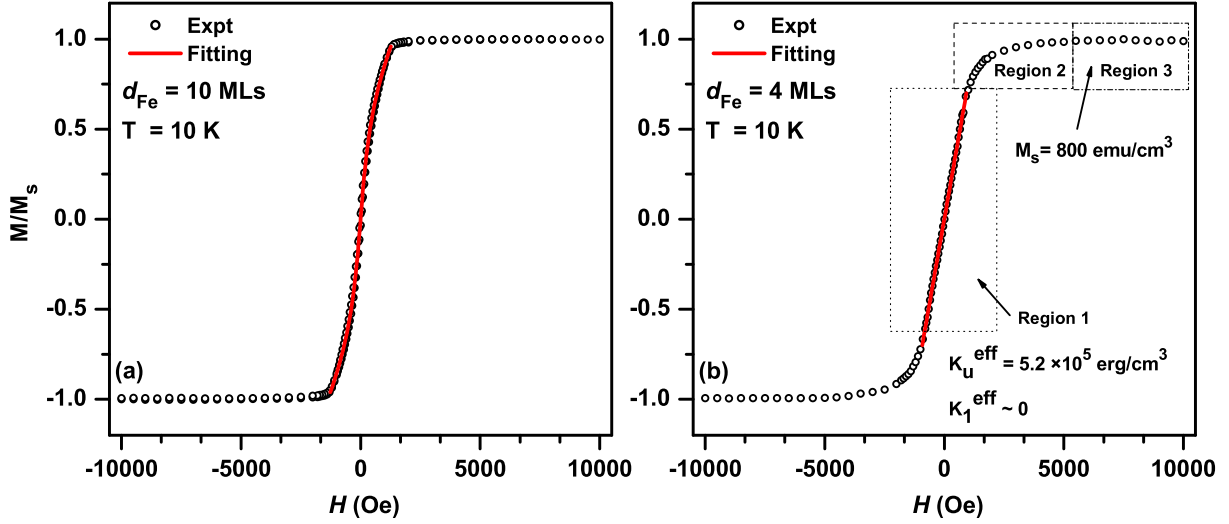


Figure 3.16: Illustration of the analytical fitting used to evaluate anisotropy constants in ultrathin Fe films with  $d_{\text{Fe}} \leq 50$  MLs. Fitting of the magnetization curve of (a) 10 ML and (b) 4-ML-thick sample at 10 K for magnetic field applied along  $[\bar{1}10]$ . For the 10-ML-thick sample the fitting was performed using Eq. (3.7) in the range,  $-1 < m < 1$ . For the 4-ML-thick sample the fitting was performed in the region 1 using Eq. (3.8). The open circles represent experimental data whereas the solid lines represent the fits.

### 3.4.6 Thickness dependence of anisotropy constants

To understand the origin of the UMA, we study the thickness dependence of the magnetic anisotropy constants. The anisotropy constants are derived from the magnetization curves in the following ways.

**Fitting of the Hard axis loops** For film thicknesses  $d_{\text{Fe}} \leq 50$  MLs, we use the hard axis magnetization curves along  $[\bar{1}10]$ , for which the magnetization rotates coherently with the applied magnetic field. For the magnetic field applied along this direction ( $\phi = \pi/2 - \theta_M$ ), an analytical expression of the inverse magnetization loop,  $H(m)$ , can be obtained by minimizing the energy given by Eq. (3.4), i.e., by solving  $dE_{\text{IPMA}}/d\theta_M = 0$  and  $M = M_s \cos(\pi/2 - \theta_M)$ :

$$H||[\bar{1}10] : H(m) = K_1^{\text{eff}}(384m^3 - 280m)/121M_s + 2K_u^{\text{eff}}m/M_s, \quad (3.7)$$

where  $m = M/M_s$  is the normalized component of the magnetization. Eq. (3.7) is valid in the range of coherent rotation of the magnetization, i.e., for  $-1 < m < 1$  and for a magnetic field along  $[\bar{1}10]$ . Note that this equation is very similar for the case of an  $[001]$ -oriented film with a cubic and a linear part. An example of the fit is shown in Fig. 3.16(a) for a 10-ML-thick sample at 10 K.

**The Stoner-Wohlfarth model (SWM) for thicker films** For Fe film thicknesses  $d_{\text{Fe}} \geq 70$  MLs, the above analytical model of coherent rotation [in other words Eq. (3.7)] is not valid since the magnetization curves along all directions exhibit hysteresis. Thus one needs to model the hysteresis behavior of the sample. We have performed this using

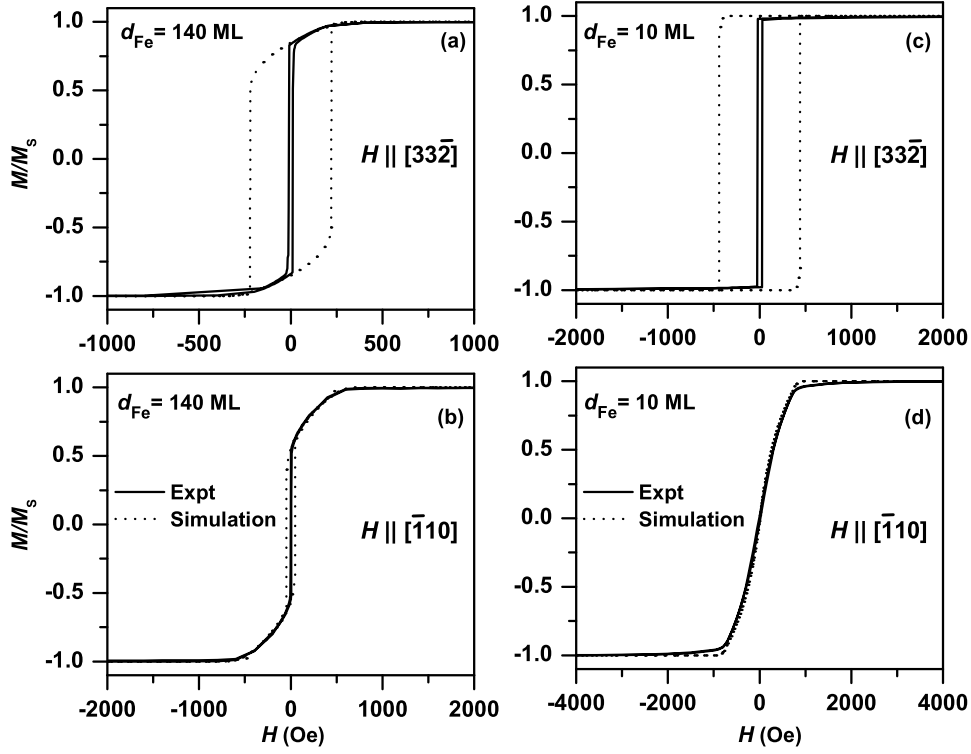


Figure 3.17: Illustration of the simulation using the Stoner-Wohlfarth model (SWM) to evaluate anisotropy constants in thick Fe films with  $d_{\text{Fe}} \geq 70$  MLs. 140-ML-thick sample: hysteresis loop at 300 K along (a)  $[33\bar{2}]$  and (b)  $[\bar{1}10]$ , and the corresponding simulation (dotted lines) with  $K_{\text{u}}^{\text{eff}}/M_{\text{s}} = 110$  Oe and  $K_{\text{l}}^{\text{eff}}/M_{\text{s}} = 275$  Oe. Idem in (c) and (d) are for a 10-ML-thick sample with  $K_{\text{u}}^{\text{eff}}/M_{\text{s}} = 316$  Oe and  $K_{\text{l}}^{\text{eff}}/M_{\text{s}} = 135$  Oe, obtained from the fitting of the hard axis magnetization loop using Eq. (3.7) as described in the text. The coercive fields do not match with the experiment since the SWM does not take into account the micro-magnetic structure of the sample [3].

the simple SWM, where the magnetization follows the local minimum of the magnetic free energy. Hence for  $d_{\text{Fe}} \geq 70$  MLs, the anisotropy constants were evaluated by fitting the hysteresis loops obtained by numerically tracking the local minimum of the free energy in Eq. (3.4) as the field was swept. An example of the fitting is shown in Fig. 3.17 for a 140-ML-thick sample with magnetic field applied along (a)  $[33\bar{2}]$  and (b)  $[\bar{1}10]$ . The parameters used in the simulation are  $K_{\text{u}}^{\text{eff}}/M_{\text{s}} = 110$  Oe and  $K_{\text{l}}^{\text{eff}}/M_{\text{s}} = 275$  Oe. As can be seen, the reversible part of the magnetization curve agrees well with the experiment where the magnetization rotates coherently and the single domain model is valid. The coercive field (i.e., the irreversible part) does not match the experiment, since the SWM does not take into account the micro-magnetic structure of the sample [3].

It is worth mentioning that this method of fitting of hysteresis loops can also be used for Fe films below 50 MLs. But for simplicity we have determined the anisotropic constants from the fitting of the hard axis magnetization curves along  $[\bar{1}10]$  with the inverse magnetization loop  $H(m)$  of Eq. (3.7) for all samples below 50 ML. However, using the same anisotropy constants the magnetization curves of the experiment can be correctly reproduced in other directions as well. As an example we compare the

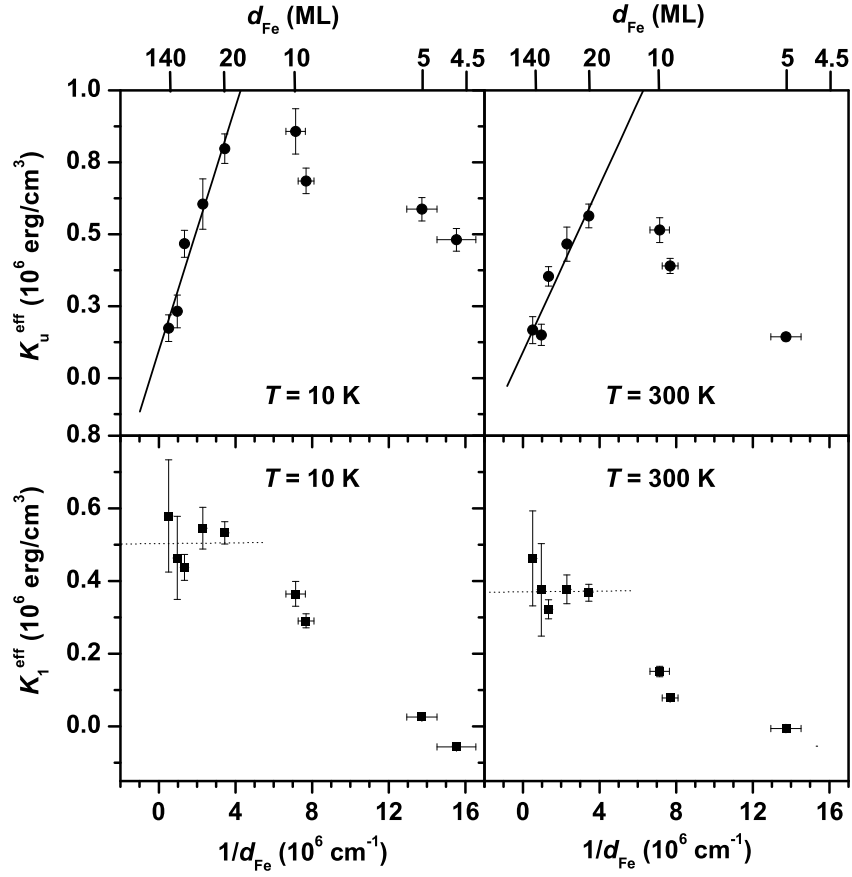


Figure 3.18: Variation of effective uniaxial,  $K_u^{\text{eff}}$  (first row) and four-fold,  $K_1^{\text{eff}}$  (second row) anisotropy constants with inverse Fe film thickness  $1/d_{\text{Fe}}$  at 10 K (first column) and 300 K (second column). Individual film thicknesses are also indicated at the top. A linear fit to the variation  $K_u^{\text{eff}}$  vs  $1/d_{\text{Fe}}$  for Fe film thickness above 20 MLs yields the surface/interface anisotropy constant  $K_u^{\text{int}} = (2.1 \pm 0.5) \times 10^{-1} \text{ erg/cm}^2$  at 10 K and  $(1.4 \pm 0.5) \times 10^{-1} \text{ erg/cm}^2$  at 300 K.  $K_1^{\text{eff}}$  in the second row remains almost constant above 20 MLs as shown by the dotted lines.

calculated magnetization curves using the SWM with experiments in Fig. 3.17 for a 10-ML-thick sample with magnetic field applied along (c)  $[33\bar{2}]$  and (d)  $[\bar{1}10]$ . The anisotropic parameters,  $K_u^{\text{eff}}/M_s = 316 \text{ Oe}$  and  $K_1^{\text{eff}}/M_s = 135 \text{ Oe}$  used for this sample were obtained by fitting the inverse magnetization loop of Eq. (3.7) for a magnetization curve along  $[\bar{1}10]$ . The agreement between the two different techniques used in finding the anisotropic constants can be clearly seen.

### The interfacial origin of UMA

In Fig. 3.18 we present plots of  $K_u^{\text{eff}}$  and  $K_1^{\text{eff}}$  versus the inverse Fe film thickness  $1/d_{\text{Fe}}$  at 300 K and 10 K obtained from the fits. At all examined temperatures,  $K_u^{\text{eff}}$  decreases below and above 20 MLs, whereas  $K_1^{\text{eff}}$  decreases only below 20 MLs and remains almost constant above 20 MLs. To understand the decrease of  $K_1^{\text{eff}}$  and  $K_u^{\text{eff}}$  below 20 MLs we compare the evolution of the integrated RHEED intensity during Fe growth as shown in Fig. 3.6(c).

Table 3.2: Table of the in-plane and out-of-plane anisotropy constants for different epitaxial Fe/GaAs systems at 300 K. The first column represents the results obtained in this work on Fe/GaAs(113)A substrates. The constants have not been adjusted to remove the effect of the capping layer.

Constant	Al/Fe/ GaAs(113)A	Au/Fe/ GaAs(001) [129]	Au/Fe/ GaAs(001) [130]	Cu/Fe/ GaAs(001) [133]	Au/Fe/ GaAs(110) [132]
$K_u^{\text{int}}$ ( $10^{-1}$ erg/cm <sup>2</sup> )	$1.4 \pm 0.5$	$1.0 \pm 0.1$	$1.2 \pm 0.2$	$0.32 \pm 0.12$	$-1.4 \pm 0.2$
$K_u^{\text{v}}$ ( $10^5$ erg/cm <sup>3</sup> )	$2.0 \pm 0.1$	—	0	—	$2.7 \pm 0.8$
$K_1^{\text{int}}$ ( $10^{-1}$ erg/cm <sup>2</sup> )	—	$0.32 \pm 0.05$	$-0.46 \pm 0.02$	$0.51 \pm 0.05$	$0.39 \pm 0.09$
$K_1^{\text{v}}$ ( $10^5$ erg/cm <sup>3</sup> )	$3.7 \pm 1.7$	$3.7 \pm 0.3$	$4.3 \pm 0.2$	$4.6 \pm 0.3$	$3.6 \pm 0.7$
$K_p^{\text{int}}$ ( $10^1$ erg/cm <sup>2</sup> )	$-0.11 \pm 0.02$	$-0.09 \pm 0.01$	—	$-0.17 \pm 0.01$	—
$K_p^{\text{v}}$ ( $10^5$ erg/cm <sup>3</sup> )	$0.5 \pm 0.5$	$1.2 \pm 0.7$	—	—	—

The integrated RHEED intensity increases rapidly up to about 20 MLs, and then remains almost constant. As already discussed before, this indicates islanding below 20 MLs. Above this thickness, the film becomes two-dimensional. The decrease of  $K_u^{\text{eff}}$  and  $K_1^{\text{eff}}$  below 20 MLs in Fig. 3.18 can thus be attributed to the formation of three-dimensional Fe islands below 20 MLs. It should be mentioned that a similar decrease of  $K_u^{\text{eff}}$  was also observed for Fe films on GaAs(001) [129, 130, 131]. However, the thickness at which such a decrease was observed was far below 20 MLs. To find the interface contribution of the UMA, we perform a weighted least square fit to Fig. 3.18(a) above 20 MLs, since only in this region is the 2D-thin film relation of Eq. (3.6) is valid. This yields  $K_u^{\text{int}} = (2.1 \pm 0.5) \times 10^{-1}$  erg/cm<sup>2</sup> at 10 K and  $K_u^{\text{int}} = (1.4 \pm 0.5) \times 10^{-1}$  erg/cm<sup>2</sup> at 300 K. The RT values are comparable to the reported values in literature for the Fe/GaAs(001) [129, 130] and Fe/GaAs(110) [132] systems as shown in Table 3.2. This points towards an identical origin of the UMA in all these systems. The strong  $1/d_{\text{Fe}}$  dependence of the UMA implies a dominant interfacial contribution of UMA in Fe/GaAs(113)A, similar to Fe/GaAs(001). Hence, the uniaxial interface anisotropy is independent of the epitaxial orientation and is an inherent property of the Fe/GaAs interface. The four-fold anisotropic constant  $K_1^{\text{eff}}$  did not show a strong thickness dependence for films larger than 20 MLs. In fact, it reaches nearly the bulk value of  $4.7 \times 10^5$  erg/cm<sup>3</sup> at about 20 MLs.

**A further support for the interfacial origin of UMA** An interfacial origin would imply that, for ultrathin Fe films, the anisotropy is dominated completely by the UMA. We analyze this in Fig. 3.16(b), where the magnetization curve of the thinnest ferromagnetic

film of 4 MLs of Fe is examined at 10 K for a magnetic field along  $[\bar{1}10]$ . For the ultrathin region, Eq. (3.7) can be modified with the assumption that  $K_1^{\text{eff}} \ll K_u^{\text{eff}}$ :

$$H(m) = 2K_u^{\text{eff}}m/M_s, \quad (3.8)$$

which has just a linear part. This means that the magnetization should be a linear function of the applied field in the range of  $-1 < m < 1$ . However, the real magnetization curve of Fig. 3.16(b) is much more complex. By simple visual inspection, we distinguish three regions in the magnetization curve. Region 1 shows the expected linear variation. Region 2, where the magnetization changes gradually to saturation (region 3), was observed for all ultrathin Fe films below 7 MLs. This region can not be reproduced by the cubic terms in Eq. (3.7). Hence we attribute this region to the structural properties of the films, i.e., the presence of islands in this thickness range. Nevertheless, region 1 can be well described by Eq. (3.8) as evidenced by the good fit shown in Fig. 3.16(b). The linear behavior and almost zero four-fold anisotropy constant imply an interfacial origin of the UMA.

**On the origin of UMA in Fe/GaAs(113)A** The interfacial contribution of UMA in Fe/GaAs(113)A is similar to that of Fe/GaAs(001). The origin of the UMA can thus be similarly attributed to the anisotropic bonding structure at the interface according to the recent results on Fe/GaAs(001) [104, 116, 129]. However, several other possible origin for UMA in Fe on GaAs(113)A can be discussed. A particularly interesting possible origin of UMA in Fe on GaAs(113)A could be the surface structure of the reconstructed GaAs(113)A surface, which exhibits a surface corrugation with step edges parallel to the  $[3\bar{3}2]$  direction [53, 54, 134] (see Sec. 1.1). It is known that Fe films grown on stepped surfaces exhibit a UMA [135, 136]. For Fe on stepped W(001), Chen *et al.* [135] reported a step-induced UMA with the easy axis perpendicular to the steps, whereas for Fe on stepped Ag(001) Kawakami *et al.* [136] reported an easy axis parallel to the step edges. However, we did not observe any split loop in the magnetization curves like in the cases of Fe on stepped metallic surfaces [135, 136] or in other systems e.g., Co on vicinal Cu(001) [137]. Moreover, we observe qualitatively similar magnetic properties for Fe/GaAs(113)A compared to Fe/GaAs(001). So we conclude that these reconstruction-induced steps are probably not responsible for the observed UMA. The hard axis of UMA was along the in-plane  $[\bar{1}10]$  axis, which is also a hard axis for Fe/GaAs(001). The easy axis of UMA in Fe on GaAs(113)A found along the  $[3\bar{3}2]$  direction can be considered as a projection of the  $[110]$  axis onto the (113) surface. Hence, the atomic configuration along both the  $[3\bar{3}2]$  and  $[110]$  directions should be similar. We thus believe that there is a common origin for UMA in the Fe/GaAs(113)A and the Fe/GaAs(001) systems. For Fe/GaAs(001), the surface reconstruction of GaAs was shown not to be responsible for the observed UMA [104, 114]. Since the UMA in our samples is found to be originating from the Fe/GaAs interface and independent of the epitaxial orientation, we propose that the UMA in the Fe/GaAs system is determined by the anisotropy of the bonding between Fe and As, Ga at the Fe-GaAs interface. This is supported by the results of Kneedler *et al.* [104], who suggested the directional nature of the Fe-As bonding as a possible origin of the observed UMA, from a combined STM and MOKE study. Thus a detailed study of the atomic configuration at the Fe-GaAs interface could provide more insight into the microscopic origin of the observed UMA. It should be mentioned that strain anisotropy mediated by magnetoelastic coupling was ruled out as a cause for the observed UMA [116].

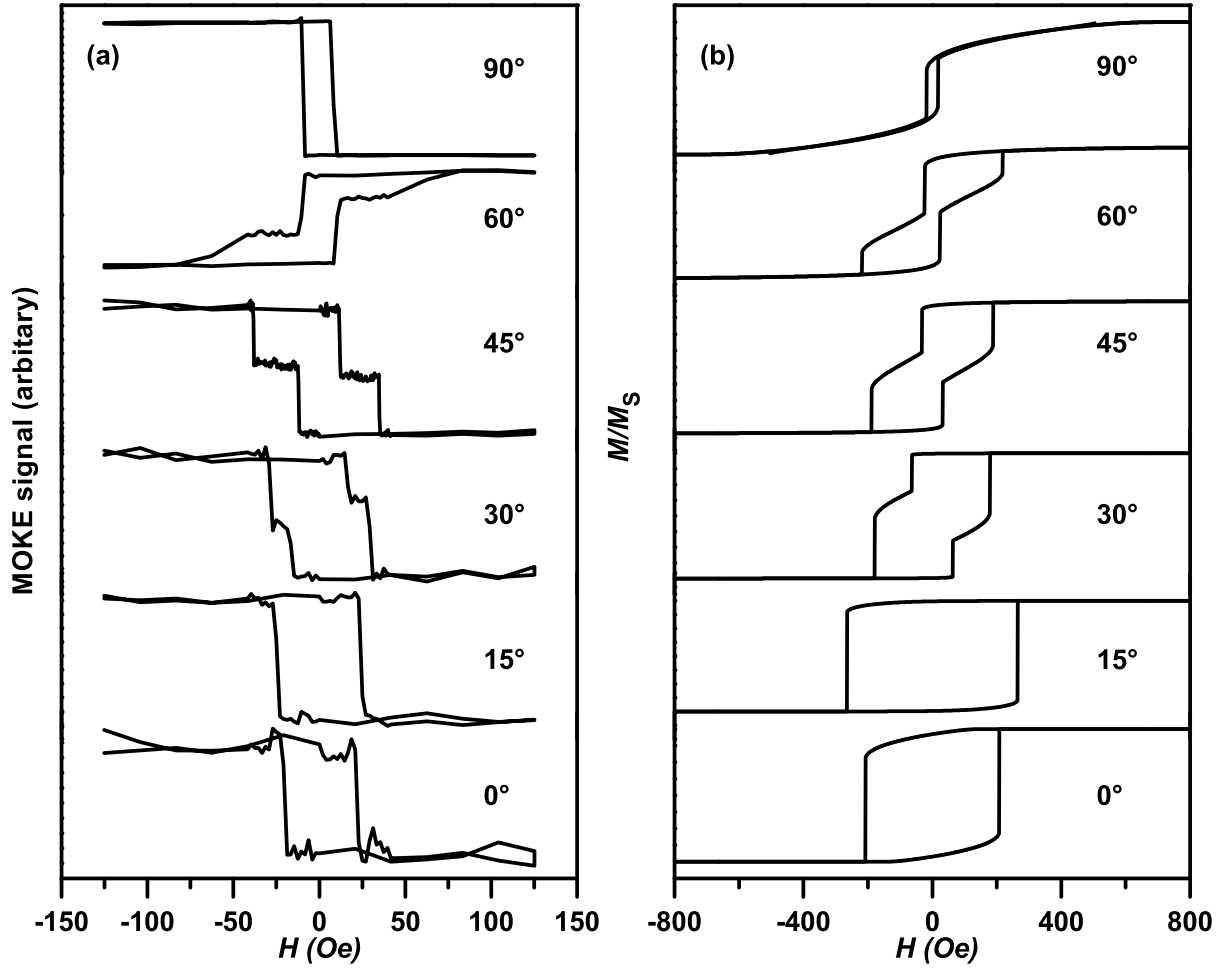


Figure 3.19: (a) *in situ* MOKE loops for Fe (26 nm)/GaAs(113)A for different in-plane directions. Here,  $0^\circ$  and  $90^\circ$  indicate the  $[33\bar{2}]$  and  $[\bar{1}10]$  direction, respectively. The easy axis of magnetization is near to the  $[03\bar{1}]$  direction or  $45^\circ$ . Note that the magnetization is not completely saturated in all directions. (b) Simulated hysteresis loops for the Fe(113) film with a uniaxial ratio  $r = 0.6$  and  $2K_1/M_s = 440$  Oe.

### 3.4.7 Mechanism of magnetization reversal

Magnetization reversal refers to the switching of magnetization between its initial and final remanent states under the influence of an externally applied magnetic field. To study the magnetization reversal we employ *in situ* MOKE (see Sec. 2.4.1) since the direction of the applied field can be varied more easily in MOKE compared to SQUID magnetometry. The switching behavior was studied as a function of the angle of the in-plane applied field,  $\theta_H$  measured with respect to the  $[33\bar{2}]$  axis. Figure 3.19(a) shows a set of MOKE loops for a 26-nm-thick Fe film. From SQUID magnetometry (not shown), the sample is well-known to exhibit a dominant four-fold magnetic anisotropy with a weak UMA. In fact, the anisotropy ratio  $r$  as determined from the fitting of the SQUID magnetization curves is about 0.6. Thus the easy axes are in the neighborhood of  $45^\circ/135^\circ$  in Fig. 3.19(a) (see Fig. 3.15). However, the anisotropy is not resolved in Fig. 3.19(a), since the sample is not completely saturated in all directions due to the low field available in our MOKE

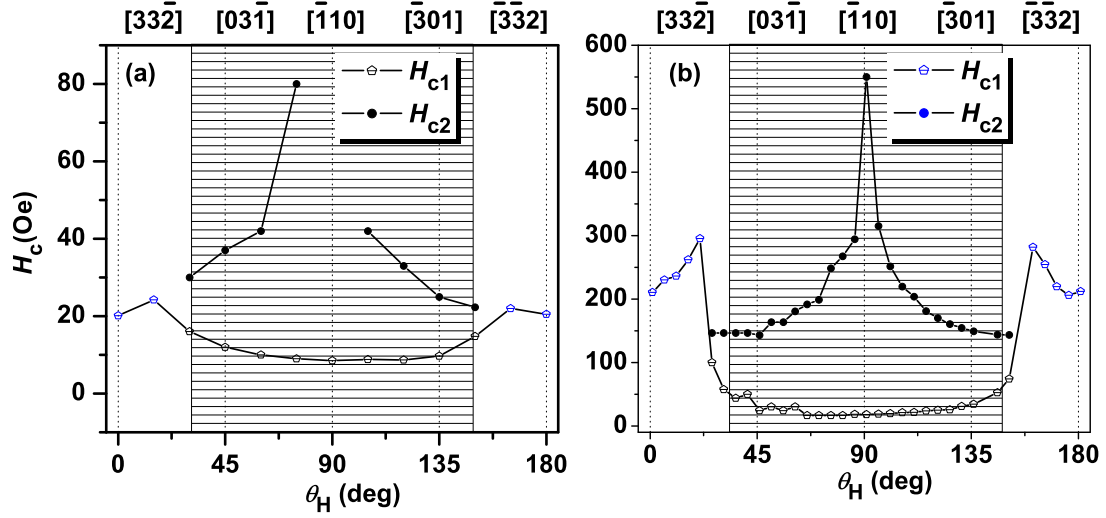


Figure 3.20: (a) Plot of the coercive field,  $H_c$  as a function of the in-plane direction,  $\theta_H$  of the applied field for the sample presented in Fig. 3.19(a) with uniaxial ratio  $r = 0.6$ . (b) The simulated coercive fields as a function of  $\theta_H$  for a uniaxial ratio  $r = 0.6$  and  $2K_1/M_s = 440$  Oe (see text).

set-up. Nevertheless, several important observations can be made from this figure:

1. The magnetization curve along the  $[33\bar{2}]$  and  $[\bar{1}10]$  axes exhibits one reversible jump, which we call a one-jump switching process.
2. The magnetization curve along  $[03\bar{1}]$  and some other intermediate directions shows two irreversible jumps, which we call a two-jump switching process.
3. The coercive field along  $[33\bar{2}]$  is larger compared to that along  $[\bar{1}10]$ .

The angular dependence of the reversal process can be more clearly seen in Fig. 3.20(a), where the first and second coercive fields are plotted as a function of the in-plane direction of the magnetic field,  $\theta_H$ . As indicated, the behavior is distinguished into two regions depending on the two-jump (hatched) and one-jump (unhatched) switching process. The first coercive field  $H_{c1}$  increases until  $15^\circ$  and then decreases until  $90^\circ$  with a symmetric behavior on the other side, i.e., between  $90$  to  $180^\circ$ . The second coercive field  $H_{c2}$  exhibits a rapid increase from  $15$  to  $90^\circ$  in the two-jump switching region and also has a symmetrical behavior.

**The origin of the two-jump switching** We are aware of two different kinds of explanation in literature for the two-jump switching in magnetic thin films. A first explanation has been discussed in connection with Fe/GaAs system by Daboo *et al.* [3, 138] using the simple Stoner-Wohlfarth (SW) formulation. In this model, one can expect a two-jump switching depending on the exact values of  $\theta_H$  and  $r$ . Using the SWM, Daboo *et al.* obtained a qualitative agreement with the experiment though the exact value of the coercive field was not reproduced. The other explanation has been discussed in connection with ultrathin Fe films on Ag by Cowburn *et al.* [139, 140] by considering the domain



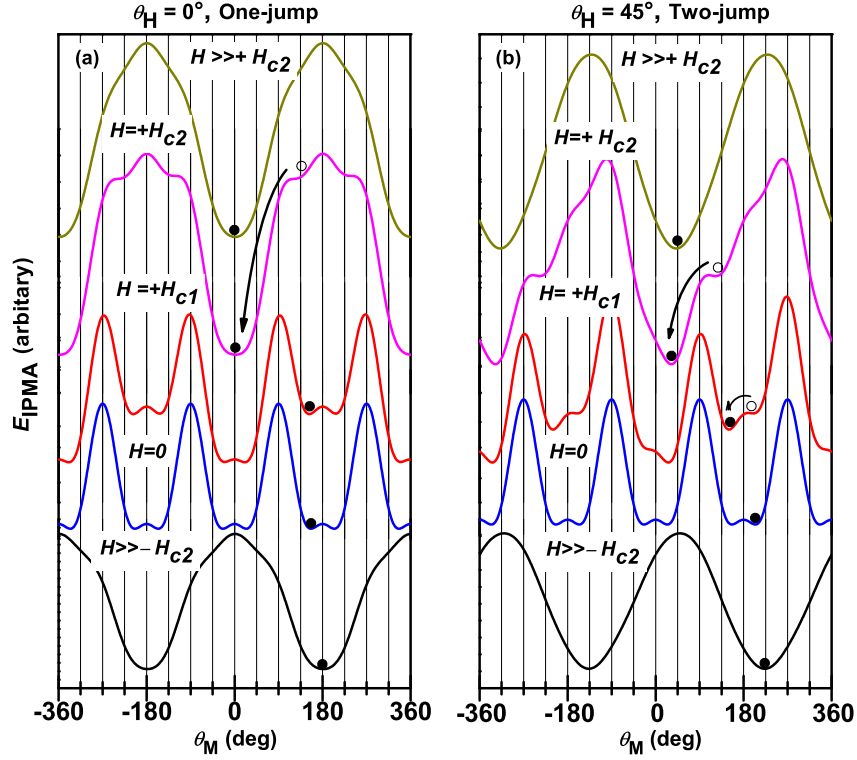


Figure 3.21: The evolution of local minima in the anisotropic energy of the Fe(113)-plane with the applied magnetic field for a uniaxial ratio of  $r = 0.6$ . The one-jump and two-jump switching process are demonstrated for (a)  $\theta_H = 0^\circ$  and (b)  $\theta_H = 45^\circ$ . Here,  $0^\circ$  indicates the  $[332]$  direction.

processes. Cowburn *et al.* assumed that depending on the field orientation, reversal can proceed either via a one-jump mechanism, (by the sweeping of  $180^\circ$  domain walls) which results in a classic square hysteresis loop, or by a two-jump mechanism, (by the sweeping of  $90^\circ$  domain walls) which results in a more unusual hysteresis loop with two irreversible transitions. By using the experimentally determined pinning energy, they obtain a quantitative agreement of the switching field. In the following the simple SW formulation, will be shown sufficient to describe the experimental observations of Fig. 3.19(a).

First, we will provide some experimental evidence to show that the explanation of Cowburn *et al.* cannot be applied to our films. Their films also exhibit a dominant four-fold magnetic anisotropy with a small non-vanishing UMA. However, the easy axis of UMA in their case coincides with the bulk easy axes  $\langle 100 \rangle$ , whereas in our samples the easy axis is along a non-easy axis of bulk Fe. The small UMA in our samples shifts the easy axes from the  $\langle 03\bar{1} \rangle$  axes towards the  $\langle 33\bar{2} \rangle$  axes. Thus the possible four domains are not perpendicular to each other. This could provide an unfavorable condition for the sweeping of  $90^\circ$  domain walls. This is indeed the case in the experiment: the angular dependence of the second coercive field shows one maximum in our samples compared to two maxima in Fig. 6 of Ref [139]. Hence, the explanation of Cowburn *et al.* cannot be applied to the sample shown in Fig. 3.19(a).

However, it is possible to understand the experimental switching behavior of Fig. 3.19 and Fig. 3.20 by using the SWM. Figure 3.21 demonstrates how one-jump and two-jump

switching can arise from a calculation using the SW formulation by simply considering the anisotropy present in the sample. The figure shows the anisotropic energy of the Fe(113) film [see Eq. (3.4)] for the magnetic field applied at an angle of 0 and 45°, measured with respect to the  $[3\bar{3}2]$  direction. The reversal process starts off with the magnetization sitting in the negative saturation energy minimum with an orientation close to the applied field direction as indicated by the solid circle (the so-called SW particle). At zero field, the magnetization switches to one of the nearest local minima as shown in the next plot. As the field reverses this minimum becomes shallower and eventually disappears. At this point the magnetization undergoes an irreversible jump and falls into a different energy minimum. In the one-jump switching process ( $\theta_H = 0^\circ$ ), this second minimum is the positive saturation energy minimum, and the magnetization remains in this minimum as the applied field is swept towards the positive saturation. However, for a two-jump switching process ( $\theta_H = 45^\circ$ ), a third intermediate energy minimum exists once the positive saturation minimum disappears, with the result that the magnetization falls into this minimum causing the first jump. However, as the field is further reversed, this intermediate minimum also disappears and magnetization eventually ends up in the positive saturation energy minimum. Thus by following the local minimum we can calculate the hysteresis loops. These calculations, as shown in Fig. 3.19(b), indicate that the reversal process can proceed either by one or two jumps depending on the exact values of  $\theta_H$  and  $r$ , and are in agreement with experiment. A clear qualitative agreement with experiment can be seen and the above mentioned three observations are well reproduced in the simulation. The angular dependence of the coercive fields also exhibits qualitatively similar behavior as shown in Fig. 3.20. However, the switching fields exhibit a large quantitative disagreement. The experimental switching field is smaller compared to that of the simulation, which was also observed for Fe/GaAs(001) system [3, 138]. As also discussed before, we attribute this difference to the detailed magnetic microstructure of the film which is not accounted for in the simple SWM.

Detailed thickness dependent calculations show good agreement with the experiment similar to that in Ref [138]. One-jump switching is predicted for dominant UMA, which agrees well with experiment. Two-jump switching is predicted only for  $r < 1$ , depending on the orientation of the in-plane field. However, in some thicker films, we observe a two-jump switching when calculation predicts a one-jump switching. This was also reported by Daboo *et al* [138]. They ascribe the phenomena to a “non-ideal” two-jump switching process governed by the magnetic microstructure of the sample.

### 3.4.8 Evolution of out-of-plane magnetic anisotropy

The out-of-plane SQUID magnetization curves for two typical samples of 5 MLs and 140 MLs thicknesses are shown in Fig. 3.22(a). The measurements were performed at 2 K with the magnetic field applied perpendicular to the film plane, i.e., along the  $[113]$  direction. The magnetization curves are completely reversible for both samples but the saturation field of the 5-ML-thick sample is significantly reduced to 7 kOe as compared to 22 kOe for the 140-ML-thick sample. The saturation field was determined from the maxima of the anisotropy field distribution  $P(H_s)$ , given by the second order derivative;  $-M(d^2M/dH^2)$  [141]. It should be mentioned that for these out-of-plane measurements, we found a small hysteresis in the low field region (not shown). However, when we assume a small misalignment of  $< 4^\circ$  and subtract the in-plane component of magnetization, the

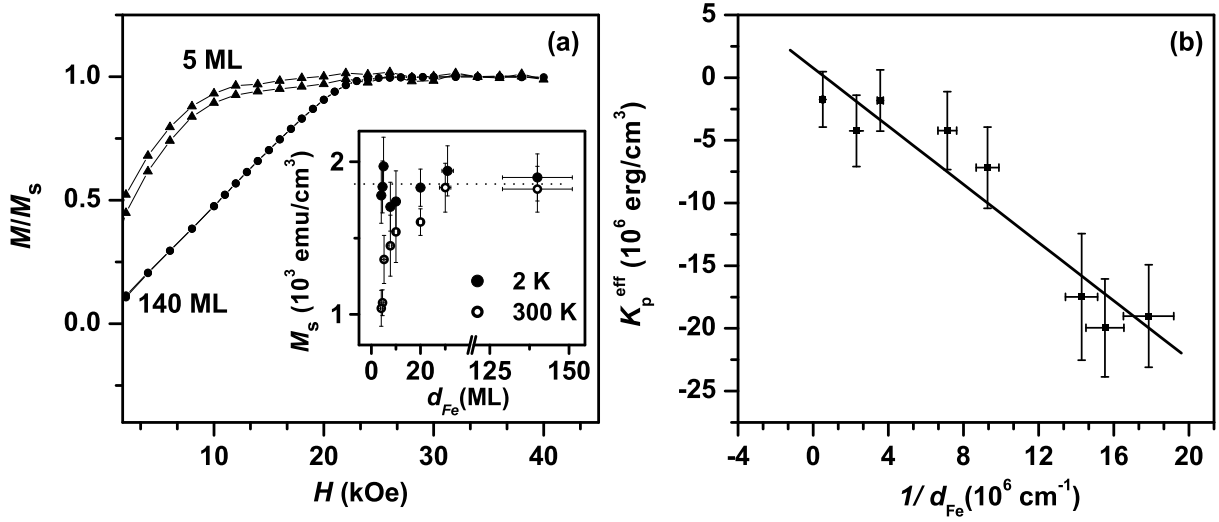


Figure 3.22: (a) Out-of-plane magnetization curves for 5 ML and 140-ML-thick Fe films on GaAs(113)A at 2 K. The inset shows the thickness variation of saturation magnetization at 300 K (open circles) and 2 K (solid circles) (b) Variation of the effective perpendicular magnetic anisotropy constant with the inverse Fe film thickness  $1/d_{Fe}$ . A linear fit (shown as a solid line) yields the interfacial contribution of PMA,  $K_p^{\text{int}} = -(0.11 \pm 0.02) \times 10^1$  erg/cm<sup>2</sup>.

hysteresis disappears. Thus this low field hysteresis was confirmed to be arising from a misalignment of the sample in the SQUID magnetometer.

To account for the reduction of  $H_s$ , we consider the free energy density for magnetic fields applied normal to the film plane. In this case only two contributions need to be considered [142] to describe the perpendicular component of the magnetization. The first is the shape or demagnetization energy [next to the last term of Eq. (3.3)] and can be written as  $N_p M_n^2/2$ , where  $M_n$  is the component of magnetization perpendicular to the film plane and  $N_p$  is the demagnetization factor, which will be taken to be  $4\pi$ , suitable for thin films. In reality the demagnetization factor can deviate from  $4\pi$  in ultrathin films (in our case below 20 MLs) due to atomic scale roughness [143]. However, this effect is rather small and hence can be neglected here. The second contribution is the free energy due to the local symmetry at the interface/surface first introduced by Néel [32]. This is given by  $K_p^{\text{eff}}(M_n^2/M_s^2)$ , where  $K_p^{\text{eff}}$  is the effective perpendicular anisotropy constant due to the local symmetry and is assumed to be a combination of the volume and interface/surface term:

$$K_p^{\text{eff}} = K_p^v + K_p^{\text{int}}/d_{Fe}. \quad (3.9)$$

Thus, using the above two energies, the free energy of a magnetized film,  $E_{\text{PMA}}$  in an external magnetic field  $H_n$  (applied normal to the film plane) can be written as:

$$E_{\text{PMA}} = 2\pi M_n^2 + K_p^{\text{eff}}(M_n^2/M_s^2) - H_n M_n, \quad (3.10)$$

where the last term represents the Zeeman energy. In general, one has to consider also the

cubic anisotropy energies. However, for the iron films studied here, the demagnetization energy alone is sufficiently large so that they can be neglected.

At equilibrium,  $dE_{\text{PMA}}/dM_n = 0$ , which on simplification provides the dependence of applied field on  $M_n$  in the following way:

$$M_n = (4\pi + 2K_p^{\text{eff}}/M_s^2)^{-1} H_n, \quad (3.11)$$

so that in this simple model the component of the magnetization perpendicular to the plane of the thin film is predicted to depend linearly on the applied field till saturation of the magnetic moments. The saturation field  $H_s$ , defined by the field at which  $M_n = M_s$  can thus be written as:

$$H_s = 4\pi M_s + 2K_p^{\text{eff}}/M_s. \quad (3.12)$$

The saturation magnetization  $M_s$  contained in this equation exhibits a strong thickness dependence at RT (300 K) as shown in the inset of Fig. 3.22(a) (open circles). To eliminate this thickness dependence, the measurements in Fig. 3.22(a) were performed at 2 K, at which the saturation magnetization remains almost constant as shown in the inset (solid circles), indicated by a dotted line. Hence, the reduction of the saturation field clearly shows the existence of a perpendicular magnetic anisotropy (PMA) in ultrathin films. Since this result is also similar to the case of Fe films on GaAs(001) [144, 145], the reduction of the saturation field in ultrathin Fe films of Fig. 3.22(a) does not arise from the specific [113] orientation of the Fe film.

To further investigate the origin of this PMA, we also studied the thickness dependence of  $K_p^{\text{eff}}$  which was determined from Eq. (3.12) using measured values of  $H_s$  and  $M_s$ . Figure 3.22(b) presents a plot of  $K_p^{\text{eff}}$  as a function of  $1/d_{\text{Fe}}$ . A weighted least squares linear fit gives the interfacial contribution of the perpendicular magnetic anisotropy:  $K_p^{\text{int}} = -(0.11 \pm 0.02) \times 10^1 \text{ erg/cm}^2$ . This value is found to be close to the corresponding values for the Fe/GaAs(001) system (see Table 3.2) [129]. This again implies a common origin of the PMA in both Fe/GaAs(001) and Fe/GaAs(113)A. Hence, we conclude that the perpendicular interface anisotropy is also independent of the epitaxial orientation and hence an inherent property of the Fe/GaAs interface. The origin of the PMA in these Fe films is attributed to the local symmetry at the interface.

### 3.4.9 Summary: Magnetic properties of Fe/GaAs(113)A

The major results of magnetic properties from SQUID and MOKE measurements are the following.

1. The onset of ferromagnetic order occurs at about 4 MLs and is ascribed to a percolation phenomenon during coalescence of Fe islands similar to that observed in Fe/GaAs(001).
2. A significant increase of the spin wave parameter in ultrathin Fe films on GaAs(113)A compared to GaAs(001) is found, which is explained as a result of the reduced UMA in this thickness range.

3. The magnetic anisotropy of these films versus film thickness is distinguished into two regions:
  - First, for Fe film thicknesses  $\leq 50$  MLs, we observe an in-plane UMA with the easy axis along the in-plane  $\langle 33\bar{2} \rangle$  axes.
  - Second, for Fe film thicknesses  $\geq 70$  MLs, we observe a four-fold magnetic anisotropy with the easy axis along the in-plane  $\langle 03\bar{1} \rangle$  axes.
4. This evolution of in-plane magnetic anisotropy can be understood from an analytical model based on the magnetic free energy density which includes a magnetocrystalline anisotropy and an additional UMA.
5. An apparent relation between the spin-reorientation transition and the relaxation of the layer has been found.
6. The two-jump reversal in some films with a small UMA  $r < 1$  has been explained on the basis of the Stoner-Wohlfarth model of magnetization rotation.
7. The existence of an out-of-plane perpendicular magnetic anisotropy is also detected in ultrathin Fe films. Similar to Fe/GaAs(001), an interfacial origin of the in-plane uniaxial and out-of-plane perpendicular magnetic anisotropy is proposed.
8. Both the uniaxial and the perpendicular interface anisotropies are found to be independent of the epitaxial orientation and are hence an inherent property of the Fe/GaAs interface.
9. The anisotropy of the bonding of Fe with As and Ga at the Fe-GaAs interface is proposed as the most likely origin of UMA in ultrathin films.
10. The origin of the perpendicular magnetic anisotropy in the ultrathin Fe films is attributed to the local symmetry at the interface.

### 3.5 Magnetotransport properties

In this section we will describe the results of magnetotransport measurements of Fe films grown on GaAs(113)A substrates, with special emphasis on the planar Hall effect (PHE), where the presence of an antisymmetric component (ASC) is found. The basics of magnetotransport can be found in Sec. 2.5. We will discuss the anisotropic magnetoresistance (AMR) and the PHE for four typical samples which differ in growth conditions, the presence/absence of the Al capping layer and thickness. For these measurements, rectangular samples with a typical size of  $2 \times 4 \text{ mm}^2$  were prepared. The current was passed along the long side of the sample, which was along  $\langle 33\bar{2} \rangle$  and  $\langle \bar{1}10 \rangle$  for two different pieces of the sample. A programmable stepper motor was used to rotate the sample in the magnetic field. Both the AMR and the PHE were measured simultaneously. We performed two different kinds of measurements. First, strength of the applied in-plane magnetic field was varied keeping the in-plane field orientation fixed along a specific in-plane direction. Second, the in-plane direction of the applied field was varied keeping the strength of the applied in-plane magnetic field fixed.

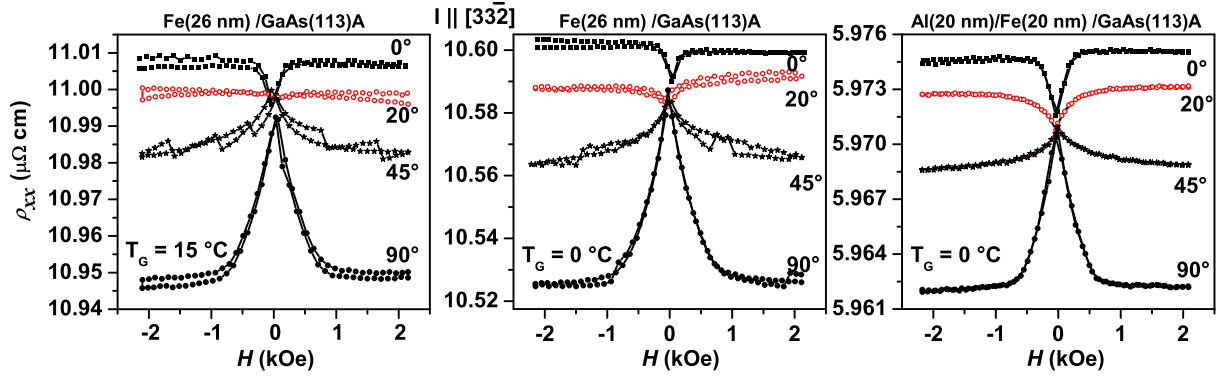


Figure 3.23: Anisotropic magnetoresistance (AMR) from a set of three Fe/GaAs(113)A samples at 300 K. Here,  $\theta_H = 0^\circ$  represents the  $[33\bar{2}]$  direction, which is also the direction of current.

### 3.5.1 Anisotropic magnetoresistance

AMR ( $\rho_{xx}$ ) data for three different samples of comparable thickness (20–26 nm) are presented in Fig. 3.23. The first sample was grown at 15 °C [see Fig. 3.3(a)] exhibits a slightly rough surface morphology compared to the next sample which was grown at 0 °C [see Fig. 3.3(b)]. The last sample has a 20-nm-thick Al capping layer grown at 0 °C. As can be clearly seen, irrespective of the nature of the samples, the AMR signal exhibits a qualitatively similar behavior. At zero field, all the curves are concentrated at one point, which corresponds to the easy axis of magnetization. The change in AMR signal with the strength of the applied field for  $\theta_H = 0^\circ$  ( $[33\bar{2}]$ ) is not the same as for  $\theta_H = 90^\circ$  ( $[\bar{1}10]$ ) indicating the inequivalence of these axes due to the presence of a small UMA in all these samples. The change is maximum for  $\theta_H = 90^\circ$ , indicating the hardest axis. When the magnetic field is applied at about 20 – 30°, the least change in the AMR signal is seen so that these directions represent the easy axes of magnetization. Thus the four-fold anisotropy and the presence of a small UMA in these samples as discussed in previous sections (see Fig. 3.14) can be clearly seen. The orientation of the easy axis allows us to determine the uniaxial ratio  $r$  of these samples which is shown in Table 3.3 along with other important parameters. For the first sample,  $r = 0.6$  and the easy axis is at about 20° to  $[33\bar{2}]$ . The AMR amplitude ( $\rho_{\parallel} - \rho_{\perp}$ ), which is the difference in  $\rho_{xx}$  between  $\theta_H = 0^\circ$  and  $\theta_H = 90^\circ$ , is nearly equal for the first two samples while it is slightly reduced for the third sample. This is attributed to the presence of the capping layer through which most current passes. Nevertheless, all the samples perfectly obey Eq. (2.12). The  $\cos^2 \theta_M$  dependence of AMR can be more clearly seen in the angular dependence of AMR shown in Fig. 3.24 for a constant in-plane saturating field of  $H = 2$  kOe. The figure also shows the low field angular dependence of AMR along with calculated curves using the SWM of magnetization rotation as discussed in Sec. 3.4.7 and Sec. 3.4.3. Numerically tracking the local minima in Eq. (3.4) yields the angle of magnetization, which is then used in Eq. (2.12) to find the AMR signal. The different parameters used in the simulation are shown in Table 3.3. A good qualitative agreement to the experiment can clearly be seen.

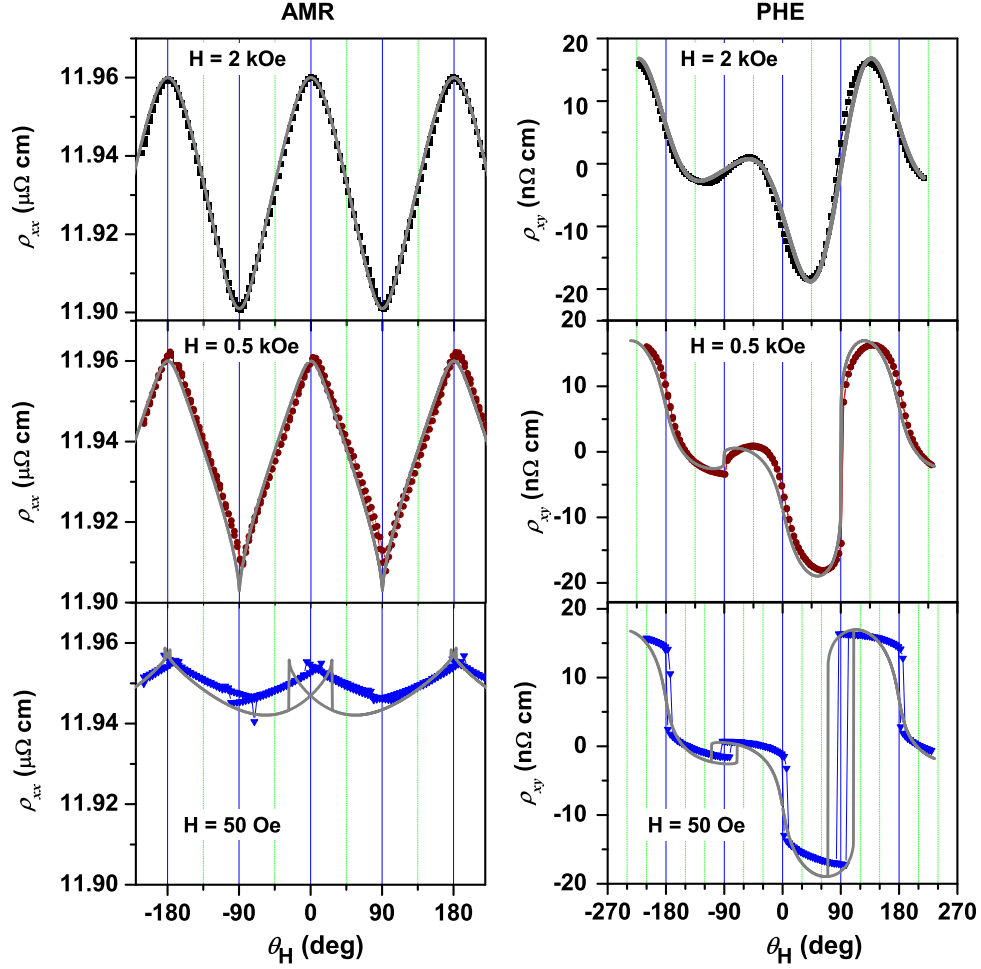


Figure 3.24: Experimental (symbols) and calculated (thick gray line) angular dependencies of the AMR (first coulumn) and the PHE (second column) for a 26-nm-thick Fe sample. Here,  $\theta_H = 0^\circ$  indicates the  $[3\bar{3}2]$  direction, which is also the direction of current. Note that the PHE is described by the modified equation Eq. (3.20) (see text). The low-field curves were calculated using the Stoner-Wohlfarth model with the parameters,  $K_1/M_s = 200$  Oe and  $r = K_u/K_1 = 0.6$ .

### AMR in ultrathin Fe films: The uniaxial regime

In Fig. 3.25 the AMR ( $\rho_{xx}$ ) response from a 10-ML-thick Fe film, with a capping layer of 3 nm Al is shown. Since the layer exhibits a UMA, the easy axis of magnetization is along the  $[3\bar{3}2]$  direction. This direction is also that of the current corresponding to  $\theta_H = 0^\circ$ . Referring to Fig. 3.25(a), the AMR signal does not change along this direction indicating an easy axis. The AMR signal for  $90^\circ$  is maximum which indicates a hard axis. The results are in perfect agreement with the results of SQUID magnetometry of Sec. 3.4.3. The noise in the AMR signal is due to the instability of the temperature during the measurement. The angular dependence can also be described by Eq. (2.12) as shown in Fig. 3.25(b). The resistivity is slightly different in (b) compared to (a) because of the different measurement time. However, the AMR amplitude ( $\rho_{\parallel} - \rho_{\perp}$ ) is nearly the same in both cases and is about  $0.025 \mu\Omega \text{ cm}$ . A slight deviation from the  $\cos^2 \theta_M$  dependence

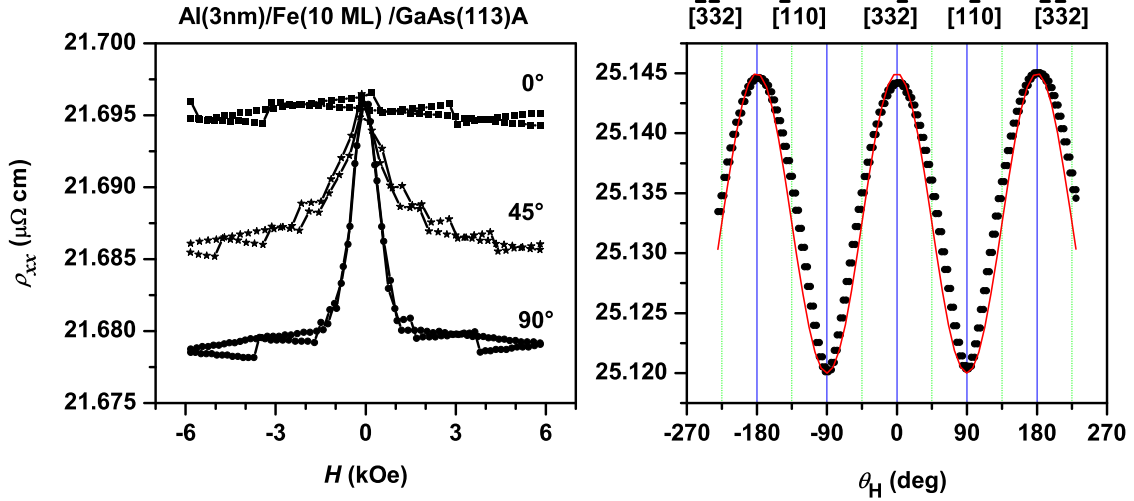


Figure 3.25: (a) Field dependence and (b) angular dependence (at high field of  $H = +2$  kOe) of AMR for a 10-ML-Fe film measured at 300 K. Here,  $0^\circ$  indicates the  $[\bar{3}3\bar{2}]$  direction, which is also the direction for current. Note that the sample is not completely saturated at  $H = +2$  kOe.

in Fig. 3.25(b) is attributed to the incomplete saturation of the magnetic moments at the applied field of 2 kOe, since along the hard axis the saturating field is about 2.5 kOe.

### 3.5.2 Planar Hall effect: *presence of an antisymmetric component*

The PHE of these Fe films on GaAs(113)A substrates are shown in Fig. 3.26 and Fig. 3.27. The PHE data of Fig. 3.26 are associated with the AMR data of Fig. 3.23. We will now

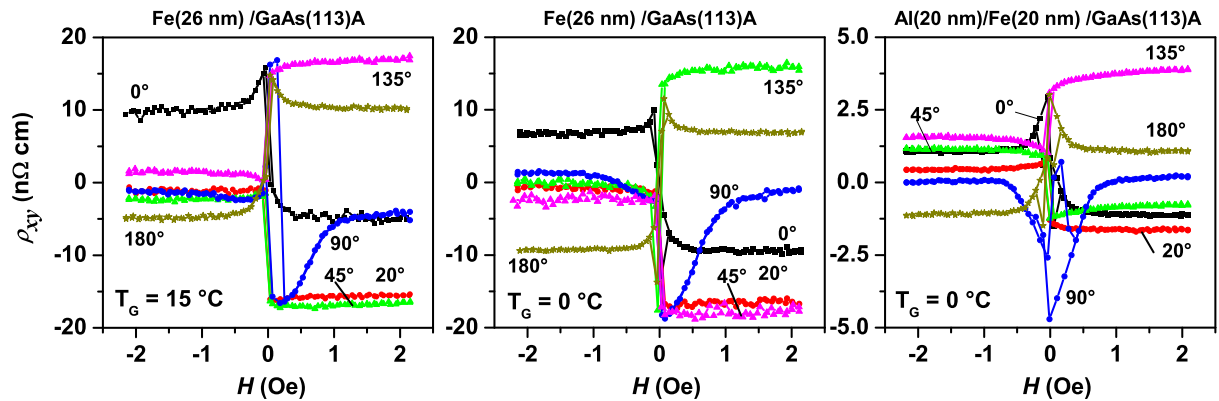


Figure 3.26: Planar Hall effect (PHE) from a set of three Fe/GaAs(113)A samples at 300 K. Here,  $\theta_H = 0^\circ$  indicates the  $[\bar{3}3\bar{2}]$  direction, which is also the direction for current. In all the samples, the presence of an antisymmetric component can be clearly seen for a magnetic field applied along any direction other than the  $\langle 110 \rangle$  axes.



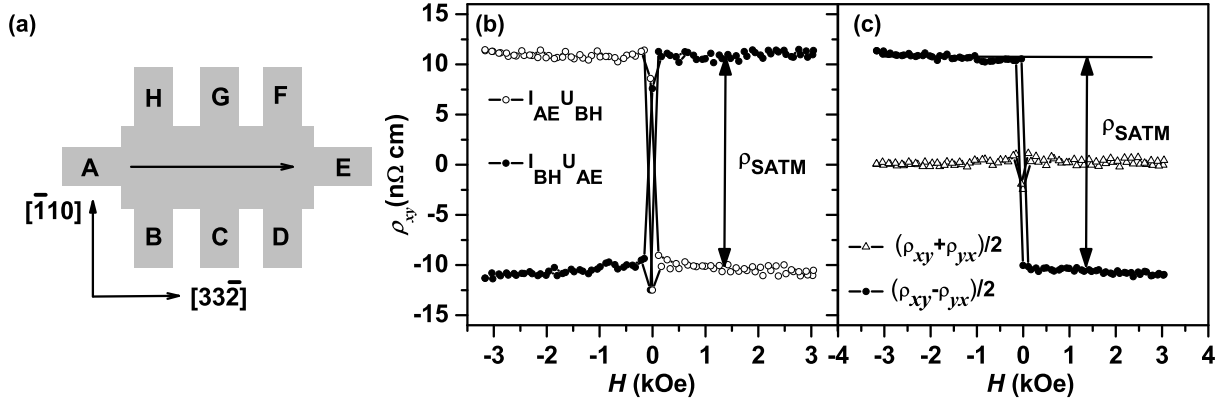


Figure 3.27: (a) Schematic presentation of the contact orientation labelled anticlockwise. The major crystallographic directions of the (113)-plane are also shown. (b) The PHE response from Fe films on GaAs(113)A at 300 K for two configurations as explained in the text. (c) Separation of the symmetric and antisymmetric contributions to the PHE.

show that the PHE described in these figures can not be described by the usual PHE Eq. (2.13) and there is an additional antisymmetric component (ASC) present in the PHE. An examination of Fig. 3.26 shows that the PHE exhibits a sign change when the direction of the applied field is reversed, for all directions other than the  $[\bar{1}10]$  axis corresponding to  $\theta_H = 90^\circ$ . This refers to an ASC in the PHE along these directions. This antisymmetry was never observed in Fe films grown on GaAs(001) substrates [146] and is completely unexpected from Eq. (2.13), which predicts only a symmetric contribution [39, 147]. However, experimentally the effect was first reported for Fe films on GaAs(113)A and GaAs(133)A substrates [64]. Since the antisymmetric component vanishes along the  $[\bar{1}10]$  axis, which is a common axis between the (001) and the (113)-plane, the phenomena must be related to the reduced symmetry of the crystal. A further confirmation of the antisymmetry can be seen in Fig. 3.27, where we measure the PHE in two configurations  $I_{AE}U_{BH}$  and  $I_{BH}U_{AE}$  with the magnetic field kept fixed along the  $[33\bar{2}]$  direction. Here, A, B, C,... etc represent different contacts to the sample as shown schematically in Fig. 3.27(a). The configurations  $I_{AE}U_{BH}$  and  $I_{BH}U_{AE}$  refer to the cases when the planar Hall voltage was measured along the contacts BH and AE for a current along AE and BH, respectively. We denote the two cases by  $\rho_{xy}$  and  $\rho_{yx}$ , respectively, by defining the positive  $x$ -axis along  $[33\bar{2}]$ . The antisymmetry requires an opposite sign for  $\rho_{xy}$  and  $\rho_{yx}$  as observed in Fig. 3.27(b). The symmetric and the antisymmetric contributions can be separated by adding and subtracting the  $\rho_{xy}$  and  $\rho_{yx}$  signals, which is shown in Fig. 3.27(c). We clearly have an additional antisymmetric contribution to the PHE superimposed onto the usual symmetric contribution of Eq. (2.13). Since the sample is completely saturated, we can rule out any contribution from the magnetic domains to this effect. We define the difference,  $\rho_{xy}(H > +H_{sat}) - \rho_{xy}(H < -H_{sat})$  as a saturated antisymmetric transverse resistivity,  $\rho_{SATM}$ , which will serve as a measure of the ASC in the following discussions.

**The role of out-of-plane misalignment** When the sample is rotated slightly out-of-plane, the contribution from the anomalous Hall effect (AHE) starts to appear as a slope

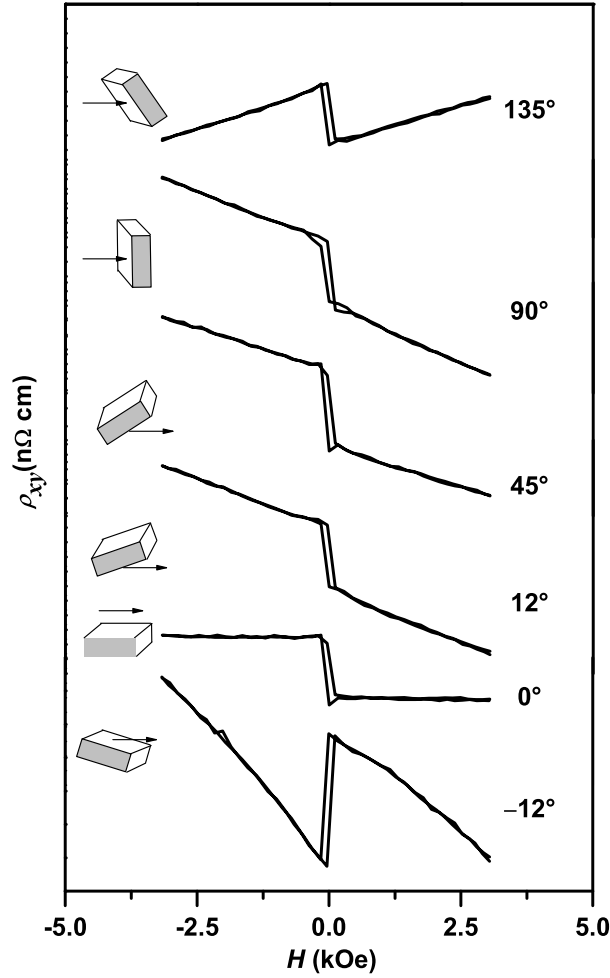


Figure 3.28: The transverse resistivity ( $\rho_{xy}$ ) from Fe films on GaAs(113)A at 300 K for different orientation of the applied field.  $0^\circ$  represents an in-plane applied field (i.e., PHE) and  $90^\circ$  represents a field applied normal to the film plane (i.e., AHE).

in the high field region as shown in Fig. 3.28 for a 26-nm-thick Fe film. As can be seen, the anomalous Hall effect simply adds to the signal but does not change  $\rho_{\text{SATM}}$ . In fact to remove the small misalignment in the sample in some cases, we have subtracted the slope of the curve at high field. Also surprising is that, when the magnetic field is applied completely out-of-plane,  $\rho_{\text{SATM}}$  does not vanish, which implies an additional effect in the AHE. This will be later discussed in the light of a phenomenological model based on the symmetry of the crystal. Nevertheless, the observed antisymmetry can not be attributed to any out-of-plane misalignment and is truly an effect arising from the symmetry of the crystal.

**Definition of the sign of the ASC** Since we are dealing with an antisymmetric contribution, the direction of the applied field relative to the current and the orientation of transverse resistivity determines the sign of  $\rho_{\text{SATM}}$ . To define the sign of  $\rho_{\text{SATM}}$ , from now on we will apply the following convention. The current is always applied along AE and the PHE is measured along BH for this direction of the current. For this configuration

Table 3.3: Summary of magnetotransport measurements of Fe films on GaAs(113)A system at 300 K.

Layer	Thick- ness	$r$	$K_1/M_s$ (Oe)	$\rho$ ( $\mu\Omega$ cm)	$(\rho_{\parallel} - \rho_{\perp})$ ( $\mu\Omega$ cm)	$\rho_{\text{PHE}}^s$ (n $\Omega$ cm)	$\rho_{\text{SATM}}^0$ (n $\Omega$ cm)	$\rho_{\text{SATM}}^1$ (n $\Omega$ cm)
Fe	26 nm	0.6	200 $\pm$ 20	11	0.06	-9.7	-15.7	8.5
Fe	26 nm	0.6	200 $\pm$ 20	10.58	0.06	-9	-14.8	7.8
Al/Fe	20 nm	0.4	200 $\pm$ 20	5.97	0.013	-2.2	-2.0	1.16
Al/Fe	1.4 nm	2.34	135	23 $\pm$ 2	0.025	-7.1	8.2	-3.5

we found a negative sign of  $\rho_{\text{SATM}}$  for Fe at 300 K with a magnetic field applied along the  $[3\bar{3}2]$  direction (see Fig. 3.26 and Fig. 3.27). Of course the sign of  $\rho_{xy}$  changes when the direction of the field is reversed by  $180^\circ$ , i.e., towards  $[\bar{3}32]$  (see plots for  $\theta_H = 180^\circ$  in Fig. 3.26). But, fortunately these two directions can be identified unambiguously from X-ray diffraction by measuring an asymmetric reflection such as GaAs(004). We can thus keep the field direction fixed along  $[3\bar{3}2]$ , which has been confirmed for all samples by XRD. The positive direction of the magnetic field was defined in such a way that the Hall voltage in this configuration is negative for an  $n$ -type semiconductor sample.

### 3.5.3 Phenomenological model

We now present a phenomenological model [38, 39] based on the symmetry of the crystal to understand the origin of the ASC observed in the PHE of single crystalline Fe films grown on low-symmetric GaAs(113)A substrates. In fact, the model to be discussed is applicable to arbitrary orientations of the films. As discussed in Sec 2.5, when a saturating field  $\mathbf{H}$  with components  $H_i = H\alpha_i$  is applied to a crystal, the relationship between the electric field  $\mathbf{E}$  and the current density  $\mathbf{J}$  is defined through the relation:

$$E_i = \rho_{ij}(\alpha)J_j, \quad (3.13)$$

where  $\rho_{ij}(\alpha)$  is the second rank magnetoresistivity tensor and  $E_i$  and  $J_j$  are components of the electric field  $\mathbf{E}$  and current density  $\mathbf{J}$ , respectively. The tensor  $\rho_{ij}(\alpha)$  depends on the direction cosines  $\alpha_i$  of the magnetization vector and hence can be expressed as a series expansion in ascending powers of the  $\alpha_i$ :

$$\rho_{ij}(\alpha) = a_{ij} + a_{kij}\alpha_k + a_{klj}\alpha_k\alpha_l + a_{klmij}\alpha_k\alpha_l\alpha_m + \dots, \quad (3.14)$$

where the Einstein summation convention is understood. The tensors with elements  $a_{ij}$ ,  $a_{kij}$ ,  $a_{klj}$ ..., simplify due to the crystal symmetry [38]. As explained in Sec. 2.5, the tensor  $\rho_{ij}(\alpha)$  being of second rank can be divided into its symmetrical  $\rho_{ij}^s$ , and antisymmetrical  $\rho_{ij}^a$ , parts and the power series of both contributions can be written as:

$$\rho_{ij}^s(\alpha) = a_{ij} + a_{klj}\alpha_k\alpha_l + \dots, \quad (3.15)$$

and

$$\rho_{ij}^a(\alpha) = a_{kij}\alpha_k + a_{klmij}\alpha_k\alpha_l\alpha_m + \dots \quad (3.16)$$

Traditionally, if one considers the leading terms (up to second order in  $\alpha_i$ ) in the above equations and neglects the higher-order terms, the associated electric fields  $\mathbf{E}_s$  and  $\mathbf{E}_a$  represent the generalized magnetoresistance and Hall effects, respectively [38, 39, 148]. Thus the PHE, for which the magnetic field is applied in-plane, should arise from  $\rho_{ij}^s$  and should also be an even function of the applied field direction. However, in our PHE experiments on Fe(113) films, we see an additional component, which is an odd function of the magnetic field direction. Consequently, this component must involve an antisymmetrical part  $\rho_{ij}^a$ .

Before proceeding further we will need to derive all the components of the magnetoresistivity tensor  $\rho_{ij}$  for the classical crystal class **m3m**, to which Fe (**Im3m**) (also Fe<sub>3</sub>Si) belong. Details can be found in Appendix A. Let us first consider the simple case of an [001]-oriented thin-film, with current  $J = (J_1, 0, 0)$  along the [100] direction. We assume that the magnetization  $\mathbf{M}$  lies in the (001) plane, making an angle  $\theta_M$  to the current. In this case the measured Hall voltage is given by:

$$E_2 = \rho_{21} J_1, \quad (3.17)$$

where the index 1, 2, and 3 refers to the  $x$ -,  $y$ - and  $z$ -axes, respectively. The  $\alpha_i$ s are given by:  $\alpha_1 = \cos \theta_M$ ,  $\alpha_2 = \sin \theta_M$  and  $\alpha_3 = 0$ . The planar Hall resistivity can be found by substituting the  $\alpha_i$ s in Eq. (A.2):

$$\rho_{21} = \frac{C_4}{2} \sin 2\theta_M, \quad (3.18)$$

which is similar to the well-known  $\sin 2\theta_M$  relation of Eq. (2.13). However, the pre-factor of  $\sin 2\theta_M$  in the above equation, i.e.  $C_4$ , is no longer equal to the AMR amplitude,  $(\rho_{\parallel} - \rho_{\perp})$ , for the single crystalline samples [149, 150]. It may be mentioned that the pre-factor  $(\rho_{\parallel} - \rho_{\perp})$  in Eq. (2.13) for polycrystalline films results from the averaging over a large number of randomly oriented crystallites [147, 149, 150]. Nevertheless, the coefficient  $C_4$  as introduced in Appendix A is a coefficient from the symmetric part of the tensor  $\rho_{ij}^s$ , and hence traditionally the PHE is attributed to an AMR effect [147, 148]. Now we consider the case of the [113]-oriented films with reduced symmetry. The measurements were performed with a current in the  $[33\bar{2}]$  direction and the Hall voltage was measured along the  $[\bar{1}10]$  direction. Thus, to find the measured planar Hall resistivity, we must perform a coordinate transformation [38, 151] of  $\rho_{21}$ . This transformation is performed in Appendix B. The final equation for the measured planar Hall resistivity in (113) films is given in Eq. (B.4) of Appendix B. If we consider terms up to third-order of  $\alpha_i$ , we can write the measured Hall resistivity for the (113) films in the following way:

$$\begin{aligned} \rho_{21}^{(113)} = & \frac{(9C_1 + 2C_4)}{22} \sin 2\theta_M + \frac{9(a_{12223} - a_{11123})}{11\sqrt{2}} \cos \theta_M \\ & - \frac{42\sqrt{2}(a_{12223} - a_{11123})}{121} \cos^3 \theta_M, \end{aligned} \quad (3.19)$$

where the coefficient  $C_1$  is also introduced in Appendix A. Here, in the symmetric part, we have considered terms up to the second order of  $\alpha_i$  as described in the first term with the well-known  $\sin 2\theta_M$  dependence. There are two additional terms which arise from

the antisymmetric part of the tensor  $\rho_{ij}^a$ . These are third-order contributions of  $\alpha_i$  and arise from the lower symmetry of the (113)-plane, in which the magnetization  $\mathbf{M}$  rotates due to the large demagnetization energy of the Fe films. The appearance of third-order contributions of  $\alpha_i$  is not surprising, since to describe the magnetoresistivity anisotropy effects, terms up to a fourth-order contribution of  $\alpha_i$  are known to be essential [152, 153]. These third-order terms in  $\alpha_i$  can be termed as a second-order Hall effect [see Eq. (3.16)]. The fourth-order terms yields additional  $\sin 2\theta_M$  and  $\sin 4\theta_M$  terms that are symmetric and are neglected for simplicity. This is justified, since to describe the experimental data, terms up to third-order, as considered in the above Eq. (3.19), are found to be sufficient.

The co-existence of even and odd terms in the component of the magnetoresistivity tensor in above Eq (3.19) has been called as Umkehr effect [154] in literature. This effect was discussed theoretically in 1975 by Akgöz *et al.* [41] based on the symmetry restrictions on the form of galvanomagnetic/thermomagnetic tensors. Experimentally, the Umkehr effect was observed in thermomagnetic effects [41, 154] and magnetotransport [155] measurements in Bismuth. As pointed out by Akgöz *et al.* [41], the effect is not restricted to the trigonal crystal structure of Antimony and Bismuth and can also be observed in cubic crystals depending on the measurement geometry as considered in the present case.

For comparison with experiment, Eq. (3.19) can also be written in the following way:

$$\rho_{xy} = \rho_s^{\text{PHE}} \sin 2\theta_M + \rho_{\text{SATM}}^0 \cos \theta_M + \rho_{\text{SATM}}^1 \cos^3 \theta_M, \quad (3.20)$$

where  $\rho_s^{\text{PHE}} = (9C_1 + 2C_4)/22$ ,  $\rho_{\text{SATM}}^0 = 9(a_{12223} - a_{11123})/(11\sqrt{2})$ , and  $\rho_{\text{SATM}}^1 = -42\sqrt{2}(a_{12223} - a_{11123})/121$ . This equation will be used in the following to interpret the experimental observations.

## Experimental agreement

The experimental agreement of the phenomenological model can be clearly seen in Fig. 3.29(b), which shows the dependence of the PHE ( $\rho_{xy}$ ) on the field orientation angle  $\theta_H$  measured at 300 K with a fixed positive saturating magnetic field ( $H = +2$  kOe). The field orientation angle  $\theta_H$  is varied from  $-220^\circ$  to  $+220^\circ$  in the plane of the sample. The high field ensures a complete saturation of the sample so that  $\theta_H = \theta_M$ . The angular dependence is completely reversible and does not follow the  $\sin 2\theta_H$  dependence of Eq. (2.13) due to the superposition of the ASC. A separation of the symmetric and antisymmetric component can be achieved by taking the sum and difference of the angular dependence of the PHE for positive and negative fields above saturation. The result is shown in Fig. 3.29(b). The symmetric part follows the well-known  $\sin 2\theta_H$  dependence of Eq. (2.13). The antisymmetric part, on the other hand, can be fitted by the equation  $\rho_{\text{SATM}}^0 \cos \theta_H + \rho_{\text{SATM}}^1 \cos^3 \theta_H$ , shown by the solid line. Thus the overall behavior of Fig. 3.29(a) can be described by the modified Eq. (3.20) of the PHE (when  $\theta_M = \theta_H$ ). The best fitting is obtained for:  $\rho_s^{\text{PHE}} = -9.7$  nΩ cm,  $\rho_{\text{SATM}}^0 = -15.6$  nΩ cm, and  $\rho_{\text{SATM}}^1 = 7.8$  nΩ cm.

At low field, the angular dependence can also be correctly reproduced by the phenomenological model. However, to produce the low-field behavior we need to model the hysteresis behavior of the sample. Using our simple SWM for magnetization rotation (see Sec. 3.4.7 and Sec 3.4.3) and the above values of  $\rho_s^{\text{PHE}}$ ,  $\rho_{\text{SATM}}^0$ , and  $\rho_{\text{SATM}}^1$  we can correctly

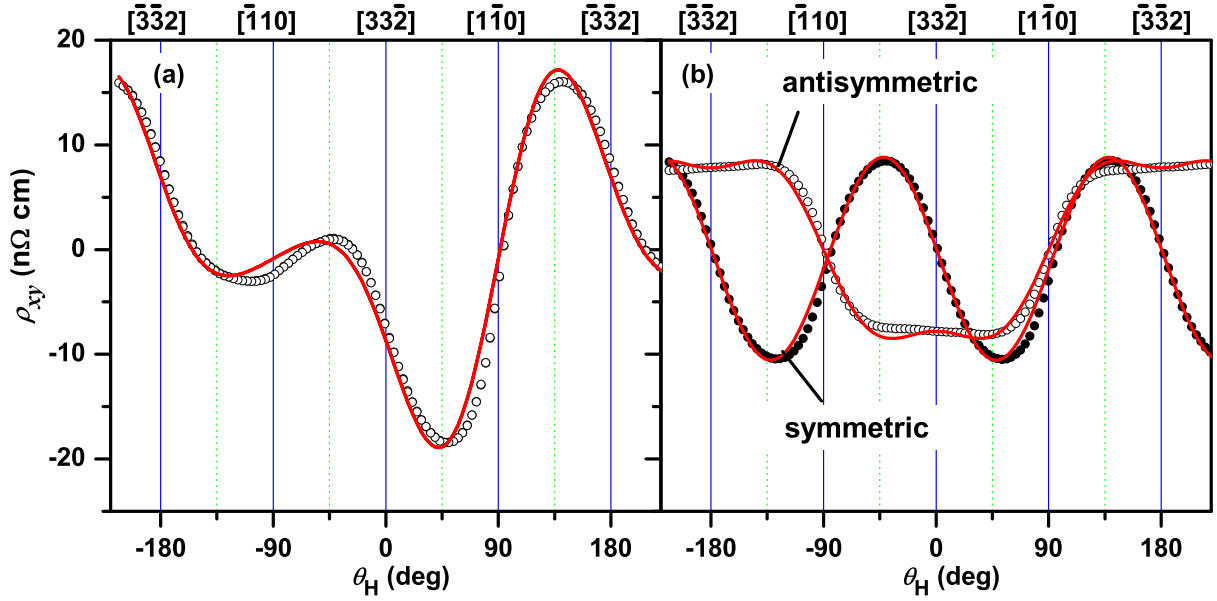


Figure 3.29: (a) Angular dependence of  $\rho_{xy}$  at 300 K of a 26-nm-thick Fe film on GaAs(113)A with a saturating in-plane magnetic field so that  $\theta_H = \theta_M$ . Open circles represent experimental data and solid line is a fit using Eq. (3.20) (see text). (b) Separation of the symmetric and antisymmetric part of the PHE. Open circles represent experimental data and solid lines are fitted curves using a  $\sin 2\theta_M$  behavior for symmetric part and  $\rho_{\text{SATM}}^0 \cos \theta_M + \rho_{\text{SATM}}^1 \cos^3 \theta_M$  type behavior for antisymmetric part.

reproduce the low-field behaviors as shown in the second column of Fig. 3.24. Other parameters used in the simulation (see Table 3.3) such as  $r$  and  $K_1/M_s$  were independently determined from AMR and SQUID magnetometry. A very good qualitative agreement with the experiment can clearly be seen.

It is also easy to show that the additional antisymmetric terms appearing in Eq. (3.20) vanish for magnetic fields applied along the  $\langle \bar{1}10 \rangle$  axes ( $\theta_M = 90^\circ$ ), and change sign with the change in the direction of the applied magnetic field along all other in-plane directions in perfect agreement with experiment.

It is also possible to show within this phenomenological approach that the classic AMR equation [Eq. (2.12)] is valid despite this low-symmetric orientation, in agreement with the experimental observations. The longitudinal resistivity,  $\rho_{xx}^{(113)}$  can be derived in the same manner:

$$\rho_{xx}^{(113)} = \rho_{11}^{(113)} \approx C_0 + \frac{9}{22}(C_1 - C_4) + \frac{126C_4 - 5C_1}{121} \cos^2 \theta_M, \quad (3.21)$$

which reproduces Eq. (2.12) for  $\rho_\perp = C_0 + 9(C_1 - C_4)/22$  and  $(\rho_\parallel - \rho_\perp) = (126C_4 - 5C_1)/121$ . This equation also provides a good explanation for the experimental observation that  $\rho_s^{\text{PHE}} \neq (\rho_\parallel - \rho_\perp)$  (see Table 3.3), which in fact is a result of the single crystalline nature of the sample.

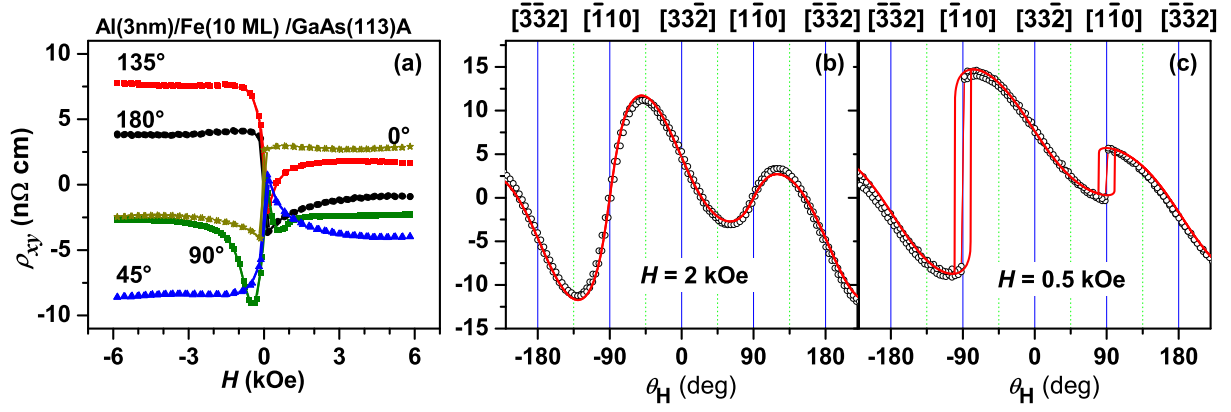


Figure 3.30: Planar Hall effect for an 10 ML-Fe(113) film at 300 K. (a) Field dependencies at different  $\theta_H$  and angular dependence with an in-plane magnetic field of (b)  $H = +2$  kOe and (c)  $H = +0.5$  kOe. Open circles represent experimental data and solid lines are calculated curves using the SWM and Eq. (3.20) (see text). The major in-plane crystallographic directions for the (113)-plane are also shown with  $0^\circ$  along  $[3\bar{3}2]$ .

### PHE in ultrathin Fe film

The PHE response from an ultrathin Fe film is shown in Fig. 3.25. The behavior is qualitatively similar to the 26-nm-thick samples in Fig. 3.26. However, the sign and magnitude of the different components are different. As shown in Fig. 3.25 and Table 3.3, the sign of  $\rho_{SATM}$  is opposite to that of the thicker films. However, this sign change is not unexpected in the phenomenological model. Because, both  $\rho_{SATM}^0$  and  $\rho_{SATM}^1$  contain the difference  $(a_{12223} - a_{11123})$ , which can be of either sign depending on the values of the either constants. Thus  $\rho_{SATM} = 2(\rho_{SATM}^0 + \rho_{SATM}^1)$  can be both positive and negative. The opposite sign implies that interface can play a significant role in determining the sign of ASC. The angular dependence in this ultrathin sample can also be well described by the Eq. (3.20) for PHE as shown in Fig. 3.30(b) and (c), where the angular dependance of PHE at applied fields of  $H = +2$  kOe and  $H = +0.5$  kOe are shown. The calculated curves shown as solid lines were obtained using the SWM for magnetization rotation as discussed before. Note that the sample is not completely saturated even at  $H = +2$  kOe.

### 3.5.4 Summary: Magnetotransport properties of Fe

1. As the most striking observation we found the presence of an antisymmetric component (ASC) in the planar Hall effect of the Fe(113) films. The ASC even changes sign with thickness of the Fe layers.
2. A phenomenological model based on the symmetry of the crystal provides a good explanation of the observed antisymmetric contribution to the PHE. The model shows that this component arises from the antisymmetric part of the magnetoresistivity tensor as a result of the reduced symmetry of the Fe(113)-plane and is basically a second order Hall effect.
3. It is shown that the observed effect can be ascribed to the Umkehr effect, which refers to the co-existence of even and odd terms in the component of the magnetoresistivity tensor.
4. The AMR of these films is found to be in agreement with the standard theory. All samples exhibit a positive value of AMR amplitude.



# Chapter 4

## Fe<sub>3</sub>Si films on GaAs(113)A substrates

A continuing problem in the field of FM/SC is the low spin injection efficiencies [19, 24, 25, 26, 156, 157, 158] into the SC from normally used FM and their alloys. As alternative materials, Heusler alloys [159] in thin film form are currently attracting much interest. In this chapter, the growth, magnetic and magnetotransport properties of the Heusler alloy Fe<sub>3</sub>Si grown on GaAs(113)A substrates will be discussed. The same orientation of GaAs(113)A was chosen for the continuity of the work performed on Fe/GaAs(113)A films. However, the main focus here is on (1) growth optimization, (2) study of the magnetic properties as a function of the composition and growth conditions, and (3) study of the dependence of the magnetotransport properties on the composition and atomic ordering in Fe<sub>3</sub>Si. The properties will also be compared with the Fe<sub>3</sub>Si films on the GaAs(001) substrates as reported recently [160, 161, 162, 163, 164, 165]. To our knowledge, the study to be presented here are the first of a Heusler alloy on a high-index semiconductor substrate. First, the properties of Fe<sub>3</sub>Si, which make it attractive for FM/SC will be discussed.

**Better thermal stability** In the preceding chapter, we discussed Fe as a FM for integration with SC substrates. Elemental ferromagnets like Fe and bcc Co or their alloys which are found to grow epitaxially on GaAs are ferromagnetic at room temperature. However, their interfaces with GaAs are thermodynamically unstable. Growth or post-growth annealing at modest temperatures lead to interdiffusion and the formation of some interfacial compounds. Relative low growth temperatures are required to suppress these interfacial reactions, which are considered to be detrimental to realize efficient spin injection from a FM into a SC [28]. For Fe or Co on GaAs, interaction and interdiffusion occur at moderate temperatures of about 200 °C [63, 89, 100, 166]. Therefore, it is highly desirable to obtain alternative FM that show improved interfacial quality as well as a higher thermal stability of the FM/SC interface. Fe<sub>3</sub>Si is one such alternative material that has been shown to have better thermal stability [163, 167, 168] compared to Fe and other elemental ferromagnets.

**Crystal structure and spin polarization** Bulk Fe<sub>3</sub>Si crystalizes in the cubic D0<sub>3</sub> structure as shown in Fig. 4.1(a). The unit cell is composed of four interpenetrating fcc sublattices A, B, C, and D, with origins at A(0, 0, 0), B(0.25, 0.25, 0.25), C(0.5, 0.5, 0.5), and D(0.75, 0.75, 0.75). In a perfectly ordered Fe<sub>3</sub>Si crystal, Fe atoms occupy the three sublattices A, B, and C, while the Si atoms fill sublattice D [169]. Fe(A,C) atoms

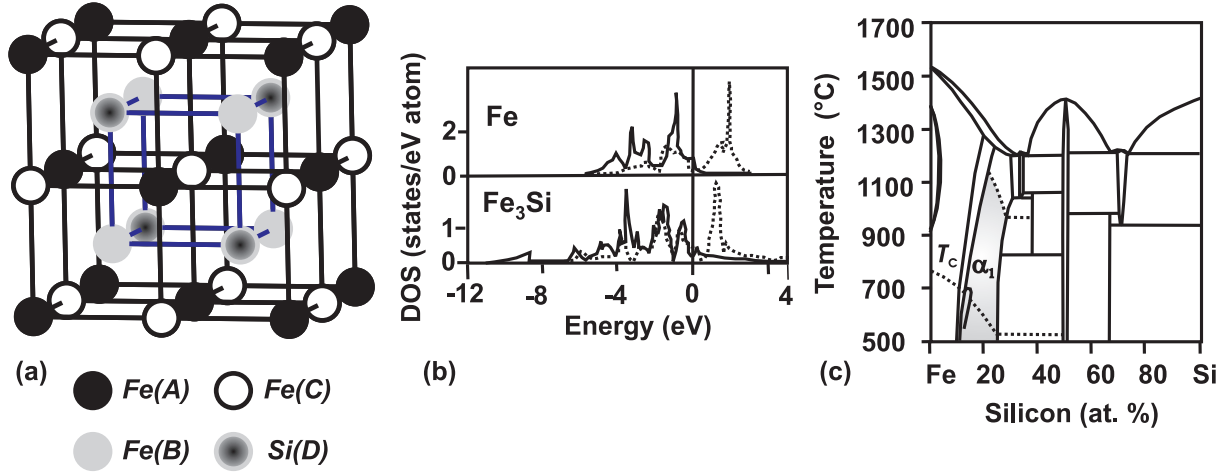


Figure 4.1: Summary of the bulk properties of  $\text{Fe}_3\text{Si}$ . (a) Ball and stick model for the bulk  $\text{Fe}_3\text{Si}$  unit cell with different sublattices. (b) The calculated density of states (DOS) of Fe and  $\text{Fe}_3\text{Si}$  for majority (closed lines) and minority (dotted lines) bands from Ref. [4]. These DOS predict no half metallic character for  $\text{Fe}_3\text{Si}$  as can be seen from the close resembles of the DOSs of the two materials. (c) The phase diagram of Fe-Si alloys from Ref [5, 6], which shows that the phase boundary of the stable  $\text{Fe}_3\text{Si}$  phase covers a range from 9 to 26.6 at.%Si (indicated in gray).

have four Fe(B) and four Si(D) first nearest neighbors and carry a magnetic moment of  $1.35 \mu_B$  per atom while Fe(B) atoms have eight Fe(A,C) first nearest neighbors and carry a magnetic moment of  $2.2 \mu_B$  per atom. Also the Si site has a magnetic moment of  $-0.07 \mu_B$  per atom [169]. Hence,  $\text{Fe}_3\text{Si}$  can be regarded as a Heusler alloy  $\text{Fe}_2\text{FeSi}$  with two distinct crystallographic and magnetic Fe sites. Heusler alloys are currently attracting much interest due to the fact that “half” Heusler alloys, which crystallize in the  $\text{C1}_b$  structure (XYZ, where X and Y are transition metals and Z is a B subgroup element, e.g.,  $\text{NiMnSb}$ ), and some of the full Heusler alloys ( $\text{X}_2\text{YZ}$ ) that crystallize in the  $\text{L2}_1$  structure, are predicted by band structure calculations to be half-metallic ferromagnets (HMFs) [170, 171, 172]. Half-metallic means that the minority-spin electrons are semi-conducting, whereas the majority-spin electrons are metallic at the Fermi level or vice versa. Consequently, these materials should be 100% spin polarized at 0 K. However, the measurement of spin-polarization of some Heusler alloy films has been disappointingly low at ( $P=58\%$  in  $\text{NiMnSb}$ , Ref. [173]) and ( $P=54\%$  in  $\text{Co}_2\text{MnSi}$ , Ref. [174]) at 4.2 K as measured by point contact Andreev reflection. It is believed that the reduced HM properties arises due to several technical issues in thin films, namely atomic ordering, surface termination and orientation, structural inhomogeneities, and nonmagnetic interfaces. A more fundamental problem is the formation of surface or interface states inside the band gap of the minority spin, as pointed out by de Wijs and de Groot [175]. The calculated density of states (DOS) [4, 176] for bulk  $\text{Fe}_3\text{Si}$ , does not predict half-metallic behavior. Indeed, the DOS of  $\text{Fe}_3\text{Si}$  shown in Fig. 4.1(b) exhibits a dip for the minority spins (dotted line) close to the Fermi level, which is just similar to Fe and hence the spin polarization should be roughly of the same order of magnitude [4] as that for Fe, i.e.,  $< 43\%$  [173].

**Easier growth control** A striking advantage of  $\text{Fe}_3\text{Si}$  is the easier control of growth, as compared to the ternary Heusler alloys. This is due to its binary nature and due to the fact that the phase stability of the  $\text{D0}_3$  ordered  $\text{Fe}_3\text{Si}$  alloy is relatively broad, with Si contents ranging from 9.5 to 26 at.% Si [5, 6] as shown in Fig. 4.1(c). The  $\text{Fe}_3\text{Si}$  phase is indicated by the gray color. Ordered  $\text{Fe}_3\text{Si}$  is nearly lattice-matched to GaAs. Additionally, the Si composition can be varied in the above range to obtain the perfect lattice match with GaAs.

**An alternative material for spin injection** As already mentioned, the room temperature spin injection from FM to SC has remained rather low. This ineffectiveness most likely results from the impedance mismatch between the high-resistance SC and the low-resistance FM in the diffusive regime [109, 177]. One way to circumvent the impedance mismatch problem is to use a tunnel barrier at the FM/SC interface [178]. The intrinsic Schottky barrier formed at the FM/SC interface [24, 26, 177] or additional insulating tunnel barriers [25, 158] represent promising options in this context, but high spin injection efficiencies are restricted to low temperatures until recently [179]. This raises the question of whether alternative FMs can be found with resistances larger than the typical value for FM's with identical or higher spin polarizations.  $\text{Fe}_3\text{Si}$  is one such candidate with spin polarization of the same order of magnitude as that for Fe. In addition, the resistance can be tuned by the Si content [162]. The high Curie temperature of 840 K [180, 181] is another big advantage of  $\text{Fe}_3\text{Si}$ . However, the spin injection efficiency as already measured for this material [182] is comparable to that previously measured for Fe films [24]. This may be due to the fact that the high resistance of  $\text{Fe}_3\text{Si}$  is still not enough to overcome the impedance mismatch problem.

The advantages to study ferromagnets on a high-index or low-symmetric substrate was discussed in Sec. 1.2 and Sec. 3.2. One major motivation came from the PHE studies of the Fe films in this orientation, where an ASC was observed due to the reduced symmetry of the [113]-orientation. The question then was whether this antisymmetry can be reproduced in other ferromagnetic thin films with the same orientation or not. In addition, the possibility of tuning the atomic ordering in  $\text{Fe}_3\text{Si}$  films by changing the composition of the films provides an additional parameter. Recently, Ishida *et al.* [183] calculated the energy band structures for thin films of  $\text{Co}_2\text{MnZ}$  ( $Z = \text{Si, Ge}$ ), the materials which are theoretically predicted HMFs in the bulk. The calculation shows that the half-metallic behavior depends sensitively on thickness, surface termination as well as surface orientation. They predict the [111]-orientated films as a better HMF compared to the [001]-orientated films. Hence, the present study of the  $\text{Fe}_3\text{Si}$  films on the [113]-orientation may be favorable for half-metallicity of the films though the statement needs to be qualified theoretically. In the following, first the growth optimization of  $\text{Fe}_3\text{Si}$  films on GaAs(113)A substrates will be discussed. In particular, we aim to achieve layers which exhibit structural properties comparable to that on GaAs(001) as reported by Herfort *et al.* [161, 162].

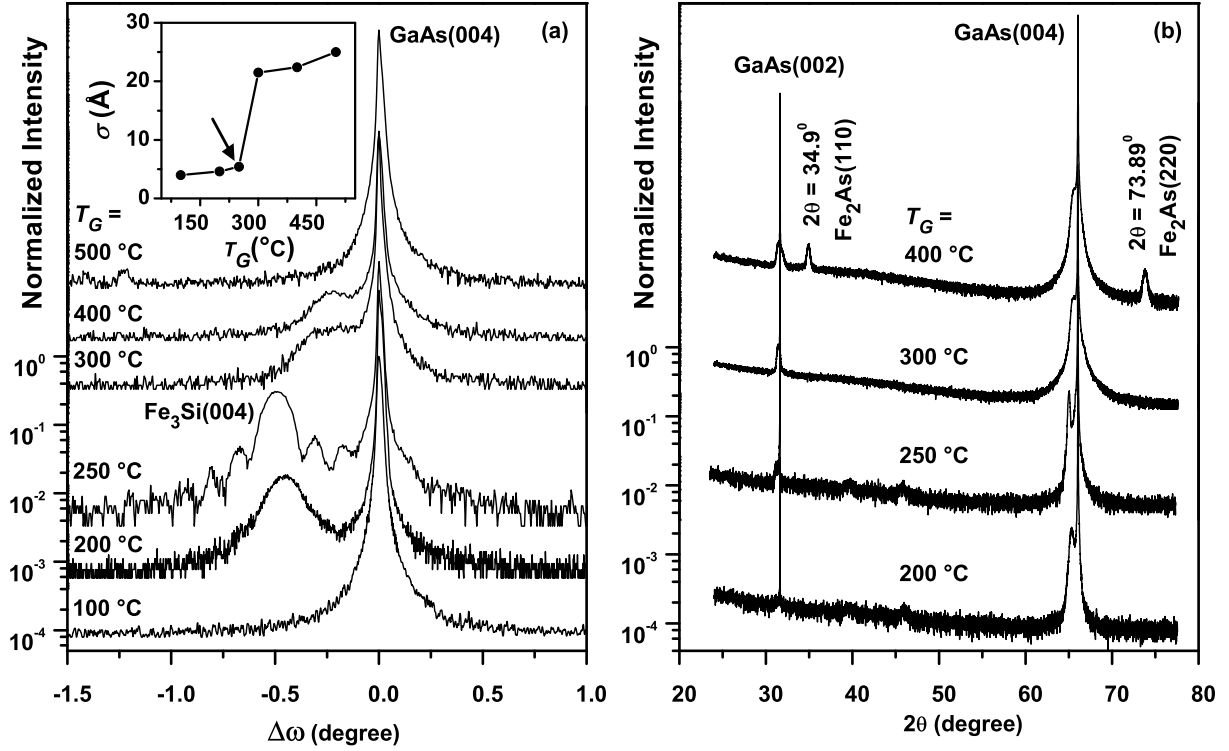


Figure 4.2: (a) Normalized *skew-symmetric*  $\omega - 2\theta$  scans for  $\text{Fe}_3\text{Si}/\text{GaAs}(113)\text{A}$  films grown at different growth temperatures  $T_G$  from 100 to 500 °C. The curves are normalized to the GaAs(004) reflection and are shifted with respect to one another for clarity. The measurements were performed with an analyzer crystal in the the diffracted beam optics. The growth rate was 0.26 nm/min. The inset shows a plot of the RMS roughness  $\sigma$  vs  $T_G$ . The arrow indicates the optimized growth temperature of 250 °C. (b) Wide-range *skew-symmetric*  $\omega - 2\theta$  scans for the same samples. The measurements were performed with an open detector.

## 4.1 Growth and structural properties

### 4.1.1 Optimization of the growth process

The growth of  $\text{Fe}_3\text{Si}$  films was performed on well-ordered As-rich GaAs(113)A templates. First, a 70-nm-thick GaAs buffer layer was prepared in a conventional III-V compound semiconductor growth chamber at a temperature of 610 °C. Similar to the case of Fe films, we chose the As-rich surface of GaAs for the growth of  $\text{Fe}_3\text{Si}$  films, which was obtained by cooling down the substrate with the As shutter open until 400 °C. The As-rich surface was chosen to avoid the formation of macroscopic defects on the surface similar to the case of Fe on GaAs(001) and GaAs(113)A substrates [63]. The growth of  $\text{Fe}_3\text{Si}$  was then performed in the separate As-free metal deposition chamber. Fe and Si were co-deposited from high-temperature effusion cells at a base pressure of  $1 \times 10^{-10}$  Torr. The following systematic approach has been adopted to optimize the growth of  $\text{Fe}_3\text{Si}$  on GaAs(113)A substrates. First we kept the Fe to Si flux ratio constant and varied the growth temperature from 100 to 500 °C. With the obtained optimum growth temperature, we then adjusted the growth rate to obtain a smooth surface morphology. Finally, to tune the Fe-Si composition, we

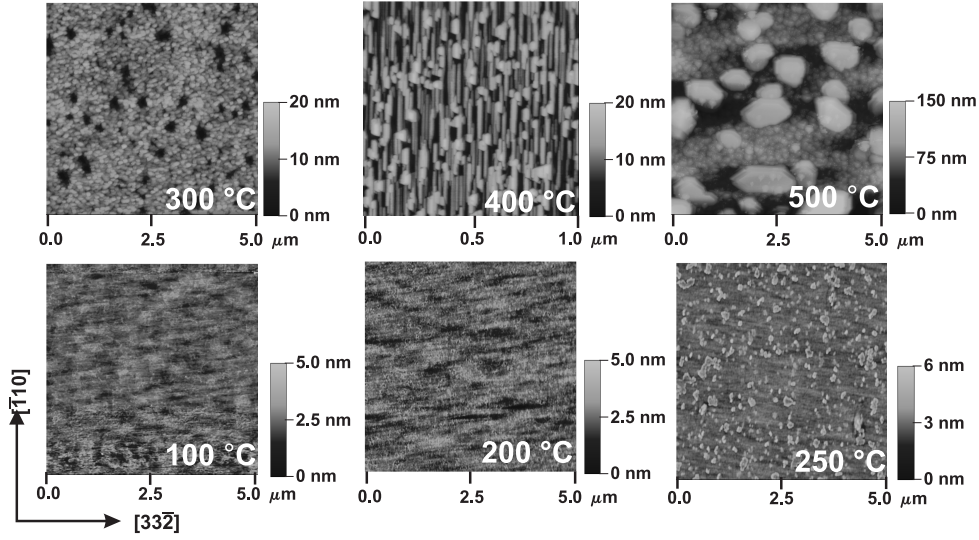


Figure 4.3: AFM images of  $\text{Fe}_3\text{Si}$  films as a function of the growth temperature. Note that the scan area of the sample grown at  $T_G = 400^\circ\text{C}$  is magnified to show the nanoscale “ripples-like” structures.

varied the Fe to Si flux ratio at these optimized growth conditions.

### Substrate temperature dependence

To obtain an optimum growth temperature, we chose an off-stoichiometric composition of the  $\text{Fe}_{3+x}\text{Si}_{1-x}$  films and varied the substrate temperature of the growth. Here  $x$  denotes the deviation from exact stoichiometry. For an off-stoichiometric composition the layer peak is well separated from that of the GaAs and this makes it easier for HRXRD studies. Figure 4.2(a) shows normalized *skew-symmetric*  $\omega - 2\theta$  scans near the GaAs(004) reflection for  $\text{Fe}_3\text{Si}$  films grown at different temperatures from 100 to 500 °C. The measurements were performed with an analyzer crystal in the diffracted beam optics with the sample tilted by  $25.24^\circ$ , the inclination angle of the (004) planes with the film plane. The *skew-geometry* for the measurement of asymmetric reflections can be found in Fig. 2.2 of chapter 2.2. The measurement in the *skew-geometry* provides a better comparison with (001)-samples. As can be seen, the sample grown at 100 °C did not show any layer peak in the  $\omega - 2\theta$  scans nor any RHEED pattern during growth, implying that the layer is amorphous. Though the samples grown at  $T_G = 200, 250, 300$ , and 400 °C show a layer peak due to the  $\text{Fe}_3\text{Si}(004)$  reflection, only the sample grown at 250 °C shows distinct interference fringes, indicating a high structural ordering and an abrupt interface. However, the temperature range where these fringes are observed is much narrower compared to that on GaAs(001) [161], indicating a narrower optimized growth temperature window on the GaAs(113)A substrates.

For the sample grown at  $T_G = 400^\circ\text{C}$ , we found additional peaks in wide-range *skew-symmetric*  $\omega - 2\theta$  scans [as shown in Fig. 4.2(b)] at  $2\theta = 34.9^\circ$  and  $2\theta = 73.9^\circ$ , which are very close to the  $\text{Fe}_2\text{As}(110)$  and  $(220)$  reflections, respectively [184]. Though the exact chemical composition for this layer at 400 °C is not known, the presence of these additional peaks indicates the formation of interfacial compounds. However, no additional

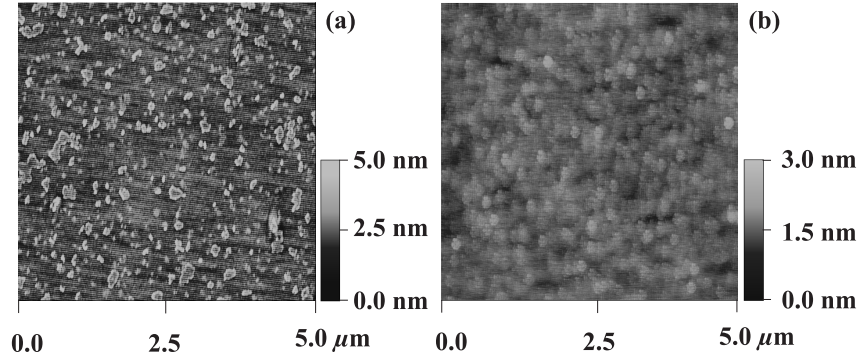


Figure 4.4: AFM images of  $\text{Fe}_3\text{Si}$  films grown at  $250^\circ\text{C}$  with growth rates of (a)  $0.26\text{ nm/min}$  and (b)  $0.13\text{ nm/min}$ , yielding RMS roughness of  $5$  and  $1.6\text{ \AA}$ , respectively.

peaks were observed for  $T_G \leq 300^\circ\text{C}$  [see Fig. 4.2(b)] indicating that the growth of  $\text{Fe}_3\text{Si}$  films on  $\text{GaAs}(113)\text{A}$  can be performed at a much higher temperature compared to  $\text{Fe}$  on  $\text{GaAs}$ . Noteworthy, the optimum growth of  $\text{Fe}_3\text{Si}$  on  $\text{GaAs}(113)\text{A}$  occurs at the same  $T_G$  (though the range is much narrower) as that for  $\text{Fe}_3\text{Si}$  on  $\text{GaAs}(001)$ , whereas for the growth of  $\text{Fe}$  films on  $\text{GaAs}(113)\text{A}$  a lower  $T_G$  was required [63] as discussed in Sec. 3.3. For the sample grown at  $T_G = 500^\circ\text{C}$ , neither a layer peak nor any additional peak was observed in the *skew-symmetric*  $\omega - 2\theta$  scans, which may be due to the three-dimensional growth mode and/or formation of other crystalline phases.

### Surface roughness and the effect of growth rate

Figure 4.3 presents AFM images of a set of samples for which  $T_G$  was varied. The RMS roughness of the films measured from these scans is plotted vs  $T_G$  in the inset of Fig. 4.2(a).  $\text{Fe}_3\text{Si}$  films with  $T_G \leq 250^\circ\text{C}$  exhibit minimal RMS roughness values of about  $5\text{--}6\text{ \AA}$  (measured over a  $5 \times 5\text{ }\mu\text{m}^2$  area). A significant increase in RMS roughness  $\sigma$  occurs for  $T_G > 250^\circ\text{C}$  in agreement with the structural degradation of the films observed in HRXRD. Interestingly the AFM images of the samples grown at  $T_G = 200$  and  $400^\circ\text{C}$  show the formation of a “nanoscale ripples-like” structures, which were not observed in the case of  $[001]$ -oriented films. These “nanoscale ripples” were found to be parallel to  $\langle 33\bar{2} \rangle$  and  $\langle \bar{1}10 \rangle$  for  $T_G = 200$  and  $400^\circ\text{C}$ , respectively. This seems to be some indication of the anisotropic growth of  $\text{Fe}_3\text{Si}$  layers on  $\text{GaAs}(113)\text{A}$  substrates, especially regarding the sample grown at  $T_G = 400^\circ\text{C}$ . In principle, this could be technologically promising. However, as discussed in the previous paragraph, the sample grown at  $T_G = 400^\circ\text{C}$  also shows the formation of interfacial compounds. The AFM image of the sample grown at even higher temperature of  $T_G = 500^\circ\text{C}$  shows the formation of a large number of pyramidal-shaped nanocrystals indicating a three-dimensional growth mode.

The RMS roughness of the films can be reduced even further by lowering the growth rate (determined from thickness calibration) of the  $\text{Fe}_3\text{Si}$  layer. This is demonstrated in Fig. 4.4, which shows AFM images of two samples grown at  $250^\circ\text{C}$  with a growth rate of (a)  $0.26$  and (b)  $0.13\text{ nm/min}$ . It should be noted that for the experiments reported before in Fig. 4.2, the growth rate was maintained at  $0.26\text{ nm/min}$ . For the lower growth rate [Fig. 4.4(b)], the RMS roughness is reduced from  $5$  to  $1.6\text{ \AA}$  (measured over a  $5 \times 5\text{ }\mu\text{m}^2$  area). Moreover, the growth rate reduction also improves the magnetic properties as

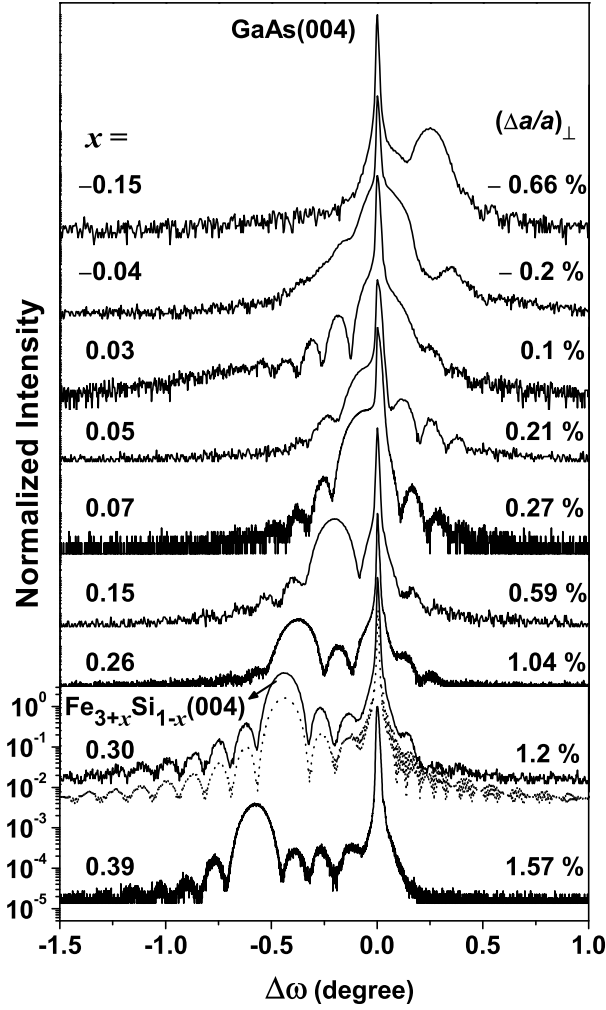


Figure 4.5: Normalized *skew-symmetric*  $\omega - 2\theta$  scans for  $\text{Fe}_{3+x}\text{Si}_{1-x}/\text{GaAs}(113)\text{A}$  films grown at 250 °C with different Si cell temperatures. The curves are normalized to the GaAs(004) reflection and are shifted with respect to each other for clarity. The dotted line shows a simulation for a sample with  $(\Delta a/a)_{\perp} = 1.2\%$ . See text and Ref [7] for simulation details.

discussed in Sec. 4.2.

#### 4.1.2 Growth of films with different composition

As already mentioned, the phase boundary of bulk  $\text{Fe}_3\text{Si}$  covers the range from 9 to 26.6 at.% Si [5, 6]. To examine the stability of the  $\text{Fe}_3\text{Si}$  phase in this range, the Fe-Si composition was varied using the above optimized growth conditions. For simplicity, we kept the Fe cell temperature constant and varied the Si cell temperature. Figure 4.5 summarizes the results of HRXRD on these samples. The  $\text{Fe}_{3+x}\text{Si}_{1-x}(004)$  peak systematically shifts with respect to the GaAs(004) substrate peak, indicating a change in lattice constant of the layers. As the Fe/Si flux ratio is varied around stoichiometry, any excess Fe will substitute into Si lattice sites and vice versa, leading to different lattice constants of the layers [169]. The perpendicular lattice mismatch  $(\Delta a/a)_{\perp}$  of the layers



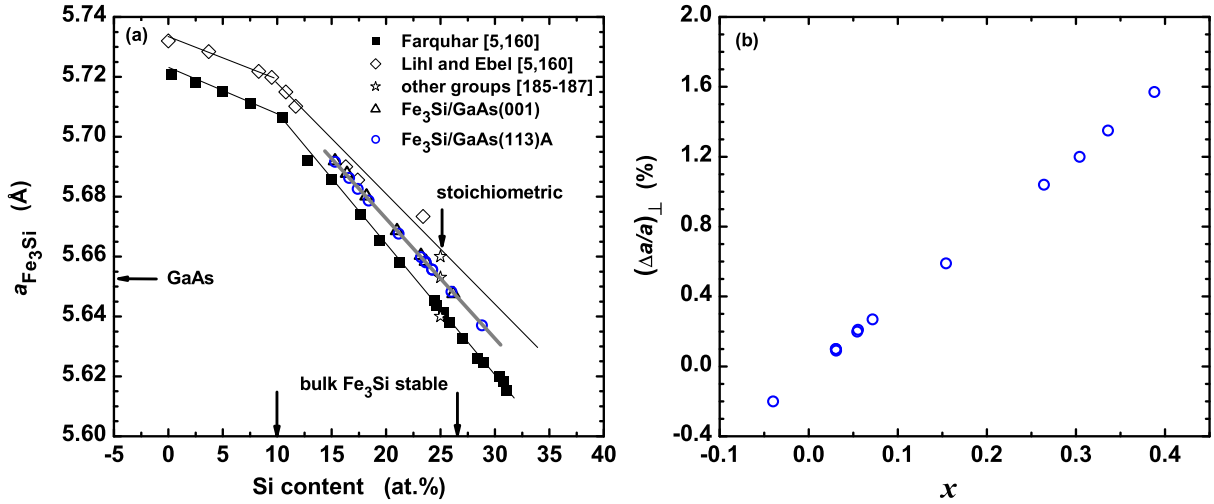


Figure 4.6: Relaxed lattice constant  $a_{\text{Fe}_3\text{Si}}$  as a function of the Si content of the  $\text{Fe}_{3+x}\text{Si}_{1-x}$  phase. Solid lines are guides for the eye. The mean value from the literature shown as the thick gray line is used to find the composition of the layers. The experimental values of  $a_{\text{Fe}_3\text{Si}}$  on GaAs(113)A substrates are shown as open circles. For comparison, the corresponding values of  $a_{\text{Fe}_3\text{Si}}$  on GaAs(001) substrates are also shown. (b) A plot of  $(\Delta a/a)_\perp$  with deviation  $x$  of  $\text{Fe}_{3+x}\text{Si}_{1-x}$  layers.

(as determined from the peak separation) was found to vary from 1.6 % to  $-0.66$  %. For a quantitative comparison, we have included a simulation of the rocking curve using the Takagi-Taupin formalism for the  $\text{Fe}_3\text{Si}$  layer with  $(\Delta a/a)_\perp = 1.2$  %. The thickness of the films was used as a fitting parameter. For the simulation in the *skew-geometry*, the (004) reflection of GaAs(113) was approximated by the symmetric (004) reflection of GaAs(001). For the dynamical X-ray diffraction formalism used in this simulation, see Ref [7]. The agreement with experiment is excellent. In fact the simulation was used to determine the thickness of the layer in conjunction with XRR simulation. The FWHM along the (004) Bragg reflection of the layer is as low as  $0.14^\circ$  for this 40-nm-thick film. The high crystal and interface qualities of these films are again reflected by the presence of the interference fringes for all samples. However, with increasing Si content, a slight degradation of the films is observed, which becomes apparent from the reduced number of interference fringes in the uppermost curves of Fig. 4.5.

**Determination of the composition of the layers** An accurate determination of the exact composition of the  $\text{Fe}_{3+x}\text{Si}_{1-x}$  layers from the HRXRD results is rather difficult due to the complex Fe-Si phase diagram and discrepancies in the published data of the relaxed lattice constants  $a_{\text{Fe}_3\text{Si}}$  of the  $\text{Fe}_{3+x}\text{Si}_{1-x}$  phase [5, 6, 160, 185, 186, 187]. In Fig. 4.6(a), we have plotted  $a_{\text{Fe}_3\text{Si}}$  as a function of the Si content and have summarized results from the literature including the results of  $\text{Fe}_3\text{Si}/\text{GaAs}(001)$ . In order to get an estimate of the composition of our layers, we have applied the method described in Ref [161]. First, we calculated  $a_{\text{Fe}_3\text{Si}}$  using  $(\Delta a/a)_\perp$  from the HRXRD rocking curves of Fig. 4.5, taking into account the elastic constants  $C_{11} = 219$  GPa and  $C_{12} = 143$  GPa of  $\text{Fe}_3\text{Si}$  [188]. All layers were found to be tetragonally distorted with a parallel lattice mismatch of less



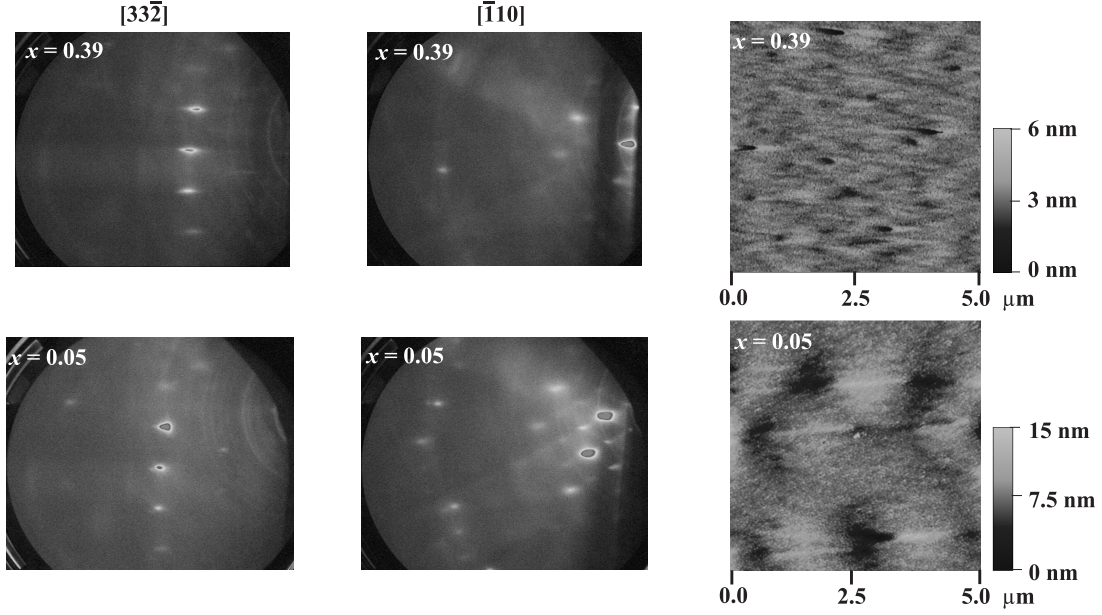


Figure 4.7: Results of RHEED and AFM experiments on  $\text{Fe}_{3+x}\text{Si}_{1-x}$  samples with composition  $x = 0.39$  (first row) and  $x = 0.05$  (second row). The first and second column represent the RHEED pattern of the  $\text{Fe}_{3+x}\text{Si}_{1-x}$  films taken immediately after growth along  $[33\bar{2}]$  and  $[\bar{1}10]$ , respectively, alongside *ex situ* AFM images (third column).

than 0.05 %, as evidenced by HRXRD profiles of asymmetric (004) Bragg reflections in GI geometry (not shown here). Hence the relaxed lattice constant of the layer was determined using Eq. 2.3 of chapter 2.2. We then placed the values of the relaxed lattice constant  $a_{\text{Fe}_3\text{Si}}$  on the gray line, which represents the mean value of the previously published data for bulk  $\text{Fe}_{3+x}\text{Si}_{1-x}$  in the range between 10 and 30 at.% Si. As shown in Fig. 4.6(a) the Si content obtained from this method was found to be in the range of 15–26 at.%, which lies within the phase boundary of the bulk  $\text{Fe}_3\text{Si}$  phase covering a range from 9 to 26.6 at.% Si [5, 6]. The Si content can also be expressed in terms of the parameter  $x$  in  $\text{Fe}_{3+x}\text{Si}_{1-x}$  layers as indicated in Fig. 4.5, which will be used henceforth to denote the Si content of the films. Fig. 4.6(b) shows the correlation of  $x$  with  $(\Delta a/a)_\perp$ . Thus films with exact stoichiometry can be obtained for lattice-matched films.

**Layer quality as a function of composition** As already mentioned in connection with the discussion of Fig. 4.5, the film quality slightly degrades with increasing Si content of the  $\text{Fe}_{3+x}\text{Si}_{1-x}$  films. This was also observed in the RHEED and AFM experiments as shown in Fig. 4.7. The figure shows the RHEED patterns (first two columns) and the AFM images (third column) of two  $\text{Fe}_{3+x}\text{Si}_{1-x}$  films with  $x = 0.39$  and  $x = 0.05$ . The RHEED patterns were taken immediately after growth along  $[33\bar{2}]$  and  $[\bar{1}10]$ , respectively. The basic geometric structure of the RHEED patterns is similar to that of Fe films on GaAs(113)A substrates. However, the RHEED pattern for higher Si content become spottier, indicating a rough surface morphology. This can be clearly seen from the AFM images of the third column. In fact the RMS roughness (measured over a  $5 \times 5 \mu\text{m}^2$  area) increases slightly with decreasing  $x$  as shown in Fig. 4.8(a). For comparison, data from  $\text{Fe}_{3+x}\text{Si}_{1-x}$  films on GaAs(001) grown in parallel with those on GaAs(113)A are also shown.

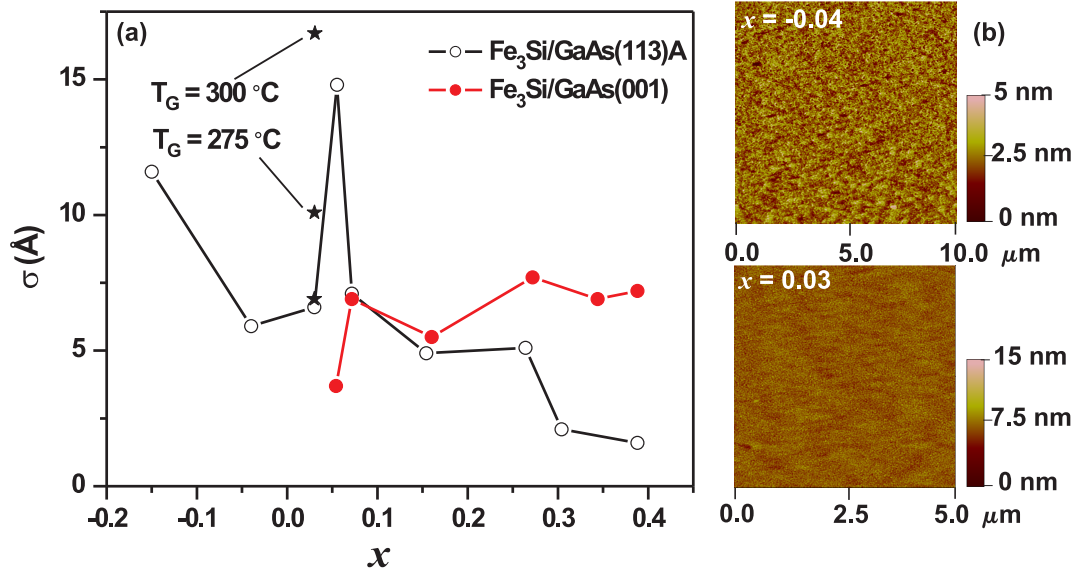


Figure 4.8: (a) AFM RMS roughness  $\sigma$  (measured over a  $5 \times 5 \mu\text{m}^2$  area) as a function of the composition  $x$  of the films. All samples were grown at  $250^\circ\text{C}$  except those shown as  $\star$ . (b) The AFM images of the most stoichiometric samples with  $x = 0.03$  and  $x = -0.04$  exhibit an RMS roughness of about  $6.5 \text{ \AA}$ . The sample with  $x = -0.04$  was found to be rather inhomogeneous.

Samples near stoichiometry ( $x \approx 0$ ) exhibit a reasonable RMS roughness of about  $6.5 \text{ \AA}$ . Nevertheless, this implies that the optimized growth conditions may be slightly different for samples with higher Si content. Hence, to check the optimized growth conditions near stoichiometry, we slightly vary the growth temperature from  $250$  to  $300^\circ\text{C}$ . The results are also included in Fig. 4.8(a), where the symbol ‘big star’ represents a set of three samples with  $x = 0.03$  for growth temperatures as indicated. A clear increase in RMS roughness with increasing  $T_G$  can be seen, which implies that the optimized growth conditions for stoichiometric samples must be near the growth temperature of  $250^\circ\text{C}$ . A growth temperature below  $250^\circ\text{C}$  was not examined since the crystal quality was found to degrade at lower temperatures as discussed in Sec. 4.1.1. Nevertheless, the most stoichiometric samples with  $x = 0.03$  and  $x = -0.04$  show a smooth surface morphology as shown in Fig. 4.8(b). The RMS roughness of about  $6.5 \text{ \AA}$  is a reasonable value though a bit higher compared to that of the films on  $\text{GaAs}(001)$  substrates.

We note that the RMS roughness of the sample with  $x = -0.04$ , when measured over a  $500 \times 500 \mu\text{m}^2$  area rather than our standard  $5 \times 5 \mu\text{m}^2$ , increased from  $6.5$  to  $15 \text{ \AA}$ . The HRXRD measurements also show inhomogeneities in composition for different pieces of this sample with  $x = -0.04$ . The RHEED pattern also shows some additional spots and becomes very complex. This complex RHEED pattern and the inhomogeneities in composition were observed for samples with negative  $x$ , i.e.,  $x = -0.04$ , and  $-0.15$ . This is attributed to the appearance of a different  $\text{Fe}_x\text{Si}_y$  phase, similar to films on  $\text{GaAs}(001)$  [161].

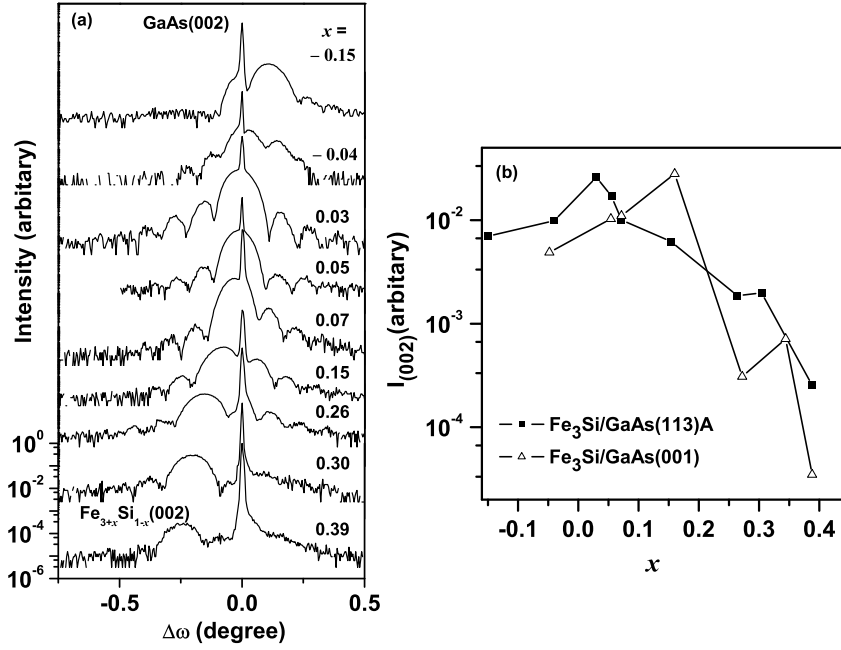


Figure 4.9: (a) Normalized *skew-symmetric*  $\omega - 2\theta$  scans of  $\text{Fe}_3\text{Si}/\text{GaAs}(113)\text{A}$  for the superlattice (002) reflection. The curves are normalized to the GaAs(002) reflection and are shifted with respect to each other for clarity. (b) Intensity of (002) reflection  $I_{(002)}$ , as a function of the composition  $x$  for  $\text{Fe}_{3+x}\text{Si}_{1-x}$  films on GaAs(113)A and (001) substrates.

#### 4.1.3 Study of long-range atomic ordering in $\text{Fe}_{3+x}\text{Si}_{1-x}$ films

In the following discussion, we examine whether the cubic  $\text{D0}_3$  structure of Fig. 4.1(a) is achieved in our samples or not. This structure is comprised of four interpenetrating fcc sublattices. Bragg reflections for this structure are produced by either all odd or all even Miller indices ( $h, k, l$ ) with the following three structure amplitudes [189, 190]:

$$\begin{aligned} F_1 &= 4|(f_A - f_C)^2 + (f_B - f_D)^2|^{1/2}, \text{ for } h, k, l \text{ all odd} \\ F_2 &= 4|f_A - f_B + f_C - f_D|, \text{ for } h, k, l \text{ all even and } h + k + l = 4n + 2 \\ F_3 &= 4|f_A + f_B + f_C + f_D|, \text{ for } h, k, l \text{ all even and } h + k + l = 4n, \end{aligned} \quad (4.1)$$

where  $f_A, f_B, f_C$ , and  $f_D$  are average scattering factors for the atoms in the respective sublattices and  $n$  is an integer. For  $\text{Fe}_3\text{Si}$ , the D sublattice is occupied by Si atoms so that  $f_A = f_B = f_C = f_{\text{Fe}}$  and  $f_D = f_{\text{Si}}$ . Hence, the structure amplitudes can be rewritten in the following way:

$$\begin{aligned} F_1 &= 4|f_{\text{Fe}} - f_{\text{Si}}| \\ F_2 &= 4|f_{\text{Fe}} - f_{\text{Si}}| \\ F_3 &= 4|3f_{\text{Fe}} + f_{\text{Si}}|. \end{aligned} \quad (4.2)$$

The reflections for which  $h, k, l$  are all even with  $(h+k+l) = 4n$  are fundamental reflections and are unaffected by the state of ordering. The reflections for which  $h, k, l$  are all even with  $(h+k+l) = 4n + 2$  are sensitive to a (A,C)  $\longleftrightarrow$  D disorder whereas the reflections with odd  $h, k, l$  are sensitive to both B  $\longleftrightarrow$  D and (A, C)  $\longleftrightarrow$  D disorder [169, 190, 191].

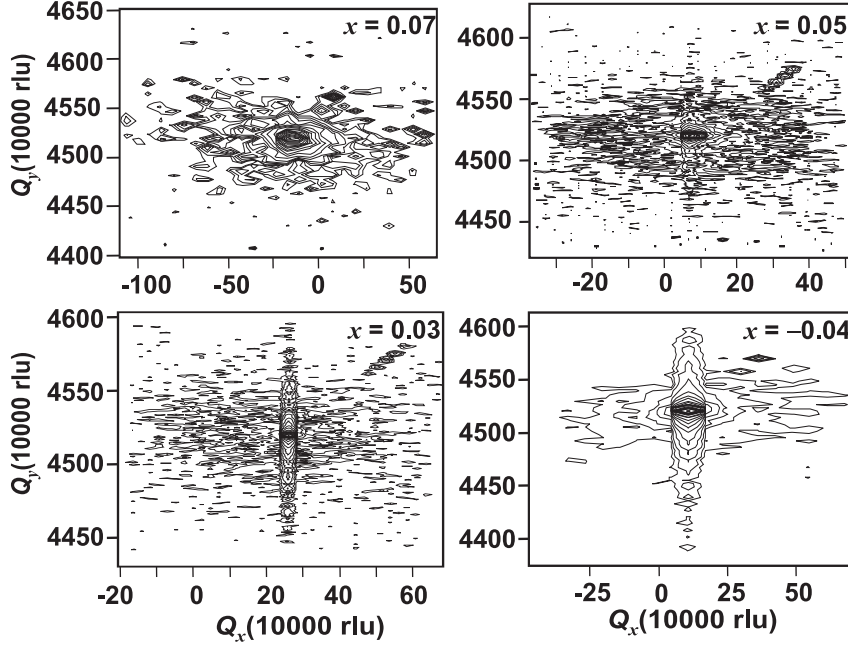


Figure 4.10: X-ray reciprocal space maps of stoichiometric  $\text{Fe}_3\text{Si}$  films grown on GaAs(113)A substrates for the symmetric and superlattice (113) reflection of GaAs. The reciprocal lattice units (rlu) are  $\lambda/2d$ , where  $\lambda$  is the wavelength of  $\text{CuK}_{\alpha 1}$  radiation and  $d$  is the lattice plane spacing of the corresponding reflection. The presence of interference fringes for the most stoichiometric samples indicate the presence of the (113) reflection.

The relative intensities of these two classes of superlattice reflections depend on the state of ordering. But for a perfectly ordered lattice, the intensities should be equal as implied by Eq. (4.2) [189, 191, 192]. For example, the (002) and the (113) reflections should have the same intensity for a perfectly ordered  $\text{Fe}_3\text{Si}$  lattice.

To investigate the crystal or atomic ordering of the  $\text{Fe}_3\text{Si}$  films on GaAs(113)A, we have performed HRXRD measurements using PANalytical X'Pert diffractometer. We analyze different superlattice reflections, similarly to recent studies of long-range ordering of  $\text{Fe}_3\text{Si}$  films on GaAs(001) [192]. The two superlattice (002) and (113) reflections were examined as a function of the composition  $x$  of the  $\text{Fe}_{3+x}\text{Si}_{1-x}$  films. The results are summarized in Fig. 4.9 and Fig. 4.10. We found an increase in the intensity of the (002) reflection with increasing Si content as shown in Fig. 4.9(b). The substrate reflection GaAs(002) is used as a reference to find the intensity  $I_{(002)}$  of the (002) layer reflection. For comparison, the intensities of the  $\text{Fe}_3\text{Si}(001)$  films grown in parallel are also shown. The behavior for both orientations is qualitatively similar, though in some cases, [113]-oriented samples exhibit slightly higher  $I_{(002)}$ . The superlattice and symmetric (113) reflections with odd  $h, k, l$  was detectable only for the most stoichiometric samples with  $x = 0.05, 0.03$  and  $-0.04$  as shown in Fig. 4.10. A slight increase in the intensity of the (113) reflection is also observed from  $x = 0.05$  to  $-0.04$ . Here, we use RSM since the layer peak is very close to the substrate peak as a result of which the layer peak was not detectable in normal symmetric  $\omega - 2\theta$  scans. In Fig. 4.10, the distinction of the layer peak from the substrate peak (for the samples with  $x = 0.05, x = 0.03$  and  $-0.04$ ) is not very clear. This is due to the fact that the GaAs(113) reflection itself is rather broad and the layer peak is very

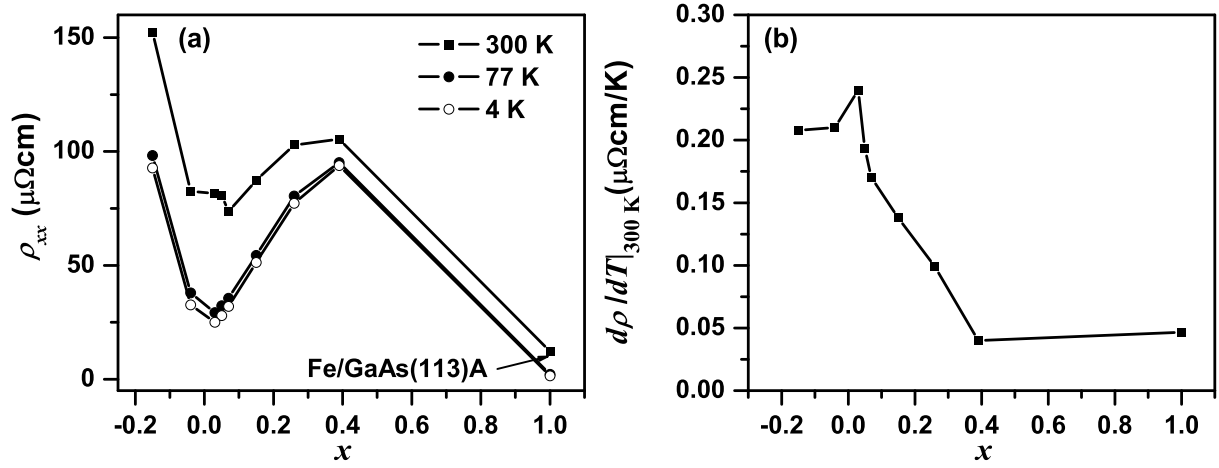


Figure 4.11: (a) Resistivity  $\rho$  as a function of composition  $x$  for the  $\text{Fe}_{3+x}\text{Si}_{1-x}$  alloys at 300 K, 77 K and 4 K. (b)  $(d\rho/dT)|_{300\text{ K}}$  as a function of composition  $x$  for the  $\text{Fe}_{3+x}\text{Si}_{1-x}$  alloys.

close to that of the substrate peak. However, the interface fringes can be easily identified, indicating the presence of the layer reflection. Thus we observe an improvement in the long-range ordering of the lattice with increasing Si content. The observation of the (002) and (113) superlattice reflections for the stoichiometric samples indicates the formation of the  $\text{D0}_3$  crystal structure. The intensity of the (113) reflection of the layer was found lower compared to the (002) reflection in all samples, indicating a finite disorder even in the most stoichiometric samples. However, a quantitative information regarding the amount of disorder has not yet been obtained, since the determination of the intensity of the (113) reflection was not very accurate given the weak distinction of the layer and substrate peaks in the RSM of Fig. 4.10.

#### 4.1.4 Electrical Resistivity

The atomic ordering of the  $\text{Fe}_3\text{Si}$  lattice described in the previous section was found to be reflected in resistivity measurements. Figure 4.11 presents a series of resistivity measurements performed on a set of  $\text{Fe}_{3+x}\text{Si}_{1-x}$  layers with varying compositions  $x$ . The resistance of the samples was measured on Hall bar structures at temperatures ranging from 4 K to 300 K. The thickness determined from the XRR/HRXRD measurements was used to calculate the resistivity  $\rho$ . The resistivity of the samples is expressed as function of the composition  $x$ . The data for  $x = 1$  represents a 26-nm-thick Fe film grown on GaAs(113)A substrates. As can be seen in Fig. 4.11(a), irrespective of the temperature, the resistivity  $\rho$  first increases with increasing Si content until  $x = 0.3$ . However with further increase of the Si content,  $\rho$  shows a strong decrease and a minimum is reached around the exact stoichiometry. For even higher Si contents  $\rho$  drastically increases again. This behavior is very similar to that of bulk samples [193] and that of  $\text{Fe}_3\text{Si}$  films on GaAs(001) substrates [162]. The values of resistivity of the stoichiometric samples at room temperature are slightly larger than those for bulk  $\text{Fe}_3\text{Si}$  [193], and those for  $\text{e}_3\text{Si}$  films on GaAs(001) substrates [162].

The above behavior of resistivity  $\rho$  with composition  $x$  can be understood in terms of

the Fe-Si site disorder information of the previous subsection. The electrical resistivity of metals is governed by phonon and impurity or alloy scattering mechanisms. To a first approximation, these two scattering mechanisms give additive contributions to the resistivity:

$$\rho(T) = \rho_0 + \rho_p(T), \quad (4.3)$$

where  $\rho_0$  is the residual resistivity due impurity or alloy scattering mechanisms and  $\rho_p(T)$  is the pure metal resistivity at temperature  $T$  due to scattering by phonons. The residual resistivity  $\rho_0$  is assumed to be temperature independent. In  $\text{Fe}_{3+x}\text{Si}_{1-x}$ ,  $\rho_0$  reflects the alloy scattering from the Si sites. As shown in the previous section, the long-range order in  $\text{Fe}_3\text{Si}$  strongly depends on their stoichiometry. Near stoichiometry, the layers are ordered and hence a decrease of the residual resistivity is expected as observed in the experiment. When Si atoms are added to pure Fe, the resistivity rapidly increases due to the enhancement of alloy scattering with the Si atoms acting as random impurities. The increase in the resistivity is suppressed beyond  $x = 0.3$ , when atomic ordering begins to occur. While the ordering is established the resistivity turns from the local maximum around  $x = 0.3$  to the minimum at the perfect ordering for stoichiometric  $\text{Fe}_3\text{Si}$ . Since in this case alloy scattering is strongly reduced and phonon scattering, which is more strongly temperature dependent, comes into play. The plot of  $d\rho/dT|_{300\text{ K}}$  vs  $x$  in Fig. 4.11(b) further supports this assumption. In fact  $d\rho/dT|_{300\text{ K}}$  is proportional to phonon scattering, which exhibits a strong temperature dependence. The observation of a peak in  $d\rho/dT|_{300\text{ K}}$  for the stoichiometric (ordered) samples clearly shows the reduction of alloy scattering and the enhancement of the phonon scattering.

#### 4.1.5 Summary of structural properties

1. The growth of the  $\text{Fe}_3\text{Si}$  films on GaAs(113)A substrates has been optimized at 250 °C with a low growth rate of 0.13 nm/min to obtain films with structural properties comparable to that on GaAs(001) substrates.
2. The layers grown under these conditions maintain the [113]-orientation of the GaAs substrate similar to Fe films but exhibit high crystal quality with a smoother interface/surface.
3. Long-range atomic ordering was found in the as-grown nearly stoichiometric films, reflecting the  $\text{D0}_3$  crystal structure. The long-range atomic ordering of the films leads to a lower resistivity.
4. Most of the structural properties were found to be very similar to those of the films on GaAs(001), except for some samples grown at  $T_G = 200$  and 400 °C which show the formation of "nanoscale ripples-like" structures.

## 4.2 Magnetic properties

### 4.2.1 Effect of growth conditions on magnetic anisotropy

In this subsection, we will demonstrate the requirement of optimized growth conditions to obtain thin films with superior magnetic properties. Figure 4.12 presents SQUID

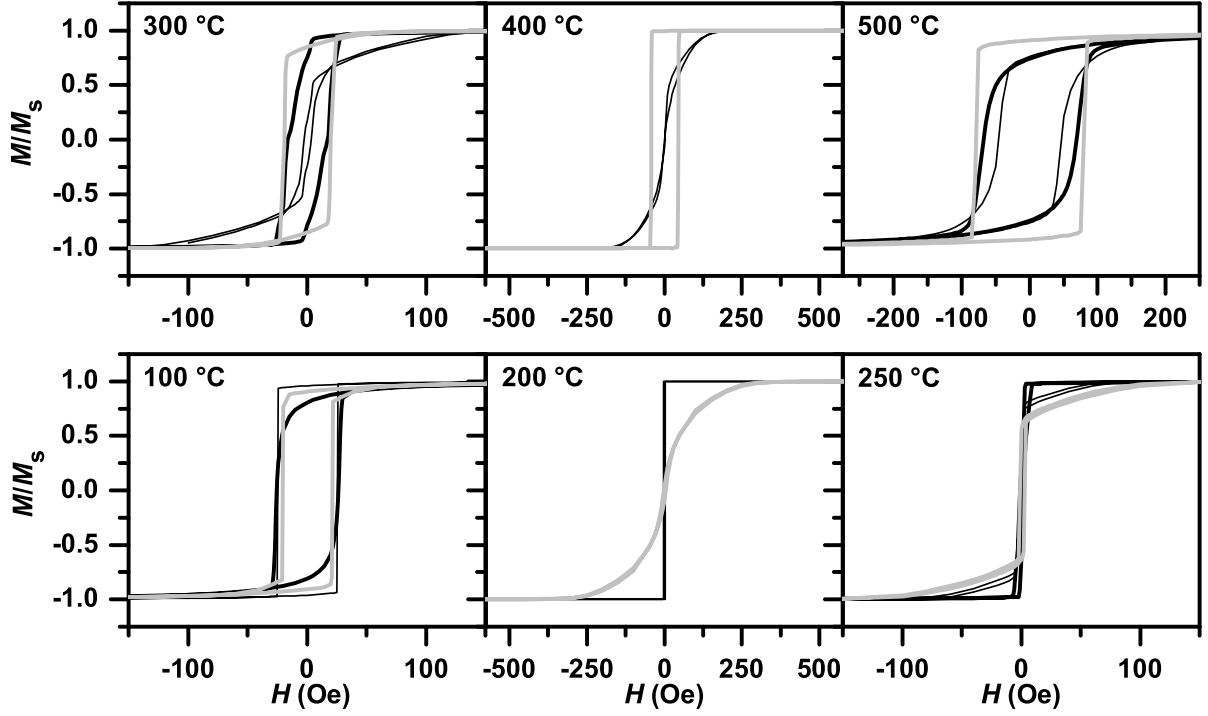


Figure 4.12: Magnetic properties of  $\text{Fe}_{3+x}\text{Si}_{1-x}$  films grown on GaAs(113)A at different of growth temperature  $T_G$  for a composition near  $x = 0.3$ . The thickness of the films is in the range 40–45 nm. The magnetization curves were measured at 300 K along  $[3\bar{3}2]$  (thin black),  $[03\bar{1}]$  (thicker black) and  $[\bar{1}10]$  (thick gray).

magnetization curves taken along various crystallographic directions for a set of  $\text{Fe}_{3+x}\text{Si}_{1-x}$  samples with  $x = 0.3$ , thickness about 40–45 nm—grown at different growth temperature  $T_G$ . The samples correspond to those shown in Fig. 4.2 and Fig. 4.3 of the previous section. As can be seen, all the samples exhibit ferromagnetism at room temperature with well-developed hysteresis. Let us first focus on the magnetization curves of the sample with best structural properties, i.e., the sample grown at  $T_G = 250$  °C. Clearly the magnetization curves exhibit an in-plane four-fold magnetic anisotropy, with the easy axis along the  $\langle 03\bar{1} \rangle$  directions. The two major in-plane crystallographic inequivalent directions, namely  $[3\bar{3}2]$  and  $[\bar{1}10]$ , are magnetically equivalent and are intermediate axes of magnetization. The observation is similar to that of thick Fe films on GaAs(113)A substrates, and hence the in-plane four-fold magnetic anisotropy in this sample can be understood in the same way, i.e., from the cubic magnetocrystalline anisotropy and large demagnetization energy of these films.

However, the magnetic anisotropy changes drastically for lower as well as higher  $T_G$ . The samples grown at  $T_G = 200$  °C and 400 °C exhibit a UMA with opposite easy axes. For the sample grown at  $T_G = 200$  °C the easy axis lies along  $[3\bar{3}2]$ , whereas for the sample grown at 400 °C the easy axis reorients to the  $[\bar{1}10]$  axis. For the sample grown at  $T_G = 100$  °C, the magnetic anisotropy is not very clear but shows the signature of the UMA present in the sample with  $T_G = 200$  °C. Similarly, the sample grown at 300 °C shows a magnetic anisotropy that is somewhat in between that of samples grown at 250 and 400 °C. The last sample with  $T_G = 500$  °C does not exhibit any clear magnetic

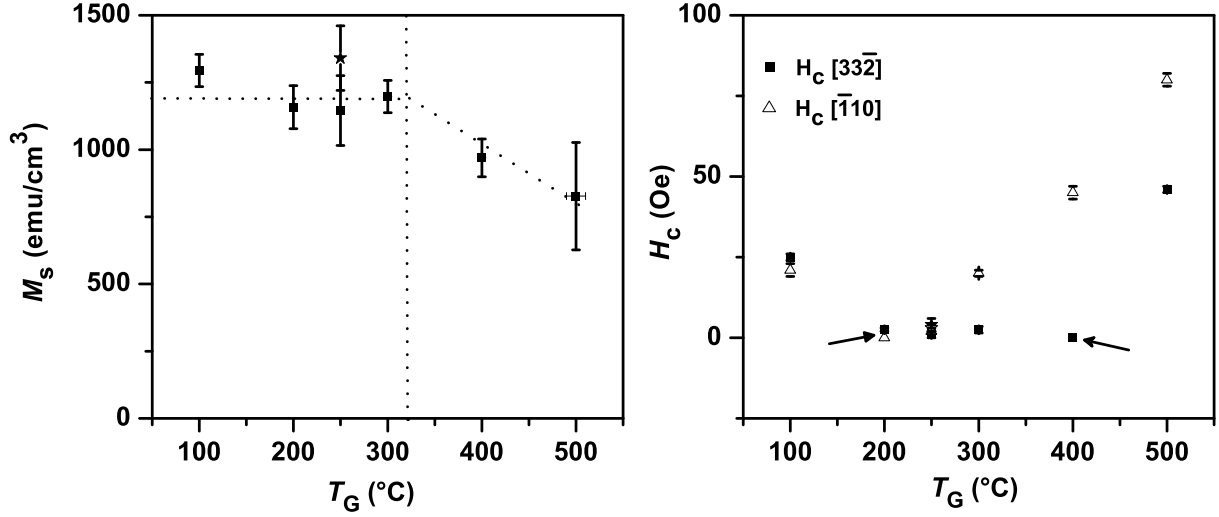


Figure 4.13: Saturation magnetization  $M_s$  and coercive field  $H_c$  of the  $\text{Fe}_{3+x}\text{Si}_{1-x}$  films as a function of  $T_G$  for a composition near  $x = 0.3$ . A minimum coercive field and an optimum value of the saturation magnetization are achieved near the optimized growth temperature  $T_G = 250$   $^\circ\text{C}$ . The arrow indicates samples with UMA whereas the dotted lines are guides to eye. The growth rate was maintained at 0.26 nm/min except the symbol ( $\star$ ) which indicates data for a sample grown at 250  $^\circ\text{C}$  with a growth rate of 0.13 nm/min.

anisotropy but shows some signature of the UMA of the sample with  $T_G = 400$   $^\circ\text{C}$ .

The magnetic properties as a function of  $T_G$  are summarized in Fig. 4.13, where a plot of saturation magnetization  $M_s$  and coercive field  $H_c$  versus  $T_G$  are shown. As can be seen, the coercive field shows a minimum for the optimized growth temperature  $T_G = 250$   $^\circ\text{C}$ , and increases rapidly for higher growth temperatures, indicating a degradation of the layer quality in agreement with AFM and HRXRD studies (see Fig. 4.2 and Fig. 4.3). Samples grown at  $T_G > 300$   $^\circ\text{C}$  also show a decrease of  $M_s$ , indicating the formation of interfacial compounds, which also agrees with the results of HRXRD [see Fig. 4.2(b)]. For  $T_G \leq 300$   $^\circ\text{C}$  (vertical dotted line),  $M_s$  is almost constant. Near the optimized growth temperature the value of  $M_s$  is close to that of  $\text{Fe}_{3+x}\text{Si}_{1-x}$  films on GaAs(001) substrates with the same composition [162].

#### Origin of UMA away from optimal growth temperature: An annealing study

As already discussed, the samples grown at 200 and 400  $^\circ\text{C}$ , which exhibit UMA also show the formation of “nanoscale ripples-like” structures in AFM. Upon reexamining the AFM images of these samples from Fig. 4.3 one finds the “ripples-like” structures oriented along the  $\langle 33\bar{2} \rangle$  and  $\langle \bar{1}10 \rangle$  axes for the samples grown at 200 and 400  $^\circ\text{C}$ , respectively. Interestingly the orientation of these “ripples-like” structures coincides with the easy axes of magnetization (see Fig. 4.12). This indicates that the UMA in these films might be a surface morphology induced phenomena. However, in HRXRD measurements we find that these samples are structurally not perfect. The sample grown at 200  $^\circ\text{C}$  does not exhibit a smooth interface whereas the sample grown at 400  $^\circ\text{C}$  shows the formation of additional interfacial compounds. In fact, the interface roughness (from XRR simulation) of the sample grown at 200  $^\circ\text{C}$  ( $\sim 11$  Å) was found to be one order of magnitude larger than



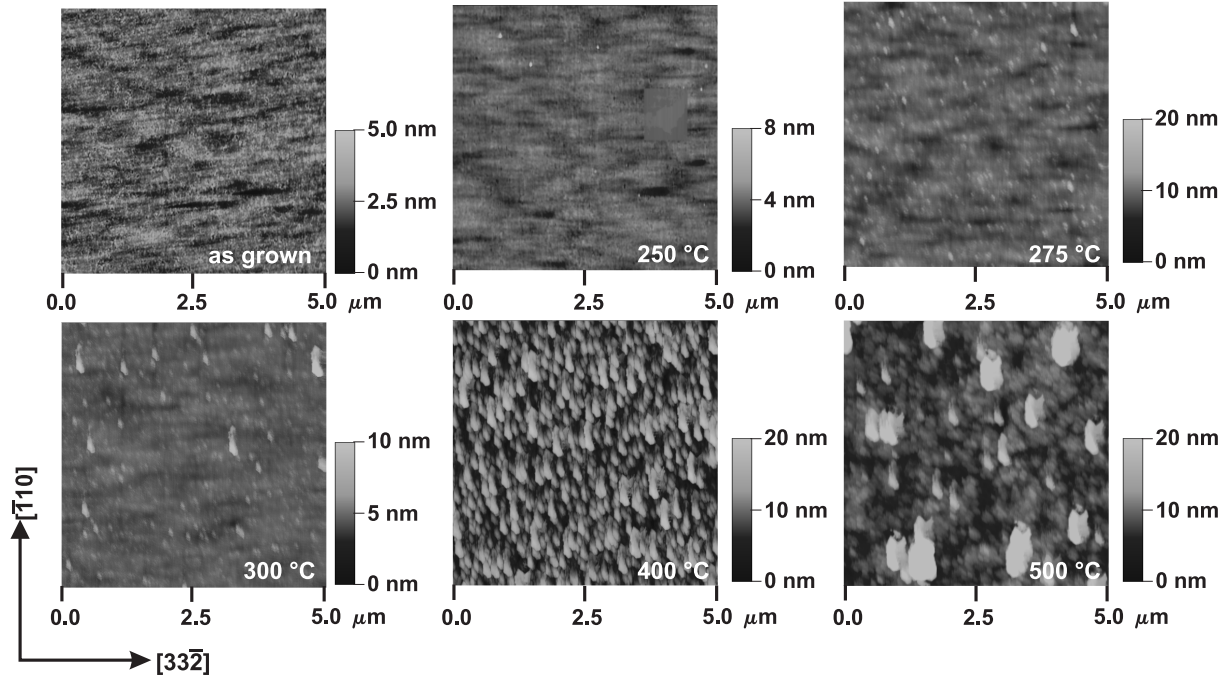


Figure 4.14: Comparison of the AFM surface morphology as a function of annealing temperature,  $T_a$ . The *as-grown* sample represents a 41.5-nm-thick  $\text{Fe}_{3+x}\text{Si}_{1-x}$  film with  $x = 0.3$  grown at  $T_G = 200$  °C with a growth rate of 0.26 nm/min.

that of the 250 °C sample ( $\sim 0.5$  Å), which exhibits a clear four-fold magnetic anisotropy. Hence these properties must also be taken into account to understand the UMA of these films. To investigate this phenomenon a bit further, we performed rapid thermal annealing (RTA) studies on several pieces of the sample grown at 200 °C and annealed it at  $T_a = 250, 275, 300, 400$  and 500 °C. The RTA was carried out for 10 min in a nitrogen ambient with a constant heating rate of 20 K/s using a Jetfirst furnace. The dependence of the RTA on the crystalline quality and surface morphology of the layers was then studied by HRXRD and AFM. The RTA was found to affect the anisotropic surface morphology of the films as shown in Fig. 4.14. The “nanoscale ripples” along the  $\langle 33\bar{2} \rangle$  axes begin to disappear at 275 °C, and completely vanish at 400 °C. Instead some additional structures are found, which are oriented in the perpendicular direction and are somewhat similar to the structures observed for the sample grown at 400 °C. However, the UMA was found preserved until 400 °C and does not completely vanish even for  $T_a = 500$  °C. This indicates that the UMA of this sample with  $T_G = 200$  °C may be related to interface rather than to the “nano-scale ripples” on the surface. Furthermore, the orientation of the easy axis of the UMA of this sample is same as that of the interface-related-UMA of Fe films on GaAs(113)A substrates. Thus the results support a interfacial origin of UMA for the sample grown at  $T_G = 200$  °C. A detailed investigation of the interface structure will be useful to further understand the origin of this UMA. Nevertheless, these studies show that both the surface and interface roughness are important parameters in determining the magnetic anisotropy of these films. To obtain the expected four-fold magnetic anisotropy, a sharper interface/smooth surface is required as achieved in our samples grown under optimized growth conditions.

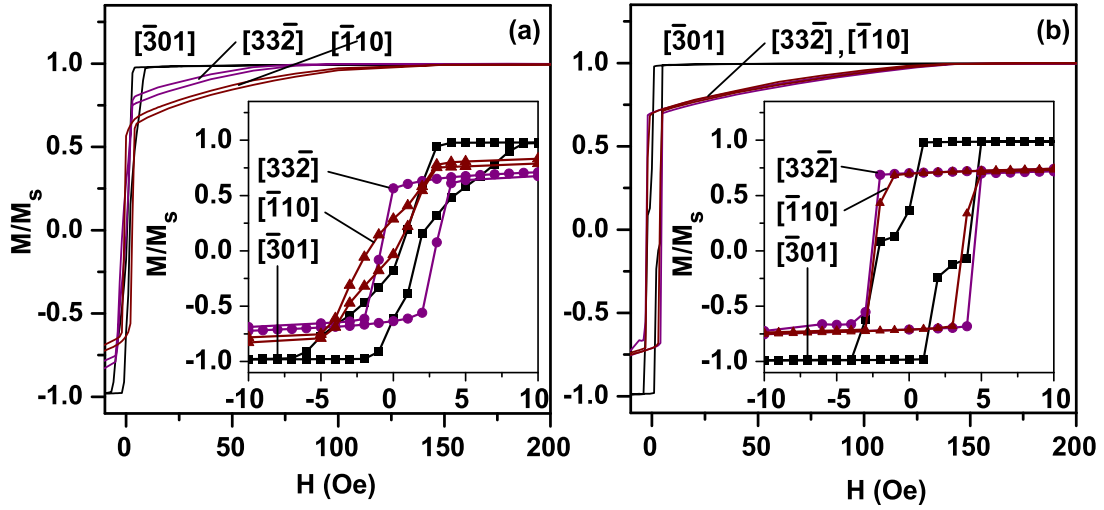


Figure 4.15: SQUID magnetization curves along different crystallographic directions for positive fields of samples with growth rate of (a) 0.26 nm/min (b) 0.13 nm/min, respectively. The insets show the magnified low-field region.

As additional comments, it should be mentioned that the RTA experiments also provides some additional insight into the thermal stability of these  $\text{Fe}_3\text{Si}$  films. We do not observe any indication for the formation of additional phases up to  $T_a = 400^\circ\text{C}$ , which indicates that these layers are thermally more stable compared to Fe films in agreement with the experiments on the [001] orientation [163]. Besides, upon annealing the sample grown at  $T_G = 200^\circ\text{C}$  to the optimum growth temperature of  $250^\circ\text{C}$ , we did not reproduce the interference fringes in HRXRD rocking curves usually observed in as-grown films. This shows the importance of growth under optimized conditions.

### Influence of growth rate

In Fig. 4.4 we showed that the reduction of the growth rate improves the structural properties. This is also found to improve the magnetic properties as shown in Fig. 4.15. The samples correspond to the AFM data presented in Fig. 4.4. The composition of the two films is comparable ( $x = 0.33$  and  $0.39$  for the first and second column). As discussed before, the sample with lower growth rate shows a smooth surface morphology as compared to the sample with higher growth rate and the latter shows the presence of some arbitrarily-shaped islands. As shown, the magnetization curves in both the samples exhibit the expected in-plane four-fold magnetic anisotropy, with the easy axis along  $\langle 03\bar{1} \rangle$ . However, the low-field behavior of the two samples differs significantly, as shown in the corresponding insets. For the sample grown at higher growth rate, the reversal is gradual and the switching width is about 5 Oe in all directions as shown in the inset of Fig. 4.15(a). On the other hand, the sample grown at a lower growth rate shows a sharp reversal, with a switching width of less than 1 Oe as shown in the inset of Fig. 4.15(b). We infer that the increased switching width in Fig. 4.15(a) is correlated with the rough surface morphology in Fig. 4.4(a). The interaction between the small particles (as seen in the AFM image) could be a possible reason for the increased switching width. Nevertheless, we see a clear improvement in the magnetic properties by the lowering of the growth rate.

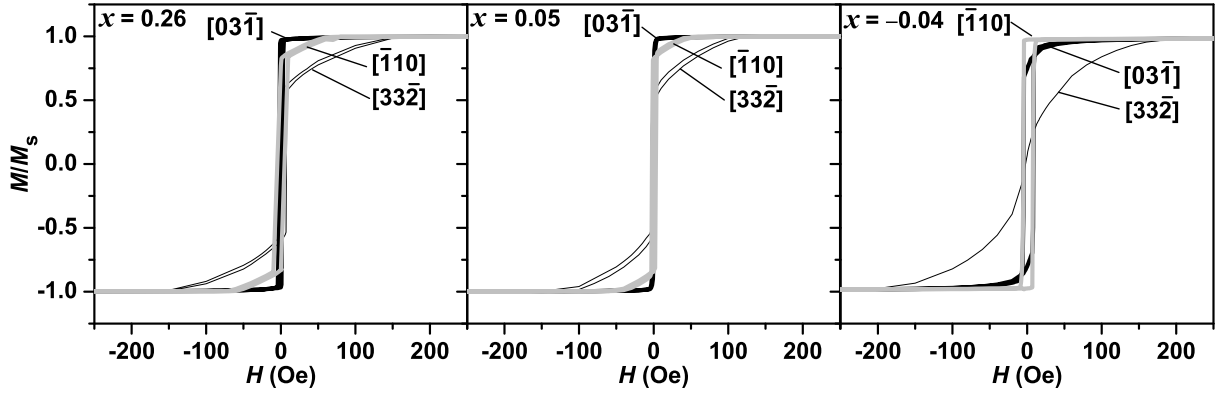


Figure 4.16: Normalized SQUID magnetization curves at 300 K along different crystallographic directions for three different compositions  $x$ . The thicknesses of these films are in the range of 35–50 nm.

As can be seen from Fig. 4.13 (the  $\star$  symbol),  $M_s$  and  $H_c$  also attain reasonable values for the sample with a low growth rate. This low growth rate will be used to study the magnetic properties as a function of Si content in the next section.

As an additional observation, the magnetization curve along  $[03\bar{1}]$  in the inset to Fig. 4.15(b) shows a two-jump reversal, which is often understood from the presence of a small UMA [3, 139] as discussed in Sec. 3.4.7 for Fe films. However, in this case the magnetization curves along  $[33\bar{2}]$  and  $[\bar{1}10]$  are found to be equivalent indicating the absence of any UMA. Thus this two-jump switching can not be produced from a coherent-rotation calculation (the SWM), when no UMA is assumed. Hence, we ascribe these steps to “non-ideal” two-jump reversal similar to the case of Fe films [3].

## 4.2.2 Composition dependence of magnetic properties

As already mentioned in the previous section, the samples grown at optimized growth conditions show a dominant four-fold magnetic anisotropy. For example, the magnetization curves of the samples in Fig. 4.15 exhibit a four-fold magnetic anisotropy with the easy axes along the  $\langle 03\bar{1} \rangle$  axes. However, these samples have a composition far from stoichiometry. To study the magnetic properties as a function of  $x$ , we use the samples grown under the optimized growth conditions of Sec. 4.1.2. In Fig. 4.16 we compare the magnetization curves at 300 K of three typical samples with  $x = 0.26$ ,  $0.05$  and  $-0.04$ . The easy axis of the magnetization for the sample with  $x = 0.26$  is also found along the  $[03\bar{1}]$  axis given the clear rectangular hysteresis ( $M_r/M_s \approx 1$ ) loop observed. However, the other two major crystallographic axes, namely  $[33\bar{2}]$  and  $[\bar{1}10]$ , are no longer equivalent in contrast to the sample with  $x = 0.39$  in Fig. 4.15(b). In fact, the  $[\bar{1}10]$  axis is more easy compared to the  $[33\bar{2}]$  axis indicating the presence of a UMA with easy axis along  $[\bar{1}10]$ . Furthermore, this UMA is found to increase with Si content in the film. For the sample with higher Si content, the inequivalence of the major axes increases, and eventually the  $[\bar{1}10]$  axis becomes the easy axis as observed for the sample with  $x = -0.04$ . The direction of this UMA is surprisingly opposite to that of the interface-related-UMA of Fe films in Sec. 3.4.3. Nevertheless, the magnetic anisotropy of these films can be modelled analytically by using the magnetic free energy density when an additional UMA is assumed to

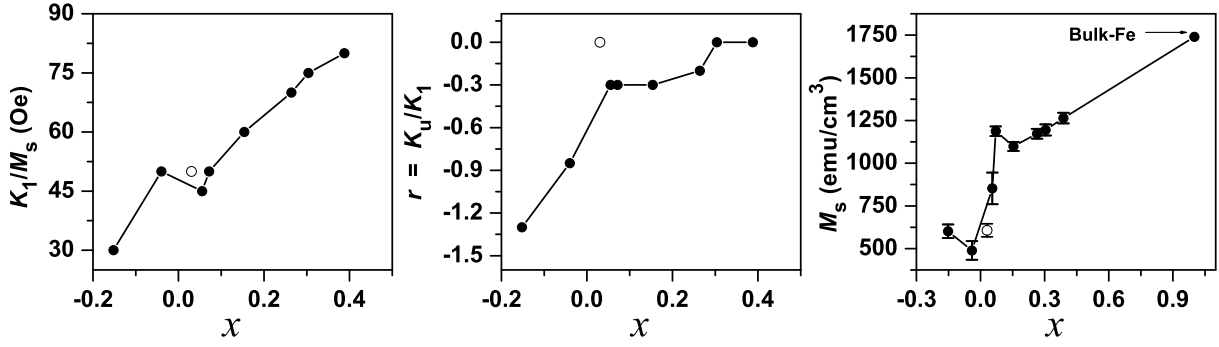


Figure 4.17: Summary of the composition dependence of magnetic properties of  $\text{Fe}_{3+x}\text{Si}_{1-x}$  films grown on GaAs(113)A substrates. The composition dependence of (a) the four-fold magnetic anisotropy constant  $K_1$  normalized w.r.t. the saturation magnetization,  $M_s$ , (b) the UMA ratio  $r = K_u/K_1$  and (c) the saturation magnetization,  $M_s$ . The open circle indicates a sample with  $x = 0.03$ .

be superimposed with the normal magnetocrystalline anisotropy. The in-plane magnetic anisotropy energy density  $E_{\text{IPMA}}$  for the (113) surface symmetry can be written in analogy to Fe/GaAs(113)A films (see Sec. 3.4.5):

$$E_{\text{IPMA}} = (K_1/484)[89 + 16 \cos 2\theta_M + 48 \cos 4\theta_M] + K_u \sin^2 \theta_M - MH \cos(\theta_H - \theta_M), \quad (4.4)$$

where  $K_1$  and  $K_u$  are the cubic and uniaxial anisotropy constants, respectively. Here,  $\theta_M$  and  $\theta_H$  are the angle of magnetization  $\mathbf{M}$  and magnetic field  $\mathbf{H}$  with respect to the  $[33\bar{2}]$  direction. The first term denotes the usual magnetocrystalline anisotropy whereas the second term represents the additional UMA observed in the experiment. The last term represents the Zeeman energy. It is easy to show that the observed magnetic properties can be qualitatively understood from this equation at  $H = 0$  similar to the case of Fe films (Sec. 3.4.5). Using this equation for  $E_{\text{IPMA}}$  the anisotropy constants,  $K_1$  and  $K_u$  can be calculated from the magnetization curves. Details of the methods of calculation are similar to that of the Fe films (Sec. 3.4.6) and hence will not be discussed here.

The anisotropy constants obtained from the fitting of the magnetization curves are shown in Fig. 4.17, which shows the plot of (a)  $K_1/M_s$  and (b)  $r = K_u/K_1$  as a function of composition  $x$ . Figure 4.17(c) shows the dependence of  $M_s$  on  $x$ . Figure 4.17(a) shows a positive value of  $K_1$  as reported for ordered bulk  $\text{Fe}_3\text{Si}$  with  $\text{D}_{03}$  crystal structure [194]. Thus the positive sign of  $K_1$  may imply that the films shown here have a  $\text{D}_{03}$  crystal structure, even though some of the  $\text{D}_{03}$ -related odd superlattice reflections were not detected in the off-stoichiometric samples. Furthermore, a decrease in the four-fold magnetic anisotropy constant with increasing Si content is also found. This can be understood from the argument of reduced symmetry environment of the Fe atoms in the crystal lattice due to the addition of Si. For stoichiometric samples, the value of  $K_1/M_s$  is equal to  $(50 \pm 5)$  Oe. From Fig. 4.17(c),  $M_s = (600 \pm 50)$  emu/cm<sup>3</sup> for the stoichiometric samples. This yields  $K_1 = (3.0 \pm 0.6) \times 10^4$  erg/cm<sup>3</sup>, which agrees well with the reported values in the literature for  $\text{Fe}_3\text{Si}$  films on GaAs(001) substrates [164, 165, 195]. The value is also comparable to the bulk value of  $K_1 = 5.4 \times 10^4$  erg/cm<sup>3</sup> in ordered  $\text{Fe}_3\text{Si}$  [194].

The ratio  $r$ , which reflects the strength of the additional UMA, is negative and increases in amplitude with increasing Si content (decreasing  $x$ )—with the exception of one sample with  $x = 0.03$  shown as open circle. The negative sign of  $r$ , which indicates an easy axis of the UMA along the  $[\bar{1}10]$  direction, is opposite to that of the interface-related-UMA in Fe films. Hence, the UMA observed here is probably not related to the interface. Besides, the thickness range studied here (35–50 nm) may be substantially too large to observe any interface-related effect. However, for  $\text{Fe}_3\text{Si}(001)$  films in this thickness range, recently a UMA [162, 165] of interfacial origin [195] is reported. For this reason, the role of the interface may not be discarded so easily and a detailed thickness dependence study is required to confirm the role of the interface on the negative  $r$  observed in these  $[11\bar{3}]$ -oriented films. The surface morphology of these films does not exhibit any anisotropic roughness, thus ruling out surface morphology related dipolar origin of the UMA. The other possible origin of the UMA includes the strain in the films, the presence of some additional phase, and the growth conditions. To investigate the influence of the latter, we varied the growth temperature for the stoichiometric sample  $x = 0.03$  which shows a clear four-fold magnetic anisotropy with  $r = 0$  as shown by the open circle in Fig. 4.17. The growth temperature was varied from 250 to 300 °C (see Fig. 4.8). However from this study we only witness an increase of  $H_c$  with  $r = 0$  remaining constant. The increase in  $H_c$  is essentially due to the degradation of the layer quality (increasing RMS roughness, see Fig. 4.8). However the preservation of  $r = 0$  indicates that the four-fold magnetic anisotropy is dominant in this growth temperature range. This shows that the growth conditions may not have a significant influence on this UMA, at least in the temperature range studied. A strong UMA is actually observed for samples with high Si content, for which the presence of some additional phase is also known from RHEED and HRXRD experiments. However, the composition of this possible phases and its relation to the UMA are not known clearly. Thus the UMA observed here is not completely understood. To further understand the origin of this UMA, a detailed analysis of the variation in the strain and/or crystal ordering in the films needs to be performed.

The composition dependence of  $M_s$  shown in Fig. 4.17 (c) is interesting for investigating the correlation between site disorder in  $\text{Fe}_{3+x}\text{Si}_{1+x}$  alloys and the magnetization of the sample [169]. Roughly speaking, a decrease of the saturation magnetization  $M_s$  with the addition of Si can be seen in Fig. 4.17. However, the behavior of  $M_s$  with  $x$  is rather complicated, unlike the case of  $\text{Fe}_{3+x}\text{Si}_{1+x}$  films on  $\text{GaAs}(001)$  substrates [162]. The non-linear composition dependence of  $M_s$  has been discussed in the literature [169] in terms of different models which assume the substitution of Si atoms into different sublattices giving rise to different magnetic moments on the Fe sites. Thus a similar phenomenon might be responsible for the complex composition dependence, though a detailed analysis is obviously required. Nevertheless, we determine the average magnetic moment per atom for the stoichiometric  $\text{Fe}_3\text{Si}$  by taking the saturation magnetization as  $(600 \pm 50) \text{ emu/cm}^3$  and the lattice constant as  $a_{\text{Fe}_3\text{Si}} = 5.652 \text{ \AA}$  (from Fig. 4.6). This yields a magnetic moment per atom equal to  $(0.73 \pm 0.06) \mu_B$  at 300 K, which is smaller compared to the bulk value of  $1.2 \mu_B$  per atom and the reported values for  $\text{Fe}_3\text{Si}$  films on  $\text{GaAs}(001)$  substrates [165].

## Temperature dependence and thermal spin excitations

The temperature dependence of the saturation magnetization  $M_s(T)$  is summarized in Fig. 4.18 for all studied  $\text{Fe}_{3+x}\text{Si}_{1-x}$  films with varying composition  $x$ . Figure 4.18(a)

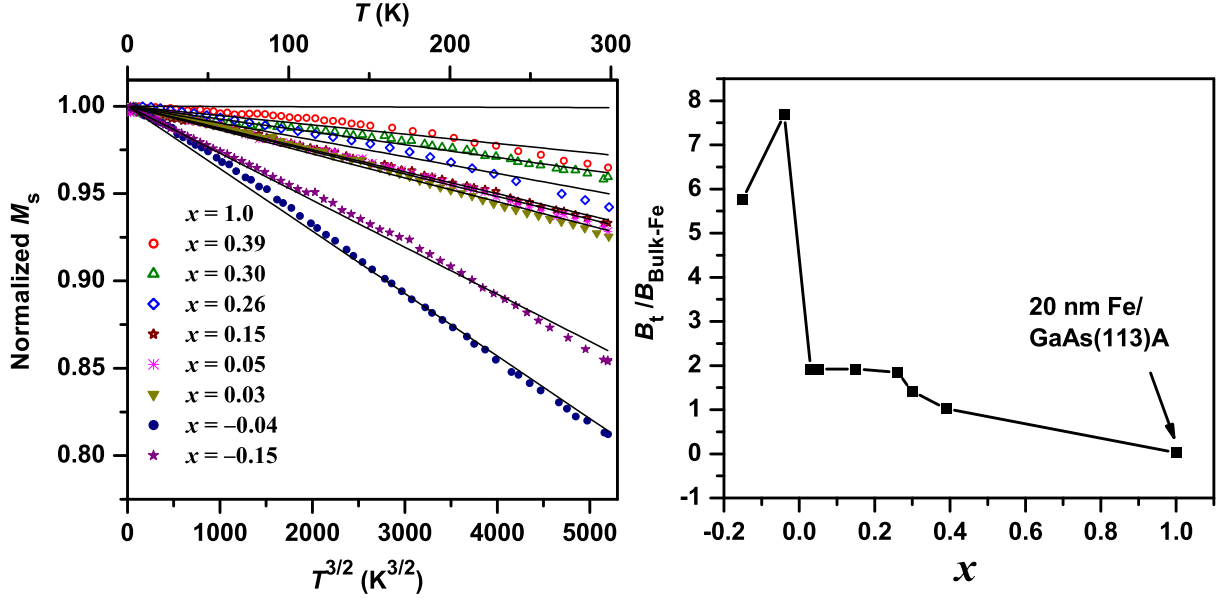


Figure 4.18: (a) Temperature dependence of the spontaneous magnetization  $M_s(T)$  normalized to  $M_0$  for  $\text{Fe}_{3+x}\text{Si}_{1-x}$  films on GaAs(113)A substrates with different composition  $x$ . The solid lines are fits of Bloch  $T^{3/2}$  law. (b) Bloch constant or spin-wave parameter  $B$  in  $\text{Fe}_{3+x}\text{Si}_{1-x}$  films on GaAs(113)A substrates normalized to the bulk value of Fe as a function of the composition  $x$ .

shows the behavior of  $M_s(T)$  normalized to the saturation magnetization,  $M_0$  at 10 K. The measurement was performed with a saturating field applied along the easy axis of magnetization. For the entire temperatures range 10 – 300 K,  $M_s$  changes by less than 20 %, which implies a high Curie temperature of the samples. For comparison, the 20 nm Fe film from Figure 3.10(a) is also included. A systematic decrease in  $M_s(T)$  with addition of Si/decrease in  $x$  can be seen (with the exception of the sample with  $x = -0.15$ ). Upon adding Si, the strength of the exchange interaction decreases and hence the Curie temperature. The temperature dependence of Fig. 4.18(a) is also found to obey the Bloch  $T^{3/2}$  law [see Eq.(3.2)], since the Curie temperature is far away from the range of the measurement temperature. Fits to the Bloch's law are shown as solid lines in Fig. 4.18(a). The Bloch constant or spin-wave parameter  $B_t$  was obtained from the slope of the fits similar to the Fe films. Figure. 4.18(b) shows a plot of  $B_t$  normalized to the bulk value of Fe  $B_{\text{bulk-Fe}} = 5.2 \times 10^{-6} \text{ K}^{-3/2}$ , as a function of  $x$ . As can be seen, the spin-wave parameter increases with increasing Si content. For stoichiometric samples, a constant value of the normalized spin-wave parameter  $B_t/B_{\text{bulk-Fe}} \sim 2$  is obtained. However the composition dependence of the spin-wave parameter is rather weak compared to the corresponding thickness dependence of Sec. 3.4.2. Nevertheless, the increase in the spin-wave parameter can be attributed to the decrease in the strength of the magnetic anisotropy as observed in Fig. 4.17(a). This observation is similar to that found for Fe films. This means that more spin-waves can be excited in  $\text{Fe}_3\text{Si}$  films compared to pure Fe films in this thickness range.

### 4.2.3 Summary of magnetic properties of $\text{Fe}_{3+x}\text{Si}_{1-x}$ films

1. All the  $\text{Fe}_{3+x}\text{Si}_{1-x}$  layers are found to be ferromagnetic at room temperature irrespective of the growth conditions and composition ( $0.39 \leq x \leq -0.15$ ) of the layers.
2. The films grown under optimized growth conditions exhibit superior magnetic properties with a very low coercive field and high saturation magnetization. A low growth rate was shown to reduce the switching width of the magnetization curves. This was found to be correlated to an improvement in the surface/interface roughness.
3. For films very close to the stoichiometric composition  $\text{Fe}_3\text{Si}$ , SQUID measurements yield a magnetic moment of  $(0.73 \pm 0.06) \mu_B$  per atom at 300 K which is smaller than the bulk value.
4. The layers grown under optimized growth conditions exhibit a dominant four-fold magnetic anisotropy, which arises from the magnetocrystalline anisotropy and the large demagnetization energy of the  $\text{Fe}_3\text{Si}$  films, similarly to Fe films.
5. The four-fold anisotropy constant for a stoichiometric composition of the  $\text{Fe}_3\text{Si}$  films was found to be  $K_1 = (3.0 \pm 0.6) \times 10^4 \text{ erg/cm}^3$ , which agrees well with the reported values in the literature for bulk  $\text{Fe}_3\text{Si}$  as well as with the value on [001] oriented films. The decrease of  $K_1$  with increasing Si content is attributed to the reduced symmetry environment of Fe atoms upon adding Si.
6. Bloch's law is found to be valid in the whole range of measurement temperatures. An increase in the spin-wave parameter with increasing Si content in the  $\text{Fe}_{3+x}\text{Si}_{1-x}$  films is observed, which is attributed to the corresponding decrease in the anisotropy constant  $K_1$ .
7. The magnetic anisotropy exhibits a complex dependence on the growth temperature for off-stoichiometric composition ( $x = 0.3$ ) and high growth rate of 0.26 nm/min. Strong UMAs are found for samples grown at  $T_G = 200$  and 400 °C with the easy axes opposite to each other. The UMA of the sample grown at  $T_G = 200$  is believed to arise from the rough interface between  $\text{Fe}_{3+x}\text{Si}_{1-x}$  and GaAs.
8. An additional UMA with an easy axis opposite to that of Fe/GaAs(113)A is found in some  $\text{Fe}_{3+x}\text{Si}_{1-x}$  films grown under optimized growth conditions. This incompletely understood UMA is found to increase with decreasing  $x$  in  $\text{Fe}_{3+x}\text{Si}_{1-x}$  films.

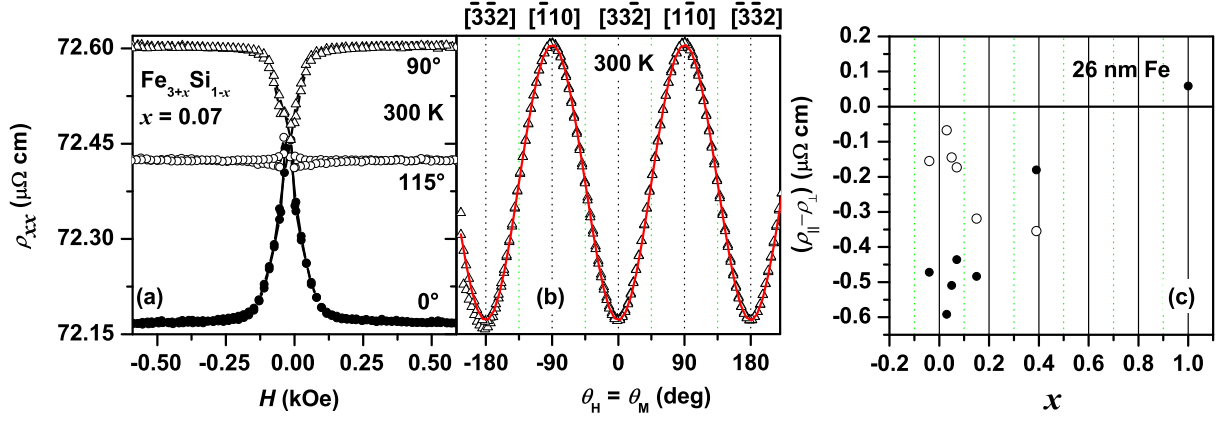


Figure 4.19: Summary of AMR studies. (a) An example of the field dependence of AMR ( $\rho_{xx}$ ) for an  $\text{Fe}_{3+x}\text{Si}_{1-x}(113)$  film with  $x = 0.07$  at  $T = 300 \text{ K}$  for different in-plane directions. (b) The angular dependence of  $\rho_{xx}$  at a fixed saturating field of  $H = 1 \text{ kOe}$  obtained at  $300 \text{ K}$ . (c) The AMR amplitude,  $(\rho_{||} - \rho_{\perp})$  as a function of composition  $x$  of the  $\text{Fe}_{3+x}\text{Si}_{1-x}(113)$  films measured at  $300 \text{ K}$  (solid circles) and  $77 \text{ K}$  (open circles).

### 4.3 Magnetotransport properties

The magnetotransport properties of  $\text{Fe}_{3+x}\text{Si}_{1-x}$  films to be discussed in this section are an extension of the work on Fe films. Specifically, we examine the observation of the ASC in the PHE and study the composition and temperature dependence of the PHE. Samples with Hall bar structures are used for measurements since the rectangular samples (as used in case of Fe films) show a phase shift in the angular dependence of symmetric component of the PHE [146], which might be related to the inhomogeneous current flow in the large rectangular samples. To make sure of homogenous current flow, we use well defined Hall bar structures for the  $\text{Fe}_{3+x}\text{Si}_{1-x}$  films. The Hall bar structures were prepared by standard lithography techniques. The Hall bars were aligned along the  $[3\bar{3}2]$  direction by a combination of photo-lithography and ion-beam sputtering. The perfect alignment of the Hall bar structures ensures a homogenous current flow. The width of the Hall bar was  $30 \mu\text{m}$  and the length between two nearest contacts, e.g., B and C was  $22.5 \mu\text{m}$  [see Fig. 4.20(a)]. Both AMR ( $\rho_{xx}$ ) and PHE ( $\rho_{xy}$ ) were measured simultaneously with a current of  $3 \text{ mA}$  along the Hall bar.

#### 4.3.1 Anisotropic magnetoresistance

In Fig. 4.19, the results of the AMR measurements are summarized. As an example, Fig. 4.19(a) shows the AMR response of an  $\text{Fe}_{3+x}\text{Si}_{1-x}$  film with  $x = 0.07$ . Similarly to the case of Fe films,  $\rho_{xx}$  was found to be a symmetric function of the applied field direction [see Fig. 4.19(a)] and the angular dependence of  $\rho_{xx}$  for a saturating field shows a perfect  $\cos^2 \theta_M$  dependence as shown by the solid line in Fig. 4.19(b). Unlike the case of Fe films, the AMR amplitude,  $(\rho_{||} - \rho_{\perp})$ , is found negative similar to that of  $\text{Fe}_{3+x}\text{Si}_{1-x}$  films on GaAs(001) substrates [196]. The composition dependence of  $(\rho_{||} - \rho_{\perp})$  measured at  $T = 300 \text{ K}$  and  $T = 77 \text{ K}$  are shown in Fig. 4.19(c): the sign of  $(\rho_{||} - \rho_{\perp})$  do not change in the whole range of composition and temperature studied. The negative



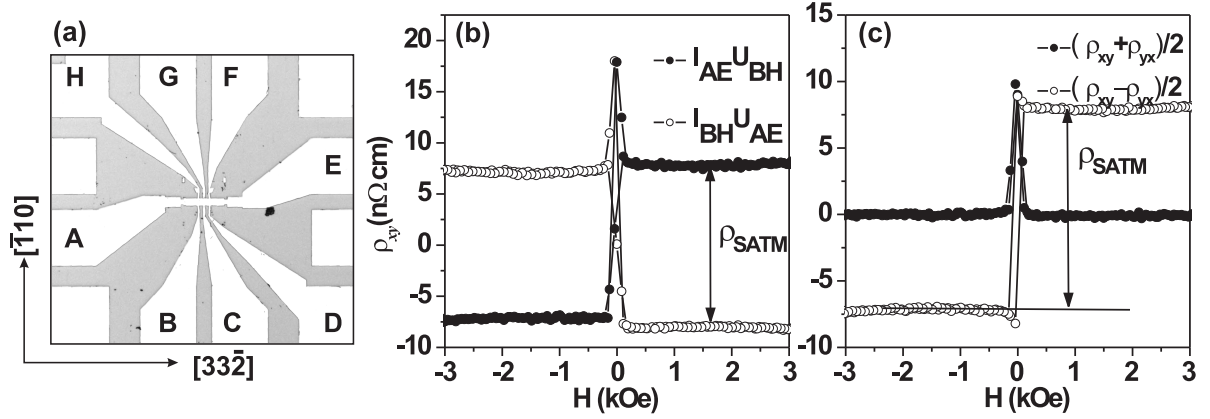


Figure 4.20: (a) Optical microscopy image of the Hall bar structure employed for the magnetotransport studies. The contacts are labelled and the crystallographic directions of the (113)-plane are shown. (b) Planar Hall effect response for an  $\text{Fe}_{3+x}\text{Si}_{1-x}$  film with  $x = 0.07$  grown on GaAs(113)A at 300 K with magnetic field applied along  $[33\bar{2}]$ . (c) Separation of the symmetric and antisymmetric contribution to the PHE.

value of  $(\rho_{\parallel} - \rho_{\perp})$  indicates that the resistance anisotropy is due to the scattering of the majority-spin electrons according to the theory of Potter [39, 197]. This is just opposite to the case of Fe where  $(\rho_{\parallel} - \rho_{\perp})$  is positive as shown in Fig. 4.19(c) for  $x = 1$ , which represents the data from a 26 nm Fe film on GaAs(113)A substrates. The behavior of  $(\rho_{\parallel} - \rho_{\perp})$  with  $x$  shows a large scattering of data. However, the stoichiometric samples exhibit a comparatively strong temperature dependence. The normalized quantity or the anisotropic magnetoresistivity ratio defined by  $\Delta\rho/\rho_{\text{ave}}$ , where  $\rho_{\text{ave}} = \frac{1}{3}\rho_{\parallel} + \frac{2}{3}\rho_{\perp}$  [39], is always less than 1 % and is about 0.71 % for the most stoichiometric sample with  $x = 0.03$  at 300 K.

It is worth to mention that the AMR measurements provide a good insight into the magnetic properties of the  $\text{Fe}_{3+x}\text{Si}_{1-x}$  films. In Fig. 4.19(a), the dominant four-fold magnetic anisotropy of the  $\text{Fe}_{3+x}\text{Si}_{1-x}$  film with  $x = 0.07$  can be seen. The change in AMR with the strength of the applied field for  $\theta_H = 0^\circ$  is less compared to that for  $\theta_H = 90^\circ$ , which indicates a magnetic inequivalence of these directions or the presence of the additional UMA as observed in Sec. 4.2.2. Also the AMR response for  $\theta_H = 115^\circ$  does not change with the applied field strength, indicating the easy axis of magnetization. This corresponds to a uniaxial ratio of about  $r = 0.4$ . Thus the sample exhibit a dominant four-fold magnetic anisotropy superimposed with a small UMA. Thus the results obtained with SQUID magnetometry in Sec. 4.2 were reproduced through AMR measurements.

### 4.3.2 Planar Hall effect: Composition dependence

The PHE of  $\text{Fe}_{3+x}\text{Si}_{1-x}$  films exhibits the ASC observed previously in Fe films. In Fig. 4.20, we show the room temperature (300 K) PHE response for a nearly stoichiometric  $\text{Fe}_{3+x}\text{Si}_{1-x}$  film with  $x = 0.07$ . An optical microscopy image of the Hall bar structure used is shown in Fig. 4.20(a) with the contacts labelled as A, B....H in a counterclockwise manner. In Fig. 4.20(b) and (c) we examine the antisymmetry by measuring the PHE for two cases with the current along the AE and BH contact points, which correspond

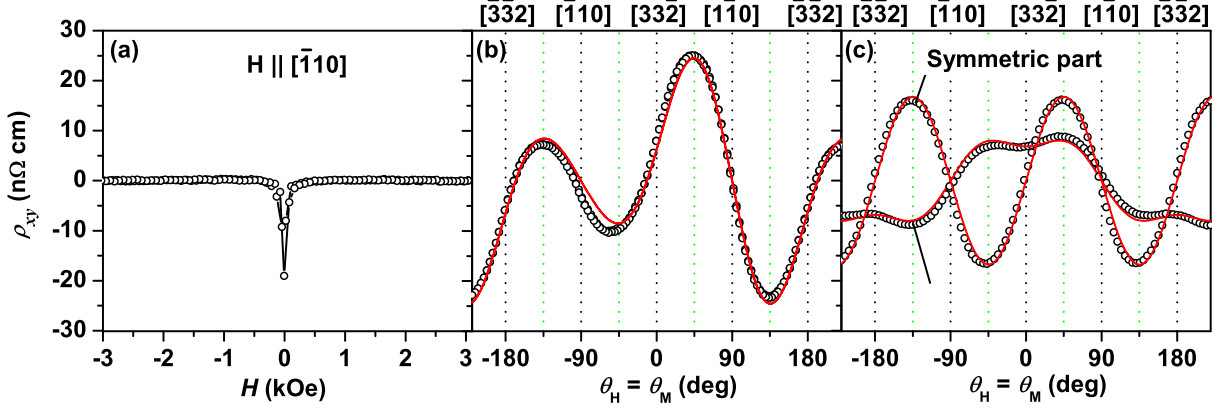


Figure 4.21: (a) Planar Hall effect response from an  $\text{Fe}_{3+x}\text{Si}_{1-x}$  ( $x = 0.07$ ) film grown on GaAs(113)A with magnetic field applied in-plane along  $[\bar{1}10]$  at 300 K, showing the vanishing ASC. (b) Angular dependence of  $\rho_{xy}$  at 300 K with a saturating in-plane magnetic field so that  $\theta_H = \theta_M$ . (c) Separation of the symmetric and antisymmetric part of the PHE. Open circles represent experimental data while the solid lines are fitted curves as discussed in Fig. 3.29.

to the  $[3\bar{3}2]$  and  $[\bar{1}10]$  directions, respectively. The magnetic field was kept fixed along the  $[3\bar{3}2]$  direction. Accordingly, the planar Hall voltage was measured along the contacts BH and AE. We denote these two cases  $I_{AE}U_{BH}$  and  $I_{BH}U_{AE}$  as  $\rho_{xy}$  and  $\rho_{yx}$ , respectively. Here, the positive  $x$ -axis is taken along the  $[3\bar{3}2]$  direction. As can be seen, the PHE is completely saturated at a rather low field of less than 0.2 kOe (see Sec. 4.2), but shows a sign change upon reversing the magnetic field direction, irrespective of the current direction. This confirms the antisymmetric nature of the component as implied by Eq. (A.4) of Appendix A. Figure 4.20(c) shows the separation of the symmetric and antisymmetric components. We find a positive sign of  $\rho_{\text{SATM}} = \rho_{xy}(H > +H_{\text{sat}}) - \rho_{xy}(H < -H_{\text{sat}})$  (in this sample with  $x = 0.07$ ) at 300 K with a magnetic field applied along the  $[3\bar{3}2]$  direction by using the sign convention as defined in Sec 3.5.2 for the Fe films.

Similarly to Fe films, when the magnetic field is aligned along the  $\langle \bar{1}10 \rangle$  axes, the ASC vanishes ( $\rho_{\text{SATM}} = 0$ ) as shown in Fig. 4.21(a). The dependence of  $\rho_{xy}$  on the field orientation angle  $\theta_H$  (defined with respect to the  $[3\bar{3}2]$  direction) can be more clearly seen in Fig. 4.21(b), which shows the angular dependence of the PHE measured at 300 K with a fixed positive saturating magnetic field ( $H = +1$  kOe) so that  $\theta_H = \theta_M$ . The angular dependence is completely reversible and does not follow the  $\sin 2\theta_H$  dependence of Eq. (2.13). A separation of the symmetric and antisymmetric components can be achieved by taking the sum and difference of the angular dependence of the PHE for positive and negative fields above saturation. The result is shown in Fig. 4.21(c). The overall behavior of  $\rho_{xy}$  on  $\theta_H$  can be well described by the modified equation of the PHE [Eq. (3.20) of Sec. 3.5.2]:

$$\rho_{xy} = \rho_s^{\text{PHE}} \sin 2\theta_H + \rho_{\text{SATM}}^0 \cos \theta_H + \rho_{\text{SATM}}^1 \cos^3 \theta_H. \quad (4.5)$$

The best fitting is obtained for:  $\rho_s^{\text{PHE}} = 16.5$  nΩ cm,  $\rho_{\text{SATM}}^0 = 16$  nΩ cm, and  $\rho_{\text{SATM}}^1 = -10$  nΩ cm at 300 K. Thus the sign of  $\rho_s^{\text{PHE}}$  and  $\rho_{\text{SATM}} = 2(\rho_{\text{SATM}}^0 + \rho_{\text{SATM}}^1)$  are opposite for this  $\text{Fe}_{3+x}\text{Si}_{1-x}$  films with  $x = 0.07$  at 300 K compared to thick Fe films on GaAs(113)A substrates (see Table 3.3).

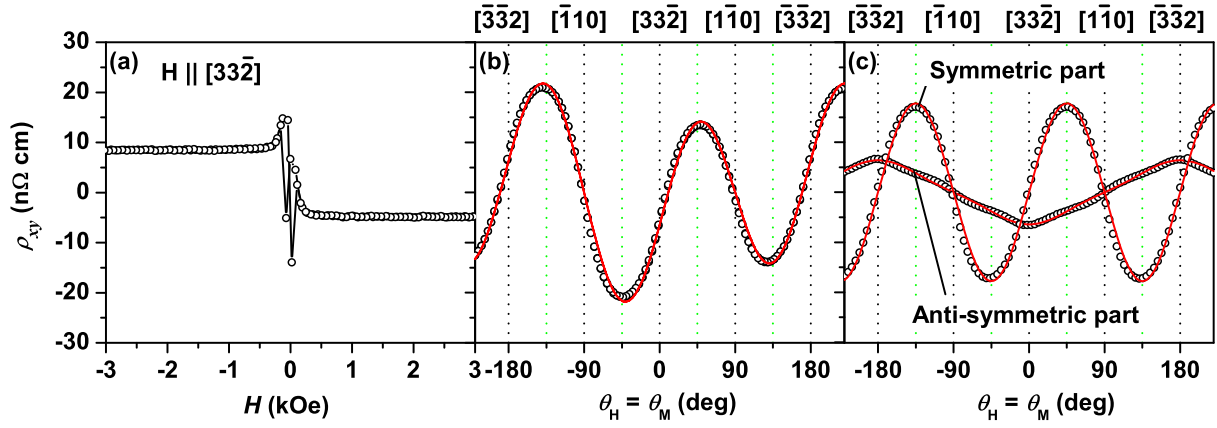


Figure 4.22: (a) PHE for an  $\text{Fe}_{3+x}\text{Si}_{1-x}(113)$  ( $x = 0.07$ ) film at 77 K with the magnetic field applied in-plane along  $[332]$ . (b) Corresponding angular dependence of  $\rho_{xy}$  at 77 K with a saturating in-plane magnetic field so that  $\theta_H = \theta_M$ . (c) Separation of the symmetric and antisymmetric part of the PHE. Open circles represent experimental data while solid lines are fitted curves as explained in Fig. 3.29.

### Composition and temperature dependence of the PHE

**Antisymmetric component (ASC)** To show the temperature dependence clearly, in Fig. 4.22 we present the field and angular dependence of  $\rho_{xy}$  for the same  $\text{Fe}_{3+x}\text{Si}_{1-x}(113)$  film ( $x = 0.07$ ) at 77 K. Figure 4.22(a) shows the field dependence of  $\rho_{xy}$  with magnetic field applied parallel to  $[332]$ . As can be seen, the sign of the ASC is reversed, i.e.,  $\rho_{\text{SATM}}$  is negative in contrast to the positive value of  $\rho_{\text{SATM}}$  at 300 K [see Fig. 4.20(a) for the configuration  $I_{\text{AE}}U_{\text{BH}}$ ]. Figures 4.22(b) and (c) show the corresponding dependencies of  $\rho_{xy}$  on  $\theta_H$  at a saturating field ( $\theta_H = \theta_M$ ). The best fitting (solid lines) is obtained for:  $\rho_s^{\text{PHE}} = 17.8 \text{ n}\Omega\text{cm}$ ,  $\rho_{\text{SATM}}^0 = -4.4 \text{ n}\Omega\text{cm}$ , and  $\rho_{\text{SATM}}^1 = -2 \text{ n}\Omega\text{cm}$ . The change in sign of  $\rho_{\text{SATM}}$  is clearly seen. To study the temperature and composition dependence of the ASC in more detail, we have measured:  $\rho_{\text{SATM}} = \rho_{xy}(H > +H_{\text{sat}}) - \rho_{xy}(H < -H_{\text{sat}})$  for a series of samples with  $x$  varying from +0.39 to -0.04 and temperatures varying from 300 to 4 K. The saturating magnetic field was applied along  $[332]$ , so that  $\rho_{\text{SATM}} = 2(\rho_{\text{SATM}}^0 + \rho_{\text{SATM}}^1)$  [see Eq. (4.5)]. The results are summarized in Fig. 4.23(a), which displays several important observations. First,  $\rho_{\text{SATM}}$  decreases with decreasing  $x$  and temperature (except the sample with  $x = -0.04$ ). Second,  $\rho_{\text{SATM}}$  changes the sign below a certain critical temperature that increases with decreasing  $x$  (increasing Si content). Interestingly, the sign of  $\rho_{\text{SATM}}$  for samples very close to stoichiometry ( $x \sim 0$ ) is negative at RT, which is the same as in Fe films grown on GaAs(113)A substrates [146]. However, for Fe films on GaAs(113)A no change in sign of  $\rho_{\text{SATM}}$  can be seen in the measurement temperature range of 4 K to 300 K.

The change in sign of the AHE in binary alloys with composition and temperature is rather well-known [198, 199, 200, 201, 202]. The origin of the sign change of  $\rho_{\text{SATM}}$  (which represents a second-order Hall effect) may be similar to that of the AHE. The anomalous Hall resistivity  $\rho_{\text{AHE}}$  for a saturating magnetic field and for the (113) symmetry is given by:

$$\rho_{\text{AHE}}^{(113)} = \frac{1}{121}(121a_{123} + 83a_{11123} + 38a_{12223}). \quad (4.6)$$

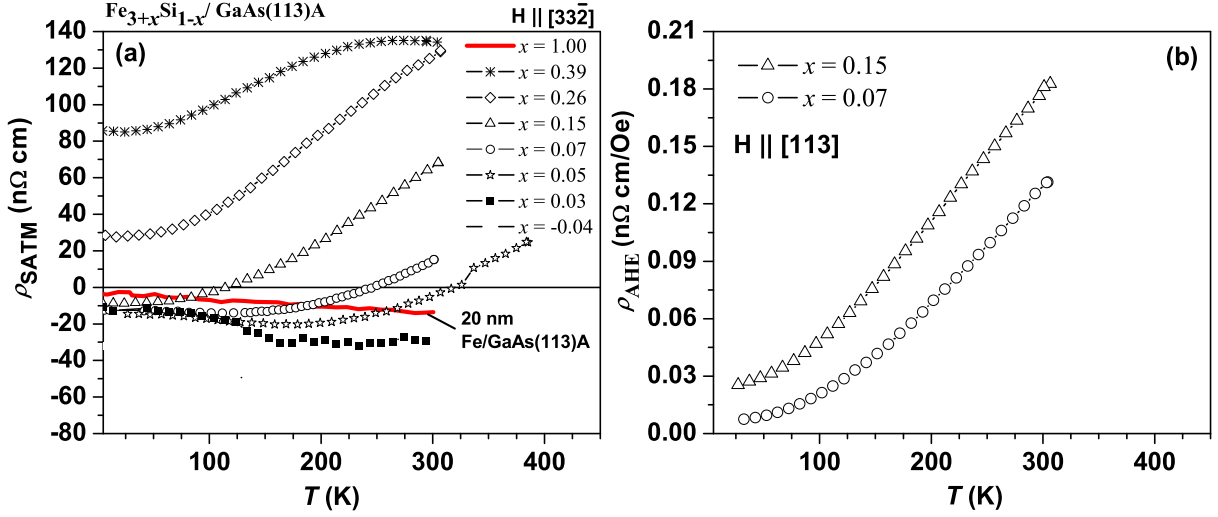


Figure 4.23: (a) Temperature and composition dependence of the  $\rho_{\text{SATM}} = \rho_{xy}(H > +H_{\text{sat}}) - \rho_{xy}(H < -H_{\text{sat}})$  measured with a saturating field applied near to the  $[33\bar{2}]$  direction. (b) Temperature dependence of  $\rho_{\text{AHE}}$  for two typical samples with  $x = 0.07$  and  $0.15$ .

This equation can be easily derived by using Eq. (A.2) and Eq. (3.17) for a saturating magnetic field applied along the  $[113]$  surface normal. In this equation, the first term containing the usual tensor element  $a_{123}$  represents a first-order contribution of  $\alpha_i$ , whereas the other two terms are third-order contributions. The presence of the same tensor elements  $a_{11123}$  and  $a_{12223}$  in PHE and AHE may imply a similar physical origin of  $\rho_{\text{SATM}}$  and  $\rho_{\text{AHE}}$ . To see whether  $\rho_{\text{AHE}}$  also changes the sign with temperature, we measured AHE for samples with  $x = 0.07$  and  $x = 0.15$ , in which a clear change in sign of  $\rho_{\text{SATM}}$  was observed at about 150 K and 250 K, respectively. In Fig. 4.23(b), we show the behavior of  $\rho_{\text{AHE}}$  with temperature for these two samples, which shows no sign change of  $\rho_{\text{AHE}}$  for either sample. However, this may be understood from the fact that  $\rho_{\text{SATM}}$  is a higher-order contribution, and in AHE this contribution is not the most significant one [see Eq. (3.19) and Eq. (4.6)].

Nevertheless, the sign change of  $\rho_{\text{SATM}}$  with composition and temperature occurs systematically. From the results of Sec. 4.1.3, it is known that the stoichiometric as-grown films exhibit a good long-range atomic order which also establishes the formation of a  $\text{D0}_3$  crystal structure. The  $\text{D0}_3$  crystal structure belongs to the same crystal class as that of Fe, i.e.,  $\mathbf{m3m}$ . Hence from a symmetry argument, the same sign of  $\rho_{\text{SATM}}$  for Fe and the “most stoichiometric”  $\text{Fe}_3\text{Si}$  films is expected and is observed in the experiment as well. This indicates a correlation between the two phenomena (the negative sign of  $\rho_{\text{SATM}}$  and the establishment of a perfect atomic ordering). A microscopic theory of electron transport may provide further understanding of this possible correlation. In principle, when all the restrictions imposed by the band structure symmetry are included in such a calculation, the form obtained for the PHE should be identical to that found from the phenomenological model.

**Symmetric component** For  $\text{Fe}_3\text{Si}$  films on  $\text{GaAs}(001)$  substrates a change in sign of the symmetric component of the PHE was recently reported [196] for nearly stoichiometric

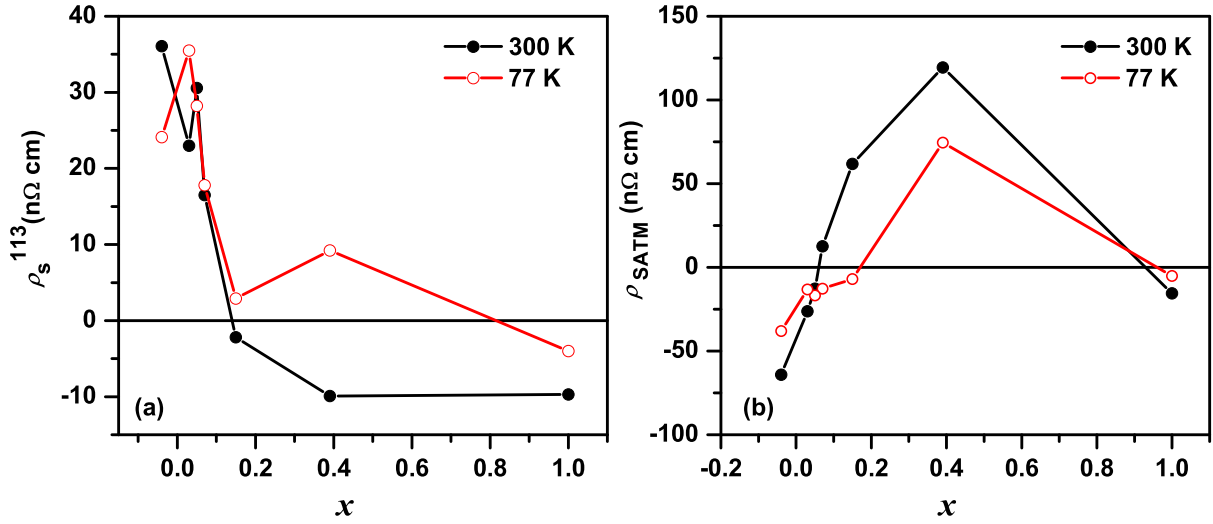


Figure 4.24: Temperature and composition dependence of the (a) symmetric PHE amplitude  $\rho_s^{113}$  and (b) antisymmetric amplitude  $\rho_{SATM} = 2(\rho_{SATM}^0 + \rho_{SATM}^1)$  measured in [113]-oriented Fe<sub>3</sub>Si films obtained from the fitting of  $\rho_{xy}$  at a saturating field.

samples. In the case of Fe<sub>3</sub>Si(113) films, the symmetric component in PHE  $\rho_s^{PHE}$  also shows a very interesting composition dependence as seen in Fig. 4.24(a), which shows the variation of  $\rho_s^{PHE}$  at 300 K and 77 K. The symmetric component was obtained by fitting the angular dependence of PHE at a saturating field with Eq. (4.5). Alternatively, the symmetric amplitude  $\rho_s^{PHE}$  can be derived from a separation of the symmetric and antisymmetric components as discussed before. For comparison a similar plot for the ASC  $\rho_{SATM} = 2(\rho_{SATM}^0 + \rho_{SATM}^1)$  is also shown in Fig. 4.24(b). As can be seen, the symmetric component  $\rho_s^{PHE}$  is negative for Fe and off-stoichiometric Fe<sub>3</sub>Si samples and then increases with decreasing  $x$ . Unlike the case of [001]-oriented films, a sign change of the symmetric component with temperature is found for off-stoichiometric samples. This different behavior of sign change in the symmetric component of PHE can be understood within the phenomenological model of Sec. 3.5.2 by comparing the PHE of [113]-oriented samples to that of the [001]-oriented samples in Ref [196]. In Sec. 3.5.3, the PHE of the [113]-oriented films was shown to be:

$$\rho_{21}^{(113)} = \frac{(9C_1 + 2C_4)}{22} \sin 2\theta_M + \frac{9(a_{12223} - a_{11123})}{11\sqrt{2}} \cos \theta_M - \frac{42\sqrt{2}(a_{12223} - a_{11123})}{121} \cos^3 \theta_M. \quad (4.7)$$

Using the same approach, the PHE of the [001]-oriented film with current along [110] can be easily shown to be [149]:

$$\rho_{21}^{(001)/[110]} = \frac{C_1}{2} \sin 2\theta_M. \quad (4.8)$$

Note that in both the above equations we have considered terms up to 3rd order in  $\alpha_i$ s. These equations show that the symmetric PHE amplitudes measured in the (001) and (113) cases, namely  $\rho_s^{001} = \frac{C_1}{2}$  and  $\rho_s^{113} = \frac{(9C_1 + 2C_4)}{22}$  are phenomenologically different.

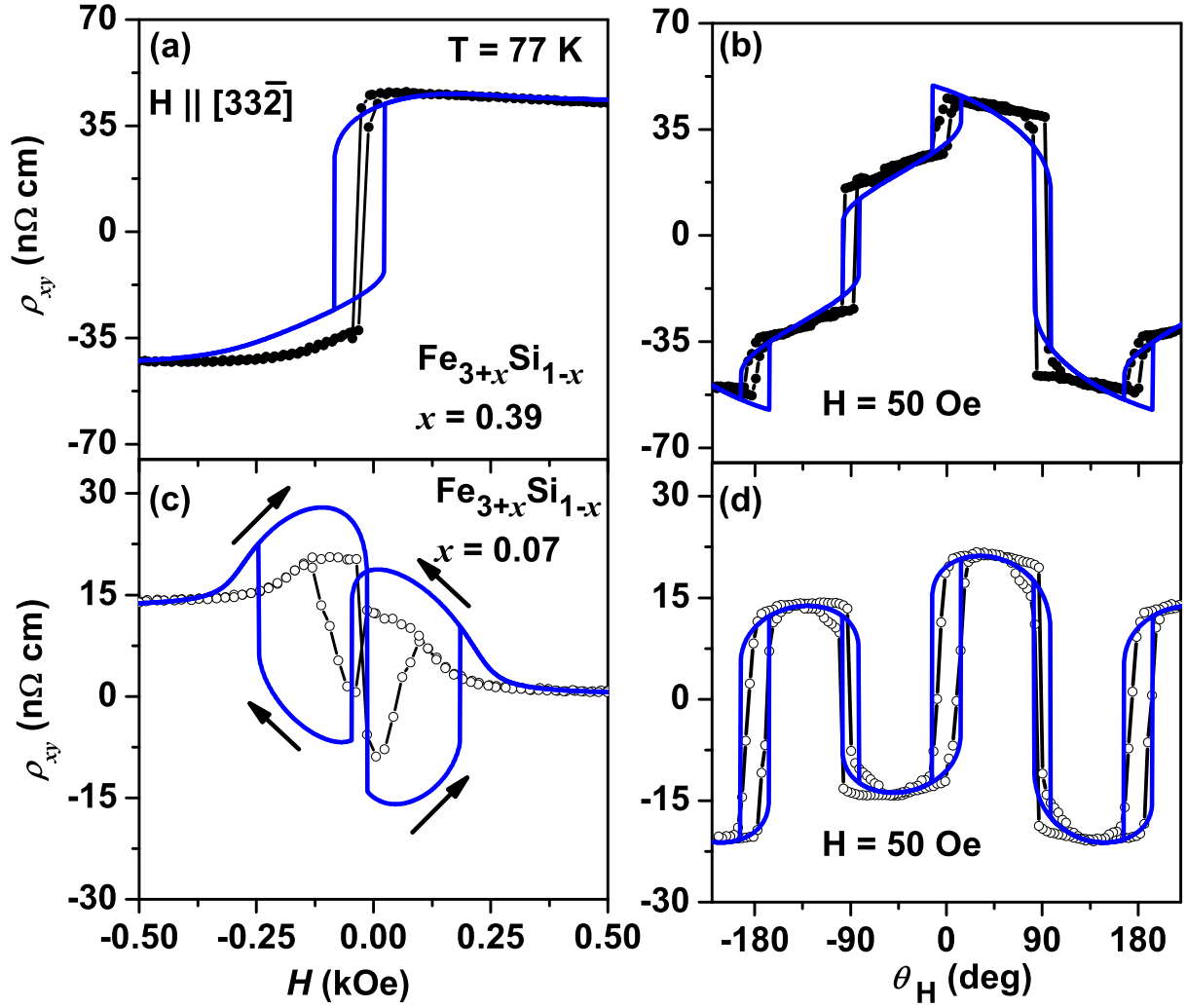


Figure 4.25: Field dependencies along  $[3\bar{3}2]$  (first column) and the low-field angular dependencies (second column) for two samples with  $x = 0.39$  (first row) and  $0.07$  (second row) measured at 77 K. Symbols indicate experimental data and the thick lines indicate simulation of the PHE as explained in the text.

Thus the change in sign in the case of an  $[001]$ -oriented film does not necessarily imply a similar sign change in  $[113]$ -oriented films. Nevertheless, the sign of different constants in transport measurements is a subtle phenomenon brought about by the spin-orbit interaction. The physical origin of the sign change of the symmetric component in these  $[113]$ -oriented films is not understood yet.

### Low field behavior and shape of the PHE curves

Due to the change in the magnitude and sign of the different components in the PHE, the shape of the PHE curves was found to change significantly. To demonstrate this phenomenon, we show in Fig. 4.25 the field dependencies (first column) and the low-field angular dependencies (second column) for two samples with  $x = 0.39$  (first row) and  $0.07$  (second row) at 77 K. The shape of the PHE curves for the sample with  $x = 0.39$

is similar to that of the Fe films, but changes significantly for the sample with  $x = 0.07$ . The hysteresis behavior for the sample with  $x = 0.07$  is completely different as indicated by the arrows.

To understand the different shapes of the PHE in this figure we calculate the PHE curves similar to the Fe films. The calculation was performed using Eq. (3.20) with  $\theta_M$ , calculated using the SWM for magnetization reversal as discussed in Sec 3.4.7 and Sec 3.4.3. The calculated curves are shown as solid thick lines. A good qualitative agreement to the experiment can be clearly seen. Since the SWM is valid for both samples, the different hysteresis behavior at low field or more appropriately the different shapes of the PHE curves are merely the result of the differences between the symmetric and antisymmetric amplitudes of the PHE. In fact, the value of symmetric and antisymmetric PHE amplitudes for these samples at 77 K from Fig. 4.23 and Fig. 4.24, are:  $\rho_s^{\text{PHE}} = 9 \text{ n}\Omega \text{ cm}$ ,  $\rho_{\text{SATM}} = 36 \text{ n}\Omega \text{ cm}$  for  $x = 0.39$ ; and  $\rho_s^{\text{PHE}} = 18 \text{ n}\Omega \text{ cm}$ ,  $\rho_{\text{SATM}} = -6.5 \text{ n}\Omega \text{ cm}$  for  $x = 0.07$ . Thus  $\rho_s^{\text{PHE}}$  has the same sign but  $\rho_{\text{SATM}}$  is of opposite sign and significantly different for the two samples. These parameters, along with anisotropic parameters such as  $r$  and  $K_1/M_s$ , (from Fig. 4.17) were used in the simulation .

### 4.3.3 Summary: Magnetotransport properties of $\text{Fe}_{3+x}\text{Si}_{1-x}$ films

1. In the magnetotransport measurements of  $\text{Fe}_3\text{Si}$  films, we reproduce the striking observation of an ASC in the planar Hall effect.
2. The dependence of PHE on the composition  $x$  shows a negative sign for the ASC of the PHE in stoichiometric  $\text{Fe}_3\text{Si}$  samples, similarly to Fe films. The improvement in atomic ordering for stoichiometric samples, which establishes the  $\text{D0}_3$  crystal structure, is proposed as a possible origin of the sign of the ASC.
3. The temperature dependence of the PHE of  $\text{Fe}_{3+x}\text{Si}_{1-x}$  films shows a sign reversal of both the symmetric and the antisymmetric components of the PHE for  $0.26 \leq x \leq 0.39$  and  $0.05 \leq x \leq 0.15$ , respectively. The sign reversal of the ASC occurs below a certain critical temperature that increases with increasing Si content.
4. All samples exhibit a negative value of the AMR amplitude in the examined range of temperatures which is opposite to that of Fe films.



# Chapter 5

## Summary

The work presented in this thesis is a unique effort to understand the growth and properties of ferromagnetic thin films on a low-symmetric surface, in particular Fe and Fe<sub>3</sub>Si on GaAs(113)A substrates. This material combination has the advantage of close lattice matching, which allows the growth of the [113] orientation of these films. The basic achievements of this work include the following: (i) establishment of the growth of Fe and Fe<sub>3</sub>Si on the high-index surface of GaAs(113)A substrates by MBE, (ii) study of the magnetic properties on the low-symmetric surface, which also provide the understanding to the incompletely understood uniaxial magnetic anisotropy (UMA) of Fe/GaAs system, (iii) substantiate correlation between structural and magnetic properties, and (iv) an important finding of an antisymmetric component (ASC) in the planar Hall effect (PHE) due to the reduced symmetry of the [113] orientation.

The growth of Fe (Sec. 3.3) and Fe<sub>3</sub>Si films (Sec. 4.1) is optimized at growth temperatures of 0 and 250 °C, respectively, at which the layers exhibit high crystal quality and smooth interface/surface. The structural properties of these Fe(113) and Fe<sub>3</sub>Si(113) films are shown to be comparable to the corresponding films on GaAs(001) substrates. The optimized growth temperature for Fe films, and the optimized growth rate for the Fe<sub>3</sub>Si films are found lower compared to the corresponding films on GaAs(001) substrates. The stability of the Fe<sub>3+x</sub>Si<sub>1-x</sub> phase over a wide range of composition, around the Fe<sub>3</sub>Si stoichiometry, is also demonstrated.

The magnetic properties of the Fe and Fe<sub>3</sub>Si films are studied with special emphasis on the study of the magnetic anisotropy as a function of thickness (for Fe films, Sec. 3.4.3), growth conditions (for Fe<sub>3</sub>Si films, Sec. 4.2.1), and composition (for Fe<sub>3</sub>Si films, Sec. 4.2.2). The evolution of the in-plane magnetic anisotropy of the [113]-oriented Fe films with thickness exhibits two regions of magnetic anisotropy, which is qualitatively similar to the case of Fe films on GaAs(001) substrates. First, for Fe film thicknesses  $\leq 50$  MLs, an in-plane UMA with the easy axis along the in-plane  $\langle 3\bar{3}2 \rangle$  axes is observed. Second, for Fe film thicknesses  $\geq 70$  MLs, a four-fold magnetic anisotropy with the easy axis along the in-plane  $\langle 03\bar{1} \rangle$  axes is observed. The reorientation of the easy axis from  $[3\bar{3}2]$  to the in-plane  $\langle 03\bar{1} \rangle$  axes is found to take place between 50 and 70 MLs, the same thickness range where the relaxation of the layer starts. The hard axis of the UMA is found to lie along the in-plane  $\langle \bar{1}10 \rangle$  axes, similarly to that of the Fe films on GaAs(001) substrates. The existence of an out-of-plane perpendicular magnetic anisotropy is also detected in ultrathin Fe films. Similarly to Fe on GaAs(001), the results provide evidence for the interfacial origin of the in-plane uniaxial and out-of-plane perpendicular magnetic anisotropy. The interfacial



contribution of both the uniaxial and the perpendicular anisotropy constants derived from the thickness-dependent study are found to be independent of the [113] orientation and are hence an inherent property of the Fe/GaAs interface. The results thus provide an understanding to the UMA of the Fe/GaAs system and support the hypothesis of anisotropic bonding between Fe and As or Ga at the interface as the possible origin of the UMA. In addition, the onset of ferromagnetism, spin-reorientation transition and the thickness dependent behavior of anisotropy constants shows correlation between structural and magnetic properties.

The growth conditions (Sec. 4.2.1) and composition dependence (Sec. 4.2.2) of the magnetic anisotropy in Fe<sub>3</sub>Si (35–50 nm) on GaAs(113)A are found to exhibit a complex behavior. In general, all the samples, irrespective of composition and growth conditions, exhibited a combination of the expected four-fold magnetic anisotropy and an additional UMA. The additional UMA was found for at least two different cases. First, for samples grown under optimized growth conditions, an additional UMA (with easy axis along  $\langle\bar{1}10\rangle$ ) was found, which increases with increasing Si content. Second, for off-stoichiometric composition, a UMA was observed for samples grown at 200 and 400 °C with easy axes opposite to each other. The origin of these UMAs is incompletely understood so that further studies such as the thickness dependence, the role of strain and/or atomic ordering and investigation of interface structure, need to be performed. Nevertheless, the four-fold magnetic anisotropy shows a very systematic composition dependence and the four-fold magnetic anisotropy constant  $K_1$  is found to decrease with Si content with a positive sign over the entire range of composition studied. The decrease of  $K_1$  with increasing Si content is attributed to the reduced symmetry environment of Fe atoms upon adding Si.

Magnetotransport measurements were focused on the study of anisotropic magnetoresistance (AMR), the PHE and in some cases the anomalous Hall effect as a function of composition, measurement temperature and thickness (for Fe films) (Sec. 3.5 and Sec. 4.3). In both cases of Fe and Fe<sub>3</sub>Si films on GaAs(113)A substrates, a striking observation of an ASC in the PHE is found. The ASC refers to a change in the sign of the PHE upon reversing the direction of the applied field, which is never observed on an [001]-oriented film. This ASC shows a maximum along the major in-plane  $\langle 33\bar{2} \rangle$  axes and vanishes along the other major in-plane  $\langle\bar{1}10\rangle$  axes. AMR was found to be a symmetric function of the applied field direction in both Fe and Fe<sub>3</sub>Si films, but a negative sign of the anisotropic magnetoresistivity was found for Fe<sub>3</sub>Si films in the whole range of composition studied. A phenomenological model based on the symmetry of the crystal provides a good explanation to both the ASC in the PHE as well as the symmetric AMR. The model shows that the ASC component arises from the antisymmetric part of the magnetoresistivity tensor and is basically a second-order Hall effect. Pure Fe films and nearly stoichiometric Fe<sub>3</sub>Si films exhibit an identical sign of the ASC. The improvement of atomic ordering in stoichiometric samples, which establishes the D0<sub>3</sub> crystal structure is proposed as a possible origin of the sign of this ASC. In addition, the temperature dependence of PHE of the Fe<sub>3+x</sub>Si<sub>1-x</sub>(113) films shows a sign reversal of both the symmetric and the antisymmetric PHE components for  $0.26 \leq x \leq 0.39$  and  $0.05 \leq x \leq 0.15$ , respectively. The sign reversal of the ASC in slightly off-stoichiometric samples ( $0.05 \leq x \leq 0.15$ ) occurs below a certain critical temperature that increases with increasing Si content.

# Appendix A

## Complete magnetoresistivity tensor elements for the crystal class **m3m**

In matrix notation the magnetoresistivity tensor  $\rho_{ij}$  can be written as:

$$\rho = \begin{pmatrix} \rho_{11} & \rho_{12} & \rho_{13} \\ \rho_{21} & \rho_{22} & \rho_{23} \\ \rho_{31} & \rho_{32} & \rho_{33} \end{pmatrix}. \quad (\text{A.1})$$

The elements  $\rho_{ij}$  can be expressed in terms of the tensors  $a_{ij}$ ,  $a_{kij}$ ,  $a_{kl ij}$  etc.. Neumann's principle states that any type of symmetry exhibited by the point group of the crystal group is possessed by every physical properties of the crystal. Thus elements  $a_{ij}$ ,  $a_{kij}$ ,  $a_{kl ij}$  etc..which represents a macroscopic property of the crystal must reflect the symmetry of the crystal. In other words, these tensors elements simplify due to the crystal symmetry. For the crystal class **m3m**, the non-zero elements are tabulated by Birss [38]. McGuire and Potter, [39] derived the elements of the symmetric magnetoresistivity tensor  $\rho_{ij}^s$  through fifth order for the crystal class **m3m**. The antisymmetric magnetoresistivity tensor  $\rho_{ij}^a$  can be derived using the non-zero coefficients of the tensors  $a_{kij}$ ,  $a_{klmij}$ ... etc listed by Birss [38]. The resulting elements  $\rho_{ij}$  of Eq. (A.1) can be written as follows:

$$\begin{aligned}
\rho_{11} &= C_0 + C_1\alpha_1^2 + C_2\alpha_1^4 + C_3\alpha_2^2\alpha_3^2 \\
\rho_{12} &= C_4\alpha_1\alpha_2 + C_5\alpha_1\alpha_2\alpha_3^2 + (a_{123}\alpha_3 + a_{12223}\alpha_1^2\alpha_3 \\
&\quad + a_{12223}\alpha_2^2\alpha_3 + a_{11123}\alpha_3^3) \\
\rho_{13} &= C_4\alpha_1\alpha_3 + C_5\alpha_1\alpha_3\alpha_2^2 - (a_{123}\alpha_2 + a_{12223}\alpha_1^2\alpha_2 \\
&\quad + a_{11123}\alpha_2^3 + a_{12223}\alpha_2\alpha_3^2) \\
\rho_{21} &= C_4\alpha_1\alpha_2 + C_5\alpha_1\alpha_2\alpha_3^2 - (a_{123}\alpha_3 + a_{12223}\alpha_1^2\alpha_3 \\
&\quad + a_{12223}\alpha_2^2\alpha_3 + a_{11123}\alpha_3^3) \\
\rho_{22} &= C_0 + C_1\alpha_2^2 + C_2\alpha_2^4 + C_3\alpha_3^2\alpha_1^2 \\
\rho_{23} &= C_4\alpha_2\alpha_3 + C_5\alpha_2\alpha_3\alpha_1^2 + (a_{123}\alpha_1 + a_{11123}\alpha_1^3 \\
&\quad + a_{12223}\alpha_1\alpha_2^2 + a_{12223}\alpha_1\alpha_3^2) \\
\rho_{31} &= C_4\alpha_1\alpha_3 + C_5\alpha_1\alpha_3\alpha_2^2 + (a_{123}\alpha_2 + a_{12223}\alpha_1^2\alpha_2 \\
&\quad + a_{11123}\alpha_2^3 + a_{12223}\alpha_2\alpha_3^2) \\
\rho_{32} &= C_4\alpha_2\alpha_3 + C_5\alpha_2\alpha_3\alpha_1^2 - (a_{123}\alpha_1 + a_{11123}\alpha_1^3 \\
&\quad + a_{12223}\alpha_1\alpha_2^2 + a_{12223}\alpha_1\alpha_3^2) \\
\rho_{33} &= C_0 + C_1\alpha_3^2 + C_2\alpha_3^4 + C_3\alpha_1^2\alpha_2^2,
\end{aligned} \tag{A.2}$$

where  $C_0, C_1, C_2, C_3, C_4$  and  $C_5$  are short-hand notations of McGuire and Potter [39] for the coefficients in the symmetric part of magnetoresistivity tensor  $\rho_{ij}^s$  given by the following equations:

$$\begin{aligned}
C_0 &= a_{11} + a_{1122} + a_{111122} \\
C_1 &= a_{1111} - a_{1122} - 2a_{111122} + a_{112211} \\
C_2 &= a_{111111} + a_{111122} - a_{112211} \\
C_3 &= a_{112233} - 2a_{111122} \\
C_4 &= a_{2323} + a_{111212} \\
C_5 &= a_{112323} - a_{111212}.
\end{aligned} \tag{A.3}$$

The factors in the parentheses of Eq. (A.2) arise from the antisymmetric part of the tensor  $\rho_{ij}^a$ . For the diagonal elements, the antisymmetric part is zero, whereas the off-diagonal elements satisfy the following relation.

$$\rho_{ij}^a = -\rho_{ji}^a, \text{ when } i \neq j \tag{A.4}$$

# Appendix B

## Transformation into the (113) system

We use the following matrix  $l$  which transforms the (001) basis vector system to the basis vector system of (113):

$$l = \begin{pmatrix} \frac{3}{\sqrt{22}} & \frac{3}{\sqrt{22}} & -\sqrt{\frac{2}{11}} \\ -\frac{1}{\sqrt{2}} & \frac{1}{\sqrt{2}} & 0 \\ \frac{1}{\sqrt{11}} & \frac{1}{\sqrt{11}} & \frac{3}{\sqrt{11}} \end{pmatrix}. \quad (\text{B.1})$$

The elements of this matrix  $l_{ij}$  are determined by the relative orientation of the old and new sets of axes, e.g.,  $l_{12} = \cos \widehat{x_2 O x'_1}$ , where  $Ox_2$  and  $Ox'_1$  are the old  $y$ -axis and the new  $x$ -axis, respectively (see Birss [38] for details). In our case  $l_{12}$  presents the cosine of the angle between the  $[010]$  and the  $[33\bar{2}]$  axis. According to the measurements, we choose the new  $x$ -axis along  $[33\bar{2}]$ ,  $y$ -axis along  $[\bar{1}10]$  and  $z$ -axis along  $[113]$ . To find the measured planar Hall resistivity in the new coordinate system we need to use the transformation properties of a second rank tensor [38], which is given by:

$$\rho'_{ij} = l_{ip} l_{jq} \rho_{pq}. \quad (\text{B.2})$$

Using Eqs. (B.1) and (B.2), the measured planar Hall resistivity in the (113) system,  $\rho_{21}^{(113)}$ , can now be derived:

$$\begin{aligned} \rho_{21}^{(113)} &= \frac{3}{2\sqrt{11}}(\rho_{21} + \rho_{22} - \rho_{11} - \rho_{12}) \\ &\quad + \frac{1}{\sqrt{11}}(\rho_{13} - \rho_{23}). \end{aligned} \quad (\text{B.3})$$

Since the demagnetization energy of these  $\text{Fe}_3\text{Si}$  films is rather large, the magnetization  $\mathbf{M}$  is restricted to the (113) plane. In this case, the direction cosines of  $\mathbf{M}$  can be shown to be  $\alpha_1 = (3/\sqrt{22}) \cos \theta_M - (1/\sqrt{2}) \sin \theta_M$ ,  $\alpha_2 = (3/\sqrt{22}) \cos \theta_M + (1/\sqrt{2}) \sin \theta_M$ ,  $\alpha_3 = -(\sqrt{2/11}) \cos \theta_M$ , where  $\theta_M$  is measured with respect to the  $[33\bar{2}]$  axis. Using these direction cosines in Eqs. A.2, we can derive the measured planar Hall resistivity for the case of  $[113]$ -oriented films in terms of  $\theta_M$ :

$$\begin{aligned}
\rho_{21}^{(113)} = & \frac{9C_1}{11} \cos \theta_M \sin \theta_M + \frac{81C_2}{121} \cos^3 \theta_M \sin \theta_M \\
& + \frac{9C_2}{11} \cos \theta_M \sin^3 \theta_M - \frac{18C_3}{121} \cos^3 \theta_M \sin \theta_M \\
& + \frac{2C_4}{11} \cos \theta_M \sin \theta_M - \frac{9C_5}{121} \cos^3 \theta_M \sin \theta_M \\
& + \frac{C_5}{11} \cos \theta_M \sin^3 \theta_M + \frac{15(a_{12223} - a_{11123})}{121\sqrt{2}} \cos^3 \theta_M \\
& + \frac{9(a_{12223} - a_{11123})}{11\sqrt{2}} \cos \theta_M \sin^2 \theta_M.
\end{aligned} \tag{B.4}$$

This equation is valid up to fourth-order contribution and contains both symmetric and antisymmetric contributions. The symmetric part contains the coefficients  $C_i$ 's. Note that terms containing the coefficients  $C_2$ ,  $C_3$  and  $C_5$  are fourth-order contribution of  $\alpha_i$  [see Eq. (A.2)]. Other symmetric terms containing the coefficients  $C_1$  and  $C_4$  are second-order contributions of  $\alpha_i$ . The antisymmetric part contains tensor elements  $a_{12223}$  and  $a_{11123}$  are third-order contributions of  $\alpha_i$ . Thus, if we consider terms up to third-order in  $\alpha_i$ , we can write the above equation in the following form:

$$\begin{aligned}
\rho_{21}^{(113)} = & \frac{(9C_1 + 2C_4)}{22} \sin 2\theta_M + \frac{15(a_{12223} - a_{11123})}{121\sqrt{2}} \cos^3 \theta_M \\
& + \frac{9(a_{12223} - a_{11123})}{11\sqrt{2}} \cos \theta_M \sin^2 \theta_M.
\end{aligned} \tag{B.5}$$

which can also be expressed in the following form:

$$\begin{aligned}
\rho_{21}^{(113)} = & \frac{(9C_1 + 2C_4)}{22} \sin 2\theta_M + \frac{9(a_{12223} - a_{11123})}{11\sqrt{2}} \cos \theta_M \\
& - \frac{42\sqrt{2}(a_{12223} - a_{11123})}{121} \cos^3 \theta_M.
\end{aligned} \tag{B.6}$$

# Bibliography

- [1] K. Jacobi, L. Geelhaar, and J. Márquez. *Appl. Phys. A*, 75:113, 2002.
- [2] J. Clarke. *Scientific American*, 271:46, 1994.
- [3] C. Daboo, R. J. Hicken, E. Gu, M. Gester, S. J. Gray, D. E. P. Eley, E. Ahmad, J. A. C. Bland, R. Ploessl, and J. N. Chapman. *Phys. Rev. B*, 51:15964, 1995.
- [4] E. G. Moroni, W. Wolf, J. Hafner, and R. Podlucky. *Phys. Rev. B*, 59:12860, 1999.
- [5] M. Hansen. *Constitution of Binary Alloys*. McGraw-Hill, New York, 1958.
- [6] R. P. Elliot. *Constitution of Binary Alloys, Suppl. 1*. McGraw-Hill, New York, 1965.
- [7] O. Brandt, P. Waltereit, and K. H. Ploog. *J. Phys. D*, 35:577, 2002.
- [8] M. Schulz. *Nature*, 399:729, 1999.
- [9] M. N. Baibich, J. M. Broto, A. Fert, F. Nguyen van Dau, F. Petroff, P. Etienne, G. Creuzet, A. Friederich, and J. Chazelas. *Phys. Rev. Lett.*, 61:2472, 1988.
- [10] G. Binasch, P. Grünberg, F. Saurenbach, and W. Zinn. *Phys. Rev. B*, 39:4828, 1989.
- [11] M. Julliere. *Phys. Lett. A*, 54:225, 1975.
- [12] *Science*, 282:1660, 1998.
- [13] S. Das Sarma, J. Fabian, X. Hu, and I. Žutić. *Superlattices Microstruct.*, 27:289, 2000.
- [14] S. A. Wolf, D. D. Awschalom, R. A. Buhrman, J. M. Daughton, S. von Molnár, M. L. Roukes, A. Y. Chtchelkanova, and D. M. Treger. *Science*, 294:1488, 2001.
- [15] M. Ziese and M. J. Thornton, editors. *Spin Electronics*. Springer-Verlag, Berlin Heidelberg New York, 1st edition, 2001.
- [16] D. D. Awschalom, D. Loss, and N. Samarth, editors. *Semiconductor Spintronics and Quantum Computation*. Springer-Verlag, Berlin Heidelberg New York, 1st edition, 2002.
- [17] D. Grundler. *Phys. World*, 15:39, 2002.
- [18] J. F. Gregg, I. Petej, E. Jouguelet, and C. Dennis. *J. Phys. D*, 35:121, 2002.
- [19] I. Žutić, J. Fabian, and S. Das Sarma. *Rev. Mod. Phys.*, 76:323, 2004.

- [20] G. Schmidt. *J. Phys. D*, 38:107, 2005.
- [21] S. Datta and B. Das. *Appl. Phys. Lett.*, 56:665, 1990.
- [22] R. Fiederling, M. Keim, G. Reuscher, W. Ossau, G. Schmidt, A. Waag, and L. W. Molenkamp. *Nature*, 402:787, 1999.
- [23] Y. Ohno, D. K. Young, B. Beschoten, F. Matsukura, H. Ohno, and D. D. Awschalom. *Nature*, 402:790, 1999.
- [24] H. J. Zhu, M. Ramsteiner, H. Kostial, M. Wassermeier, H.-P. Schönherr, and K. H. Ploog. *Phys. Rev. Lett.*, 87:016601, 2001.
- [25] A. T. Hanbicki, B. T. Jonker, G. Itskos, G. Kioseoglou, and A. Petrou. *Appl. Phys. Lett.*, 80:1240, 2002.
- [26] A. T. Hanbicki, O. M. J. van't Erve, R. Magno, G. Kioseoglou, C. H. Li, B. T. Jonker, G. Itskos, R. Mallory, M. Yasar, and A. Petrou. *Appl. Phys. Lett.*, 82:4092, 2003.
- [27] C. Adelmann, X. Lou, J. Strand, C. J. Palmstrøm, and P. A. Crowell. *Phys. Rev. B*, 71:121301, 2005.
- [28] T. Zega and M. Yasar. *APS Meeting Abstracts*, page 10008, 2005.
- [29] G. Wastlbauer and J. A. C. Bland. *Adv. Phys.*, 54:137, 2005.
- [30] S. Blügel. *Magnetism goes Nano*, page C1. Forschungszentrum, Institute für Festkörperforschung, Jülich, first edition, 2005.
- [31] G. Bihlmayer. *Magnetism goes Nano*, page C2.14. Forschungszentrum, Institute für Festkörperforschung, Jülich, first edition, 2005.
- [32] L. Néel. *J. Phys. Radium*, 15:225, 1954.
- [33] N. D. Mermin and H. Wagner. *Phys. Rev. Lett.*, 17:1133, 1966.
- [34] P. Bruno. *J. Appl. Phys.*, 64:3153, 1988.
- [35] R. Arias and D. L. Mills. *Phys. Rev. B*, 60:7395, 1999.
- [36] W. T. Geng, M. Kim, and A. J. Freeman. *Phys. Rev. B*, 63:245401, 2001.
- [37] A. J. Freeman and R. Wu. *J. Magn. Magn. Mater.*, 100:497, 1991.
- [38] R. R. Birss. *Symmetry and Magnetism*. North-Holland Publishing Company, Amsterdam, 1964.
- [39] T. McGuire and R.I. Potter. *IEEE Trans. Magn.*, 11:1018, 1975.
- [40] J. P. Jan. Galvanometric and Thermomagnetic effects in Metals. In F. Seitz and D. Turnbull, editors, *Solid State Physics*, volume 5, pages 1–96. Academic Press Inc., New York, 1957.

- [41] Y. C. Akgöz and G. A. Saunders. *J. Phys. C*, 8:1387, 1975.
- [42] Z. M. Wang, V. R. Yazdanpanah, J. L. Shultz, and G. J. Salamo. *Appl. Phys. Lett.*, 81:2965, 2002.
- [43] D. J. Chadi. *Phys. Rev. B*, 29:785, 1984.
- [44] R. C. Sangster. In R. K. Willardson and H. L. Goering, editors, *Compound Semiconductors*, volume 1, page 241. Reinhold, London, 1962.
- [45] R. Nötzel, N. N. Ledentsov, L. Däweritz, K. Ploog, and M. Hohenstein. *Phys. Rev. B*, 45:3507, 1992.
- [46] R. Nötzel. *Microelectron. J.*, 28:875, 1997.
- [47] R. Nötzel, J. Menniger, M. Ramsteiner, A. Trampert, H. P. Schönherr, L. Däweritz, and K. H. Ploog. *J. Cryst. Growth*, 175:1114, 1997.
- [48] R. Nötzel, U. Jahn, Z. Niu, A. Trampert, J. Fricke, H.-P. Schönherr, Th. Kurt, D. Heitmann, L. Däweritz, and K. H. Ploog. *Appl. Phys. Lett.*, 72:2002, 1998.
- [49] R. Nötzel, Z. C. Niu, M. Ramsteiner, H.-P. Schönherr, A. Trampert, L. Däweritz, and K. H. Ploog. *Nature*, 392:56, 1998.
- [50] R. Nötzel, Q. Gong, M. Ramsteiner, U. Jahn, K.-J. Friedland, , and K. H. Ploog. *Microelectron. J.*, 33:573, 2002.
- [51] K. Stiles and A. Kahn. *J. Vac. Sci. Technol. B*, 3:1089, 1985.
- [52] L. Ö. Olsson, M. Björkqvist, J. Kanski, L. Ilver, and P. O. Nilsson. *Surf. Sci.*, 366:121, 1996.
- [53] R. Nötzel, N. N. Ledentsov, L. Däweritz, M. Hohenstein, and K. Ploog. *Phys. Rev. Lett.*, 67:3812, 1991.
- [54] M. Wassermeier, J. Sudijono, M. D. Johnson, K. T. Leung, B. G. Orr, L. Däweritz, and K. Ploog. *Phys. Rev. B*, 51:14721, 1995.
- [55] W. Braun, O. Brandt, M. Wassermeier, L. Däweritz, and K. Ploog. *Appl. Surf. Sci.*, 104/105:35, 1996.
- [56] C. Setzer, J. Platen, P. Geng, W. Ranke, and K. Jacobi. *Surf. Sci.*, 377-379:125, 1997.
- [57] C. Setzer, J. Platen, W. Ranke, and K. Jacobi. *Surf. Sci.*, 419:291, 1999.
- [58] J. Platen, A. Kley, C. Setzer, K. Jacobi, P. Ruggerone, and M. Scheffler. *J. Appl. Phys.*, 85:3597, 1999.
- [59] O. Brandt, K. Kanamoto, Y. Tokuda, N. Tsukada, O. Wada, and J. Tanimura. *Phys. Rev. B*, 48:17599, 1993.
- [60] Y. Hsu, W. I. Wang, and T. S. Kuan. *Phys. Rev. B*, 50:4973, 1994.



- [61] Y. Hsu, W. I. Wang, and T. S. Kuan. *J. Vac. Sci. Technol. B*, 12:2584, 1994.
- [62] Y. Hsu, W. I. Wang, and T. S. Kuan. *J. Vac. Sci. Technol. B*, 14:2286, 1996.
- [63] H.-P. Schönherr, R. Nötzel, W. Ma, and K. H. Ploog. *J. Appl. Phys.*, 89:169, 2001.
- [64] K.-J. Friedland, R. Nötzel, H.-P. Schönherr, A. Riedel, H. Kostial, and K.H. Ploog. *Physica E*, 10:442, 2001.
- [65] L. Däweritz, L. Wan, B. Jenichen, C. Herrmann, J. Mohanty, A. Trampert, and K. H. Ploog. *J. Appl. Phys.*, 96:5056, 2004.
- [66] S. Fölsch, B.-Ch. Choi, and K. H. Rieder. *Phys. Rev. B*, 54:10855, 1996.
- [67] A. Y. Cho. *J. Vac. Sci. Technol.*, 8:S31, 1971.
- [68] A. Y. Cho. *Prog. Solid-State Chem.*, 10:157, 1975.
- [69] J. E. Mahan, K. M. Geib, G. Y. Robinson, and R. G. Long. *J. Vac. Sci. Technol. A*, 8:3692, 1990.
- [70] W. Braun. *Applied RHEED*. Springer-Verlag, Berlin and Heidelberg, first edition, 1999.
- [71] A. Ichimiya and Philip I. Cohen. *Reflection High Energy Electron Diffraction*. Cambridge University Press, Cambridge CB2 2RU, UK, first edition, 2004.
- [72] C. S. Lent and P. I. Cohen. *Phys. Rev. B*, 33:8329, 1986.
- [73] P. I. Cohen, P. R. Pukite, J. M. Van Hove, and C. S. Lent. *J. Vac. Sci. Technol. A*, 4:1251, 1986.
- [74] D. K. Bowen and B. K. Tanner. *High Resolution X-ray Diffractometry and Topography*. Taylor and Francis, London, first edition, 1998.
- [75] P. F. Fewster. *X-ray Scattering from Semiconductors*. Imperial College Press, London, 2nd edition, 2005.
- [76] P. F. Fewster. *Rep. Prog. Phys.*, 59:1339, 1996.
- [77] A. Krost, G. Bauer, and J. Woitok. High Resolution X-Ray Diffraction. In G. Bauer and W. Richter, editors, *Optical Characterization of Epitaxial Semiconductor Layers*. Springer-Verlag, New York, 1996.
- [78] L. G. Parratt. *Phys. Rev.*, 95:359, 1954.
- [79] S. K. Sinha, E. B. Sirota, S. Garoff, and H. B. Stanley. *Phys. Rev. B*, 38:2297, 1988.
- [80] For more information see, <http://www.panalytical.com/>.
- [81] J. Kerr. *Philos. Mag.*, 3:339, 1877.
- [82] Z. Q. Qiu and S. D. Bader. *Rev. Sci. Instrum.*, 71:1243, 2000.

- [83] Z. Q. Qiu and S. D. Bader. *J. Magn. Magn. Mater.*, 200:664, 1999.
- [84] P. N. Argyres. *Phys. Rev.*, 97:334, 1955.
- [85] J. M. Florczak and E. Dan Dahlberg. *J. Appl. Phys.*, 67:7520, 1990.
- [86] C.-Y. You and S.-C. Shin. *Appl. Phys. Lett.*, 69:1315, 1996.
- [87] MPMS from Quantum Design, see <http://www.qdusa.com/products/mpms.html>.
- [88] R. R. Birss. *Symmetry and Magnetism*, page 70. North-Holland Publishing Company, Amsterdam, 1964.
- [89] J. R. Waldrop and R. W. Grant. *Appl. Phys. Lett.*, 34:630, 1979.
- [90] G. A. Prinz and J. J. Krebs. *Appl. Phys. Lett.*, 39:397, 1981.
- [91] G. A. Prinz, G. T. Rado, and J. J. Krebs. *J. Appl. Phys.*, 53:2087, 1982.
- [92] K. Hathaway and G. A. Prinz. *J. Appl. Phys.*, 53:1913, 1982.
- [93] J. J. Krebs, F. J. Rachford, P. Lubitz, and G. A. Prinz. *J. Appl. Phys.*, 53:8058, 1982.
- [94] F. J. Rachford, G. A. Prinz, J. J. Krebs, and K. B. Hathaway. *J. Appl. Phys.*, 53:7966, 1982.
- [95] T. R. McGuire, J. J. Krebs, and G. A. Prinz. *J. Appl. Phys.*, 55:2505, 1984.
- [96] C. Vittoria, F. G. Rachford, J. J. Krebs, and G. A. Prinz. *J. Appl. Phys.*, 56:1247, 1984.
- [97] C. Vittoria, F. J. Rachford, J. J. Krebs, and G. A. Prinz. *Phys. Rev. B*, 30:3903, 1984.
- [98] S. B. Qadri, M. Goldenberg, G. A. Prinz, and J. M. Ferrari. *J. Vac. Sci. Technol. B*, 3:718, 1985.
- [99] K. Schroder, G. A. Prinz, K.-H. Walker, and E. Kisker. *J. Appl. Phys.*, 57:3669, 1985.
- [100] J. J. Krebs, B. T. Jonker, and G. A. Prinz. *J. Appl. Phys.*, 61:2596, 1987.
- [101] E. D. Dahlberg, K. Riggs, and G. A. Prinz. *J. Appl. Phys.*, 63:4270, 1988.
- [102] M. Rubinstein, F. J. Rachford, W. W. Fuller, and G. A. Prinz. *Phys. Rev. B*, 37:8689, 1988.
- [103] K. T. Riggs, E. D. Dahlberg, and G. A. Prinz. *Phys. Rev. B*, 41:7088, 1990.
- [104] E. M. Kneedler, B. T. Jonker, P. M. Thibado, R. J. Wagner, B. V. Shanabrook, and L. J. Whitman. *Phys. Rev. B*, 56:8163, 1997.
- [105] J. M. Florczak and E. D. Dahlberg. *Phys. Rev. B*, 44:9338, 1991.

- [106] A. Filipe, A. Schuhl, and P. Galtier. *Appl. Phys. Lett.*, 70:129, 1997.
- [107] M. Zölfl, M. Brockmann, M. Köhler, S. Kreuzer, T. Schweinböck, S. Miethaner, F. Bensch, and G. Bayreuther. *J. Magn. Magn. Mater.*, 175:16, 1997.
- [108] Y. B. Xu, E. T. M. Kernohan, D. J. Freeland, A. Ercole, M. Tselepi, and J. A. C. Bland. *Phys. Rev. B*, 58:890, 1998.
- [109] G. Schmidt, D. Ferrand, L. W. Molenkamp, A. T. Filip, and B. J. van Wees. *Phys. Rev. B*, 62:R4790, 2000.
- [110] Y. B. Xu, E. T. M. Kernohan, D. J. Freeland, M. Tselepi, A. Ercole, and J. A. C. Bland. *J. Magn. Magn. Mater.*, 198:703, 1999.
- [111] M. Gester, C. Daboo, R. J. Hicken, S. J. Gray, A. Ercole, and J. A. C Bland. *J. Appl. Phys.*, 80:347, 1996.
- [112] B. Lépine, C. Lallaizon, S. Ababou, A. Guivarc'h, S. Députier, A. Filipe, F. N. Van Dau, A. Schuhl, F. Abel, and C. Cohen. *J. Cryst. Growth*, 201-202:702, 1999.
- [113] Y. Chye, V. Huard, M. E. White, and P. M. Petroff. *Appl. Phys. Lett.*, 80:449, 2002.
- [114] R. Moosbühler, F. Bensch, M. Dumm, and G. Bayreuther. *J. Appl. Phys.*, 91:8757, 2002.
- [115] J. Herfort, W. Braun, A. Trampert, H.-P. Schönherr, and K. H. Ploog. *Appl. Surf. Sci.*, 237:181, 2004.
- [116] O. Thomas, Q. Shen, P. Schieffer, N. Tournierie, and B. Lépine. *Phys. Rev. Lett.*, 90:017205, 2003.
- [117] M. C. D. Santos, J. Geshev, J. E. Schmidt, S. R. Teixeira, and L. G. Pereira. *Phys. Rev. B*, 61:1311, 2000.
- [118] A. J. Melmed and J. J. Carroll. *J. Vac. Sci. Technol.*, 10:164, 1973.
- [119] F. Bensch, G. Garreau, R. Moosbühler, and G. Bayreuther. *J. Appl. Phys.*, 89:7133, 2001.
- [120] W. Kipferl, M. Dumm, M. Rahm, and G. Bayreuther. *J. Appl. Phys.*, 93:7601, 2003.
- [121] J. Mathon and S. B. Ahmad. *Phys. Rev. B*, 37:660, 1988.
- [122] M. Przybylski, J. Korecki, and U. Gradmann. *Appl. Phys. A: Solids Surf.*, 52:33, 1991.
- [123] M. Brockmann, L. Pfau, G. Lugert, and G. Bayreuther. *Mater. Res. Soc. Symp. Proc.*, 313:685, 1993.
- [124] W. Kipferl, M. Sperl, T. Hagler, R. Meier, and G. Bayreuther. *J. Appl. Phys.*, 97:10B313, 2005.
- [125] G. Lugert and G. Bayreuther. *Phys. Rev. B*, 38:11068, 1988.

- [126] C. M. Boubeta, A. Cebollada, J. F. Calleja, C. Contreras, F. Peiró, and A. Cornet. *J. Appl. Phys.*, 93:2126, 2003.
- [127] E. Gu, J. A. C. Bland, C. Daboo, M. Gester, L. M. Brown, R. Ploessl, and J. N. Chapman. *Phys. Rev. B*, 51:3596, 1995.
- [128] B. D. Cullity. *Introduction to Magnetic Materials*, page 234. Addison-Wesley, Reading, MA, first edition, 1972.
- [129] S. McPhail, C. M. Gürtler, F. Montaigne, Y. B. Xu, M. Tselepi, and J. A. C. Bland. *Phys. Rev. B*, 67:024409, 2003.
- [130] M. Brockmann, M. Zöfl, S. Miethaner, and G. Bayreuther. *J. Magn. Magn. Mater.*, 198-199:384, 1999.
- [131] J. Herfort, H.-P. Schönherr, P. K. Muduli, and K. H. Ploog. In *International Symposium on Compound Semiconductors: Post-Conference Proceedings*, edited by M. R. Melloch and C. Tu,, pages 96–101, IEEE, Piscataway, 2004.
- [132] R. Höllinger, M. Zöfl, R. Moosbühler, and G. Bayreuther. *J. Appl. Phys.*, 89:7136, 2001.
- [133] T. L. Monchesky, B. Heinrich, R. Urban, K. Myrtle, M. Klaua, and J. Kirschner. *Phys. Rev. B*, 60:10242, 1999.
- [134] R. Nötzel and K. Ploog. *J. Vac. Sci. Technol. A*, 10:617, 1992.
- [135] J. Chen and J. L. Erskine. *Phys. Rev. Lett.*, 68:1212, 1992.
- [136] R. K. Kawakami, E. J. Escorcia-Aparicio, and Z. Q. Qiu. *Phys. Rev. Lett.*, 77:2570, 1996.
- [137] R. K. Kawakami, M. O. Bowen, Hyuk J. Choi, E. J. Escorcia-Aparicio, and Z. Q. Qiu. *Phys. Rev. B*, 58:R5924, 1998.
- [138] C. Daboo, R. J. Hicken, D. E. P. Eley, M. Gester, S. J. Gray, A. J. R. Ives, and J. A. C. Bland. *J. Appl. Phys.*, 75:5586, 1994.
- [139] R. P. Cowburn, S. J. Gray, J. Ferre, J. A. C. Bland, and J. Miltat. *J. Appl. Phys.*, 78:7210, 1995.
- [140] R. P. Cowburn, S. J. Gray, and J. A. C. Bland. *Phys. Rev. Lett.*, 79:4018, 1997.
- [141] G. Bottoni, D. Candolfo, and A. Cecchetti. *J. Appl. Phys.*, 81:3794, 1997.
- [142] U. Gradmann. *J. Magn. Magn. Mater.*, 6:173, 1977.
- [143] E. Schlömann. *J. Appl. Phys.*, 41:1617, 1970.
- [144] Y. B. Xu, M. Tselepi, C. M. Guertler, C. A. F. Vaz, G. Wastlbauer, J. A. C. Bland, E. Dudzik, and G. van der Laan. *J. Appl. Phys.*, 89:7156, 2001.
- [145] Y. Zhai, L. Shi, W. Zhang, Y. X. Xu, M. Lu, H. R. Zhai, W. X. Tang, X. F. Jin, Y. B. Xu, and J. A. C. Bland. *J. Appl. Phys.*, 93:7622, 2003.

- [146] K.-J. Friedland, J. Herfort, P. K. Muduli, H.-P. Schönherr, and K. H. Ploog. *J. Supercond.* 18 (2005) In press.
- [147] D. A. Thompson, L. T. Romankiw, and A. F. Mayadas. *IEEE Trans. Magn.*, 11: 1039, 1975.
- [148] I. A. Campbell and A. Fert. *Transport Properties of Ferromagnets.* volume 3, page 747. North-Holland Publishing Company, 1982.
- [149] T. T. Chen and V. A. Marsocci. *Physica*, 59:498, 1972.
- [150] T. T. Chen and V. A. Marsocci. *Solid State Commun.*, 10:783, 1972.
- [151] J. F. Nye. *Physical properties of crystals: their representation by tensors and matrices*, page 9. Oxford University Press, London, reprint edition, 1985.
- [152] W. Döring. *Ann. Phys.*, 32:259, 1938.
- [153] E. Fawcett and W. A. Reed. *Phys. Rev. Lett.*, 9:336, 1962.
- [154] This term was first introduced by E. Gruneisen and J. Gielessen, *Ann. Phys. (Leipzig)* **27**, 243 (1936).
- [155] B. Lenoir, F. Brochin, and J.-P. Michenaud. *Europhys. Lett.*, 58:93, 2002.
- [156] K. H. Ploog. *J. Appl. Phys.*, 91:7256, 2002.
- [157] C. H. Li, G. Kioseoglou, O. M. J. van 't Erve, A. T. Hanbicki, B. T. Jonker, R. Mallory, M. Yasar, and A. Petrou. *Appl. Phys. Lett.*, 85:1544, 2004.
- [158] V. F. Motsnyi, J. De Boeck, J. Das, W. Van Roy, G. Borghs, E. Goovaerts, and V. I. Safarov. *Appl. Phys. Lett.*, 81:265, 2002.
- [159] F. Heusler. *Verh. Dtsch. Phys. Ges.*, 5:219, 1903.
- [160] S. H. Liou, S. S. Malhotra, J. X. Shen, M. Hong, J. Kwo, H. S. Chen, and J. P. Mannaerts. *J. Appl. Phys.*, 73:6766, 1993.
- [161] J. Herfort, H.-P. Schönherr, and K. H. Ploog. *Appl. Phys. Lett.*, 83:3912, 2003.
- [162] J. Herfort, H.-P. Schönherr, K.-J. Friedland, and K. H. Ploog. *J. Vac. Sci. Technol. B*, 22:2073, 2004.
- [163] J. Herfort, H.-P. Schönherr, A. Kawaharazuka, M. Ramsteiner, and K. H. Ploog. *J. Cryst. Growth*, 278:667, 2005.
- [164] A. Ionescu, C. A. F. Vaz, T. Trypiniotis, C. M. Gürtler, M. E. Vickers, H. García-Miquel, and J. A. C. Bland. *J. Magn. Magn. Mater.*, 286:72, 2005.
- [165] A. Ionescu, C. A. F. Vaz, T. Trypiniotis, C. M. Gurtler, H. Garcia-Miquel, J. A. C. Bland, M. E. Vickers, R. M. Dalgliesh, S. Langridge, Y. Bugoslavsky, Y. Miyoshi, L. F. Cohen, and K. R. A. Ziebeck. *Phys. Rev. B*, 71:094401, 2005.

- [166] F. Xu, J. J. Joyce, M. W. Ruckman, H. W. Chen, F. Boscherini, D. M. Hill, S. A. Chambers, and J. H. Weaver. *Phys. Rev. B*, 35:2375, 1987.
- [167] Y.F. Hsieh, M. Hong, J. Kwo, A.R. Kortan, H.S. Chen, and J.P. Mannaerts. In G. B. Stringfellow, editor, *GaAs and Related Compound*, volume 154, page 95. IOP Conf. Ser. No. 120, Institute of Physics, London, 1992.
- [168] D. Y. Noh, Y. Hwu, J. H. Je, M. Hong, and J. P. Mannaerts. *Appl. Phys. Lett.*, 68:1528, 1996.
- [169] W. A. Hines, A. H. Menotti, J. I. Budnick, T. J. Burch, T. Litrenta, V. Niculescu, and K. Raj. *Phys. Rev. B*, 13:4060, 1976.
- [170] R. A. de Groot, F. M. Mueller, P. G. van Engen, and K. H. J. Buschow. *Phys. Rev. Lett.*, 50:2024, 1983.
- [171] V. Y. Irkhin and M. I. Katsnel'son. *Phys. Usp.*, 37:659, 1994.
- [172] S. Fujii, S. Ishida, and S. Asano. *J. Phys. Soc. Jpn.*, 63:1881, 1994.
- [173] R. J. Soulen, J. M. Byers, M. S. Osofsky, B. Nadgorny, T. Ambrose, S. F. Cheng, P. R. Broussard, C. T. Tanaka, J. Nowak, J. S. Moodera, A. Barry, and J. M. D. Coey. *Science*, 282:85, 1998.
- [174] L. J. Singh, Z. H. Barber, Y. Miyoshi, Y. Bugoslavsky, W. R. Branford, and L. F. Cohen. *Appl. Phys. Lett.*, 84:2367, 2004.
- [175] G. A. de Wijs and R. A. de Groot. *Phys. Rev. B*, 64:020402, 2001.
- [176] J. Kudrnovsky, N. E. Christensen, and O. K. Andersen. *Phys. Rev. B*, 43:5924, 1991.
- [177] G. Schmidt and L. W. Molenkamp. *Semicond. Sci. Technol.*, 17:310, 2002.
- [178] E. I. Rashba. *Phys. Rev. B*, 62:R16267, 2000.
- [179] X. Jiang, R. Wang, R. M. Shelby, R. M. Macfarlane, S. R. Bank, J. S. Harris, and S. S. Parkin. *Phys. Rev. Lett.*, 94:056601, 2005.
- [180] G. Schlatter, G. Inden, and W. Pitch. *Z. Metallkd.*, 65:94, 1974.
- [181] H. Wever and G. Froberg. *Z. Metallkd.*, 65:747, 1974.
- [182] A. Kawaharazuka, M. Ramsteiner, J. Herfort, H.-P. Schönherr, H. Kostial, and K. H. Ploog. *Appl. Phys. Lett.*, 85:3492, 2004.
- [183] S. Ishida, T. Masaki, S. Fujii, and S. Asano. *Physica B*, 245:1, 1998.
- [184] B. Lépine, S. Ababou, A. Guivarc'h, G. Jézéquel, S. Députier, R. Guérin, A. Filipe, A. Schuhl, F. Abel, C. Cohen, A. Rocher, and J. Crestou. *J. Appl. Phys.*, 83:3077, 1998.
- [185] M. Hong, H. S. Chen, J. Kwo, A. R. Kortan, J. P. Mannaerts, B. E. Weir, and L. C. Feldman. *J. Cryst. Growth*, 111:984, 1991.

- [186] P. J. Webster and K. R. A. Ziebeck. Crystallographic structure, Heusler alloys. In P. J. Webster and K. R. A. Ziebeck, editors, *Landolt-Börnstein- Group III Condensed Matter*, volume 19, page 101. Springer-Verlag GmbH, 1988.
- [187] M. Fanciulli, G. Weber, H. van Känel, and N. Onda. *Phys. Scr.*, 54:16, 1994.
- [188] G. Kötter, K. Nembach, F. Wallow, and E. Nembach. *Mater. Sci. Eng. A*, 114:29, 1989.
- [189] P. J. Webster and K. R. A. Ziebeck. Crystallographic structure, Heusler alloys. In P. J. Webster and K. R. A. Ziebeck, editors, *Landolt-Börnstein- Group III Condensed Matter*, volume 19, pages 75–79. Springer-Verlag GmbH, 1988.
- [190] V. Niculescu, K. Raj, J. I. Budnick, T. J. Burch, W. A. Hines, and A. H. Menotti. *Phys. Rev. B*, 14:4160, 1976.
- [191] V. Niculescu, J. I. Budnick, W. A. Hines, K. Raj, S. Pickart, and S. Skalski. *Phys. Rev. B*, 19:452, 1979.
- [192] B. Jenichen, V. M. Kaganer, J. Herfort, D. K. Satapathy, H.-P. Schönherr, W. Braun, and K. H. Ploog. *Phys. Rev. B*, 72:075329, 2005.
- [193] W. B. Muir, J. I. Budnick, and K. Raj. *Phys. Rev. B*, 25:726, 1982.
- [194] M. Goto and T. Kamimori. *J. Phys. Soc. Jpn.*, 52:3710, 1983.
- [195] K. Lenz, E. Kosubek, K. Baberschke, H. Wende, J. Herfort, H.-P. Schönherr, and K. H. Ploog. *Phys. Rev. B*, 72:(to be published), 2005.
- [196] M. Bowen, K.-J. Friedland, J. Herfort, H.-P. Schönherr, and K. H. Ploog. *Phys. Rev. B*, 71:172401, 2005.
- [197] R. I. Potter. *Phys. Rev. B*, 10:4626, 1974.
- [198] F. P. Beitel and Jr. E. M. Pugh. *Phy. Rev.*, 112:1516, 1958.
- [199] E. R. Sanford, A. C. Ehrlich, and E. M. Pugh. *Phy. Rev.*, 123:1947, 1961.
- [200] H. Ashworth, D. Sengupta, G. Schnakenberg, L. Shapiro, and L. Berger. *Phy. Rev.*, 185:792, 1969.
- [201] S. Foner, F. E. Allison, and Emerson M. Pugh. *Phy. Rev.*, 109:1129, 1958.
- [202] A. Sinha and A. K. Majumdar. *J. Appl. Phys.*, 50:7533, 1979.

# List of Acronyms

AFM .....	atomic force microscopy
AHE .....	anomalous Hall effect
AMR .....	anisotropic magnetoresistance
ASC .....	antisymmetric component
DMS .....	diluted magnetic semiconductors
FM .....	ferromagnetic metal
FM/SC .....	ferromagnet semiconductor hybrid structures
FWHM .....	full-width-at-half-maximum
GI .....	grazing incidence
GE .....	grazing exit
GMR .....	giant magnetoresistance
HMF .....	Half metallic ferromagnet
HRXRD .....	high resolution X-ray diffraction
MBE .....	molecular beam epitaxy
MOKE .....	magneto-optic Kerr effect
OHE .....	ordinary Hall effect
PHE .....	planar Hall effect
RHEED .....	reflection high-energy electron diffraction
RT .....	room temperature
RTA .....	rapid thermal annealing
RSM .....	reciprocal space map
SC .....	semiconductors
SQUID .....	superconducting quantum interference device
STM .....	scanning tunnelling microscopy
SWM .....	Stoner-Wohlfarth model
TEM .....	transmission electron microscopy
UHV .....	ultra high vacuum
UMA .....	uniaxial magnetic anisotropy
XRD .....	X-ray diffraction
XRR .....	X-ray reflectivity



# Acknowledgement

I avail this opportunity to express my deep sense of gratitude to the following persons, whose significant contributions make it possible to bring out this thesis.

.....Prof. Dr. Klaus H. Ploog for providing me with an excellent scientific environment and for providing the financial means during my stay at PDI.

.....Prof. Dr. Kurt R. A. Ziebeck and Prof. Dr. W. Ted Masselink for taking their valuable time to review this work.

.....Dr. J. Herfort for his consistent help, guidance, support and constant encouragement throughout this work. I sincerely thank him for his really cool and co-operative discussions and sharing of several ideas. I also thank him for help with German language, arranging apartment for stay in Berlin, and for very good holiday guidance !

.....Dr. K.-J. Friedland not only for his constant guidance during magnetotransport measurements but also for several following discussions which finally lead to a very significant contribution to this work. I also extend my thanks for including part of this work as a contribution to several national and international conferences.

.....Mr. H.-P. Schönherr for his truly invaluable technical help not only with the growth in MBE system but also with the HRXRD and AFM measurements. I also express my sincere thanks for keeping M5 working in spite of several accidents due to me.

.....Dr. M. Bowen for his truly invaluable help during magnetotransport measurements, discussions of several ideas, and careful reading of this thesis. I also enjoy his non-scientific discussion specially at tea parties !

.....Dr. L. Perez for several scientific discussions related to magnetism, and careful reading of this thesis. We had a very good time together sharing the same office with many more physics and non-physics discussions.

.....Dr. L. Däweritz for several scientific discussions specially related to RHEED and symmetry. I also thank him for his interest in my work and careful reading of this thesis.

.....Mrs. E. Wiebicke and Mrs. A. Riedel for pre-patterning and Hall bar sample preparation. I also extend my thanks to the entire staff of clean room.

.....Dr. R. Hey for several scientific discussions specially related to symmetry of (113) surfaces.

.....Dr. O. Brandt for several scientific discussions specially related to HRXRD and RHEED.

.....Dr. B. Jenichen for his help during HRXRD measurements and several related discussions. I extend my thanks for keeping the HRXRD Lab in an excellent working conditions.

.....Dr. W. Braun for his help during RHEED experiments and related discussions.

.....Dr. D. Kolovos-Vellianitis for his valuable suggestions during preparation of seminars and writing of the thesis. I also extend my thanks for arranging several memorable parties, picnics and get-to-gather. Especially, I thank him for his help during the shifting of my apartment.

.....Dr. M. Hashimoto for several discussions on ordering and magnetic properties and for his help during SQUID measurements.

.....Dr. A. Kawaharazuka for fruitful discussions related to magnetization reversal and help with MOKE measurements.

.....Mrs. C. Herrmann and Dr. D. Schaadt for their help during AFM and SQUID measurements.

.....Dr. Y. Takagaki for his help during SEM measurements of Fe films on prepatterned GaAs and for some related discussions.

.....Dr. M. Moreno and Dr. J.-M. Chauveau for her help during SQUID and HRXRD measurements and several discussions.

.....Our librarians Mrs. D. Dormeyer, Mrs. S. Räther for their help in getting old articles and books. Both of them are very kind, also in cases where I forget to bring back the books.

.....Mrs. P. Grasnick for her help for everything starting from my arrival until now. I would like to thank Mrs. I. Schuster for the poster printing for the conferences and Mr. J. Schönberg for his help with computers.

.....My Ph.D. colleagues, namely Mr. T. Ive, Mr. Y.-J. Sun, Ms. D. Hu, Mr. R. Engel-Herbert and Dr. G. Müßler for many discussions. I enjoyed many discussions during the Ph.D. talks by all my friends and especially the presence of Dr. Oliver Brandt, Dr. Manfred Ramsteiner, Dr. Paulo Santos and Dr. Carsten Hucho.

.....Mr. D. K. Satapathy for several RHEED and HRXRD related discussions.

.....My Indian friends, Mr. P. Misra, Mr. D. K. Satapathy, Dr. J. Mohanty and Dr. S. Dhar not only for physics discussions but also for giving me extra enjoyment and "truly Indian" excitements.

Lastly, my deepest appreciation goes to my parents and my brothers. Their patience, love, sacrifice and support is beyond words.

# Curriculum Vitae

Name:	Pranaba Kishor Muduli
Geburtstag:	01.November 1978
Geburtsort:	Jagatsingpur, Orissa (Indien)
Seit 05.09.2002	Promotionsstudent an der Humboldt-Universität zu Berlin und am Paul Drude Institut für Festkörperelektronik in der Arbeitsgruppe von Herrn Priv.-Doz. Dr. L. Däweritz unter Betreuung von Herrn Prof. Dr. K. H. Ploog
03.02.2003	Master of Technology (M.Tech.) Indian Institute of Technology, Kharagpur, Indien Thema: "Study of ruthenium/3C-silicon carbide Schottky junctions for hydrogen gas sensor applications"
07.2000 – 02.2002	Studium der Materialwissenschaft und -technik Indian Institute of Technology, Kharagpur, Indien
05.01.2002	Master of Science (M.Sc.) in Physik Utkal University, Orissa, Indien
07.1998 – 06.2000	Studium der Physik Utkal University, Orissa, Indien
03.02.2000	Bachelor of Science (B.Sc.) Sambalpur University, Orissa, Indien
07.1995 – 06.1998	Studium der Physik, Chemie und Mathematik Sambalpur University, Orissa, Indien

# Selbständigkeitserklärung

Hiermit erkläre ich, die vorliegende Arbeit selbständig ohne fremde Hilfe verfaßt und nur die angegebene Literatur und Hilfsmittel verwendet zu haben.

Ich habe mich an keiner anderen Universität um einen Doktorsgrad beworben und besitze auch keinen entsprechenden Doktorsgrad.

Ich erkläre die Kenntnis der dem Verfahren zugrunde liegenden Promotionsordnung der Mathematisch-Naturwissenschaftlichen Fakultät I der Humboldt-Universität zu Berlin.

Pranaba Kishor Muduli  
29. September 2005